Feasibility of Lidar Missions in Low Altitude Orbits Maintained by Electric Propulsion

Nicolas Didier Robert Roger Lévêque

MSc, BEng (Hons), DUT

This thesis is submitted in partial fulfilment

of the requirements of Kingston University

for the Degree of Doctor of Philosophy

August 2012

© Nicolas D.R.R. Lévêque

Abstract

Lidars are very promising instruments for the remote-sensing of the Earth, and are eagerly awaited for operational missions, particularly in the observation of the atmosphere. However, spaceborne lidars are still in their early development and there have been many setbacks associated with their technology. The high energy of the laser beam contributes to the formation of contamination deposit on laser optics, leading to the degradation of the lidar performance and eventual failure of the instrument. This high energy requirement can partially or totally be offset by a larger telescope and / or a lower orbit, with the implication of a greater drag force acting on the satellite.

This work investigates the options for satellite and lidar telescope configuration which minimise their contribution to drag while maximising the telescope aperture diameter for lidar performance. A MATLAB/Simulink trajectory model is developed to establish the propulsion requirements for drag compensation. Parametric models are used to size the satellite, its subsystem and the lidar.

This study elaborates the conditions under which a lidar mission might work in a low altitude orbit. In particular, it explores the feasibility and applicability of four concepts against the requirements of some challenging lidar missions. The model developed also identifies that past studies may have under-estimated the electric propulsion requirements for lidar missions in low altitudes.

Acknowledgments

With so many years since I first started my PhD, the list of people I am indebted to is unavoidably long.

I am grateful to my supervisor, and also former lecturer and colleague, Dr Chris Welch, who has been an inspiration since I first came to Kingston University some 14 years ago. He has played a major part in my career in the space industry by first teaching me the basics during my undergraduate studies, giving me the opportunity of pursuing a research degree, and being an example for my (rather short) teaching career. All the best in Strasbourg!

I am also thankful to Dr Andy Curley for the KTP funding I received in the first couple of years of this adventure.

My work at Astrium has been a major influence on this research, and I am truly indebted to many of my colleagues. To Mick Johnson, Carl Warren and the Mission Systems group in Stevenage, who have been very flexible and helpful in me completing my PhD. To my former manager, Tony Sephton, who has given me the chance to work on the A-SCOPE Phase 0 study. To my colleagues in Germany, the true lidar experts, Hans-Reiner Schulte, Paul Zeller and Christian Wührer, for sharing some of their knowledge and taking the time to explain some basics – if errors still remain in this manuscript, they are solely mine. I would also like to thank Paolo Bensi, Yannig Durand and Jérôme Caron at ESA for their role in the A-SCOPE Phase 0 study.

Cependant, tout ceci n'aurait jamais été possible sans mes parents à qui je dois tout... et bien plus davantage ! L'éducation qu'ils m'ont donnée, leurs encouragements à étudier tout en me laissant le temps de rêver, les sacrifices qu'ils se sont imposés en silence, et avant tout l'amour et la vie qu'ils nous ont donnés. Il me faudrait plus de pages que cette thèse n'en contient pour vous remercier.

Il y a des décisions que l'on prend soudainement dans une vie, et l'on se demande parfois quelle vie on aurait eue s'ils avaient été différents. Je me suis souvent posé cette question, et je sais que plusieurs de mes choix ont été influencés par mes sœurs, Delphine et Chrystelle : partir à l'étranger et suivre mes rêves, notamment. Vous avez été (et êtes toujours !) des modèles pour moi, et sans vous je ne serais jamais arrivé où je suis maintenant. Merci aussi à leurs maris et enfants, nos familles, pour les rires et les bonheurs simples partagés.

Je n'oublie pas non plus Elie et Anneso, qui occupent une place particulière depuis tant d'années déjà, et qui ont été un support tout au long.

मेरे ससुराल वालों को बहुत घनयवाद सब कुछ के लिये।

While this project started many years ago, most of the progress was made over the last few years, partly because of my career change, but mostly because of the invaluable support of my dear wife, Rachna. Her love, care and patience have been vital during this process. It has been as much of a sacrifice, if not more, for her as it has been for me!

मुझको तुमसे बहुत प्यार हैं।

Table of Content

ABSTRACT i

Acknowledgment ii

List of Figures x

List of Tables xvi

Acronyms xxi

Nomenclature xxv

CHAPTER 1 INTRODUCTION 1

1.1 Background 1

1.2 Motivation 2

1.3 Goal 2

1.4 Thesis outline 2

CHAPTER 2 SPACEBORNE LIDAR REMOTE SENSING 4

2.1 Introduction 4

2.2 A brief history 5

2.3 Fundamentals of Lidar 9

2.4 Types of Lidars 13

2.4.1 Altimetry Lidar 13

2.4.2 Backscatter Lidar 13

2.4.3 DIAL 16

2.4.4 Doppler Lidar 17

2.5 Technical challenges 19

2.5.1 Fundamentals of laser 19

2.5.2 Laser-induced damage and contamination 22

2.6 Lidar mission requirements and study boundaries 25

2.6.1 Type of orbit *25*

2.6.2 Spacecraft size *26*

2.6.3 Lidar performance *27*

2.6.4 Telescope diameter requirements *30*

2.7 Conclusion 38

CHAPTER 3 SATELLITE AND INSTRUMENT CONFIGURATION 39

3.1 Introduction 39

3.2 Satellite Configuration 40

3.2.1 Lidar accommodation options *40*

3.2.2 Ballistic coefficient *41*

3.2.3 Launch Vehicle Fairing *45*

3.2.4 Other satellite configuration aspects *47*

3.2.5 Satellite configuration trade-off *49*

3.3 Telescope Designs for Front-Mounted Lidars 51

3.3.1 Optical aberrations *51*

3.3.2 Telescope configuration options *52*

3.3.3 Telescope configuration selection *58*

3.3.4 Telescope Sizing for front-mounted lidars *60*

3.3.5 Applicability of compact Lidar designs *68*

3.3.6 Aerodynamic properties *68*

3.4 Large Lidar Missions Configuration and Sizing 71

3.4.1 Configuration and telescope sizing *71*

3.4.2 Aerodynamic properties *71*

3.5 Conclusions 73

CHAPTER 4 LOW-THRUST TRAJECTORY MODELLING 75

4.1 Introduction 75

4.2 Low altitude dawn-dusk orbit 76

4.2.1 The Classical Orbit Elements *76*

4.2.2 Sun-synchronous orbit ... *78*

4.2.3 Frozen orbit ... *78*

4.3 Equations of motion for a low-thrust spacecraft ... 80

4.3.1 Gauss Equation ... *80*

4.3.2 Equinoctial Orbital Elements ... *82*

4.3.3 Equinoctial-to-Cartesian transformation ... *85*

4.3.4 The rotating radial frame ... *86*

4.4 Perturbation forces and modelling ... 88

4.4.1 Forces relevant to dawn-dusk orbits ... *88*

4.4.2 Atmospheric drag ... *89*

4.4.3 Non-spherical Earth gravity ... *102*

4.4.4 Luni-solar gravity perturbation ... *107*

4.4.5 Solar radiation pressure ... *112*

4.4.6 Propulsive force ... *116*

4.5 Trajectory model ... 117

4.5.1 Overview ... *117*

4.5.2 Model validation ... *119*

4.5.3 Solar activity and atmospheric density ... *125*

4.5.4 Simulation cases and initial conditions ... *126*

4.6 Results ... 126

4.6.1 Propulsive acceleration required ... *126*

4.6.2 Total impulse ... *129*

4.7 Conclusion ... 130

CHAPTER 5 ELECTRIC PROPULSION FOR LOW-EARTH ORBITS ... 131

5.1 Introduction ... 131

5.2 Key Characteristics of a Propulsion System ... 132

5.3 Propulsion Requirements ... 133

5.3.1 Concept 1 ... *133*

5.3.2 Concept 2 ... *134*

5.3.3 Concept 3 ... *135*

5.3.4 Concept 4 ... *135*

5.4 Types of Electric Propulsion ... 136

5.4.1 Electrothermal ... *136*

5.4.2 Electrostatic ... *137*

5.4.3 Electromagnetic ... *139*

5.4.4 Summary of EP characteristics ... *140*

5.5 Trade-off for Atmospheric Drag Compensation ... 141

5.5.1 Unsuitable options ... *141*

5.5.2 Trade-off criteria ... *141*

5.5.3 Trade-off for Concept 1 ... *141*

5.5.4 Trade-off for Concept 2 ... *144*

5.5.5 Trade-off for Concept 3 ... *146*

5.5.6 Trade-off for Concept 4 ... *148*

5.5.7 Summary ... *150*

5.6 The GOCE mission and the T5 Thruster ... 151

5.6.1 Overall Description ... *151*

5.6.2 The T5 Thruster ... *153*

5.7 Ion Thruster Durability ... 155

5.8 Electric Propulsion System for the Lidar Concepts ... 158

5.8.1 Mass budget ... *161*

5.8.2 Power budget ... *161*

5.8.3 Summary ... *163*

5.9 Conclusion ... 165

CHAPTER 6 INSTRUMENT AND PLATFORM SIZING ... 166

6.1 Introduction ... 166

6.2 Overall Requirements ... 168

6.2.1 General configuration *168*

6.2.2 Pointing requirements *171*

6.2.3 Thermal requirements *172*

6.3 Instrument Detailed Design 173

6.3.1 Instrument Architecture *173*

6.3.2 Opto-mechanical configuration of the four concepts *175*

6.3.3 Mass budget *176*

6.3.4 Power Budget and Thermal Load *178*

6.3.5 Data Rate and Volume *181*

6.4 Sizing of platform subsystems 182

6.4.1 Thermal control system *182*

6.4.2 Electrical power system *189*

6.4.3 Structure *205*

6.4.4 Onboard Data Handling *207*

6.4.5 Payload Data Handling and Transmission *208*

6.4.6 Telemetry, Tracking and Command *209*

6.4.7 Attitude and Orbit Control System *210*

6.4.8 Harness *214*

6.5 Mass and Power Budgets 215

6.5.1 Margin philosophy *215*

6.5.2 Validation of the sizing process *215*

6.5.3 Concept 1 ..... *216*

6.5.4 Concept 2 ..... *217*

6.5.5 Concept 3 ..... *218*

6.5.6 Concept 4 ..... *219*

6.6 Conclusion 220

CHAPTER 7 APPLICABILITY OF THE MISSION CONCEPTS 221

7.1 Introduction 221

7.2 Concept 1: front-mounted lidar, 1150 mm diameter 222
7.2.1 Concept summary *222*
7.2.2 Applicability of concept *223*
7.3 Concept 2: front-mounted lidar, 1800 mm diameter 224
7.3.1 Summary of concept *224*
7.3.2 Applicability *225*
7.4 Concept 3: nadir-mounted lidar, 3000 m diameter 226
7.4.1 Summary of concept *226*
7.4.2 Applicability *228*
7.5 Concept 4: nadir-mounted lidar, 3500 mm diameter 228
7.5.1 Summary of concept *228*
7.5.2 Applicability *230*
7.6 Comparison with other studies 230
7.7 Synthesis 232

CHAPTER 8 SUMMARY AND FURTHER WORK 233

8.1 Summary 233
8.2 Key Thesis Contributions 235
8.3 Further Work 235

REFERENCES 237

APPENDIX A – TRAJECTORY MODEL 252

List of Figures

Figure 2-1. Searchlight scene geometry [Eltermann, 1966] 6

Figure 2-2. Typical lidar setup with a biaxial configuration 10

Figure 2-3. Direct vs. Heterodyne/Homodyne measurement 12

Figure 2-4. Illustration of the three processes that can occur when EM radiation interacts with atoms. 20

Figure 2-5. Schematic representations of lasers 21

Figure 2-6. Optical microscopy of LIC deposits. 23

Figure 2-7. GLAS laser pulse energy history for operating periods up to campaign 3d. 25

Figure 2-8. Representation of the trade space between the three parameters of the simplified lidar equation. 30

Figure 2-9. Power-aperture product, corrected for altitude, for a range of missions 31

Figure 2-10. Engineering drawing of ALADIN [Morancais, 2006] 32

Figure 2-11. Aeolus instrument scaling 33

Figure 2-12. One of the two WALES concepts proposed during the Phase A study [ESA, 2004b] 34

Figure 2-13. WALES instrument scaling 35

Figure 2-14. A-SCOPE Spacecraft configuration for the 1.57-μm IPDA lidar [ESA, 2008] 36

Figure 2-15. A-SCOPE instrument scaling 37

Figure 3-1. Lidar accommodation options (blue = lidar, green = platform) 40

Figure 3-2. Artist impression of Aeolus (left) and EarthCARE (right) 41

Figure 3-3. Drag coefficient as a function of altitude for various satellite shapes (spherical, flat plate, S3-1 satellite, and longitudinal cylinder) [Moe, 2006] 42

Figure 3-4. Illustration of the configuration options for the front wall of the satellite. 44

Figure 3-5. Vega fairing dimensions and payload volume 45

Figure 3-6. Soyuz fairing volume in single (left) and dual launch configuration (right). 46

Figure 3-7. Illustration of the accommodation options of the satellite inside Vega fairing and Soyuz lower volume (not to scale). 47

Figure 3-8. Non-exhaustive list of solar array accommodation options. 48

Figure 3-9. Illustration of the two accommodation options retained 50

Figure 3-10. On-axis, all-reflective telescope concepts 53

Figure 3-11. Off-axis telescope concepts. 55

Figure 3-12. Tilted-mirror telescope concepts. 55

Figure 3-13. Catadioptric telescope concepts. 55

Figure 3-14. Telescope design trade-off tree. 56

Figure 3-15. Telescope accommodation options. 57

Figure 3-16. Cassegrain telescope layout and parameters 60

Figure 3-17. Computation process of Cassegrain telescope optical properties 61

Figure 3-18. Envelope parameters for the front-mounted Cassegrain telescope. 63

Figure 3-19. Lidar diagonal for a range of primary mirror diameters and altitudes, and for a footprint diameter of 50 m (top) and 100 m (bottom). 66

Figure 3-20. Influence of the pinhole diameter on the lidar size 67

Figure 3-21. Comparison of the power-aperture products of the two front-mounted telescopes (bottom) with the mission specific ones (top) 69

Figure 4-1. Representation of Classical Orbital Elements 77

Figure 4-2 Orbit parameters required for a frozen orbit. 79

Figure 4-3. Representation of the Equinoctial Reference Frame. 85

Figure 4-4. Representation of the RTN frame 87

Figure 4-5 Magnitude of various accelerations exerted on a spacecraft in LEO [Fortescue et al, 2003] 88

Figure 4-6. Effect of the rotation of the Earth on the velocity of the satellite relative to the atmosphere 91

Figure 4-7. Drag coefficient as a function of the satellite's lateral-to-front area ratio (including solar arrays) and incidence angles 92

Figure 4-8. Ballistic Coefficient distribution for various combinations of cross-section areas, drag coefficients and masses. 93

Figure 4-9. Illustration of the atmospheric bulge occuring 2 hours after noon 96

Figure 4-10 Relative error in density for intermediate altitudes between the reference altitudes of 240, 300 and 360 km. 101

Figure 4-11 Geoid of equal gravitational potential (EGM96 model) [ESA, 2006] 102

Figure 4-12. Examples of the different kinds of spherical harmonics [Universität Stuttgart, 2009].. 103

Figure 4-13. The third-body perturbation problem geometry. 108

Figure 4-14. Error in Moon's distance from the Earth as calculated by the expansion series with respect to the JPL's Horizons data: absolute (top) and relative (bottom). 110

Figure 4-15. Force due to incident solar radiation onto a surface. 112

Figure 4-16. Conical shadow model 114

Figure 4-17. Illustration of the Simulink model for the trajectory simulations. 118

Figure 4-18. Semi-major axis, eccentricity and inclination behaviour under J_2 effect only, for the first couple of orbits 121

Figure 4-19. Examples of COEs under J2 only, for the developed model (left) and STK simulation (right). 123

Figure 4-20. Comparison of COEs under drag only, between the developed model (left) and STK (right). 124

Figure 4-21. F10.7-cm flux theoretical curve, and simulation periods 125

Figure 4-22. Thrust profile for BC = 60 kg/m^2, h = 260 km and peak solar activity 127

Figure 4-23. Thrust profile for BC = 180 kg/m^2, h = 350 km and minimum solar activity 127

Figure 4-24. Maximum thrust level during peak solar activity. 128

Figure 4-25. Maximum thrust level during minimum solar activity. 128

Figure 4-26. Total impulse for a mission during peak solar activity. 129

Figure 4-27. Total impulse for a mission during minimum solar activity. 129

Figure 5-1. Schematic view of a resistojet 136

Figure 5-2. Operation principle of a Gridded Ion Engine [NASA, 2008] 137

Figure 5-3. Operation principle of a HET [Arakawa & Komurasaki Lab., 2007] 138

Figure 5-4. Schematic view of a Pulsed Plasma Thruster (PPT) 139

Figure 5-5. Specific power vs. specific impulse for various electric propulsion systems. 140

Figure 5-6. Propellant mass fraction (continuous) and power (dashed) of propulsion systems for Concept 1 142

Figure 5-7. Thrust profile for Concept 1, during peak (top) and minimum solar activity. 143

Figure 5-8. Propellant mass fraction (continuous) and power (dashed) of propulsion systems for Concept 2 144

Figure 5-9. Thrust profile for Concept 2, during peak (top) and minimum solar activity. 145

Figure 5-10. Propellant mass fraction (continuous) and power (dashed) of propulsion systems for Concept 3 146

Figure 5-11. Thrust profile for Concept 3 during peak (top) and minimum solar activity. 147

Figure 5-12. Propellant mass fraction (continuous) and power (dashed) of propulsion systems for Concept 4 148

Figure 5-13. Thrust profile for Concept 3 during peak (top) and minimum solar activity. 149

Figure 5-14. Schematic diagram of the GOCE IPA architecture 152

Figure 5-15. Schematic view of the T5 mkV Thruster..... 153

Figure 5-16. Geometric configuration and electric potential for two- and three-grid systems..... 154

Figure 5-17. Schematic representation of the charge-exchange process. 157

Figure 5-18. Actual erosion pattern on the downstream side of an accel grid due to charge-exchange erosion (left) and corresponding idealised patterns (right)..... 157

Figure 5-19. Mass of Xenon for a range of total impulse and three values of specific impulse..... 160

Figure 6-1. CAD model illustrating the FoV constraints 170

Figure 6-2. In Concept 1 and 2, the star trackers (white) are mounted on the opposite side of the baseplate from the Rx telescope (brown) and the Tx telescope (orange). 172

Figure 6-3. A-SCOPE instrument architecture [ESA, 2008]..... 173

Figure 6-4. Overall opto-mechanical configuration of the 1.57-µm A-SCOPE instrument concept proposed at Phase 0 [ESA, 2008]..... 174

Figure 6-5. CAD views of the front-mounted instrument 175

Figure 6-6. CAD view of the nadir-mounted concept..... 175

Figure 6-7. Properties of some common telescope materials. 176

Figure 6-8. Heat exchanges of an electrical system. 183

Figure 6-9. Illustration of the parameters involved in the computation of the view factors..... 186

Figure 6-10. Left: eclispse geometry as seen from 18:00 LST, and right: location of the operational modes in the orbit (seen from 12:00 LST) 191

Figure 6-11. Sun incidence angle for 3 angles of the solar array wrt the orbit plane. 196

Figure 6-12. Solar array steady-state temperature for a solar panel angle of 13° wrt to the orbit plane (red), during summer solstice at an altitude of 300 km. 197

Figure 6-13. Illustration of solar cell packing factor. 199

Figure 6-14. Typical ABSL Battery design [ABSL, 2009] 201

Figure 6-15. Energy vs. mass for a range of AEA Technology batteries. 203

Figure 6-16. Left: A-SCOPE platform structure in Phase 0 [ESA, 2008]; right: Exploded view of Mars Express showing the internal shear walls [ESA, 2001] 205

Figure 6-17. Honeycomb sandwich panel with skin (blue) and adhesive (green). 206

Figure 6-18. Schematic diagram of the Command and Data Handling architecture. 207

Figure 6-19. PDHT architecture. 208

Figure 6-20. TT&C architecture 209

Figure 6-21. Example of electric propulsion momentum build-up (260 km, 180 kg/m^2, 2000 kg) ... 212

Figure 6-22. Illustration of the thrust vector 213

Figure 6-23. Torques generated by electric propulsion thruster for peak thrust angle. 213

Figure 7-1. Dimensions of concept 1 (left) and accommodation in the Vega fairing 223

Figure 7-2. Dimensions of concept 2 (left) and accommodation in the Soyuz fairing. 225

Figure 7-3. Dimensions of concept 3 (left) and accommodation in the Soyuz fairing. 227

Figure 7-4. Dimensions of concept 4 (left) and accommodation in the Soyuz fairing. 229

List of Tables

Table 2-1. Summary of spaceborne lidar missions and instruments. 8

Table 2-2. Properties of some common lasers..... 10

Table 2-3. Launchers for the missions of the Earth Explorer and GMES programmes. 27

Table 2-4. Description of the terms constituting the lidar equation 28

Table 2-5. Characteristics of the ALADIN instrument 33

Table 2-6. Characteristics of one of two WALES concepts at the end of the Phase A study [Price et al, 2005]. 35

Table 2-7. Characteristics of one of the A-SCOPE Phase 0 mission concepts..... 37

Table 3-1. Product of C_D and area for three accommodation options and three front wall configurations for a given volume..... 44

Table 3-2. Satellite configuration trade-off..... 50

Table 3-3. Telescope accommodation trade-off table. 59

Table 3-4. Validation of the model with one of the A-SCOPE telescope designs. 62

Table 3-5. Limits of the diagonal length of a front-mounted lidar instrument in Vega and Soyuz..... 64

Table 3-6. Telescope design parameters used in the sensitivity analysis. 65

Table 3-7. Summary of the front-mounted lidar telescope options. 67

Table 3-8. Aerodynamic characteristics of the front-mounted lidar telescopes 70

Table 3-9. Aerodynamic characteristics of the two options for a front-mounted lidar instrument..... 70

Table 3-10. Summary of the very large nadir-mounted lidar telescopes..... 71

Table 3-11. Aerodynamic characteristics of the very large telescopes..... 72

Table 3-12. Spacecraft aerodynamic characteristics for the very large telescope options. 72

Table 3-13. Summary of the four lidar mission concepts to be investigated..... 73

Table 4-1. Likely combinations of cross-section areas, masses and drag coefficients..... 93

Table 4-2. Exponential atmospheric model for selected altitudes, adapted from [Wertz, 1978]..... 95

Table 4-3 Reference data for the Harris-Priester upper atmospheric density model, as extracted from [Harris & Priester, 1962b]..... 101

Table 4-4. Values of un-normalised coefficients C_{nm} (units of 10^{-9}) from JGM-2 model to degree (n) and order (m) 6..... 104

Table 4-5. Values of un-normalised coefficients S_{nm} (units of 10^{-9}) from JGM-2 model to degree (n) and order (m) 6..... 104

Table 4-6. Zonal harmonic coefficients, Legendre polynomial and its derivative for the first four degrees..... 107

Table 4-7. Properties of common MLI and solar cells..... 113

Table 4-8. Summary of perturbation effects from Klinkrad [2006] and Vallado [2007]..... 120

Table 4-9. Initial conditions for the validation of the drag model against STK..... 122

Table 4-10. Simulations start date..... 125

Table 4-11. Trajectory simulation cases..... 126

Table 5-1. Aerodynamic characteristics of the 1150 mm front-mounted lidar..... 134

Table 5-2. Propulsion requirements of Concept 1 for peak solar activity..... 134

Table 5-3. Aerodynamic characteristics of the 1800 mm front-mounted lidar..... 134

Table 5-4. Propulsion requirements of Concept 2 for peak solar activity..... 134

Table 5-5. Aerodynamic characteristics of the 3000 mm nadir-mounted lidar..... 135

Table 5-6. Propulsion requirements of Concept 3 for peak solar activity..... 135

Table 5-7. Aerodynamic characteristics of the 3500 mm nadir-mounted lidar..... 135

Table 5-8. Propulsion requirements of Concept 4 for peak solar activity..... 135

Table 5-9. Typical performance characteristics of some electric propulsion systems..... 140

Table 5-10. Summary of requirements and suitable propulsion options..... 150

Table 5-11. Characteristics of some European ion thrusters. 151

Table 5-12. Xenon mass required for each concept. 160

Table 5-13. Characteristics of the T5 gridded ion thruster when used for atmospheric drag compensation [Price et al, 2005]. 162

Table 5-14. Mass and mean power budgets for the electric propulsion system for concept 1. 163

Table 5-15. Mass and mean power budgets for the electric propulsion system for concept 2. 164

Table 5-16. Mass and mean power budgets for the electric propulsion system for concept 3. 164

Table 5-17. Mass and mean power budgets for the electric propulsion system for concept 4. 165

Table 6-1. Degree of variability of the platform systems with altitude. 167

Table 6-2. Typical operating temperature ranges for spacecraft subsystems. Adapted from Gilmore et al. (2003) and Panetti (1999). 172

Table 6-3. Mass budget for Concept 1 lidar (1150 mm) 177

Table 6-4. Mass budget for Concept 2 lidar (1800 mm) 177

Table 6-5. Mass budget for Concept 3 lidar (3000 mm) 178

Table 6-6. Mass budget for Concept 4 lidar (3500 mm) 178

Table 6-7. Effect of altitude on distance between measurements. 179

Table 6-8. Wall-plug efficiency for three European lidar missions. 180

Table 6-9. Transmitter power for a range of beam energy and wall-plug efficiency at 100 Hz PRF. 180

Table 6-10. Power budget of the lidar instrument for spacecraft sizing. 181

Table 6-11. Heat load budget and temperature requirement of the lidar instrument under operational conditions for the spacecraft sizing. 181

Table 6-12. Power exchanges between a radiator and its environment for the purpose of thermal control system sizing 184

Table 6-13. Mass and power budgets of the Thermal Control System 189

Table 6-14. Radiator optical properties 189

Table 6-15. Operational modes to be considered for the EPS sizing. 191

Table 6-16. Azur Space triple-junction solar cell characteristics [Azur Space, 2009] 195

Table 6-17. List of degradations and losses for the sizing of the solar array. 195

Table 6-18. Characteristics of the SONY 18650HC, from Spurrett et al [2002] 201

Table 6-19. Electrical Power System mass and power budgets 204

Table 6-20. Mass properties of Aluminium honeycomb sandwich panel materials. 206

Table 6-21. Mass and power budgets of a combined OBC/RIU unit [RUAG, 2009]. 207

Table 6-22. PDHT mass and power budgets 208

Table 6-23. Mass and power budgets of the TT&C subsystem 209

Table 6-24. AOCS hardware involved in Nominal Mode and Safe Mode 211

Table 6-25. AOCS mass and power budgets 211

Table 6-26. Comparison of the performance of reaction wheels and CMG. 214

Table 6-27. Errors in the predictions are sufficiently small for a preliminary design. 215

Table 6-28. Mass budget of concept 1, altitude of 290 km. 216

Table 6-29. Power budget of concept 1, altitude of 290 km 216

Table 6-30. Mass budget of concept 2, altitude of 290 km. 217

Table 6-31. Power budget of concept 2, altitude of 290 km 217

Table 6-32. Mass budget for concept 3, altitude of 320 km. 218

Table 6-33. Power budget for concept 3, altitude of 320 km. 218

Table 6-34. Mass budget for concept 4, altitude of 320 km. 219

Table 6-35. Power budget for concept 4, altitude of 320 km. 219

Table 7-1. Summary of the overall mission requirements 221

Table 7-2. Key characteristics of the satellite for concept 1 222

Table 7-3. Key characteristics of the satellite for concept 2 224

Table 7-4. Key characteristics of the satellite for concept 3 227

Table 7-5. Key characteristics of the satellite with the 3.5 m diameter telescope. 229

Table 7-6. Comparison with previous electric propulsion studies 231

Acronyms

ADM	Atmospheric Dynamics Mission (previous name of the Aeolus mission)
AIAA	American Institute of Aeronautics and Astronautics
ALADIN	Atmospheric LAser Doppler INstrument
AME	Absolute Measurement Error
AOCS	Attitude and Orbit Control System
APD	Avalanche Photo-Diode
APE	Absolute Pointing Error
A-SCOPE	Advanced Space Carbon and Climate Observation of Planet Earth
AST	Autonomous Star Tracker
ATLID	ATmospheric LIDar
ATOX	Atomic Oxygen
BC	Ballistic Coefficient
BOL	Biginning Of Life
CAD	Computer-Assisted Design
CALIOP	Cloud-Aerosol Lidar with Orthogonal Polarisation
CALIPSO	Cloud-Aerosol Lidar and Infrared Pathfinder Satellite Observation
CEOI	Centre for Earth Observation Instrumentation
CFRP	Carbon Fibre Reinforced Plastic
CNES	Centre National d'Etudes Spatiales
COE	Classical Orbital Elements
CoM	Centre of Mass
CPS	Chemical Propulsion System
CSS	Coarse Sun Sensor
DCM	Direction Cosine Matrix
DERA	Defence Evaluation and Research Agency
DET	Direct Energy Transfer
DFACS	Drag-Free and Attitude Control System
DIAL	Differential Absorption Lidar
DOD	Depth Of Discharge
DWL	Doppler Wind Lidar
EarthCARE	Earth Clouds, Aerosols and Radiation Explorer
ECI	Earth Centred Inertial

ECSS	European Cooperation for Space Standardisation
EE	Earth Explorer
EO	Earth Observation
EOE	Equinoctial Orbital Elements
EOL	End Of Life
EP	Electric Propulsion
EPS	Electrical Power System
EQF	Equinoctial Frame
ES	Earth Sensor
ESA	European Space Agency
ESO	European Southern Observatory
EUV	Extreme Ultra-Violet
FDIR	Fault Detection, Isolation and Recovery
FEEP	Field Emission Electric Propulsion
FOG	Fibre-Optic Gyroscope
FoV	Field of View
GIE	Gridded Ion Engine
GIT	Gridded Ion Thruster
GLAS	Geoscience Laser Altimeter System
GOCE	Gravity field and Ocean Circulation Explorer
GPS	Global Positioning System
GRACE	Gravity Recovery And Climate Experiment
GSFC	NASA Goddard Space Flight Center
GTDS	Goddard Trajectory Simulation System
HET	Hall-Effect Thruster
HSRL	High Spectral Resolution Lidar
ICESat	Ice, Cloud, and land Elevation Satellite
ICU	Instrument Control Unit
IPA	Ion Propulsion Assembly
IPCU	Ion Propulsion Control Unit
IPDA	Integrated-Path Differential Absorption (lidar technique)
IR	Infra-Red
ITA	Ion Thruster Assembly
JPL	Jet Propulsion Laboratory

Table 5-11. Characteristics of some European ion thrusters. 151

Table 5-12. Xenon mass required for each concept. 160

Table 5-13. Characteristics of the T5 gridded ion thruster when used for atmospheric drag compensation [Price et al, 2005]. 162

Table 5-14. Mass and mean power budgets for the electric propulsion system for concept 1. 163

Table 5-15. Mass and mean power budgets for the electric propulsion system for concept 2. 164

Table 5-16. Mass and mean power budgets for the electric propulsion system for concept 3. 164

Table 5-17. Mass and mean power budgets for the electric propulsion system for concept 4. 165

Table 6-1. Degree of variability of the platform systems with altitude. 167

Table 6-2. Typical operating temperature ranges for spacecraft subsystems. Adapted from Gilmore et al. (2003) and Panetti (1999). 172

Table 6-3. Mass budget for Concept 1 lidar (1150 mm) 177

Table 6-4. Mass budget for Concept 2 lidar (1800 mm) 177

Table 6-5. Mass budget for Concept 3 lidar (3000 mm) 178

Table 6-6. Mass budget for Concept 4 lidar (3500 mm) 178

Table 6-7. Effect of altitude on distance between measurements. 179

Table 6-8. Wall-plug efficiency for three European lidar missions. 180

Table 6-9. Transmitter power for a range of beam energy and wall-plug efficiency at 100 Hz PRF. 180

Table 6-10. Power budget of the lidar instrument for spacecraft sizing. 181

Table 6-11. Heat load budget and temperature requirement of the lidar instrument under operational conditions for the spacecraft sizing. 181

Table 6-12. Power exchanges between a radiator and its environment for the purpose of thermal control system sizing 184

Table 6-13. Mass and power budgets of the Thermal Control System 189

PPT	Pulsed Plasma Thrusters
PRF	Pulse Repetition Frequency
PVT	Position, Velocity, Time
PXFA	Proportional Xenon Feed Assembly
RAAN	Right Ascension of Ascending Node
RAE	Royal Aircraft Establishment
RF	Radio Frequency
RIT	Radiofrequency Ion Thruster
RIU	Remote Interface Unit
RPE	Relative Pointing Error
RTN	Radial, Tangential, Normal
RW	Reaction Wheel
Rx	Receiver
SDRAM	Synchronous Dynamic Random Access Memory
SM	Safe Mode
SNR	Signal-to-Noise Ratio
SOC	State of Charge
SPT	Stationary Plasma Thrusters
SSMM	Solid State Mass Memory
STR	Star Tracker
TAS	Thales Alenia Space
TC	Telecommand
TCS	Thermal Control System
TIR	Thermal Infra-Red
TM	Telemetry
TT&C	Tracking, Telemetry and Command
TWTA	Travelling Wave Tube Amplifier
Tx	Transmitter
UAH	University of Alabama at Huntsville
UV	Ultra-Violet
VCL	Vegetation Canopy Lidar
WALES	Water vApour and Lidar Experiment in Space
YAG	Yttrium aluminium garnet

Nomenclature

Capital Latin Symbols

A	Surface area of the receiver telescope
A_{rad}	Surface area of a radiative surface
C	Battery capacity
C_{nm}	Tesseral ($n \neq m$) and sectorial ($n = m$) harmonic coefficient for the cosine function
D	Diameter of the receiver telescope
D_1	Diameter of the primary mirror
D_2	Diameter of the secondary mirror
E	Eccentric anomaly
E_e	Energy of the laser pulse
F	Focal length of the telescope
F	View factor
$F_{10.7}$	Flux of radiation at 10.7-cm wavelength (decimetric flux)
F_d	Drag force
H	Density scale height
I	Total impulse
I_{sp}	Specific impulse
$J_{2,...,n}$	Earth gravitational potential zonal harmonic of degree 2,..., n
L	Length of the telescope envelope
L	True longitude of a satellite in its orbit
M	Mean anomaly
N	Molecule number density
$O(R)$	Laser beam / receiver FoV overlap function
P_e	Power of the emitted beam
P_{lidar}	Electric power consumed by the lidar
P_{nm}	Associated Legendre polynomials of the first kind, of degree n and order m
P_{off}	Power received at the offline wavelength (DIAL system)
P_{on}	Power received at the online wavelength (DIAL system)
P_r	Power of the received signal
P_{Rx}	Electric power consumed by the receiver stage of the lidar instrument
P_{Tx}	Electric power consumed by the transmitter stage of the lidar instrument
Q_{diss}	Heat dissipated by a source

R	Range
R	Direction cosine matrix
R	Sunspot number
R_1	Radius of curvature of the primary mirror
R_2	Radius of curvature of the secondary mirror
R_E	Mean radius of the Earth
S	Satellite cross-section area
S_{nm}	Tesseral ($n \neq m$) and sectorial ($n = m$) harmonic coefficient for the sine function
T	Transmission of light through the atmosphere
T	Thrust force
$T_{1,2,\ldots,n}$	Duration of operational mode 1, 2,…,n
T_{orbit}	Orbital period
T_{rad}	Temperature of a radiative surface
T_{SA}	Duration of the period during which the solar arrays generate power
U	Geopotential function
U_B	Vector of the diurnal bulge apex of the atmosphere
V	Satellite velocity
V_{bus}	Bus voltage
$V_{c.o.}$	Orbital velocity of a circular orbit
V_e	Rocket exhaust velocity of the propellant
W	Width of the telescope envelope

Small Latin Symbols

a	Semi-major axis of an orbit
$a_{R,T,N}$	Acceleration along the radial, tangential and normal directions
b	Length of the baffle above the secondary mirror
b	Semi-minor axis of an orbit
c	Speed of light in vacuum
c_d	Drag coefficient
e	Distance between the apex of the primary mirror and the telescope focal point
e	Eccentricity of the orbit
f_1	Focal length of the primary mirror
f_{rep}	Pulse repetition frequency

g_0	Gravitational acceleration at sea level
h	Altitude
h	Specific angular momentum of an orbit
i	Inclination of the orbit with respect to the equator
m	mass
m_p	Propellant mass
m	Order of the geopotential harmonic coefficients
n	Mean index of refraction of the propagation media
n	Orbital mean motion
n	Degree of the geopotential harmonic coefficients
p	Distance between the focal point of the primary mirror and the apex of the secondary mirror
p_{SR}	Solar radiation pressure
q	Distance between the apex of the secondary mirror and the telescope focal point
q	Energy per unit surface area (heat)
s	Distance between the apexes of the primary and secondary mirrors
t	Time
u	Argument of latitude of a satellite in its orbit

Greek Symbols

α	Extinction coefficient due to molecules and particles by scattering and absorption
α	Absorptance of a surface finish
α_s	Right ascension of the Sun
β	Backscatter coefficient
β	Sun incidence angle on the secondary mirror
$\Delta\Phi$	Wavefront error
$\Delta\sigma$	Differential absorption cross-section between on- and off-line wavelengths (DIAL)
Δt	Round-trip time of the laser pulse
δ	Declination of the satellite
δ_s	Declination of the Sun
ε	Emissivity of a surface finish
ϕ	Geocentric latitude
η	Overall efficiency of the lidar system
η_T	Overall efficiency of the thruster

η_{wp}	Wall-plug efficiency
λ	Wavelength
λ	Geocentric longitude
λ_{lag}	Longitude angle between the sub-solar point and the apex of the atmospheric bulge
μ_e	Gravitational parameter of the Earth
ν	True anomaly
ρ	Atmospheric density
ρ	Angular radius of the Earth as seen by the spacecraft
ρ	Reflectivity of a surface finish
σ	Stefan-Boltzmann constant
τ	Laser pulse duration
Ψ	Angle between the position vector of the satellite and the diurnal bulge apex of the atmosphere
Ω	Right-ascension of the ascending node of an orbit
ω	Argument of perigee of an orbit
ω_{atm}	Angular velocity of the atmosphere about the polar axis

Other Symbols

∇	Nabla function
$\in$	Obliquity of the ecliptic plane

Chapter 1

Introduction

1.1 Background

Lidars are very promising instruments for the remote-sensing of the Earth, in particular for the study of the atmospheric structure and composition. A few lidar missions are currently flying or being prepared, but primarily as demonstrators for technology and end-to-end validation. Lidars are not yet ready for operational missions.

Indeed, problems occurring during NASA's ICESat mission and in the development of ESA's ADM-Aeolus have casted doubts over the ability to operate high power lasers in vacuum, and thus over the implementation of lidars in long-term operational missions. One particular problem is the contamination of optics due to the interaction of intense laser radiation with outgassing material, leading to a drastically reduced lifetime. The laser fluence has an influence on this deposit [Schröder, Borgmann, Riede & Wernham, 2008].

No long term solution has yet been found, primarily because the mechanism through which this contamination occurs is still poorly understood [Canham, 2004]. Currently, the main objective is to reduce the presence of contamination source and reduce the laser beam energy.

1.2 Motivation

The question for scientists and users of lidar data is to know when lidar instruments will be available to complement the current suite of space instrumentation. If the development of lidar technology is going to be further delayed, can the problem be partially or totally compensated for at mission design level?

One possibility of reducing the beam energy would be by counterbalancing it with a larger telescope and/or a lower orbit. However, as the orbit altitude diminishes, a satellite experiences a stronger atmospheric drag which must be compensated for to sustain the mission. Electric propulsion systems have been employed as drag compensation system on missions like GOCE. Electric propulsion has also been suggested for lidar missions in order to fly them in lower orbits and improve their performance [Price et al, 2007]. Lidars are typically bulky instruments with aerodynamic characteristics not suited to low altitude orbits. So far, no study has looked into optimising the design of lidar instruments in that respect.

1.3 Goal

The objectives of the present work are thus to:

- establish a lidar and spacecraft configuration that are tailored for low altitude orbits;
- derive the requirements for a propulsion system to compensate for drag
- derive the characteristic of the satellite
- establish the merit of a concept to significantly reduce the laser beam energy while maintaining the lidar performance.

1.4 Thesis outline

Chapter 2 provides a background on spaceborne lidar, the technical challenges faced and present the requirements to be met in order to successfully reduce the laser beam energy while maintaining the desired performance. Chapter 3 investigates satellite and instrumentation configuration options that maximise the aperture diameter of the lidar

telescope while minimising the drag they can generate. A trajectory model is developed in Chapter 4, leading to the requirements definition, trade-off, and selection of the propulsion system in Chapter 5. The process to size the lidar instrument and the satellite is presented in Chapter 6 and the results in Chapter 7, with comparison to other studies. Chapter 8 provides concluding remarks.

Chapter 2

Spaceborne Lidar Remote Sensing

2.1 Introduction

Light Detection and Ranging (LIDAR, often written lidar or Lidar) is the most widespread name for many instruments that can also be known as optical radar, laser radar or LADAR (Laser Detection and Ranging). Some of these names imply that the source of the electromagnetic radiation is not necessarily a laser. Indeed, this type of remote-sensing predates the invention of the laser [Kamerman, 1993].

Lidars can be seen as the type of instruments bridging the gap between optical instruments and radars, combining advantages of both types. Like optical instruments, lidars operate at shorter wavelengths than radars and can therefore measure gases and small-scale phenomena that radar cannot. But lidars, like radars, are range-resolved devices and can perform atmospheric profiling, but at a much improved horizontal resolution than radars. This is also a major improvement compared to passive optical systems which can either be nadir-viewing (high horizontal resolution with poor vertical resolution) or limb-viewing (high vertical resolution with poor horizontal resolution). Lidars also benefit from the special properties of lasers, such as high power, monochromaticity, short duration, and a highly collimated beam

[Measures, 1984]. Since they rely on their own source of illumination, lidar measurements are independent of solar illumination.

Lidars are therefore extremely useful devices in the study of atmospheric composition (molecules and aerosol particles), structure (vertical distribution of constituents), properties (temperature, pressure, humidity information can be retrieved) and dynamic behaviour (wind). [Measures, 1984, Wandinger, 2005]. Atmospheric lidars can either be ground-based, airborne or spaceborne, with their own spatial and temporal resolutions. Lidars can also be used in the study of the Earth's surface (texture, terrain profiling, oceanography).

This chapter presents a brief history and the fundamentals of lidar remote-sensing, followed by a review of the main lidar techniques. It then describes some of the technical difficulties identified during the operation and/or development of some spaceborne lidar instruments, and their impact on the sizing of spaceborne lidar instruments.

2.2 A brief history

The principle of lidar measurements date back to the 1930's, well before the invention of the laser. Then dubbed by an author as a "poor man's radar" [Weitkamp, 2005], the instrument would make measurements of air density profiles in the upper atmosphere using searchlight beams (Figure 2-1).

The development of the lidar then suddenly accelerated with the invention of the laser in 1960 and especially the invention of the Q-switched laser[1] by McClung and Hellwarth in 1962, which led the way to the first observations with a ruby laser in 1963 of the upper atmosphere by Fiocco and Smullin and the troposphere by Ligda [Measures, 1984].

Within a decade all basic lidar techniques had been suggested and demonstrated [Wandinger, 2005]. Airborne downward-pointing lidars have been flown since 1977 [Kramer, 2002], where surface scattering and reflection were the main type of interaction, with surface-wave studies, bathymetry, and water turbidity the first applications [Measures, 1984].

[1] *Q-switching is a method to control both the time duration of laser oscillation and the pulse shape of the laser's output power to provide a single-spike behaviour.*

Further applications, in particular those related to atmospheric measurements, became possible with the advance in technology development, especially on the laser side. Indeed, many lasers have been specifically designed to meet the ever-growing requirements of new lidars: pulse energy, wavelength, pulse width, beam shape, or spectral purity [Wandinger, 2005]. Other technologies in the receiver also required development, such as optical filters with high transmission and narrow bandwidth, efficient detectors for broad wavelength regions, and back-end electronics to handle the growing payload data rate associated with high pulse repetition frequency [Wandinger, 2005].

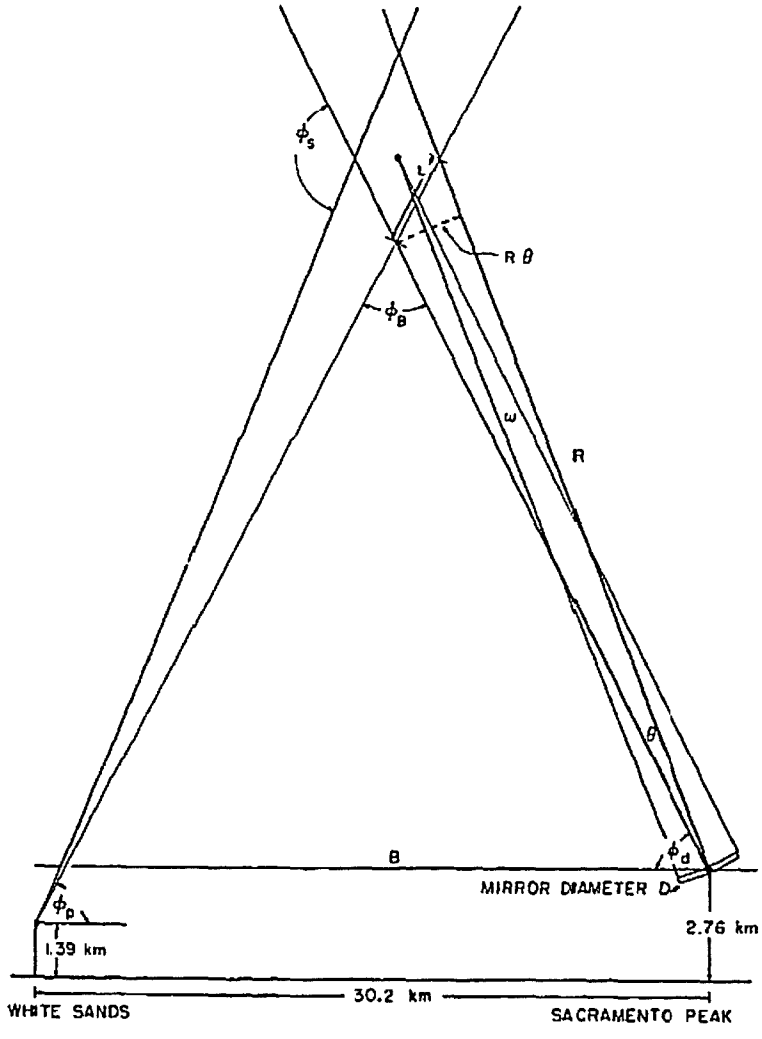

Figure 2-1. Searchlight scene geometry [Eltermann, 1966]

Most airborne instruments were developed during the late 1980s and the 1990s, paving the way for the first spaceborne lidar. NASA developed the Lidar In-space Technology Experiment (LITE) which was flown on the Space Shuttle in September 1994 [Kramer, 2002]. This was followed by other atmospheric lidars: the Russian Balkan-1 on MIR/Spektr module (May 1995), the French ALISSA on MIR/Priroda module (April 1996), with ESA preparing ALADIN and ATLID for the Aeolus (formerly known as ADM) and EarthCARE missions, respectively [Kramer, 2002]. Altimeter lidars were also developed and flown in parallel, primarily by NASA: two models of the Shuttle Laser Altimeter were flown in January 1996 and August 1997, while the Geoscience Laser Altimeter System (GLAS) has been flying on the ICESat mission (launched in 2001) [Kramer, 2002]. The Vegetation Canopy Lidar (VCL) mission initiated in 1996 with a then launch date of 2000 was eventually ceased in 2002 due to implementation difficulties and escalating costs, although development of its Multi-Beam Laser Altimeter (MBLA) was recommended to continue [NASA, 2003].

Table 2-1 gives some information on a selection of spaceborne lidar missions. It should be pointed out that LITE, and ALISSA were experimental instruments, and as a result were both heavy and power hungry. Balkan-1 was light and had a moderate power consumption, but the latter is due to a very small PRF. Thus there is little interest in comparing these experimental instruments / demonstrators with more recent instruments and they have therefore been excluded on the comparison table. However, more information can be found in Kramer [2002] and McCormick [2004].

Mission	ICESat		CALIPSO		VCL	Aeolus	EarthCARE
Instrument	GLAS		CALIOP		MBLA	ALADIN	ATLID
Launch date	Jan. 2003		Apr. 2006		*Cancelled*	2013	2015
Altitude	600 km		705 km		*400 km*	408 km	393 km
Lidar technique	Backscatter & altimetry		Backscatter		Altimetry	Doppler	Backscatter
Mission objectives	Cloud & atmospheric properties, ice & land elevation		Aerosol & cloud backscatter and extinction profiles		Tree canopy height, ground topography	Global wind profile	Cloud and aerosols profiles
Laser type	Nd:YAG		Nd:YAG		Nd:YAG	Nd:YAG	Nd:YAG
Wavelengths	532 nm	1064 nm	532 nm	1064 nm	1064 nm	355 nm	355 nm
Laser beam energy	36 mJ	73 mJ	110 mJ	110 mJ	10 mJ	150 mJ	19 mJ
PRF	40 Hz		20 Hz		242 Hz	100 Hz	100 Hz
Pulse length	6 ns		20 ns		5 ns	15 ns	< 20 ns
Laser beam divergence	110 μrad		100 μrad		?	< 400 μrad	8 μrad
Aperture diameter	1 m		1 m		0.9 m	1.5 m	0.6 m
Rx FOV	160 μrad	475 μrad	130 μrad		300 μrad	15 μrad	25 μrad
Mass	300 kg		156 kg		133 kg	464 kg	231 kg
Power	330 W		124 W		220 W	840 W	370 W
Dimensions	1100 (W) × 1100 (L) × 1750 (H)		1000 (W) × 1490 (L) × 1310 (H)		?	∅1600 × 2000 (H) approx.	1600 (W) × 1480 (L) × 9330 (H)
Data rate	450 kbps		332 kbps		?	11 kbps	822 kbps

Table 2-1. Summary of spaceborne lidar missions and instruments.

Based on data collected from McCormick [2005], Winker et al [2004], NASA [2002], McCormick [2004], Zwally [2002], Wilson & Munzenmayer [2004] and Durand et al [2006].

2.3 Fundamentals of Lidar

The main two parts of a lidar are the transmitter (abbreviated as Tx) and the receiver (Rx). The overall configuration of a spaceborne lidar instrument can be of two types: coaxial or biaxial; referring to the relative position of the Tx and Rx stages. If the laser is transmitted along the optical axis of the receiver, the lidar is said to be coaxial. If the two are physically separated (by more than one Rx primary mirror radius), then it is a biaxial system, and the Tx stage requires a separate Tx telescope (or beam expander). These two types can also be called monostatic and bistatic, respectively, although this is somewhat incorrect, as these terms should normally be used to indicate the relative positions of the Rx and Tx but on a scale comparable to that of the target distance [Kramer, 2002]. Many spaceborne lidars have been referred to as "bistatic", when in fact they are monostatic but biaxial.

The transmitter consists of a laser emitting short pulses of light lasting a few to several nanoseconds, at wavelengths ranging from 250 nm (in the UV spectrum) to about 11 μm (thermal infrared) [Weitkamp, 2005]. The actual wavelength depends on the type of laser used (Table 2-2); for instance, the most common laser source in spaceborne lidar is the solid-state neodymium-doped yttrium aluminium garnet (more commonly encountered in its acronym form of Nd:YAG) laser, which emits at a wavelength of 1064 nm. However, other wavelengths not directly obtainable with lasers can nevertheless be obtained by means of non-linear crystals in a technique known as frequency doubling, tripling or even quadrupling (532, 355 and 266 nm, respectively, with a Nd:YAG laser source). Higher wavelengths have also been available to differential-absorption lidars, first with dye lasers (where the active medium is an organic fluorescent dye dissolved in a liquid solvent [Weichel, 1993]) but these are now being replaced with solid-state lasers and the wide-tuning-range but complex Optical Parametric Oscillators (OPO – another form of nonlinear frequency conversion) [Weitkamp, 2005].

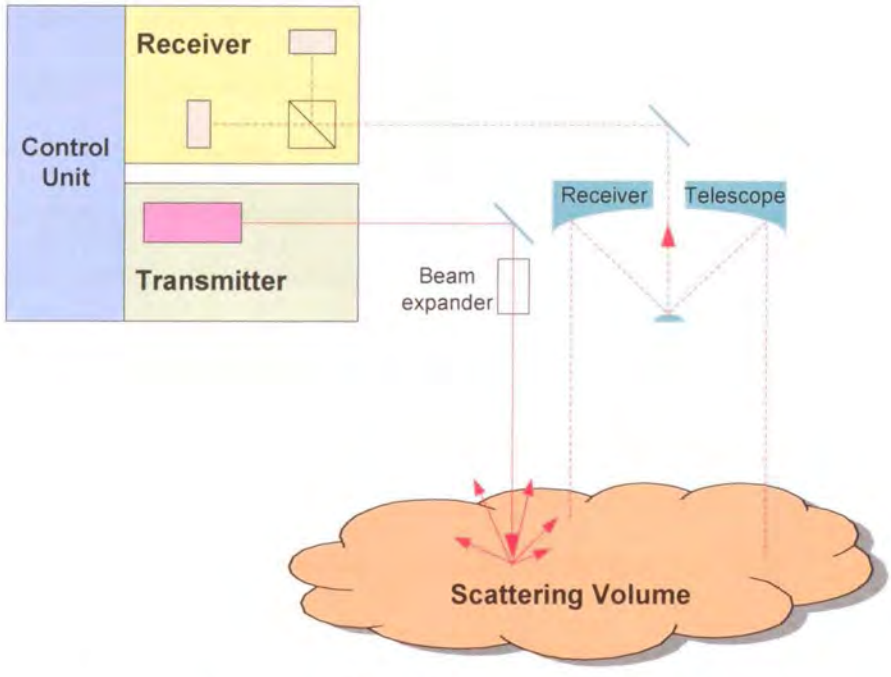

Figure 2-2. Typical lidar setup with a biaxial configuration

Name	Type	Wavelength (nm)	Bandwidth (Hz)
HeNe	Gas	633	2×10^{9}
CO2	Gas	10,600	6×10^{7}
KrF (excimer)	Gas	248	1×10^{13}
Ruby	Solid-state	694	3×10^{11}
Nd:YAG	Solid-state	1064	1.2×10^{11}
Ti:Al2O3 (Ti:Sapphire)	Solid-state	760	1.5×10^{14}
Semiconductor	Semiconductor	800	1×10^{14}

Table 2-2. Properties of some common lasers.

Adapted from Weichel [1993] and Sifvast [2008].

The Tx laser Pulse Repetition Frequency (PRF) is typically a few tens of shots per second. However, many applications do not require this very high temporal resolution, in which cases the measurements are averaged over a few seconds.

Once the beam to be transmitted has been converted (if necessary) to the desired wavelength, then it passes through a beam expander (the Tx telescope), to further reduce the divergence of the already highly collimated laser beam, to values of the order of 100 μrad. This is often necessary so as to choose an Rx telescope with a FoV of only a few hundred μrad, which gives the following advantages [Weitkamp, 2005]:

- Reduction in background light from the atmosphere;
- Reduction in the number of detected photons that went through multiple scattering;
- Some lidar methods with high-spectral resolution have wavelength-selective optical devices (e.g. grating mirrors) with small acceptance angles.

A field stop placed in the focal plane of the Rx telescope optics sets the FoV. A chopper – a mechanical device that can block or let the light through – can be used in place of the field stop when only the backscatter signal of certain regions (i.e. altitude ranges) of the atmosphere is desired [Weitkamp, 2005].

It is often desirable to suppress some spectral portions of the received signal to retain only the wavelength of interest. This can simply be done with a bandpass filter, although some applications require somewhat more complex techniques (such as polarizers, grating spectrometers, interferometers or atomic-vapour filters).

The detector can be a photomultiplier tube (PMT) or an avalanche photodiode (APD), with the mode of operation (photon-counting or analogue recording) depending on the strength of the back scattered signal (weak and strong, respectively).

Finally, there are two types of detection techniques that need to be differentiated between. The simplest one is the direct detection (also referred to as incoherent detection) where the signal received by the Rx telescope is directly focussed onto the detector which produces a current proportional to the intensity of the received light. The alternative to this technique is

the coherent detection, where a reference signal (known as the local oscillator) is mixed to the received signal, and this mixed signal is then sent towards the detector. The coherent detection technique by default is the heterodyne detection. If the received signal and the local oscillator are spatially coherent, aligned with respect to each other and with identical polarisation, then temporal interference occurs at a frequency equal to the difference in the frequencies of the two signals; this is the heterodyne signal [Kamerman, 1993]. This heterodyne signal recovers the phase information of the backscattered signal, whereas the direct detection signal recovers the amplitude [Kramer, 2002].

In a heterodyne system, the local oscillator is generated by some laser (usually a continuous wave laser). Because a lidar requires a laser to be transmitted to the target in the first place, this laser can also be used as the source of the local oscillator, in which case the coherent detection technique is not a heterodyne but a homodyne detection [Kamerman, 1993].

Note that coherent systems tend to produce a greater amount of data than direct detection lidars [Kramer, 2002].

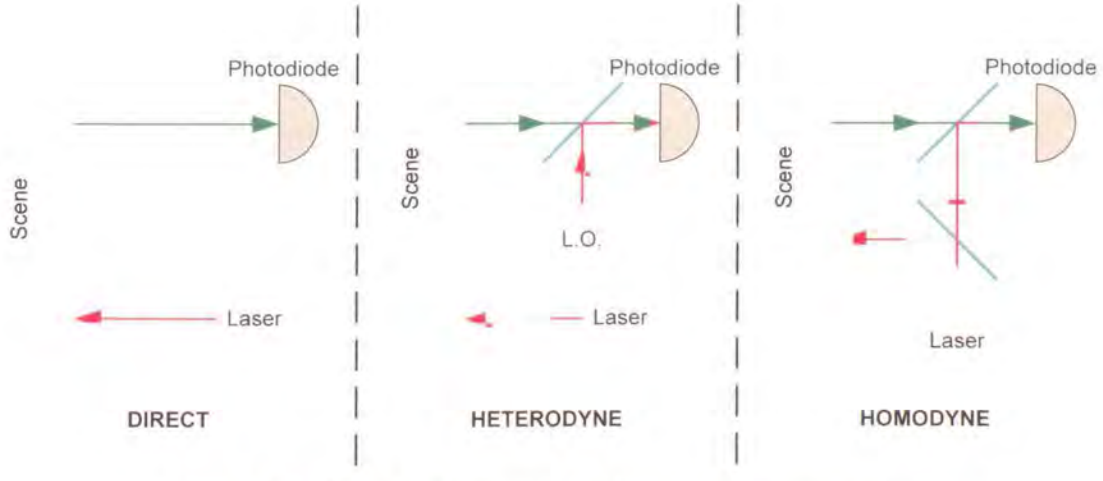

Figure 2-3. Direct vs. Heterodyne/Homodyne measurement

2.4 Types of Lidars

Lidar instruments are versatile, by their applications and by the number of measurement techniques. There is not one single way of classifying lidars; they can be grouped for instance according to the physical process (e.g. elastic scattering, Doppler shift, etc.), the detection region (atmosphere, solid Earth, vegetation, hydrosphere), or the subject to be studied (e.g. aerosols, temperature, wind velocity, etc.). The subject of the present work is not to consider all applications, but instead to concentrate on some of the spaceborne lidars. Based on [Singh et al, 2005] and [Wandinger, 2005], the most common techniques in space-based remote-sensing are presented hereafter.

2.4.1 Altimetry Lidar

Altimetry is the simplest concept of lidar measurements. The range of the reflecting surface from the device is determined from the time it takes a light pulse to travel down and back up. It is simply half the round-trip time multiplied by the speed of light in the medium:

$$R = \frac{c\Delta t}{2n} \tag{2-1}$$

where R is the range, c is the speed of light in vacuum, Δt is the round-trip time of the laser pulse, and n is the mean index of refraction of the propagation media [Kamerman, 1993].

The GLAS instrument onboard ICESAT employs this technique to determine the elevation of ice, clouds, and land. Three Nd:YAG lasers operating sequentially transmit 4-ns pulses in the infrared (1064 nm) for surface altimetry and dense cloud heights, and in the visible spectrum (532 nm) for the vertical distribution of clouds and aerosols [Zwally et al, 2002].

2.4.2 Backscatter Lidar

There are different types of backscatter lidar, classified by the type of scattering that the light undergoes. We start with a review of some scattering processes.

Molecular Rayleigh scattering

The Rayleigh scattering model applies to the particles that are very small compared to the wavelength λ of the scattered radiation. The intensity of Rayleigh scatter is inversely proportional to λ^4. At low altitudes, the atmosphere is constituted at 99% of Nitrogen and Oxygen molecules, which have a diameter of about 3 Angstroms; molecular Rayleigh scattering dominates mainly in the UV and the lower-wavelength portion of the visible spectrum [Rees, 2001] and is the cause of the blue sky. It is an elastic (or coherent) scattering, meaning that the incident and scattered radiations have the same wavelengths [Hecht, 1987], unlike the Raman scattering, which is an inelastic process (described later).

Aerosol or Mie scattering

The scattering theory developed by Gustav Mie is not limited to a specific particle size or radiation wavelength; thus Mie theory also covers Rayleigh scattering [Wandinger, 2005]. The term "Mie scattering" is often used in remote-sensing literature to describe scattering from particles of size similar to (or larger than) the wavelength of the scattered radiation [Lo, 1986; Szekielda, 1988]. In the visible spectrum, this type of scattering occurs with aerosols of radii in the range 10 nm to 10 μm (typical of dust particles and water droplets) [Rees, 2001].

With aerosols of size similar to the wavelength, the wavelength-dependence of the particle scattering properties varies greatly; with very large particles, scattering becomes independent of wavelength, and it can be referred to as non-selective scattering [Lo, 1986].

Mie scattering theory assumes that the particles are spherical; but most often, they are not. In some cases, an approximation of Mie theory is that some "average" particle size can be assumed [Rees, 2001]. For other non-spherical particles, when it is not possible to make this assumption, studying the resulting depolarisation of the backscattered radiation provides data on such large non-spherical particles (such as dust and ice crystals of cirrus clouds).

Elastic Backscatter lidar

This is the classical form of atmospheric lidar, also referred to as a Rayleigh-Mie lidar [Wandinger, 2005]. It provides information on extent, height distribution and optical thickness of aerosol and cloud layers, which are relevant to climatology and operational weather forecasting; furthermore it is the least demanding instrument in terms of technology risk and development needs [Hueber, 1991].

ATLID (Atmospheric Lidar) is the European backscatter lidar, which was initiated in 1988 [Hueber, 1991] and is due to be launched onboard EarthCARE in 2013 [ESA, 2008]. Due to its lower altitude, it requires a lower pulse energy and aperture diameter than GLAS and CALIOP on the ICESAT and CALIPSO missions, respectively, as shown in Table 2-1. It should be noted however that ALTID has a greater PRF.

Raman scattering

The wavelength of a backscattered radiation is mainly the same as that of the radiation incident onto the particle, but very weak side bands can appear in its spectrum. This frequency shift corresponds to a change in the energy (or vibrational-rotational quantum state) of the molecule [Wandinger, 2005] [Hecht, 1987]. A Raman lidar would measure the frequency shift, thus a useful application is atmospheric temperature profiling. However, because the side bands are very weak, this technique requires gases present in fairly high concentrations; water vapour is thus a frequent target of Raman lidars [Wandinger, 2005].

Fluorescence scattering

The resonance fluorescence lidar is yet another type of scattering lidar, particularly relevant in the study of metal ions and atoms in the mesopause. This type is not going to be discussed further in this study, but [Abo, 2005] is a recommended reference for further reading on the subject.

2.4.3 DIAL

A differential-absorption lidar (DIAL) emits two pulses: the online pulse has a wavelength matching the resonant absorption line of the atmospheric constituent of interest, while the offline pulse is emitted at a wavelength very close to that of the online pulse but that is free of absorption [Lutz et al, 1989].

For an idealised case, the molecule number density of the trace gas can be written as [Gimmestad, 2005]:

$$N = \frac{1}{2\Delta\sigma} \cdot \frac{d}{dR} \ln\left(\frac{P_{on}(R)}{P_{off}(R)}\right) \tag{2-2}$$

where R is the range, P is the power received (at the online and offline wavelengths, respectively), and $\Delta\sigma$ is the differential absorption cross-section between the two wavelengths, which is already known for the gas atoms or molecules being sensed.

The DIAL method allows to determine the number density profile of many trace gases, such as O_3, NO_2, NO, N_2O, SO_2, CH_4, HCl, NH_4, etc [Wandinger, 2005].

At a wavelength of 730 nm [Lutz et al, 1989], it is used to determine profiles of water vapour, which is the most important atmospheric greenhouse gas. However, the absorption lines of the water molecule are very narrow; therefore the laser pulse needs high stability and spectral purity [Wandinger, 2005]. Water vapour absorption lines are numerous, but for DIAL applications those at 730, 820 and 930 nm are particularly useful [Bösenberg, 2005].

Another application of DIAL is the measurement of temperature profiles by using an absorption line of oxygen because it has a constant mixing ratio in the atmosphere and its absorption cross section is temperature dependent [Wandinger, 2005]. Similarly pressure profiles are obtained with the absorption line of molecular oxygen at 760 nm [Lutz et al, 1989].

A DIAL presents many similarities with the simple backscatter lidar, but it has much more stringent requirements for the laser sources (multiple wavelengths) as well as the receiver (high sensitivity, spectral resolution) [Hueber, 1991].

ESA proposed the WALES mission as an Earth Explorer core mission candidate. The DIAL would emit two pairs of pulses in the 935 nm spectral range [Hélière et al, 2004].

Yet another Earth Explorer core mission candidate, A-SCOPE, was studied for feasibility. It would carry an Integrated Path Differential Absorption (IPDA) lidar to measure the total column of CO_2, around the absorption lines of either 1.56 or 2.05 μm. The IPDA is an alternative to DIAL when a total column rather than a concentration profile is required, and when the backscattering targets are only present in very small quantity (making the backscatter signal at a given altitude range very weak). Since the ground echo is much larger than the atmospheric echo, the size of the instrument is significantly reduced (as compared to a DIAL). However, the IPDA requires an onboard radiometric calibration system [Durand et al, 2009] that the DIAL does not need.

2.4.4 Doppler Lidar

As its name implies, a Doppler lidar measures the shift in the apparent frequency that occurs when the lidar and the subject move relative to each other, the frequency shift being proportional to the relative velocity. In Earth Observation, this has applications to wind velocimetry (e.g. ESA's Aeolus mission) as well as coherent ocean and river surface currents [Singh et al, 2005]. The advantage of lidars over microwave or millimetre-wave radars is that the Doppler shift is proportional to the carrier frequency (i.e. inversely proportional to its wavelength), hence the higher frequency (respectively smaller wavelength) of a laser pulse yields a greater Doppler shift, allowing a more accurate and precise measurement of the velocity [Kamerman, 1993]. ALADIN, the Wind Doppler Lidar of the Aeolus mission, will operate in the ultraviolet (355 nm). The emitted light is scattered by aerosols, clouds particles or air molecules at different altitudes, which are assumed to be travelling (on average) at the wind velocity. However, there are two main difficulties with Doppler Wind Lidar (DWL): first, the backscattered signal is very weak even with a powerful emission; second, frequency shift is proportional to the fraction of wind speed over the speed

of light and is therefore extremely small, thus requiring very narrow spectral lines [Werner, 2005].

Coherent Doppler lidar relies on the detection of the frequency difference between the backscattered signal from atmospheric aerosols and a local oscillator. Heterodyne detection is used, in which the frequency of the local oscillator is offset with respect to that of the emitted laser pulse. This is necessary so that not only the magnitude but also the sign of the shift (i.e. the direction of the wind) can be determined [Wandinger, 2005]. Because of the low aerosol content in the free troposphere (2 to 20 km altitude), long-range energy transport cannot be assessed with the coherent detection method [Kramer, 2002]. However, most aerosols are found in the planetary boundary layer (PBL) – the lowest kilometre of the atmosphere – where transport processes are dominated by wind turbulence and atmospheric convection [Rees, 2001]. Coherent Doppler lidars are more suitable for these atmospheric processes in the PBL.

Direct detection lidars use the molecular (Rayleigh) backscatter, which is strong in the UV spectrum. The backscatter signal is passed through a filter (such as Fabry-Perot interferometers or etalons), producing circular interference fringes; the Doppler shift is determined from the measurement of small fringe displacements [Kramer, 2002] [Werner, 2005].

ALADIN is a direct detection lidar based on a frequency tripled Nd:YAG laser, emitting in the UV (355 nm). The optical bench assembly includes a Rayleigh spectrometer (based on a sequential Fabry-Perot), and a Mie spectrometer (based on a Fizeau spectrometer).

2.5 Technical challenges

Many lidar instruments have experienced difficulties, especially with the laser source: Laser 1 of GLAS failed after just over a month of operation [McCormick, 2004], ALADIN experienced technical problems with the development of its lasers [Singh et al, 2005], although its laser diode stacks have since passed their long-lifetime test [Morançais, 2007]. While many lasers are available commercially, their operation in the space environment has not been a main driver for laser manufacturers. Operating lasers in space tends to be difficult for various reasons, some of which are discussed below. We start with an introduction of the components, associated technologies and operation of lasers.

2.5.1 Fundamentals of laser

There are many different type of lasers; we will concentrate on the one that is most often used in spaceborne lidar instruments: the neodymium-doped yttrium aluminium garnet (or Nd:YAG).

LASER stands for Light Amplification by Stimulated Emission of Radiation. Stimulated emission results from changes in electron energy of an atom or an ion when it is driven to do so by an incoming photon (by opposition to spontaneous emission, where the electronic transition would occur by itself) as illustrated in Figure 2-4. In the case of the Nd:YAG laser, a trivalent neodymium ion, Nd^{3+}, would decay from a high level (excited state) to a lower level (the lowest being the ground state, in which the electrons reside at low temperatures [Silfvast, 1990]), emitting another photon with a frequency corresponding to the energy difference between the two levels. Furthermore, for the incident radiation to trigger the stimulated emission, it must be of the frequency which corresponds to the difference in energy levels. Consequently, a remarkable property of lasing is that the emitted photon is in phase with, has the polarisation of, and propagates in the same direction as, the stimulating radiation [Hecht, 1987]. In the case of the Nd^{3+} ion, the photon's wavelength is 1064 nm.

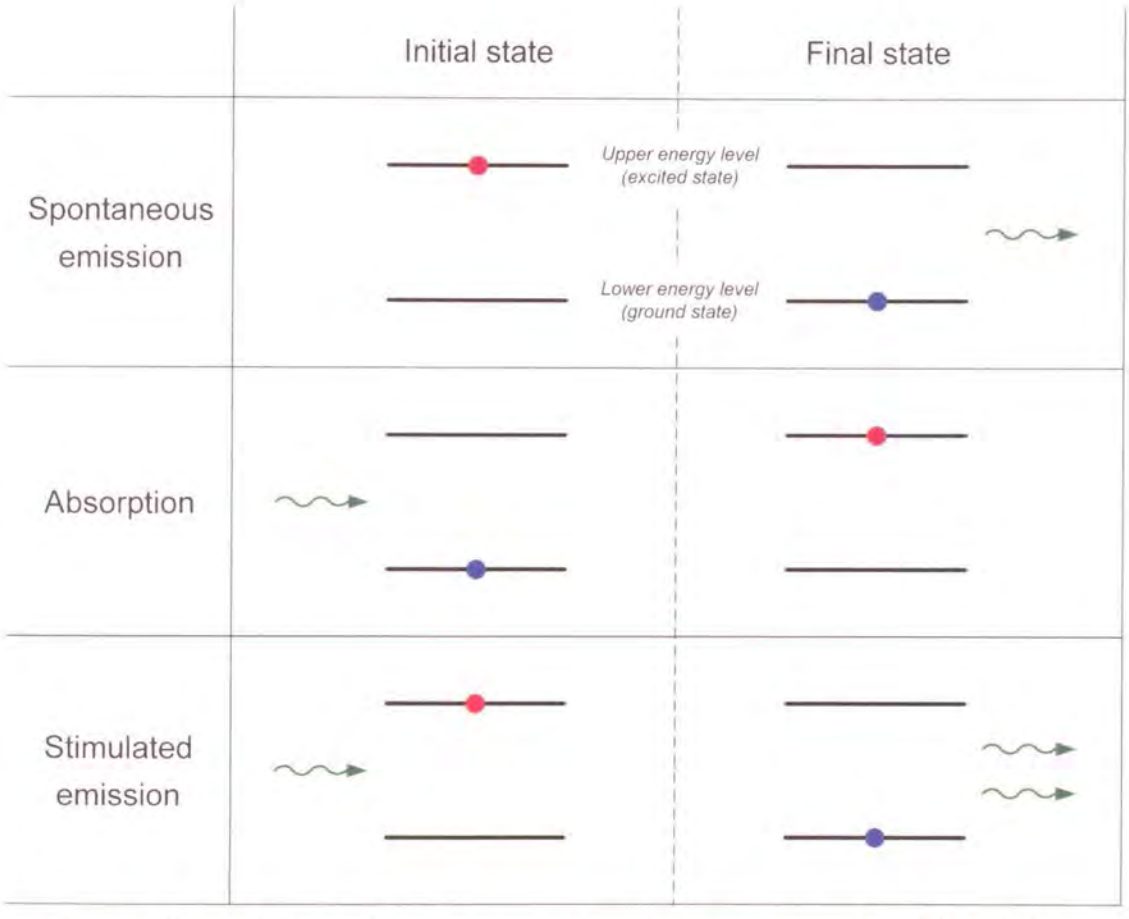

Figure 2-4. Illustration of the three processes that can occur when EM radiation interacts with atoms.

Adapted from Weichel [1993] and Silfvast [2008]

Most atoms and ions would normally be in the ground state; but the laser amplification occurs when there are more atoms/ions in a higher energy level than at a lower level. This condition, known as population inversion, is achieved by pumping energy into the gain medium to maintain this population inversion. As a result, more photons will be stimulated than absorbed and the laser beam is thus amplified. Pumping of solid-state lasers (such as Nd:YAG) is done optically, either by flash lamps with broad emission spectrum (LITE), or most often with a narrow spectrum light from laser diodes or another laser.

The neodymium ions are implanted into a crystal (yttrium aluminium garnet, YAG) with a concentration in the order of 1% [Silfvast, 1990]. YAG is a rather difficult crystal to grow, limiting the size of the laser rod to approximately 1 cm in diameter; however it has a

relatively high thermal conductivity to remove wasted heat, and can thus be operated at high PRF [Silfvast, 1990]. Removal of wasted heat is essential to avoid temperature rising of the laser medium; Weichel [1993] shows that the laser output power is directly proportional to the waste energy removal rate.

Apart from the gain medium (YAG crystal with Nd^{3+} ions) and the pumping source, the third component of the laser is the optical cavity, or optical resonator. Its purpose is to provide optical feedback to sustain laser oscillation [Weichel, 1993]. The most basic form is a pair of mirrors, one at each end of the elongated gain medium, allowing the beam to bounce back and forth between the mirrors (across the gain medium) and growing along the longitudinal direction. The mirrors can be concave to refocus the beam and reduce the diffraction losses. One of the mirrors has a reflectivity smaller than 100%, allowing some of the laser beam to be transmitted out.

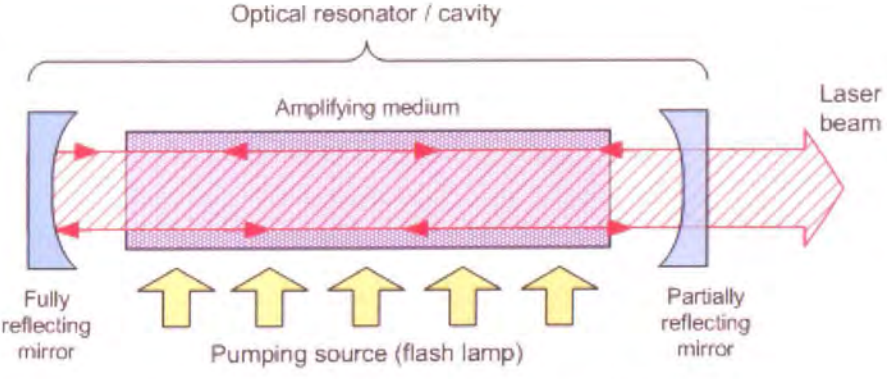

(a) general schematic representation of a laser

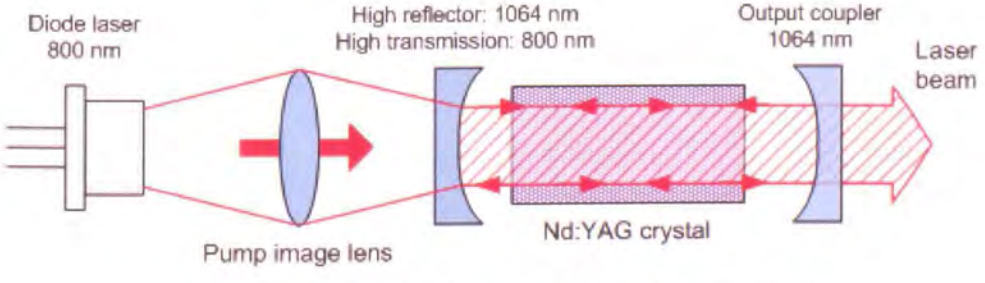

(b) example of a Nd:YAG laser pumped by laser diode

Figure 2-5. Schematic representations of lasers

Adapted from Silfvast [2008]

One way of obtaining a high-power transmitter is through the Master Oscillator / Power Amplifier (MOPA) configuration, based on multiple lasers working in tandem. A first laser serves as a Q-switched oscillator, firing a low energy pulse into a second laser that acts as an amplifier of high efficiency [Durand et al, 2008], which can in turn fire into a third laser, and so on and so forth. In the amplifier, the end mirrors are partially reflecting (or even non-reflecting). As a consequence, the cavity feedback is reduced and the laser is not self-oscillatory but instead amplifies an incident wave by stimulated emission [Hecht 1987]. The MOPA configuration is particularly well suited when a high energy pulse of high beam quality is required, such as ATLID [Durand et al, 2008].

2.5.2 Laser-induced damage and contamination

Singh, Heaps, and Komar (2005) describe the technical challenges experienced during the development and operation of lidars in space; these are:

- precision alignment of the mirrors of the resonant optical cavity;
- contamination of laser optics by outgassing materials;
- colouring of optics by radiation (a possible issue with new electro-optic materials used in frequency conversion crystals, for which such properties may not have been yet established);
- electro-optic components not designed specifically for space – tests and screening techniques must be devised for long term reliability;
- high power laser heads dissipate high heat load;
- laser to be lightweight, compact and energy efficient;
- frequency conversion systems (with non-linear optics, e.g. OPO/OPA) were never designed for space.

Some of these issues have been highlighted by the problems experienced in-orbit by GLAS and during development of ALADIN.

GLAS Laser 1 ceased operation after 35 days; probably because of the catastrophic failure of a diode pump array [Afzal, 2006]. Space qualification of laser diode arrays (LDAs) has also been one of the most critical elements during the ALADIN development, as it is a major lifetime issue; extensive testing has allowed to define a procedure for the screening of manufactured diodes [Durand et al, 2004]. NASA GSFC and LaRC have also been developing screening tests to select the right LDAs from those supplied by the manufacturer [Singh et al, 2005]. After the failure of GLAS Laser 1, it was recommended to operate Laser 2 at a reduced duty cycle (27% instead of 100%) and also to reduce the operating temperature of the lasers in other to avoid failure of the LDAs in Laser 2 [Afzal, 2006]. NASA LaRC worked with the industry on the LDA architecture to reduce the thermal resistance and improve lifetime [Singh et al, 2005], while ESA are developing passively-cooled high-power LDAs [Durand et al, 2008].

Following the measures taken, GLAS Laser 2 did not fail; however the level of transmitted energy degraded at a faster rate than anticipated [Afzal, 2006]. This is thought to be a consequence of photo-darkening on the surface of the optics [Lien et al, 2006] due to the interaction of the intense 532-nm laser beam with trace outgassing materials inside the laser [Afzal, 2006]. Such contamination is shown in Figure 2-6.

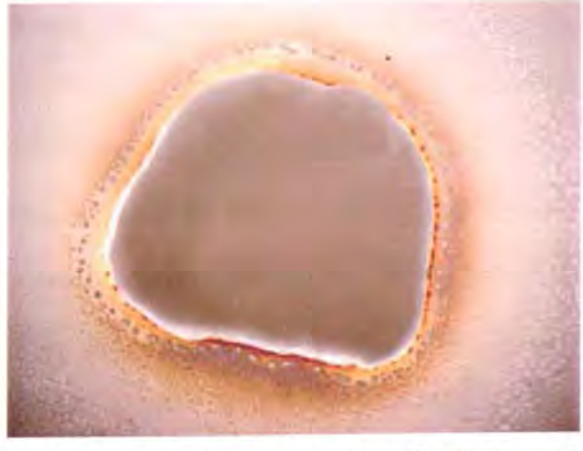

Figure 2-6. Optical microscopy of LIC deposits.

[Alves et al, 2010].

Since this process can dramatically affect the lifetime of the laser and is poorly understood, a Laser-Risk Reduction Group was put together by ESA, and three major risks associated with laser-induced damage have been identified [Lien et al, 2006]:

- Laser-induced damage where the power density of the laser exceeds the optical component (optics coating, gain medium crystal) damage threshold. This is significant because damage threshold of coatings in vacuum can be lower than in the air. It can also depend on pulse duration and possibly PRF.
- Optical fatigue over the mission duration (very little is known on optical fatigue).
- Effect of contamination on the optics in vacuum. The presence of air suppresses the formation of deposits on the irradiated optics, possibly due to a chemical reaction of the oxygen of the air with the deposit when irradiated by the laser beam.

Tests are being conducted to investigate these processes by ESA in cooperation with various labs throughout Europe [Lien et al, 2006].

As the performance of Laser 2 dropped significantly, GLAS was switched over to Laser 3, which was operated to an even lower temperature (13°C) to avoid the problems encountered by the first two lasers (Figure 2-7). This action proved to significantly decrease the degradation rate [Afzal, 2006]. However, Laser 3 eventually failed and Laser 2 was re-activated but later failed too.

Canham (2004) points out that contamination in spaceborne lasers is inevitable, and should be minimised. Soileau (2009) emphasises that residual hydrocarbons are dissociated by the laser light, resulting in the free carbon that can deposit and accumulate in the beam path. This effect can be reduced with oxygen, as any free carbon would combined with oxygen to form carbon dioxide gas. Note that this is the reason for a late design change on the ALADIN instrument for ESA's Aeolus mission, where the laser optics are kept in a low-pressure oxygen environment [Endemann, 2011]. Furthermore, on-going testing at DLR has shown that "the interaction of intense laser radiation with outgassing material constituents gives rise to a high risk of deposit formation on the optics and consequently to a drastically reduced

lifetime", and that peak fluence has an influence on the deposit structure [Schröder, Borgmann, Riede & Wernham, 2008].

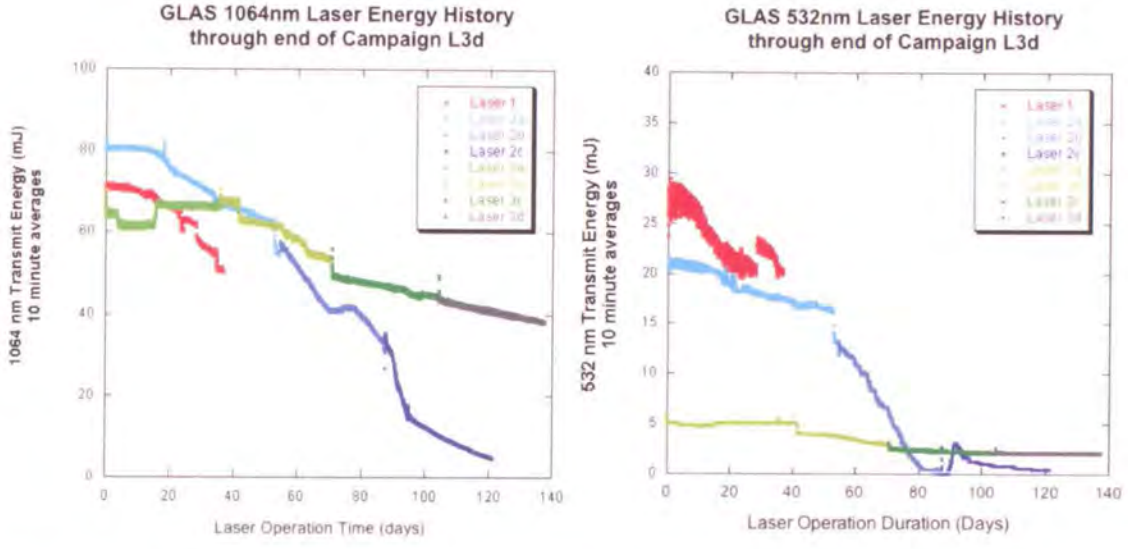

Figure 2-7. GLAS laser pulse energy history for operating periods up to campaign 3d.

[Abshire et al, 2005].

2.6 Lidar mission requirements and study boundaries

2.6.1 Type of orbit

Many parameters depend greatly on the nature of the mission itself. One of the main aspects is the orbit.

Many optical missions for the observation of the Earth fly in Sun-synchronous orbits to maintain the same illumination conditions of the scene being observed, enabling consistency in the measurements. Sun-synchronous orbits are also useful for the design of the solar arrays of the satellite; for instance, Synthetic Aperture Radar (SAR) missions, for instance Sentinel-1 or Radarsat, are flown in dawn-dusk orbits when their instruments could operate at any Local Time of the Ascending Node (LTAN).

Lidars are similar to SARs in the sense that, as they provide their own source of illumination, they could fly in orbits of any LTAN. In many cases, a slightly varying LTAN may help reducing systematic errors. However, as they are optical instruments of high spectral

accuracy, they tend to be sensitive to background solar illumination. Thus, a dawn-dusk orbit becomes particularly interesting as the Sun only illuminates the scene at shallow angles, and a minute portion of sunlight is scattered by the atmosphere to the lidar instrument. Furthermore, sun-synchronous orbits, and dawn-dusk orbits provide a very favourable environment for the thermal control.

Not all operational lidar missions are sun-synchronous. Where the coverage of polar regions is a driver of the mission, an orbit with a lesser inclination is necessary. This is the case of ICESat and its future successor ICESat-2, which flew / will fly in a 600-km orbit with a 94° inclination.

Statistically, dawn-dusk orbits are usually the preferred option for lidar missions. This study aims to be fairly generic and not targeted to a particular mission, but for practical reasons will only consider dawn-dusk orbits.

Requirement #1: The satellite shall be flown in a dawn-dusk orbit.

2.6.2 Spacecraft size

One major constraint on the design of any spacecraft is the selection of the launch vehicle, which affects the volume of the satellite, its mass and the altitude of its orbit. There are other very practical aspects to take into account beyond the merely technical constraints: political considerations mean that most often a country or agency would favour one of its own launch vehicles. Cost is also a major driver. Recent and upcoming European Earth Observation missions have been / will be launched on Russian launchers, while it is predicted that the upcoming European small launcher Vega will be increasingly used, as shown in Table 2-3. Indeed, due to the European investment into Vega, there may be non-negligible political pressure for future institutional European missions to fly on Vega, whenever possible. Note that if a satellite is compatible with Vega, it is very likely to be compatible to Rockot, and possibly Dnepr.

Requirement #2: the satellite shall be compatible with a small launcher like Vega (Goal), or on Soyuz (Threshold).

Mission	Launch mass	Orbit characteristics	Launcher
GOCE	1050 kg	270 km, SSO	Rockot
SMOS	658 kg	758 km, SSO	Rockot
CryoSat-2	720 kg	717 km, non-SSO (92°)	Dnepr
Aeolus	1100 kg	408 km, SSO	Dnepr / Vega (TBC)
Swarm	1500 kg (3 × 500 kg)	Near polar, 300 × 460 km, or 530 km	Rockot
EarthCARE	~2000 kg	393 km, SSO	Soyuz, Zenit
Sentinel-1A	2300 kg	693 km, SSO	Soyuz
Sentinel-2A	1200 kg	786 km, SSO	Rockot
Sentinel-3A	1250 kg	814.5 kg, SSO	Rockot

Table 2-3. Launchers for the missions of the Earth Explorer and GMES programmes.

2.6.3 Lidar performance

The performance of a lidar is calculated by the lidar equation [Wandinger, 2005]:

$$P(R,\lambda) = P_0 \frac{c\tau}{2} A \eta \frac{O(R)}{R^2} \beta(R,\lambda) \exp\left[-2\int_0^R \alpha(r,\lambda)dr\right] \quad (2\text{-}3)$$

The right-hand side terms of the equation are explained in Table 2-4.

For an isotropic scatterer, a simplified equation for the ratio of received-to-emitted light power is (adapted from Wandinger [2005]):

$$\frac{P_r}{P_e} = \frac{A\beta c\tau}{2R^2} \quad (2\text{-}4)$$

where P_r and P_e are the powers of the received and emitted signals, respectively, A is the surface area of the receiver telescope, β is the backscatter coefficient, c is the speed of light, τ is the laser pulse duration, and R is range between the lidar and the scattering

volume under investigation. The term $c\tau$ is the length of the scattering atmospheric volume being illuminated by the laser pulse at a given time.

Parameter	Term	Comment
Performance of the lidar system	$P_0 \frac{c\tau}{2} A\eta$	P_0 is the averaged power of a single laser pulse of temporal length τ. The length of the illuminated volume is $c\tau/2$. A is the area of the primary mirror of the receiver telescope, while η is the overall efficiency of the system, including the optical efficiency of both transmitter and receiver stages, as well as the detection efficiency.
Geometric factor	$\frac{O(R)}{R^2}$	O(R) is a function representing the overlap of the laser beam and receiver FoV. The term R^{-2} stands for the decrease in signal intensity because the receiver telescope area is part of the surface of a sphere of radius R centred at the scattering volume.
Backscatter coefficient	$\beta(R,\lambda)$	Backscattering coefficient of all molecules and particles within an atmospheric volume being probed, which is situated at a distance R from the lidar and reacting to a wavelength λ. It is the scattering coefficient for a scattering angle of 180°.
Transmission	$T(R,\lambda) = \exp\left[-2\int_0^R \alpha(r,\lambda)dr\right]$	T(R,λ) accounts for the transmission of light in both directions. The sum of all extinction losses is called light extinction; α(R,λ) is the extinction coefficient due to molecules and particles, both by scattering and absorption.

Table 2-4. Description of the terms constituting the lidar equation

Based on [Wandinger, 2005].

Equation (2-4) can be further simplified if we assume that for a given observation:

- β is constant for any type of lidar instrument making a measurement;
- the lidar pulse length is also constant, so that the atmospheric volume being sensed is the same in all cases;

- the power of the received signal is the same (this is necessary to compare different concepts of instruments with identical performances).

Under these assumptions, Equation (2-4) can be re-arranged into:

$$\frac{P_e \cdot A}{R^2} = \text{constant} \tag{2-5}$$

The numerator is known as the power-aperture product. It is possible to replace the power of the emitted pulse by the pulse energy $E_e = P_e\tau$, for a given pulse length. Or by using the Pulse Repetition Frequency (PRF), denoted f_{rep}, the equation becomes:

$$\frac{E_e \cdot f_{rep} \cdot \pi D^2/4}{R^2} = \text{constant} \tag{2-6}$$

This equation gives the power-aperture product of a lidar, adjusted for the range. It has the advantage of enabling the comparison of different spaceborne lidars flying at different altitudes.

Figure 2-8 is a simple representation of the trade space that can be drawn from Equations (2-5) and (2-6). It gives the advantages of a larger (yellow) or a smaller (green) value of each of the three parameters.

While the performance can be improved by either increasing the instrument power and/or the aperture, and the atmospheric drag reduced by decreasing the aperture or increasing the altitude, the only way of limiting laser-induced damage at mission level (i.e. apart from an engineering solution at the level of the laser) is to reduce the power of the laser beam.

Figure 2-7 showed that ICESat delivered 5 mJ at 532 nm, with little degradation. The low power oscillator of ALADIN provides a 10 mJ beam, which is subsequently amplified by the power laser head, with the LIC occurring on the optics downstream of the Power Amplifier stage.

Requirement #3: The mission shall minimise the laser beam energy while maintaining performance.

Requirement #4: At UV / visible wavelengths, the laser beam energy shall be 5 mJ (Goal), 10 mJ (Objective), 15 mJ (Threshold).

Requirement #5: The spacecraft shall be designed for flying in a low orbit (below 350 km).

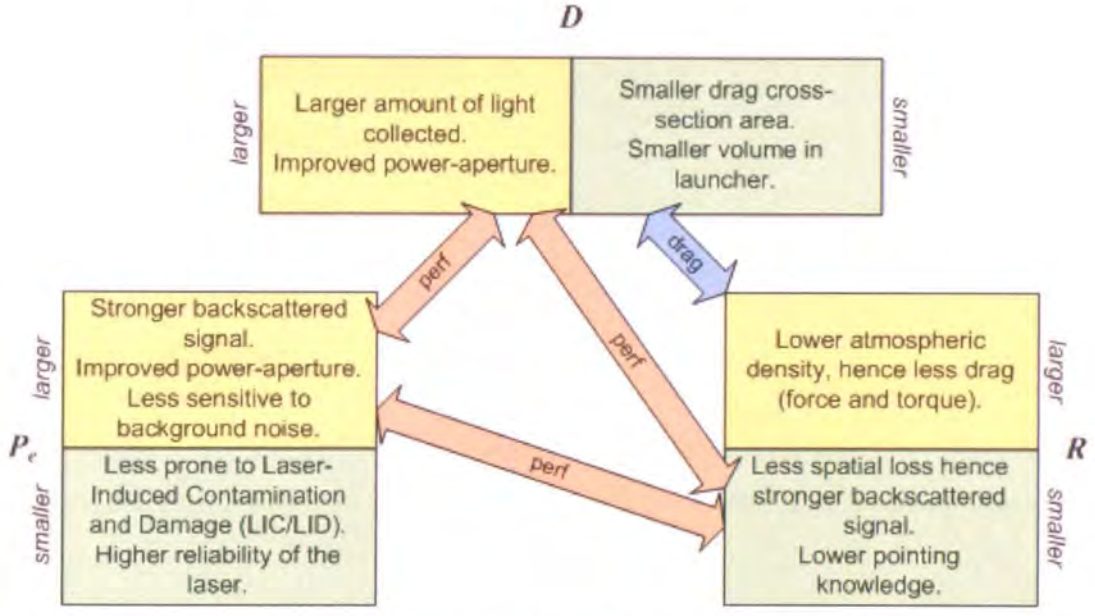

Figure 2-8. Representation of the trade space between the three parameters of the simplified lidar equation.

2.6.4 Telescope diameter requirements

With requirements defined on the beam energy and the altitude of the orbit, it is possible to derive the diameter requirement of the telescope for a given power-aperture product.

Figure 2-9 shows power-aperture-products for various lidar missions. In order to compare them, they are corrected for altitude, according to Equation (2-6).

It can be seen that most missions have power-aperture products of 10×10^{-12} W or below, with the exception of ESA's ADM-Aeolus about two orders of magnitude greater, and Earth Explorer past candidates WALES and A-SCOPE about two orders of magnitude higher than the likes of EarthCARE, CALIPSO or ICESat.

The three largest lidar instruments are discussed further hereafter.

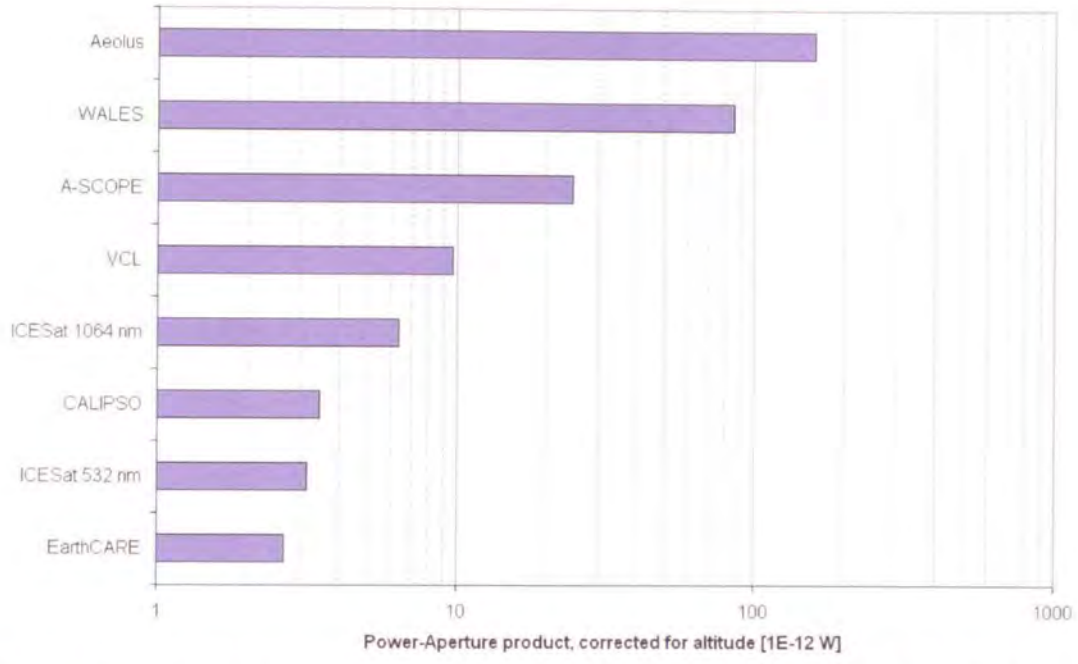

Figure 2-9. Power-aperture product, corrected for altitude, for a range of missions.

2.6.4.1 ALADIN

The Atmospheric Laser Doppler Instrument (ALADIN) is an incoherent (direct) wind Doppler Lidar operating in the UV, measuring the frequency shift with respect to the frequency of the laser pulse of the Mie backscatter (from aerosols below 2 km) and Rayleigh backscatter (due to the absence of aerosols above 4-5 km) [ESA, 2005]. Because of the way it separates aerosol and molecular backscatter, ALADIN works on the same principle as an HSRL.

Figure 2-10 shows a CAD view of ALADIN. It is dominated at the top by the baffle structure, which is bevelled so that it is long enough to protect the secondary mirror from direct sunlight while minimising its drag surface. The 1.5-m primary mirror is located at the bottom of the baffle and mounted on the upper side of the instrument baseplate. The transmitter and receiver stages are mounted on the lower side of the baseplate, inside an octagonal structure shown in yellow. The lasers (both seed and power units) dissipate a large amount of heat power through heat pipes connected to two large radiators (bottom right).

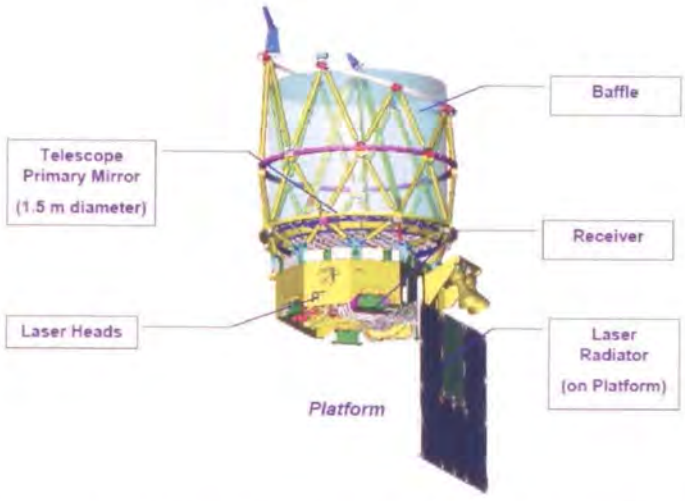

Figure 2-10. Engineering drawing of ALADIN [Morancais, 2006]

These radiators are an integral part of the instrument, and once assembled with the platform sit on the anti-sun side of the satellite. Two star trackers (one nominal and one redundant) are mounted on the baseplate, on the side of the octagonal structure. This location is justified by the need to minimise the thermo-elastic distortions between the star tracker and the Line Of Sight (LOS) of the instrument, and accommodating the requirements of the star tracker (exclusion of the Sun and Earth from the star tracker FoV).

Table 2-5 is a summary of the ALADIN characteristics. A very good signal-to-noise ratio (SNR) is ensured by combining the large aperture telescope with a high laser beam energy (120 mJ). The lasers operate at a high PRF (100 Hz) but only for 7 seconds every 28 seconds. This is equivalent to 700 measurements being averaged over a distance of about 50 km. An averaged point is thus taken every 200 km, as required by models for numerical weather prediction (NWP) [ESA, 2005].

Figure 2-11 shows the scaling options for a mission like Aeolus. The combination of a very large telescope and low altitude is necessary to reduce the beam energy significantly. Even with a telescope diameter of about 3.5 m, only a beam energy of 15 mJ could be targeted, at an altitude of 300 km or so. However, this kind of size is quite extreme for an Earth Observation mission. This is larger than the Hubble Space Telescope, and at par with the

Herschel infrared telescope, which do not fly in such a low orbit. Thus, the Aeolus mission is indeed a true challenge.

Parameter	Value
Altitude [km]	400
Off-nadir pointing	35°
Line of Sight range [km]	506
Telescope diameter [mm]	1500
PRF [Hz] (over 7 seconds, every 28 seconds)	100
Pulse energy at 355 nm [mJ]	120
Mass [kg]	480 kg
Power [W] Total Transmitter Rest	 830 510 320

Table 2-5. Characteristics of the ALADIN instrument

From [Reitebuch et al, 2008]

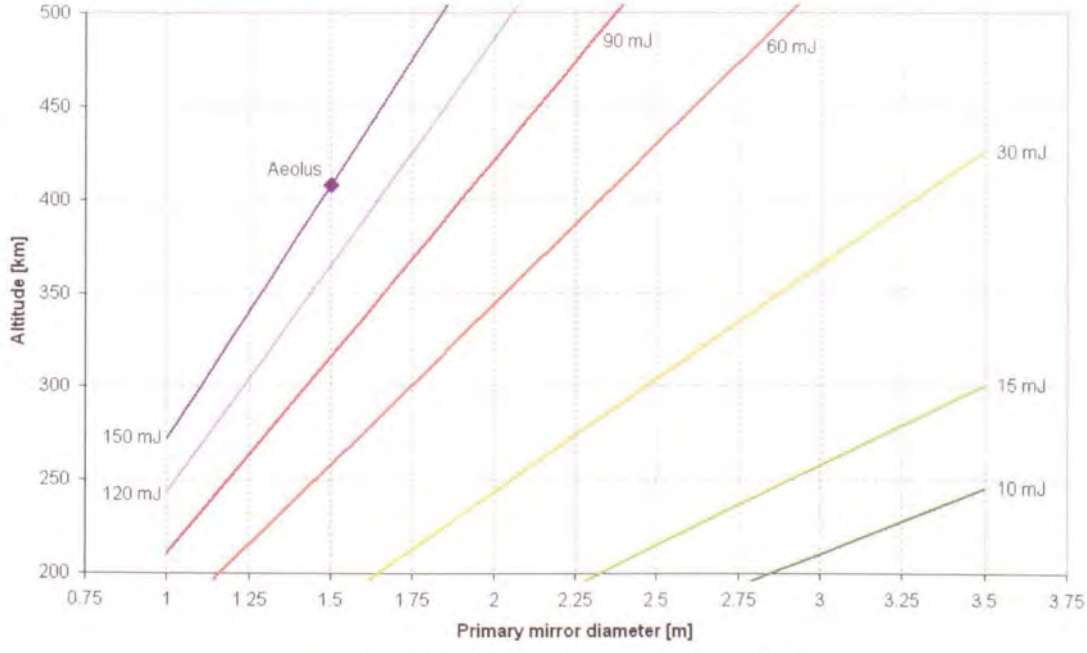

Figure 2-11. Aeolus instrument scaling

2.6.4.2 WALES

The Water Vapour Lidar Experiment in Space (WALES) is a mission concept proposed for the measurement of the vertical profiles of atmospheric water vapour, aerosols and clouds. It relies on the Differential Absorption Lidar (DIAL) observation technique, at wavelengths around 935 nm.

One of the concepts proposed in the course of the Phase A study inherits to a certain extent from ADM-Aeolus, as can be seen in Figure 2-12. The main visible difference is the introduction of a beam expander for the transmission of the laser due to the WALES lidar concept being bi-axial. The laser beam source architecture is quite different from Aeolus, though, as two frequency-doubled Nd:YAG lasers are used to pump titanium-sapphire (Ti-Sa) power lasers. Other subsystems also differ.

The characteristics of the instrument are given in Table 2-6. It is a very power-hungry instrument as it is designed to transmit four laser beams at an equivalent PRF of 100 Hz.

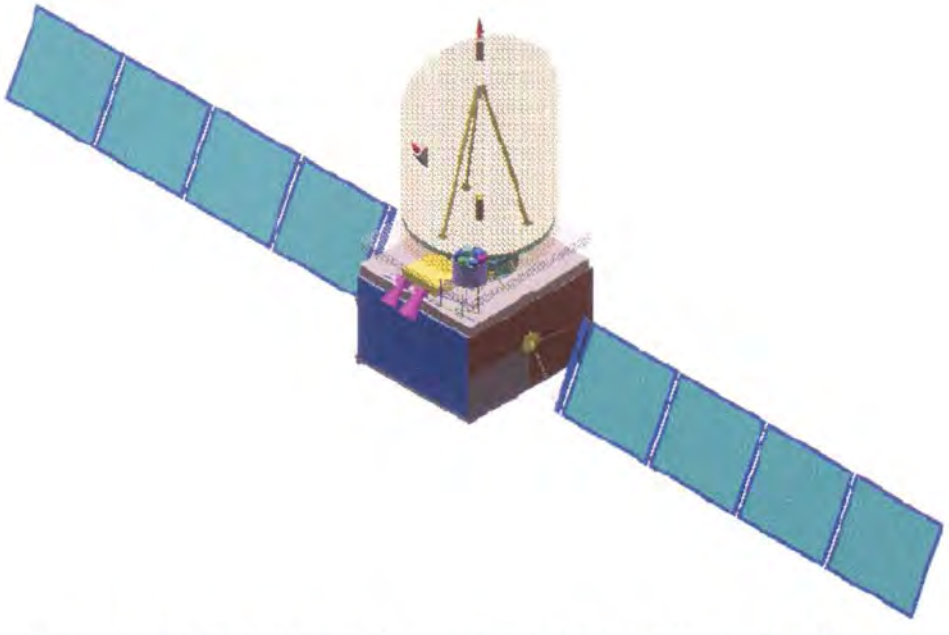

Figure 2-12. One of the two WALES concepts proposed during the Phase A study [ESA, 2004b]

Parameter	Value
Transmitted wavelengths [nm]	935.685 935.561 935.906 935.852
Altitude [km]	450
Telescope diameter [mm]	1750
PRF [Hz] (per wavelentgh)	25
Pulse energy [mJ]	72
Mass [kg]	827 kg
Power [W] Total Transmitter Rest	 1645 1125 520

Table 2-6. Characteristics of one of two WALES concepts at the end of the Phase A study [Price et al, 2005].

Figure 2-13 shows the scaling options for a lidar like WALES. It appears that a telescope diameter above 2.5 m is required for a 15 mJ beam, or 3.25 m if a 10 mJ beam is targeted, with an altitude above 300 km.

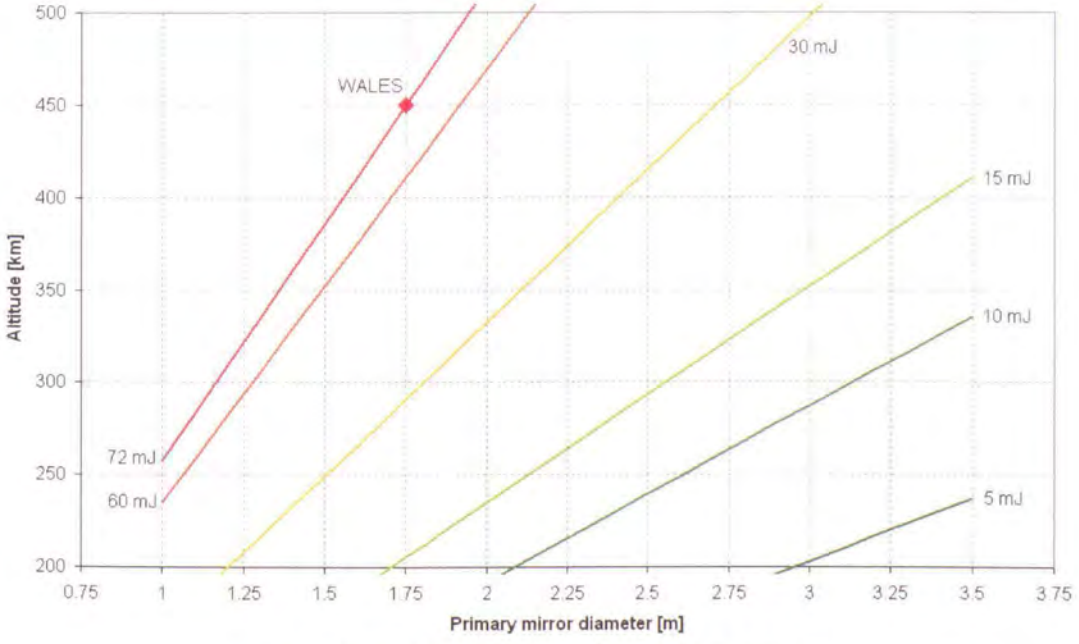

Figure 2-13. WALES instrument scaling

2.6.4.3 A-SCOPE

The Advanced Space Carbon and Climate Observation of Planet Earth (A-SCOPE) is a mission concept considered under the Earth Explorer Core Mission 4. It aims to improve our understanding of the global carbon cycle and regional carbon dioxide fluxes.

The payload is an Integrated Path Differential Absorption (IPDA) lidar which, as the name implies, uses the same differential absorption technique as DIAL but only measures total column by cumulating the signals at all altitudes. Thus, the measurements are not range-resolved.

Two instrument concepts have been considered, targeting the 1.57-μm and 2.05-μm CO_2 absorption bands, respectively. Both concepts generate two laser beams at an overall PRF of 50 Hz and pulse energy of about 50 mJ. In the case of the instrument at 1.57 μm, a Nd:YAG Master Oscillator/Power Amplifier (MOPA) generates a laser beam at 1064 nm and an Optical Parametric Oscillator / Amplifier (OPO/OPA) converts it into a 1.57-μm beam.

This instrument concept is for a 1-m receiver telescope at an altitude of 400 km. It consumes 550 W of power, of which 400 W are for the transmitter stage, as shown in Table 2-7. The overall satellite configuration for this A-SCOPE concept is shown in Figure 2-14.

Figure 2-14. A-SCOPE Spacecraft configuration for the 1.57-μm IPDA lidar [ESA, 2008].

Parameter	Value
Transmitted wavelengths [nm]	1572.024 1573.193
Altitude [km]	400
Telescope diameter [mm]	1000
PRF [Hz] (per wavelength)	50
Pulse energy [mJ]	50
Mass [kg]	380 kg
Power [W] Total Transmitter Rest	 550 400 150

Table 2-7. Characteristics of one of the A-SCOPE Phase 0 mission concepts.

Adapted from [ESA, 2008].

A-SCOPE can clearly benefit from a larger telescope in a lower altitude, as shown by Figure 2-15. Increasing the aperture diameter to 1.4 to 1.8 m at an altitude between 300-350 km would allow the beam energy to be reduced to 10 to 15 mJ. For a 5 mJ beam, the telescope needs to be increased to about 2.5 m.

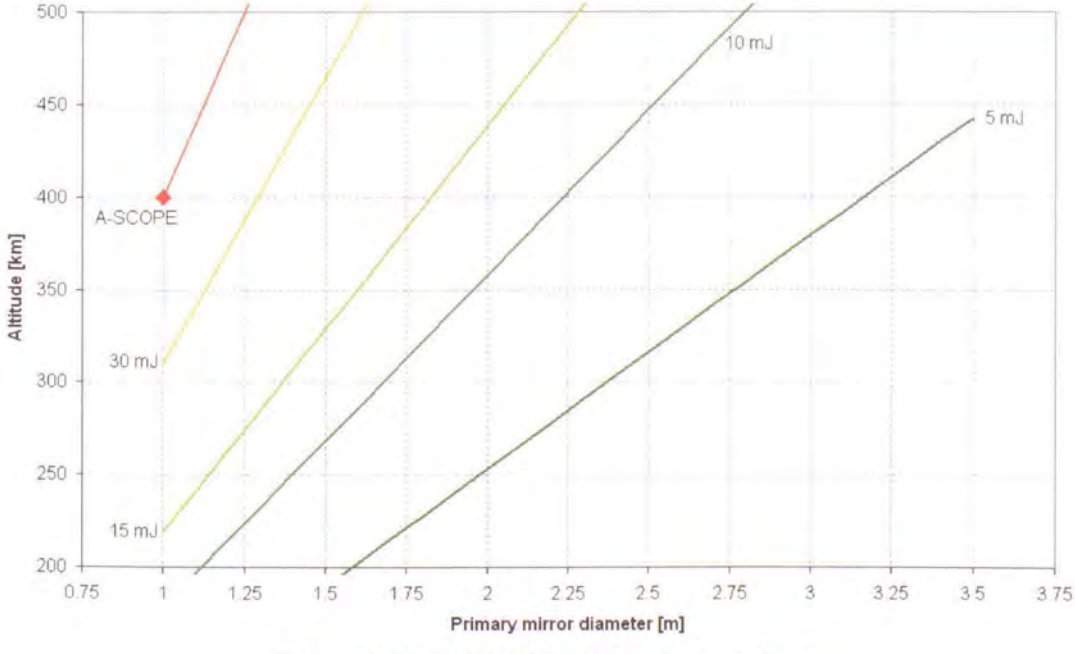

Figure 2-15. A-SCOPE instrument scaling

2.7 Conclusion

Lidar instruments will open up possibilities in Earth Observation, and particularly in atmospheric remote-sensing. Major technology development is underway, most notably in Europe and in the USA, in order to improve their lifetime, which has proven to be a complex challenge. The most critical issues, until they are eventually resolved by new technology, are found in the laser and are related to the thermal resistance of LDAs and the laser-induced damage and contamination of optics. It is clear that reducing the power consumption can greatly help in reducing these issues. From a lidar performance view point, this can be achieved by trading the laser beam energy against the aperture diameter of the receiver telescope and the altitude of the satellite. The aim is to reduce the beam energy in the range 5-15 mJ to avoid or at least limit contamination of the lidar transmission optics.

The aperture diameter cannot be chosen freely: it is limited by the dimensions of the launch vehicle fairing, accommodation constraints and manufacturing considerations. Similarly, the altitude is mostly limited by the atmospheric density and resulting drag and its impact on the propulsion system.

Chapter 3 discusses options for the configuration of a lidar satellite.

Chapter 3

Satellite and Instrument Configuration

3.1 Introduction

A lidar is often a very bulky and power-hungry instrument which drives the overall spacecraft configuration and mission design. Thus, it is necessary to address the instrument and spacecraft configurations together. In particular, a suitable telescope design, the bulkiest component of a lidar, needs to be selected accordingly.

This chapter presents the design drivers and requirements of a lidar, investigates the configuration options of both the satellite and the instrument, and reviews the telescope options for the desired mission characteristics. Four options are selected and sized.

3.2 Satellite Configuration

3.2.1 Lidar accommodation options

There are several ways in which a lidar instrument can be accommodated on a satellite, illustrated in Figure 3-1. In this representation, the satellite motion is along the X axis, and nadir along Z. In a dawn-dusk orbit with a local time of the ascending node (LTAN) of 18:00, the Y axis points away from the Sun. The lidar instrument is represented by the blue cube, and the platform in green.

Option (a) and Option (d) are well-known as they correspond to the EarthCARE and Aeolus configurations, respectively, as shown in Figure 3-2. Options (b) and (c) are similar to (a) only rotated in the horizontal plane. Two other options have not been considered: the opposite of option (d), with the lidar on the zenith face, has little interest since the lidar must point to nadir, and the opposite of option (a), with the lidar behind the platform, is deemed inconvenient as it would make the accommodation of the propulsion system awkward.

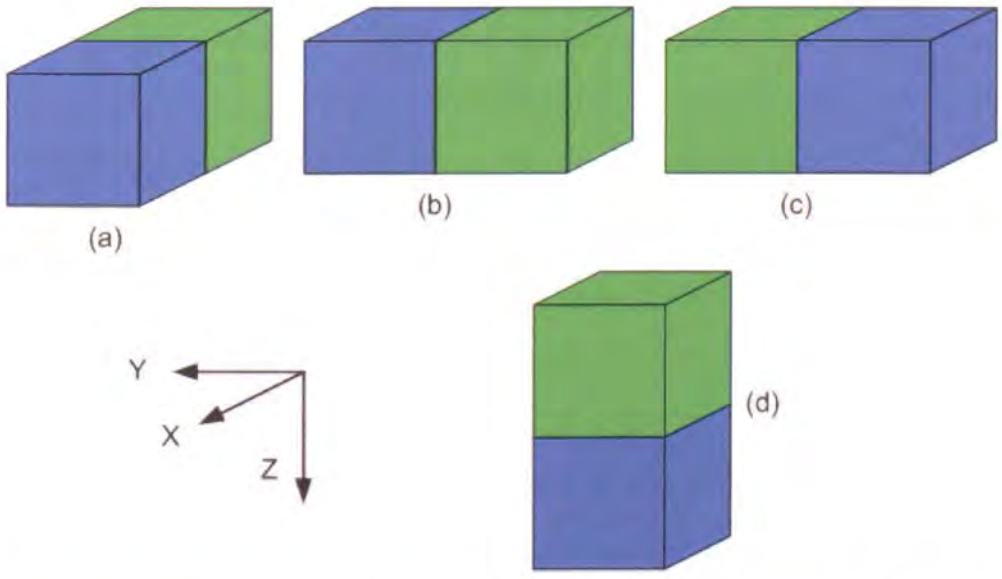

Figure 3-1. Lidar accommodation options (blue = lidar, green = platform).

Figure 3-2. Artist impression of Aeolus (left) and EarthCARE (right)

Adapted from ESA [2009a] and ESA [2009b]

3.2.2 Ballistic coefficient

The ballistic coefficient, BC, of the satellite is defined as:

$$BC = \frac{m_{SC}}{SC_D} \tag{3-1}$$

While the mass of the spacecraft m_{SC} can be known quite accurately, the cross-section area S exposed to the atmospheric molecular flow is variable and less easily predicted at any given moment, but the most difficult to determine is the drag coefficient C_D.

The drag coefficient is a function of many parameters: it primarily depends on the shape and surface materials of the satellite, but is also affected by a combination of the thermosphere composition at the altitude of the satellite, the type of reflection of the incident molecule on the surface of the satellite, as well as the incidence angle which depends on the attitude of the satellite [Gaposchkin, 1994 cited in Vallado & Finkleman, 2008].

For the purpose of aerodynamics, a satellite is often symbolised by a flat plate, unless its shape is obviously different. For a flat plate normal to the flow, and assuming a diffuse re-emission of the incident molecule, the theoretical drag coefficient can be estimated by the Schamberg formula [Cook, 1965]:

$$C_D = 2\left(1 + \frac{2}{3}\sqrt{1-\alpha}\right) \tag{3-2}$$

The thermal accommodation coefficient α is the ratio of the change in energy of the incident molecule over the maximum energy loss that could occur [Cook, 1965], which is not easily predicted. Gaposchkin [1994] calculated values of α for various gases and altitudes. Thus, C_D varies with altitude because the thermosphere molecular content (species and density) also varies with altitude. The drag coefficient–altitude relationship is illustrated by Figure 3-3.

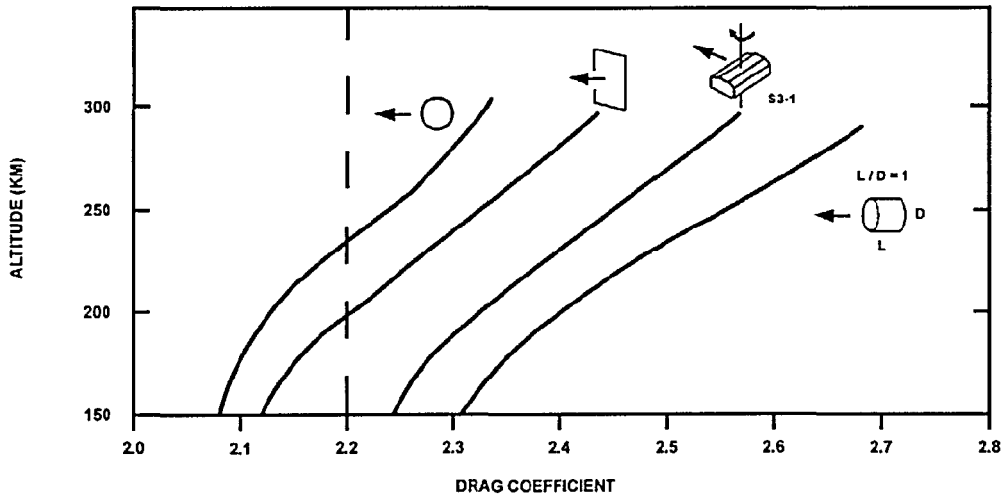

Figure 3-3. Drag coefficient as a function of altitude for various satellite shapes (spherical, flat plate, S3-1 satellite, and longitudinal cylinder) [Moe, 2006].

The aerodynamics of a body depends strongly on the flow regime; which at orbital altitudes above 175 km can be considered to be a hyperthermal free-moecular flow for most satellites [Cook, 1965]. Under these conditions, Sentman's expression of the drag coefficient is [Doombos et al, 2009]:

$$c_D A = \left(\frac{P}{\sqrt{\pi}} + \gamma Q Z + \frac{\gamma}{2} \frac{V_{out}}{V_r} \left(\gamma \sqrt{\pi} Z + P \right) \right) A \tag{3-3}$$

where:

$$P = \frac{1}{S_\infty} \exp\left(-S_n^2\right) \tag{3-4}$$

$$Q = 1 + \frac{1}{2S_\infty^2} \tag{3-5}$$

$$Z = 1 + erf(S_n) \tag{3-6}$$

$$S_n = S_\infty \gamma \tag{3-7}$$

$$\gamma = \cos(\theta) \tag{3-8}$$

with θ being the flow incidence angle with respect to the normal of the surface.

In addition, S_∞ is the speed ratio, V_r is the relative speed of the flow and V_{out} is the most probable velocity of the re-admitted molecules after impact with the surface of the satellite:

$$S_\infty = \sqrt{\frac{m_g V_r^2}{2RT_\infty}} \tag{3-9}$$

$$V_{out} = V_r \sqrt{\frac{2}{3}\left[1 + \alpha_E\left(\frac{T_{wall}}{T_{in}} - 1\right)\right]} \tag{3-10}$$

$$T_{in} = \frac{m_g V_r^2}{3R} \tag{3-11}$$

R is the universal gas constant (8.31 $J.K^{-1}.mol^{-1}$), m_g is the molecular mass of the gas (~16 $g.mol^{-1}$), and α_E is the accommodation coefficient, defined as the ratio of the change in energy of the incident molecule over the maximum energy loss that could occur [Cook, 1965]. However, values of α_E are difficult to ascertain, and values in the range 0.6 to 1.0 are employed [Doombos et al, 2009]. T_∞ is the atmospheric temperature, while T_{in} is the kinetic temperature of the incoming particles, and T_{wall} is the temperature of the satellite wall, typically in the range 0-30°C.

By summing up the contributions of all its faces, it is possible to determine the equivalent drag coefficient of a satellite with a reference cross-section area normal to the flow A_{ref}:

$$C_{D_{equiv}} = \frac{\sum_1^n \left(A_n C_{D_n}\right)}{A_{ref}} \tag{3-12}$$

Note that A_n is a physical surface area, not a projected area.

Table 3-1 summarises the $(C_D A)$ product for the three accommodation options and three front wall configurations, as illustrated in Figure 3-4.

Option (a) has a $(C_D A)$ 74% smaller than the other options, although its C_D is larger due to its elongated shape. For all accommodation options, the front wall configuration has no substantial impact (less than 5%) on C_D. Hence, from a purely aerodynamic viewpoint, it is essential to seek a configuration that minimises the front cross-section area. However, this may not always be feasible and depends also on the volume available inside the fairing of the launch vehicle.

Configuration	Dimensions	(C_D.A)		
		Flat plates	Angled half-plate	Double-angled quarter-plate
Option (a)	1.5 (H) × 1.5 (W) × 3.0 (L)	6.28 (C_D = 2.79)	6.17 @ 60° (C_D = 2.74)	6.07 @ 30° (C_D = 2.70)
Option (b) and (c)	1.5 (H) × 3.0 (W) × 1.5 (L)	10.92 (C_D = 2.43)	10.68 @ 60° (C_D = 2.37)	10.37 @ 30° (C_D = 2.30)
Option (d)	3.0 (H) × 1.5 (W) × 1.5 (L)	10.92 (C_D = 2.43)	10.59 @ 60° (C_D = 2.35)	10.46 @ 30° (C_D = 2.32)

Table 3-1. Product of C_D and area for three accommodation options and three front wall configurations for a given volume.

Figure 3-4. Illustration of the configuration options for the front wall of the satellite.

Flat plate (left), angled half-plate (middle) and double-angled quarter-plate (right).

3.2.3 Launch vehicle fairing

The dimensions of the launch vehicle fairing can constrain the dimensions of the lidar. Indeed, the small launch vehicles (Vega, Rockot, Dnepr, etc.) tend not to be limited so much by the payload mass they can deliver in a particular orbit, but rather by the dimensions of their respective fairings. The payload volume of the Vega fairing is shown in Figure 3-5 (Rockot is not shown but has similar dimensions). The Soyuz fairing is shown in Figure 3-6 for single and dual launch.

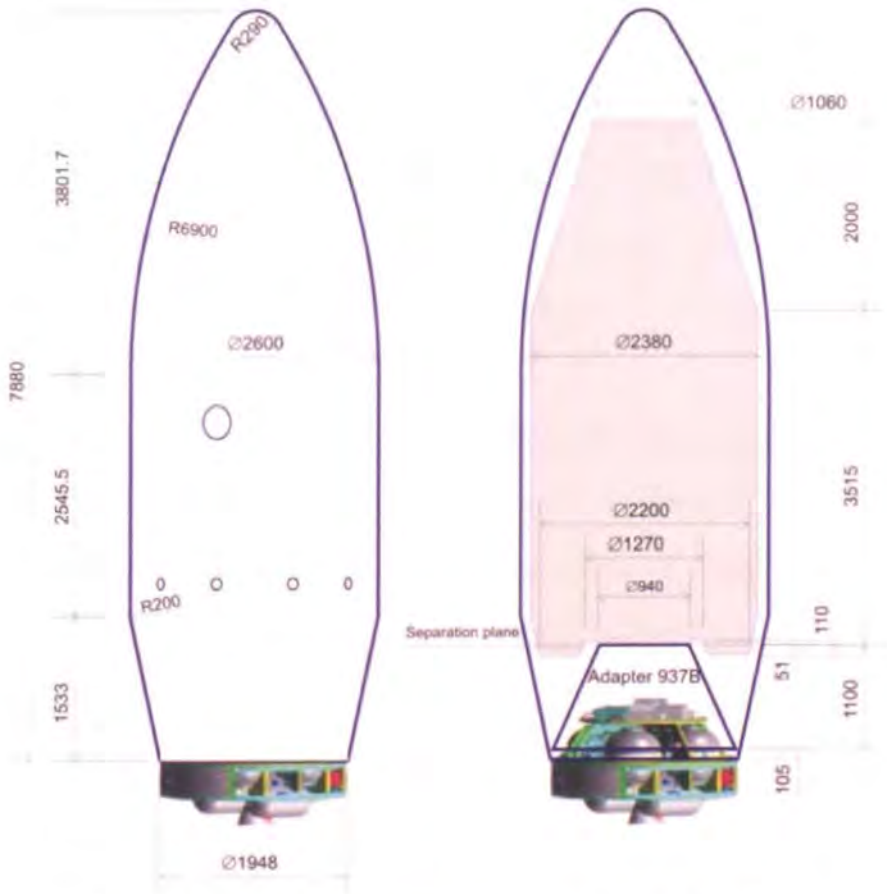

Figure 3-5. Vega fairing dimensions and payload volume.

From Arianespace [2006a].

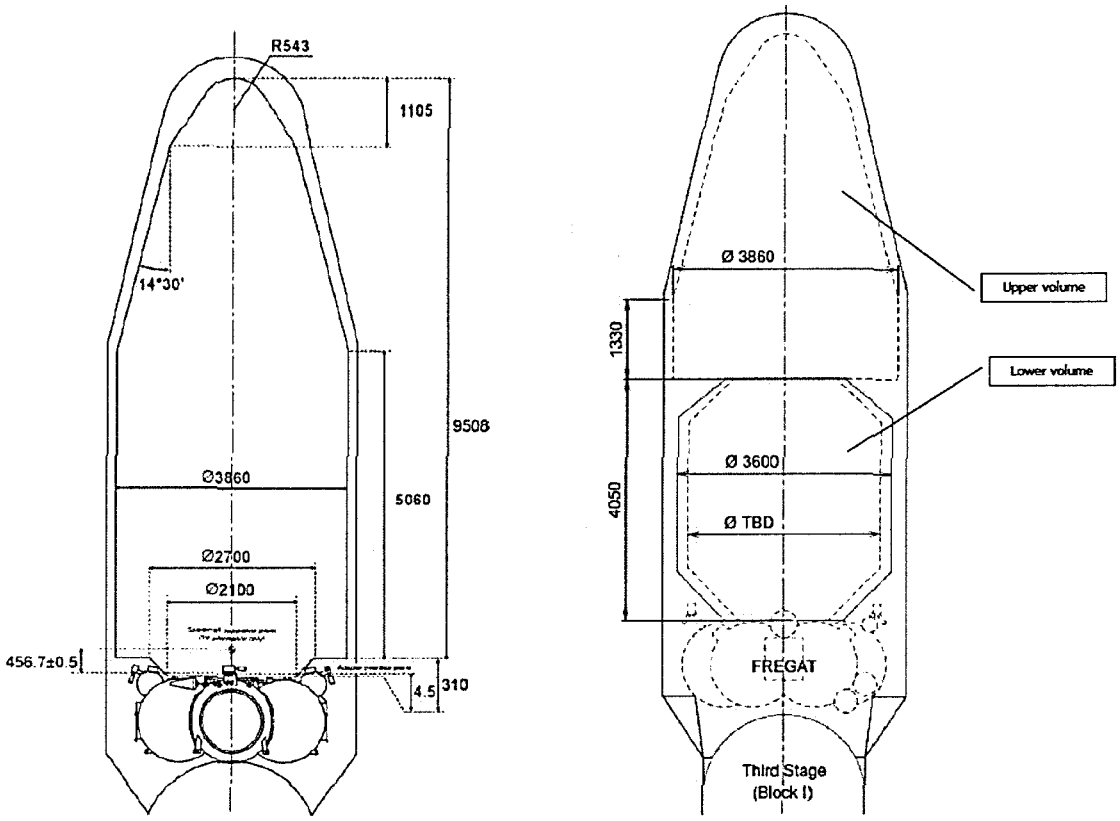

Figure 3-6. Soyuz fairing volume in single (left) and dual launch configuration (right).

From Arianespace [2006b].

Spacecraft configurations (a), (b) and (c) would be accommodated inside the launch vehicle fairing in a way similar to EarthCARE, while configuration (d) would be accommodated like Aeolus. Illustrations of these are shown in Figure 3-7 (IV) and (II), respectively.

In Figure 3-7, it is possible to see that the diameter of a small launcher fairing is the limiting factor on the primary mirror diameter, while the fairing height could restrict the focal length (case II). In a configuration like EarthCARE, the diameter of the fairing constrains both the aperture diameter and the focal length of the lidar, and more generally its external envelope (case IV).

As a secondary payload on Soyuz, a nadir-mounted instrument is primarily limited in height (case I), however it becomes possible to increase the volume of the instrument when mounted horizontally (case III).

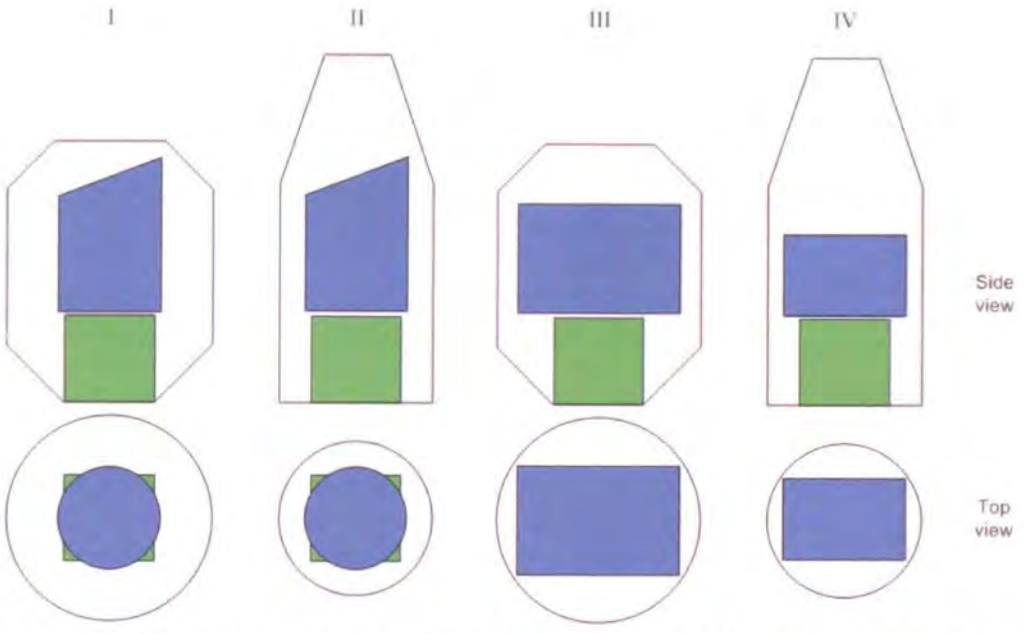

Figure 3-7. Illustration of the accommodation options of the satellite inside Vega fairing and Soyuz lower volume (not to scale).

Cases I *and* II *refer to the nadir-mounted lidar (Aeolus-like, Figure 3-1 (d)) and* III *and* IV *to the front-mounted lidar (EarthCARE-like, Figure 3-1 (a)). Cases* I *and* III *represent the lower volume in Soyuz dual launch. Cases* II *and* IV *represent the fairing of a launcher in single payload.*

3.2.4 Other satellite configuration aspects

While the drag and the launch vehicle accommodation are the main drivers for the satellite configuration, other aspects should not be neglected.

While deployable, solar arrays may not necessarily be easy to accommodate. Figure 3-8 illustrates some of the options available. The main constraints for the solar array design are that they must not interfere with the Field of View (FoV) of the lidar instrument, and must not stand within the plume area of the propulsion system.

The most logical position for the propulsion system is on the –X face of the satellite, pushing the satellite against the drag force. It may be possible to have solar arrays along the –X axis, provided that the propulsion thrusters are arranged in a cluster, at some angle away from the –X axes.

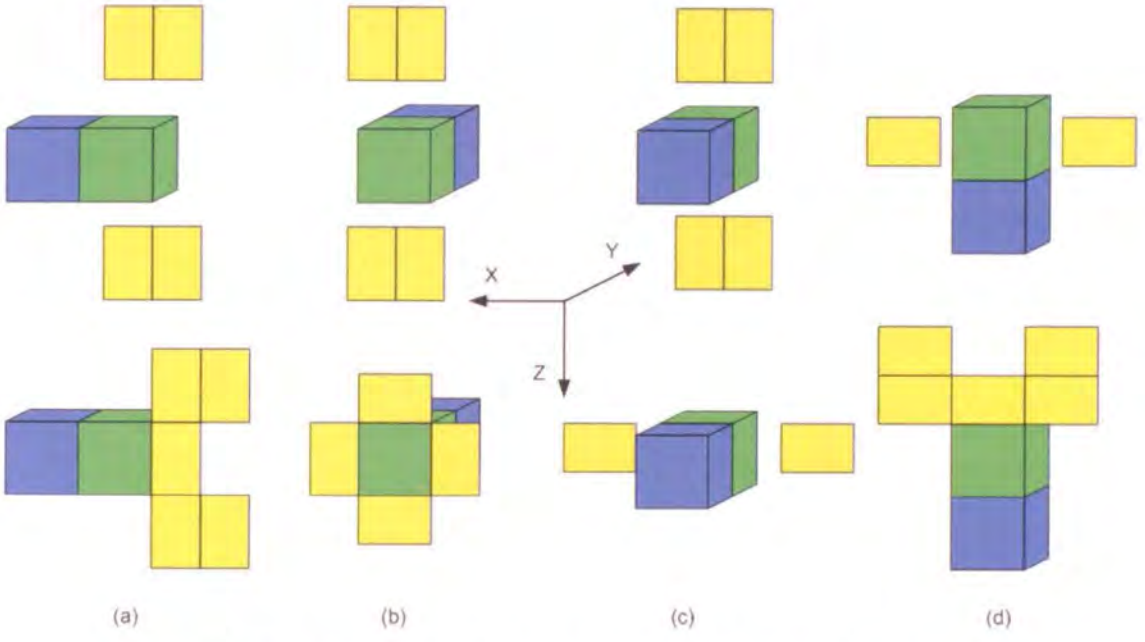

Figure 3-8. Non-exhaustive list of solar array accommodation options.

Thermal control of the lidar instrument necessitates a wall hidden from the sun for the radiator. It is clear that Option (c) with the instrument on the sun-side of the platform is strongly penalised. Option (b) seems to be best suited in this respect, however the telescope would most likely stand between the electronics and the deep space (+Y) wall.

The Attitude Determination and Control System (ADCS) will need to compensate for all torques, with the most important coming from the drag itself. Configurations where the Centre of Mass (CoM) and Centre of Pressure (CoP) are offset will be most disadvantaged.

Finally, the structure must provide a load path from the lidar instrument to the launch vehicle adapter ring. This can be somewhat difficult for options (a), (b) and (c), while it is rather straightforward for option (d).

3.2.5 Satellite configuration trade-off

Table 3-2 presents an assessment of the configuration options against aerodynamics, launch vehicle accommodation and satellite subsystems considerations.

The main criteria are the allowable size of the telescope with respect to the launcher, and the drag force the spacecraft would generate, and are attributed a weighting factor of 3. With Vega as the baseline launcher and Soyuz as an alternative, the allowable size for a dual launch is given slightly less importance with a factor of 2. Other factors, related to the platform subsystems are given a weighting factor of 1, as they are not the most critical. In effect, the configuration option that comes on top in the first two criteria should normally come first overall, unless it is judged impossible on the other criteria.

For the drag force, option (a) is clearly most advantageous, as demonstrated by Table 3-1. Section 3.2.3 showed that option (d) can provide the largest telescope diameter. For a launch as a second passenger on Soyuz, option (d) is less favourable than the others.

For the minor criteria, option (b) rates highest for the accommodation of the solar arrays (Figure 3-8), option (c) is the worst for the thermal control of the instrument, option (a) is best for propulsion and AOCS, as a consequence of a lower drag force.

From the assessment presented in Table 3-2, it is clear that options (b) and (c) can be eliminated. The most suitable configuration is the one with the lidar instrument installed on the +X face of the satellite. The configuration with the lidar mounted on the +Z face allows for a larger instrument if restricted to the Vega launcher.

Due to the small difference in scores between Options (a) and (d), both configurations are retained. Section 3.3 looks at the telescope design and sizing for the front-mounted instrument, while the sizing of the nadir-mounted instrument is addressed in section 3.4.

The two options are represented in Figure 3-9.

	Weighting	Option (a)	Option (b)	Option (c)	Option (d)
Drag force	3	+ +	0	0	0
Allowable size in launcher (single payload)	3	0	0	0	+ +
Allowable size in Soyuz (dual launch)	2	+	+	+	0
Solar array accommodation	1	0	+ +	–	+
Propulsion	1	+	0	0	0
Thermal	1	+	0	– –	+
AOCS	1	+	0	0	0
Structure	1	0	0	0	+
Total		**11**	**4**	**-1**	**9**

Table 3-2. Satellite configuration trade-off

The options in this table refer to the accommodation aspects described in Figure 3-1.

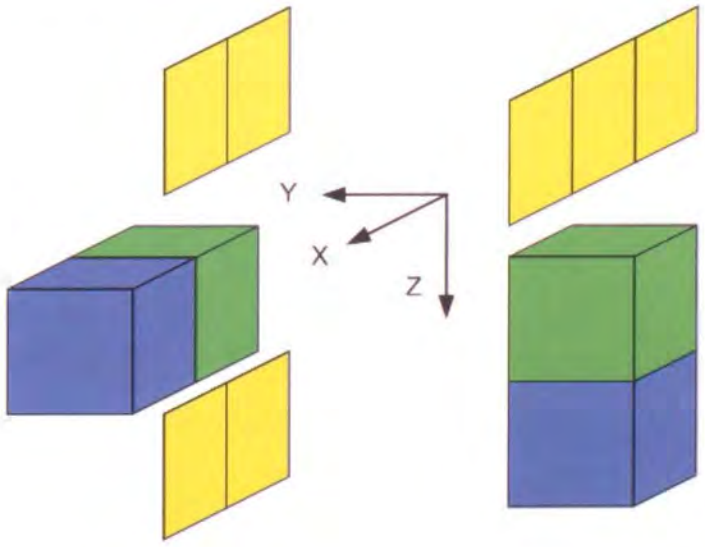

Figure 3-9. Illustration of the two accommodation options retained

3.3 Telescope Designs for Front-Mounted Lidars

This section assesses different telescope design options in order to select the one most suited to the spacecraft configuration. The sizing process of the selected concept is then explained followed by the design summary of two concepts of different aperture diameter. Optical aberrations affecting space telescopes are discussed first.

3.3.1 Optical aberrations

Some of the critical characteristics of space telescopes are their volume, mass, sensitivity to misalignment, and optical quality (surface roughness). In addition, telescopes designs can inherently suffer from different kinds of optical aberrations. For most lidar applications in particular, it is desirable to reduce blur circles due to increased coma [Goela and Taylor, 1991]. More generally, high optical quality is not paramount for lidar telescopes, as these instruments generally are photon-counting devices which do not build an image. There is an exception, however; that of heterodyne lidars, where diffraction-limited optics is desirable [NASA, 1979]. A diffraction-limited optical system is (rather arbitrarily but commonly) defined by the "rule of Maréchal", which states that image degradation due to aberrations is not noticeable if the Strehl ratio is greater than 0.8 [Malacara & Malacara, 1994]. This is expressed as:

$$\text{Strehl ratio} = 1 - \left(\frac{2\pi}{\lambda}\right)^2 (\Delta\Phi)^2 \geq 0.8 \tag{3-13}$$

where λ is the wavelength and $\Delta\Phi$ is the rms wavefront error [Bely, 2003]. Diffraction-limited systems must therefore meet the wavefront error requirement of:

$$\Delta\Phi \leq 0.071\lambda \qquad or \qquad \Delta\Phi \leq \frac{\lambda}{14} \text{ rms.} \tag{3-14}$$

However, none of the lidars considered here involve heterodyne detection. Aberrations are difficult to quantify without a ray tracing code. We will simply note at this point that the telescope of ALADIN is a very good telescope, not far from diffraction-limited quality

[Schulte, 2009], as required by the short wavelength (355 nm) at which it operates. Testing of the primary mirror of the ALADIN telescope has demonstrated a wavefront shape error below the speficied 150 nm [Korhonen et al, 2008]. Its optical quality, or that of most telescopes designed for the visible domain, would in fact probably be of suitable quality for heterodyning, as such applications are usually performed in the IR spectrum [NASA, 1979].

3.3.2 Telescope configuration options

Two distinct, although complementary, aspects are considered as part of the telescope configuration. The telescope design refers to the shapes and positions of the primary and secondary mirrors; the telescope accommodation describes the location and orientation of the telescope within the instrument and satellite.

A variety of telescope designs are considered. Previous studies at the dawn of the spaceborne lidar era [CNES, 1976; NASA, 1979; NASA, 1980] have reviewed many concepts. However, other concepts were apparently not considered, possibly because the overall accommodation was different, or some concepts may have been discarded at an earlier stage of these studies.

The most favoured telescopes in space-based astronomy have been the Cassegrain and the likes, i.e. Ritchey-Chretien and Dall-Kirkham, illustrated by Figure 3-10 (a). They are characterised by their concave primary mirror (M1) and convex secondary mirror (M2), which is located between M1 and its focal point. The shape of both mirrors is what differentiates these telescopes, resulting in various degrees of correction of optical aberration, at the price of manufacturing complexity. They are all fairly compact devices, as it is possible to manufacture and polish rather fast primary mirrors. With an aperture of 0.9, the telescope of ALADIN falls into this category. However, with any type of telescope, the faster the primary, the more sensitive to misalignment the instrument becomes [Bely, 2003].

The Gregorian is fairly similar, except for the fact that the secondary mirror is concave, as shown in Figure 3-10 (b). The main consequence is that M2 must be located behind the focal point of M1, making it longer than telescopes with a convex M2.

The Newtonian, depicted in Figure 3-10 (c), is probably the most popular configuration for amateur astronomy and is very insensitive to misalignment [Lutz et al, 1989]. It uses a tilted flat secondary mirror to move the focal point of the primary mirror on the side of the telescope. For a given M1 focal length, it can be made fairly short but M2 becomes large, increasing the central obscuration on M1. Alternatively, M2 can be made smaller by moving it away from M1, but the length of the telescope increases. Its major downfall is its high sensitivity to stray light.

The Nasmyth telescope is a modified Cassegrain telescope with a folding mirror between M2 and the focal point, to bring the latter on the side of the telescope rather than behind M1; this is demonstrated in Figure 3-10 (d). While the focal point of a Cassegrain moves with the telescope, that of a Nasmyth stays fixed (although the image rotates with the telescope elevation). This is particularly useful for large ground-based telescopes with heavy instrument suites, such as the 42-m diameter European Extremely Large Telescope (E-ELT), which is expected to start operation in 2018 [ESO, 2009].

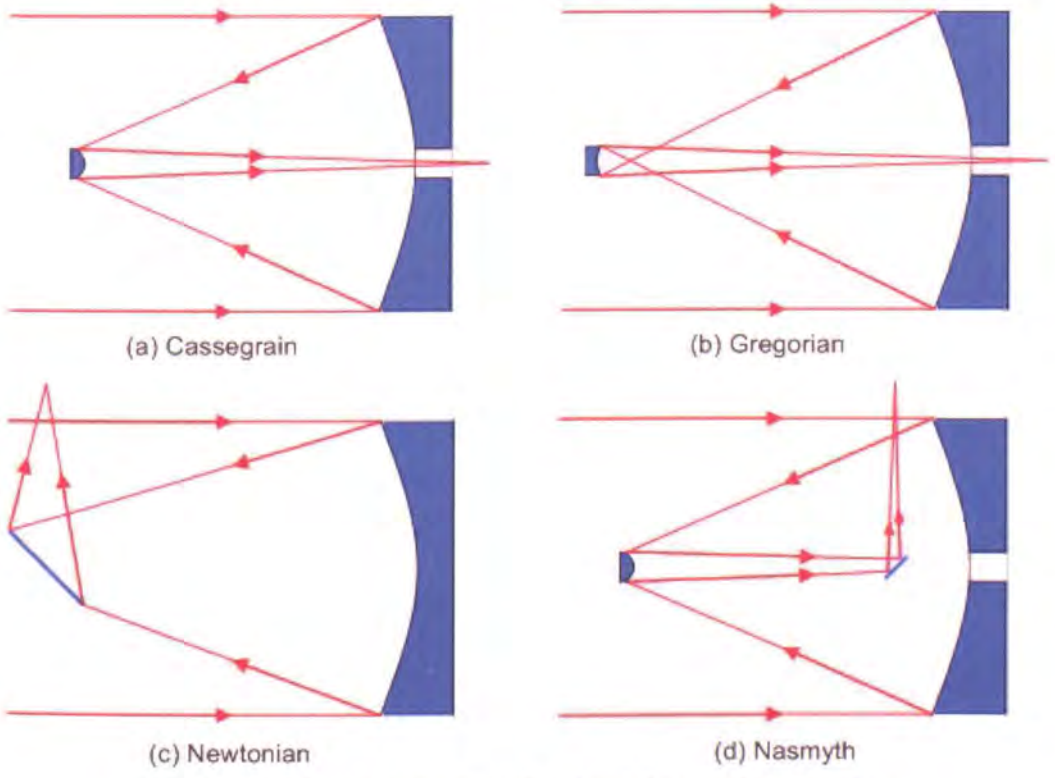

Figure 3-10. On-axis, all-reflective telescope concepts

Off-axis telescopes are interesting for their unobstructed apertures, which is a particularly desirable feature for telescopes observing the infrared and longer wavelengths [Bely, 2003]. Most often, antennas receiving microwave radiations are in effect off-axis telescopes. The primary mirror is roughly half the diameter of the parent mirror it is cut from. Unfortunately, this means that for a given accommodation volume, the off-axis telescope is twice as fast as its on-axis counterpart. However, the Center for Applied Optics at the University of Alabama in Huntsville (UAH) have designed a compact off-axis Cassegrain telescope for a 2-μm spaceborne lidar [Feng et al, 1995]. They have manufactured a 250-mm aperture prototype with an overall telescope volume of 378 × ~300 × 230 mm, although it is scalable to a 500-mm aperture [Ahmad et al, 1996]. Both Cassegrain and Gregorian designs have been used in off-axis telescopes (Figure 3-11).

Another way of avoiding obscuration and diffraction induced by the secondary mirror is to tilt the primary mirror. This is the case of the Herschelian telescope, which is similar to the Newtonian concept but with a tilted primary mirror and a secondary mirror located on the side. Alternatively, the flat secondary mirror can be made into a toroid, either concave (Yolo telescope) or convex (Schiefspiegler) – as represented in Figure 3-12 – with the former outperforming and capable of being made faster than the latter [telescope-optics.net]. However, tilting the mirror causes severe coma and astigmatism, and these telescopes are better made slow, usually by limiting the aperture diameter [telescope-optics.net].

The Schmidt-Cassegrain and Maksutov-Cassegrain (Figure 3-13) are designs with an aspheric plate and a meniscus corrector, respectively, placed at the entrance of the telescope. These would not be suitable for spaceborne lidar telescopes, though, as these additional dioptric elements would be large and heavy. Also, they provide an increased field of view, which is neither required nor desirable for a lidar.

From this brief overview, it is possible to discard the least suitable concepts. A trade-off tree is presented in Figure 3-14, summarising which telescope concepts are retained and which are dropped (coloured green and red, respectively).

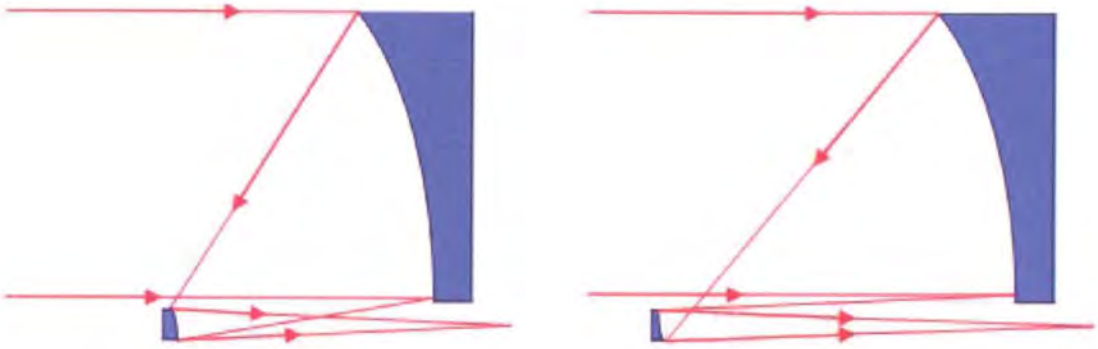

(a) Off-axis Cassegrain (b) Off-axis Gregorian

Figure 3-11. Off-axis telescope concepts.

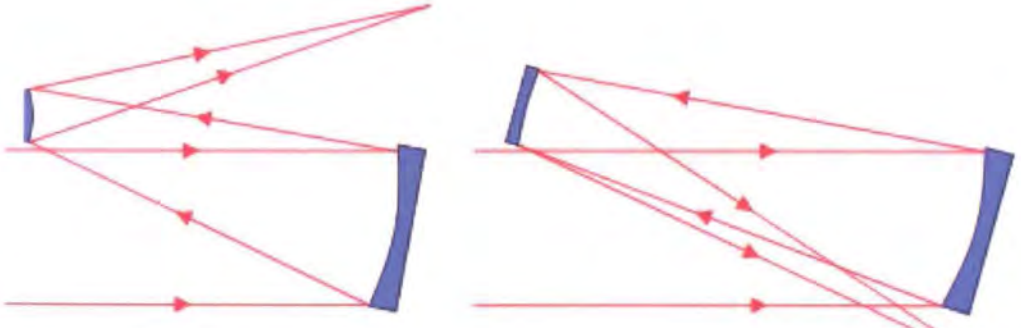

(a) Schiefspiegler (b) Yolo

Figure 3-12. Tilted-mirror telescope concepts.

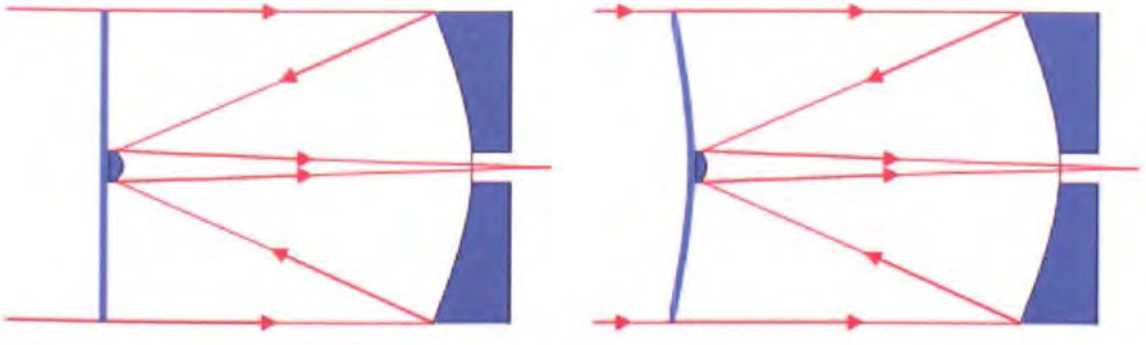

(a) Schmidt-Cassegrain (b) Maksutov-Cassegrain

Figure 3-13. Catadioptric telescope concepts.

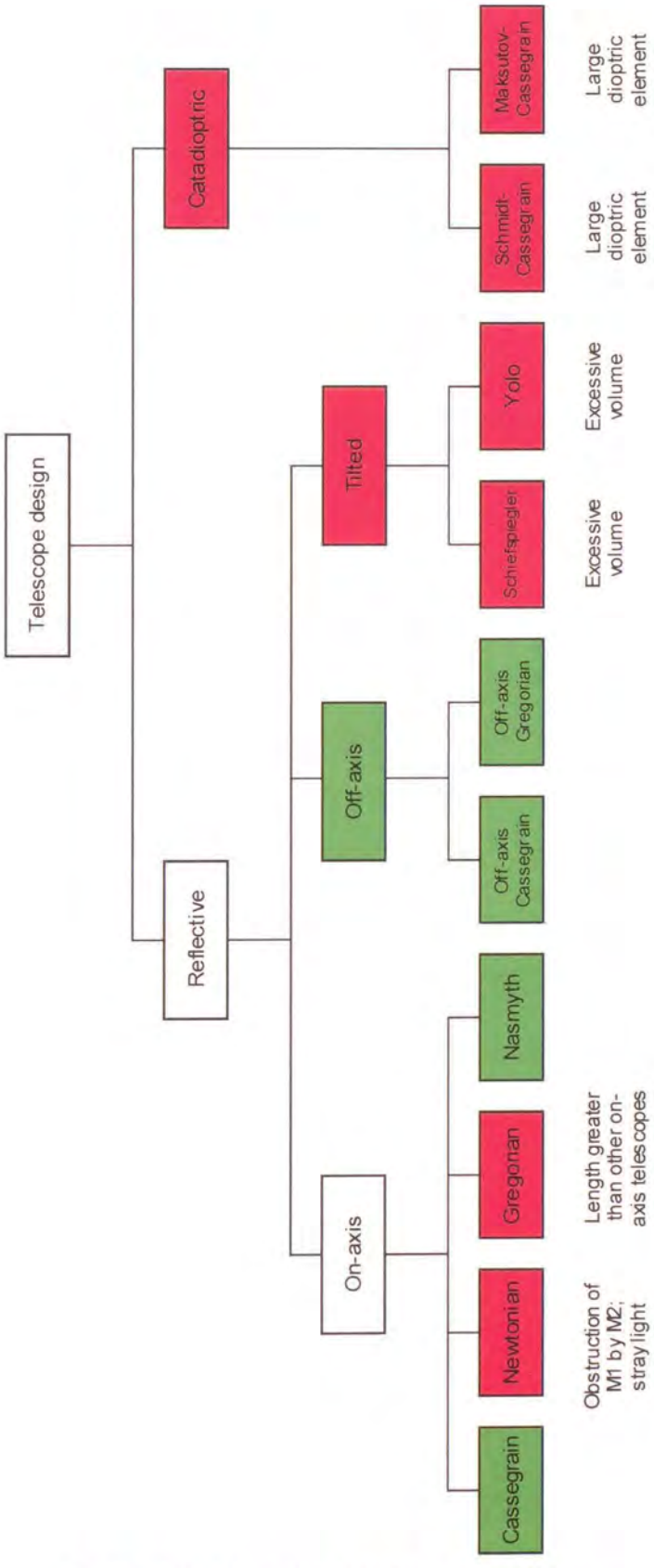

Figure 3-14. Telescope design trade-off tree.

The closed telescopes (Schmidt-Cassegrain and Maksutov-Cassegrain) are both unsuitable for large aperture spaceborne lidars. Concepts with tilted primaries have limited opportunities as they are usually limited to small angles and are quite voluminous; thus present little interest here. The on-axis Gregorian is also removed from the down-selection because of its longer length compared to the Cassegrain family of telescopes. The Newtonian design suffers from a potentially large obstruction, is potentially more sensitive to stray light and cannot take advantage of fast primary mirrors.

The selection of a telescope design is dependent on its accommodation within the instrument, and the questions of design and accommodation cannot always be separated. Five accommodation options are considered and depicted in Figure 3-15.

The first one (A) is very similar to ATLID, where the detection system is located at the back of the telescope, thus limiting the length, and consequently the aperture, of the telescope.

Concept (B) is derived from ATLID, but the detection stage is moved to the side of the telescope, which can be moved backwards, giving more room for the M1-M2 pair and allowing the aperture of M1 to be increased accordingly.

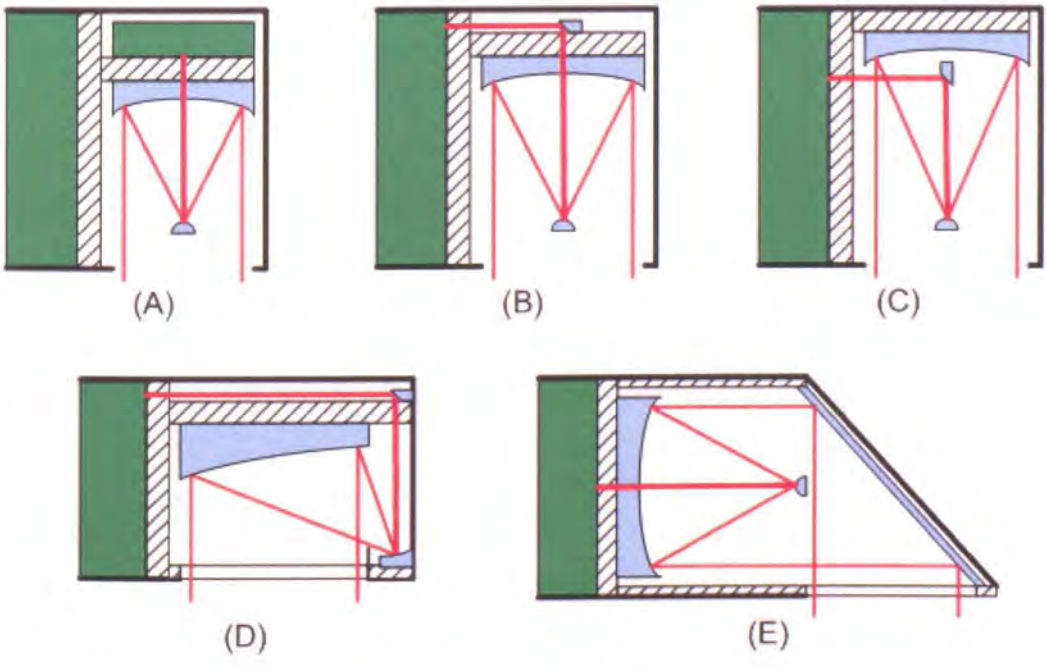

Figure 3-15. Telescope accommodation options.

The third concept (C) is similar to (B), but with a Nasmyth telescope and its primary mirror moved to the very back of the usable space to maximise the usage of the instrument's length.

Option (D) is a compact off-axis Gregorian concept based on that described by Feng et al [1995] and Ahmad et al [1996].

Finally, concept (E) consists of a Cassegrain telescope pointing horizontally with a folding mirror mounted at the front and inclined at 45°, giving the telescope a view of the Earth underneath. It has the same advantage as Aeolus, i.e. that its size is not constrained by the fairing, but without the drag penalty. This geometry is similar to whiskbroom instruments (albeit the scanning mechanism) but at a much larger scale.

3.3.3 Telescope configuration selection

The selection of the telescope configuration is based on various criteria, related to performance (telescope dimensions, stray light, misalignment) as well as practical issues (manufacturing, integration, mass distribution). The marking weight is different between the criteria, in order to allow for their relative importance. The telescope configuration trade-off is summarised in Table 3-3.

The telescope aperture and its sensitivity to misalignment are fundamental indicators of its performance and a weighting factor of 3 is applied to these criteria. Sensitivity to stray light will also affect performance but does not have the same importance as the previous ones, so is assigned a weighting factor of 2. The best option should score highly on these criteria, shown in the "score on key criteria" column, while the other three criteria, with a weighting factor of 1, should only help to differentiate between concepts of similar values on the key criteria.

Concepts (B) and (C) score highest on the key criteria, with concept (C) penalised due to its sensitivity to stray light. Concept (C) can be made somewhat larger that (B), although not by a large amount, but (C) is more sensitive to misalignment, where (B) can beneficiate from a

hard surface at the back as a support for optical elements, or even use an optical fibre as implemented on ATLID (Le Hors et al, 2008).

	Key Criteria				Secondary Criteria			Total
	Telescope length & aperture	Sensitivity to misalignment, structural stiffness	Sensitivity to stray light	Score on Key Criteria	Ease of integration	Simplicity / manufacturing cost	Mass distribution	
Weighting factor	**3**	**3**	**2**		**1**	**1**	**1**	
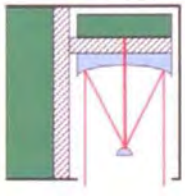 (A)	–	+ +	0	**3**	+	0	0	**4**
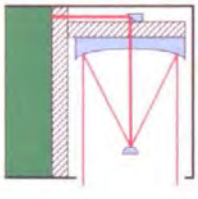 (B)	+	+ +	0	**9**	+	0	–	**9**
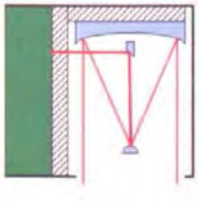 (C)	+ +	+	–	**7**	0	–	–	**5**
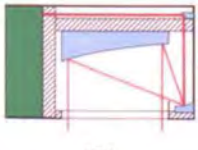 (D)	0	+	0	**3**	–	– –	0	**0**
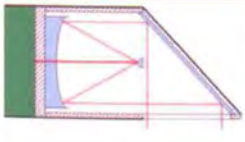 (E)	+ +	0	–	**4**	0	–	–	**2**

Table 3-3. Telescope accommodation trade-off table.

The other concepts are about similar in merit, with concept (A) being limited by a small aperture and (E) by stray light, while concept (D) does not display either strong or weak points.

The advantage of Concept (B) over Concept (C) further increases when considering the secondary criteria. Concept (C) is penalised due to the complexity introduced by the third optical element. Thus the Cassegrain telescope of Concept (B) is selected as the baseline for a front-mounted lidar.

3.3.4 Telescope Sizing for front-mounted lidars

This section covers the optical design and parametric sizing of the front-mounted lidar instrument, corresponding to satellite configuration (a) in chapter 3.2.1, followed by the computation of the external dimensions of the telescope.

3.3.4.1 Computation of the telescope optical parameters

Figure 3-16 shows the layout of a Cassegrain telescope, along with the relevant parameters. The primary mirror has a diameter D_1 and a focal length f_1. The secondary mirror has a diameter D_2 and is located at a distance s from M1. Other lengths of interest include the distance p between the focal point of M1 and the surface of M2, the distance q from the apex of M2 to the telescope focal point, and the distance e from the apex of M1 to the telescope focal point.

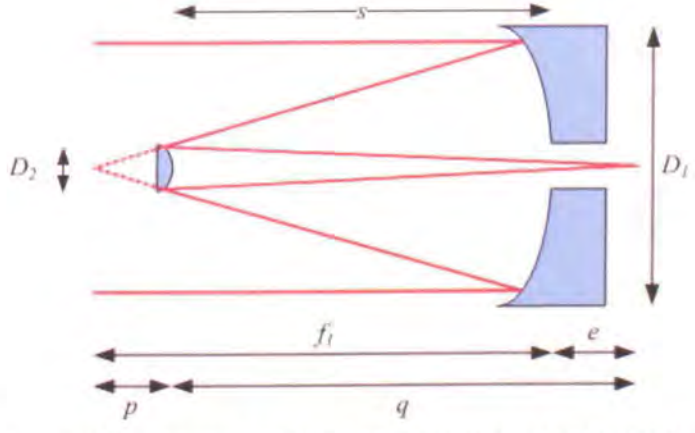

Figure 3-16. Cassegrain telescope layout and parameters

The parametric calculation of the optical parameters of a telescope is not a straightforward process, but is usually iterative. Two simplified methods are proposed here to give preliminary dimensions.

In both cases, we start with the range to the ground, the ground footprint diameter and the pinhole (or field-stop) diameter. The first one is given by the selected orbit altitude, the second by measurement requirements, while the third one is rather arbitrary but mostly inherited from previous spaceborne lidars. These parameters are essential in determining the focal length, F, of the overall telescope.

Separately, we also set the characteristics of M1, i.e. its diameter and F-number, based on past designs, and from which the focal length of M1 can easily be obtained (and the less essential radius of curvature, R_1). From the focal lengths of the overall telescope and the primary mirror, we find the magnification of the telescope, M.

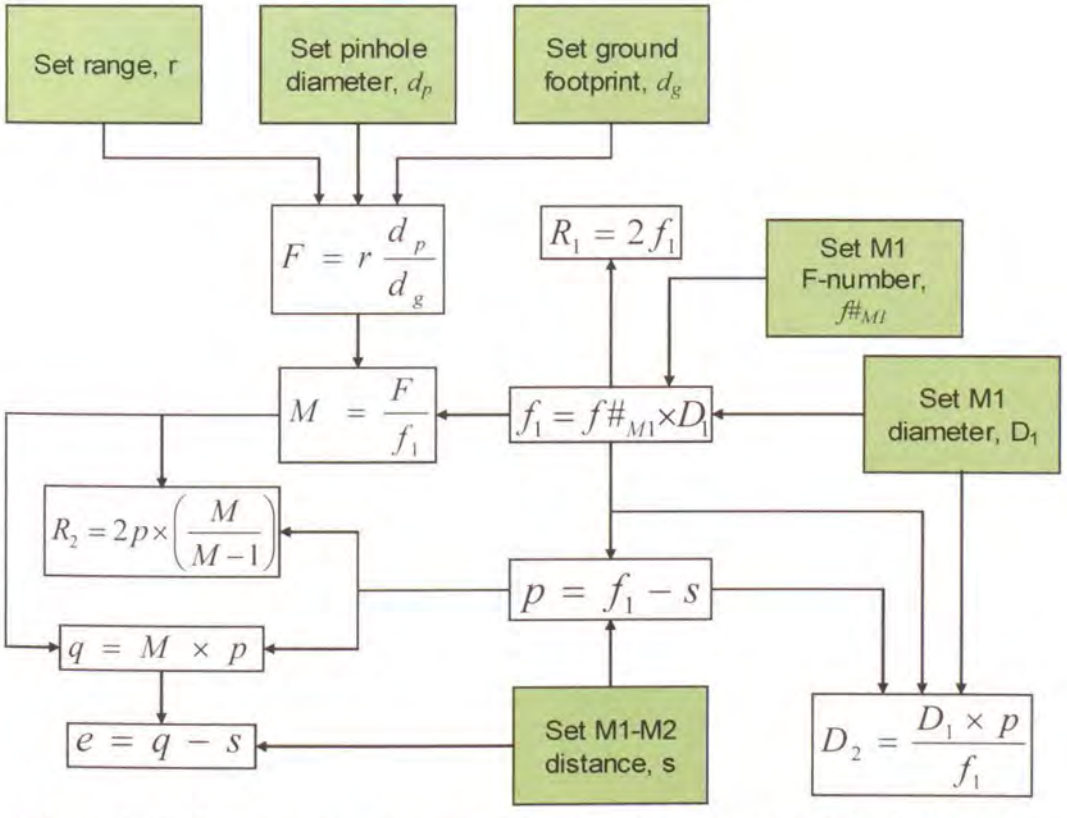

Figure 3-17. Computation process of Cassegrain telescope optical properties

The last variable we set (which is also the main design control variable in our model) is the position of the secondary mirror with respect to M1. Having just calculated f_1, we can find p which is important to establish the characteristics (diameter and radius of curvature) of the secondary mirror, M2. It is also used to calculate the distance q between the telescope focal point and M2; in turn, e can be computed.

For an afocal system, the focal length of the overall telescope, F, should tend towards infinity, which can be achieved by making the ground footprint very small and the pinhole diameter larger. As a consequence, the magnification would tend towards infinity and so would q and e. Note that afocal systems are generally defined by their angular magnification which can be computed as the ratio of input beam diameter to the output beam diameter [Boreman, 1998]. Thus the magnification must not be mistaken for the angular magnification.

This parametric model is validated against one of the two designs proposed in the A-SCOPE Phase 0 study of ESA's Earth Explorer Core Mission 4. This is illustrated by Table 3-4.

Parameter	A-SCOPE properties (one of two designs)	Calculated by model
Ground footprint, d_g [m]	100	-
Range, r [m]	400,000	-
Pinhole diameter, d_p [mm]	3.3	-
M1 diameter, D_1 [mm]	1000	-
M1 aperture, $f\#_{M1}$	1.5	-
M2 to-focal point, q [mm]	1500	-
M1 radius of curvature, R_1 [mm]	3000	3000
Telescope focal length, F [mm]	13,235	13,200
Inter-mirror distance, s [mm]	1330	1329.5
M1 vertex to focal point, e [mm]	170	170.5
M2 diameter, D_2 [mm]*	125	113.6
M2 radius of curvature, R_2 [mm]	?	384.6

* The model computes the diameter of the beam at M2; but D_2 is made larger in practice.

Table 3-4. Validation of the model with one of the A-SCOPE telescope designs.

3.3.4.2 Overall Dimensions

Figure 3-18 illustrates the accommodation of the telescope in its envelope. The angle β corresponds to the sun radiation incidence onto the secondary mirror. For a dawn-dusk orbit, this angle is about 59°. It determines the minimum length l_B of the baffle above the secondary mirror so as to shade the latter from direct sun illumination. This is required to avoid potential sun rays being focussed onto and damaging the receiver stage of the instrument. By trigonometry, the length of the baffle is approximately:

$$l_B = \frac{W/2}{\tan \beta} \tag{3-15}$$

The thickness of the primary mirror and its support structure is denoted l_{M1}. The primary mirror of the ALADIN telescope has a 100-mm sag [Breysse et al, 2004]. The supporting structure would consist of bipods in an isostatic configuration, with a height of about 100 mm too. However, the centre of the rear face of the primary mirror could be lowered within 50 mm of the baseplate, in order to allow for the dynamic response of the mirror and baseplate during the launch. Thus, we consider $l_{M1} \approx 150$ mm.

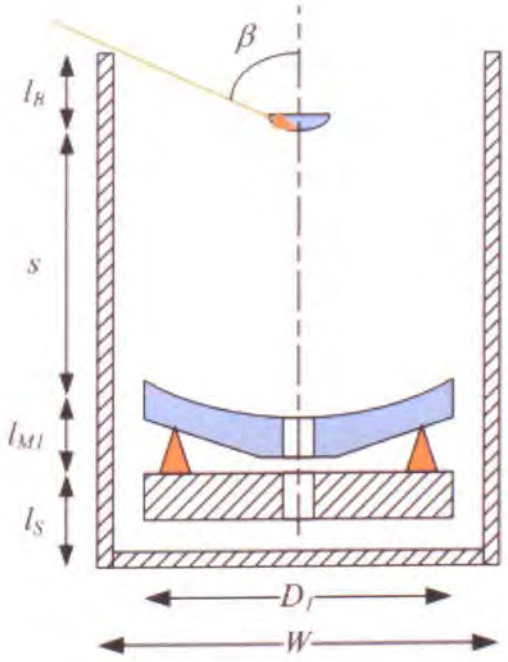

Figure 3-18. Envelope parameters for the front-mounted Cassegrain telescope.

The length l_S accounts for the thickness of the baseplate, the thickness of the outer wall and the gap between the two. The thickness of optical instrument baseplates typically varies between 50 mm and 100 mm, depending on the stiffness requirements on them. It is safe to assume that for large telescopes, a baseplate thickness of 100 mm is likely. The outer wall is a non-structural element and will not support any equipment. Aluminium honeycomb panels of 10 mm thickness are sufficiently thick to carry avionics, thus a 10-mm thickness for the outer wall is conservative. The space at the back of the baseplate must allow for optical elements to be mounted. This gap must also be sufficiently wide to also provide margin for the dynamic response of the outer wall during launch. Thus l_S = 200 mm.

Accommodation margins must also be taken into account for stiffeners, external wall and clear gap to allow, as mentioned above, for vibration of the side walls during launch. An allocation of 100 mm on either side of the telescope provides sufficient margin. Thus, W is 200 mm larger than D_l.

In order to check whether the telescope fits within a launch vehicle, its diagonal length shall be compared to the diameter of the launch vehicle fairing, as shown in Figure 3-5 and Figure 3-6. It may be necessary to take some margin on these diameters, so as allow for appendages on the satellite, such as solar arrays. Note however that the volume defined in the launch vehicle user's manual includes some margin to account for the dynamic response of the satellite and fairing. However, during the feasibility study of a mission, this should not be infringed. For the Soyuz launcher in dual launch configuration, no confirmed usable volume is specified, it is assumed to be 200 mm shorter than the physical dimension (3600 mm) of the structure housing the secondary passenger.

Launcher	Usable fairing diameter	Lidar limits
Vega	2380 mm	2150 – 2250 mm
Soyuz (dual launch)	3400 mm (TBC)	3200 – 3300 mm

Table 3-5. Limits of the diagonal length of a front-mounted lidar instrument in Vega and Soyuz.

3.3.4.3 Instrument design for a front-mounted instrument

As discussed in chapter 3.3.1, the ALADIN telescope is not far from diffraction-limited quality despite being fairly fast (*f*# of 0.9). Thus, in the following analysis a *f*# of 1 is assumed.

3.3.4.3.1 Sensitivity to range and ground footprint

A first set of cases have been evaluated with various values of ground footprint, range and primary mirror diameter, while the pinhole diameter was fixed at 3.3 mm, as shown in Table X. Most lidar missions require a ground footprint in the region of 50 m to 100 m, both values have been analysed.

Figure 3-19 shows that the lidar sizing is mildly sensitive to range and ground footprint. In order to be compatible with Vega, the primary mirror should be in the region of 1100 to 1200 mm, whereas for Soyuz the primary mirror can be increased to somewhere in the region of 1750 to 1900 mm.

Parameter	Value
Pinhole diameter	3.3 mm
Primary mirror diameter	1000 – 2000 mm
Ground footprint	50 m, 100 m
Range	260 – 350 km

Table 3-6. Telescope design parameters used in the sensitivity analysis.

3.3.4.3.2 Sensitivity to pinhole diameter

In the analysis above, the pinhole was kept constant. In the following analysis, the pinhole diameter is allowed to vary, with the ground footprint fixed at 50 m and the altitude at 350 km. Figure 3-20 shows that the telescope diameter is not very sensitive to the pinhole diameter, but that a smaller pinhole would provide a slight advantage in terms of lidar size. However, a small pinhole size can reduce the number of photons passing through. Thus, a pinhole diameter of 3-4 mm would appear reasonable.

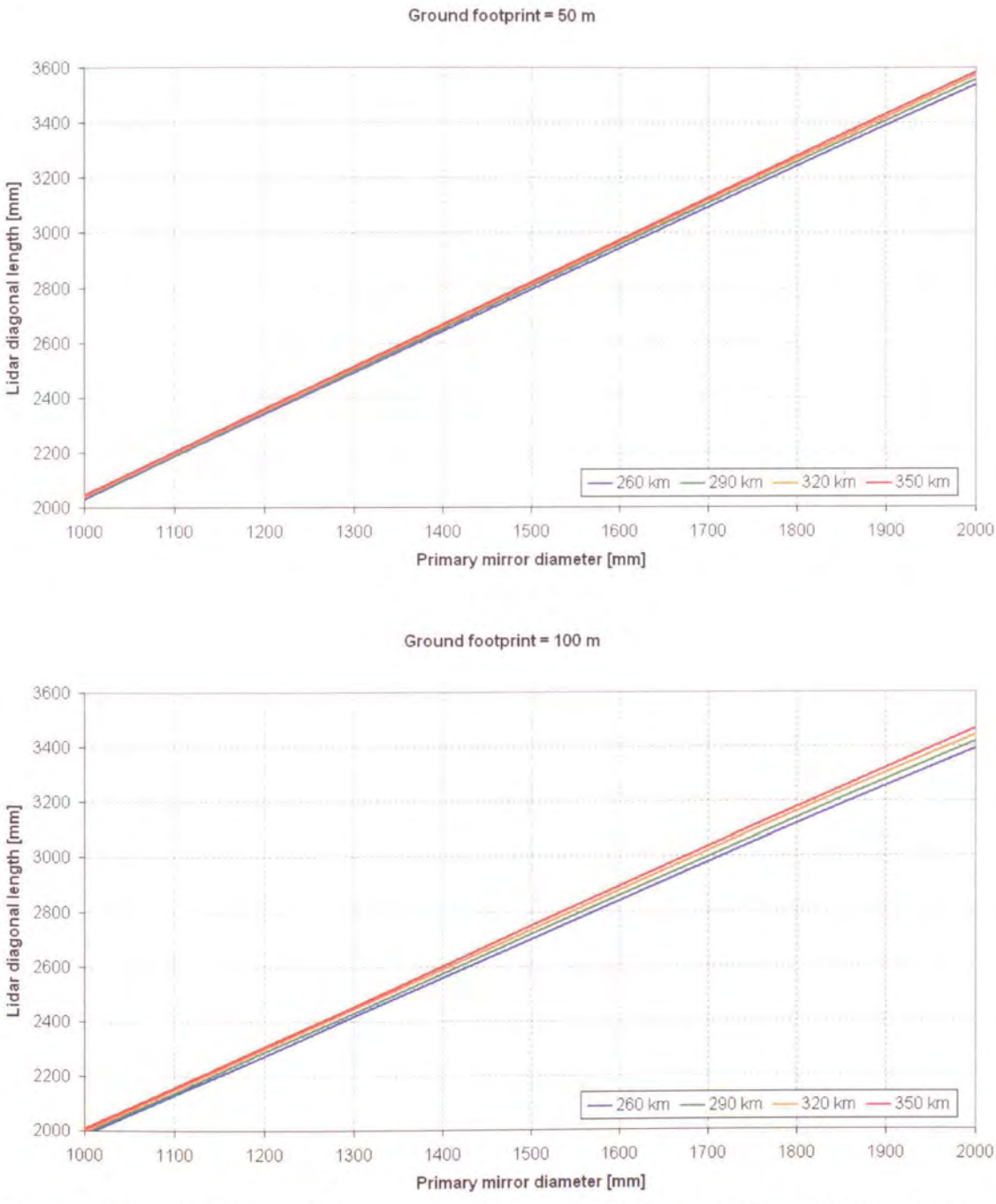

Figure 3-19. Lidar diagonal for a range of primary mirror diameters and altitudes, and for a footprint diameter of 50 m (top) and 100 m (bottom).

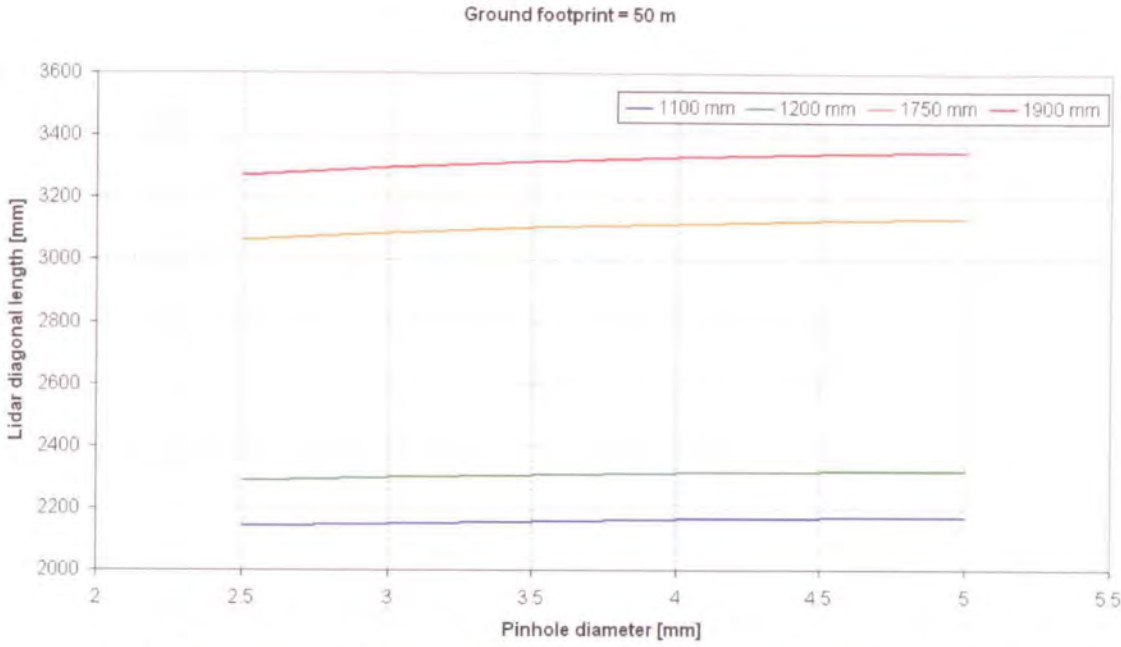

Figure 3-20. Influence of the pinhole diameter on the lidar size

3.3.4.3.3 Selected telescope designs for the front-mounted lidar instrument

From the analysis performed, the following two telescope designs are proposed for a front-mounted lidar instrument, compatible with Vega and as a secondary payload on, respectively. Their characteristics are summarised in Table 3-7.

For a given telescope design, the ground footprint would change with altitude. This can be avoided by adjusting the pinhole diameter between 3 mm (at 350 km altitude) to 4 mm (at 260 km).

Primary mirror diameter	1150 mm	1800 mm
F-number, f#	1	1
M1-M2 distance	1080 mm	1640 mm
M2 minimum diameter	75 mm	165 mm
Total length	1832 mm	2588 mm
Total width	1350 mm	2000 mm
Margin wrt fairing diameter	4.4 % (Vega)	3.8% (dual launch)

Table 3-7. Summary of the front-mounted lidar telescope options.

3.3.5 Applicability of compact Lidar designs

The applicability of this configuration and the two size of lidar instrument are best seen by comparing the power-aperture that can be accommodated for various altitudes and beam energy with the mission-specific power-aperture products given in 2.6.4.

In Figure 3-21, the 1.15-m diameter telescope is shown as a solid line, and the 1.8-m telescope as dashed. The colours correspond to the three beam energies considered, i.e. 5 mJ (orange), 10 mJ (blue) and 15 mJ (green).

Clearly, only the 1.8-m telescope can be of benefit to the A-SCOPE mission, but neither Aeolus nor WALES can be fulfilled. For all other missions below 10×10^{-12} W, then the smaller telescope can be useful.

3.3.6 Aerodynamic properties

Based on the analysis method of 3.2.2, a (C_D.A) product can be established, for each telescope size, as given in Table 3-8. Note that the dimension parallel to the flow is taken as the width of the instrument plus 500 mm to account for the housing of the payload lasers and electronic units.

The platform can be assumed to have the exact cross-section of the instrument, with a length of 1.5 m being typical, and providing the necessary volume to house the subsystems avionics. Furthermore, solar arrays with a surface area of 15 m^2 and parallel to the flow are also considered for the assessment of the spacecraft drag characteristics..

In order to determine a ballistic coefficient for the purpose of orbit analysis, a spacecraft mass range needs to be assumed. The worst case is a low ballistic coefficient, thus the mass of the satellite should not be overestimated. For the smaller telescope diameter, a satellite of these dimensions would typically have a mass of at least 1000 kg (by analogy with the A-SCOPE mission) and unlikely to be above 1500 kg. By scaling, the satellite with the 1.8-m telescope can be expected to weight in the order of 1400 to 2000 kg. The predicted range of ballistic coefficient is shown in Table 3-9.

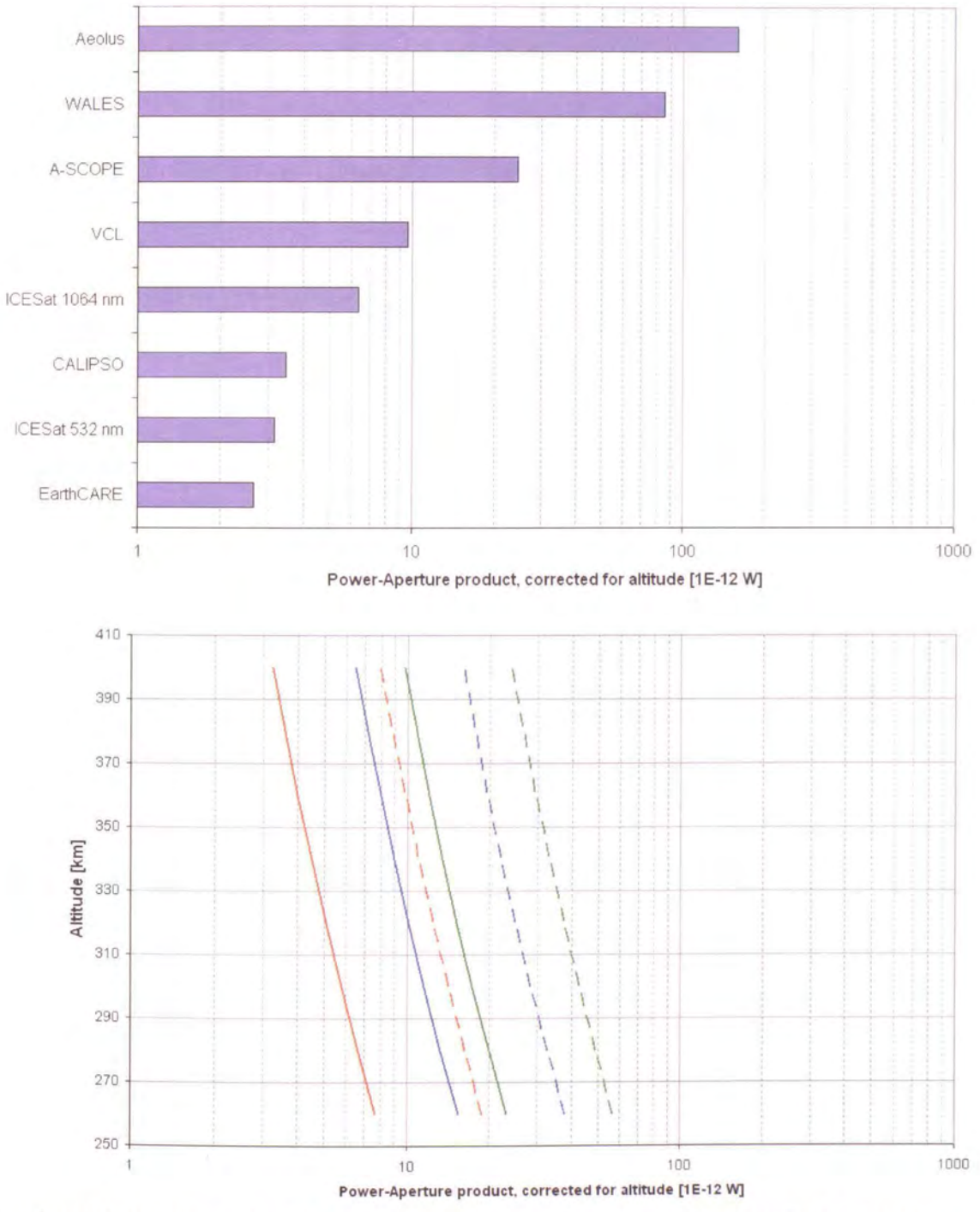

Figure 3-21. Comparison of the power-aperture products of the two front-mounted telescopes (bottom) with the mission specific ones (top)

Telescope diameter	$C_D.A$	Reference Area	Equivalent C_D
1150 mm	6.32 m^2	2.47 m^2	2.56
1800 mm	13.10 m^2	5.18 m^2	2.53

Table 3-8. Aerodynamic characteristics of the front-mounted lidar telescopes

Telescope diameter	1150 mm	1800 mm
(C_DA) of instrument	6.32 m^2	13.10 m^2
(C_DA) of platform	0.7 m^2	1.01 m^2
(C_DA) of solar arrays	1.10 m^2	1.10 m^2
Total (C_DA)	8.12 m^2	15.21 m^2
Reference area	2.47 m^2	5.18 m^2
Equivalent C_D	3.28	2.94
Mass range	1000 – 1500 kg	1400 – 2000 kg
Ballistic coefficient range	123 – 185 kg/m^2	92 – 131 kg/m^2

Table 3-9. Aerodynamic characteristics of the two options for a front-mounted lidar instrument.

3.4 Large Lidar Missions Configuration and Sizing

This section is dedicated to the considerably larger options for Aeolus and WALES, as discussed in section 2.6.4. Diameters of 3 and 3.5 m are considered, which are only possible with a dedicated launch on Soyuz. Exorbitant costs associated with the large telescope are not considered to be a show-stopper at this stage.

3.4.1 Configuration and telescope sizing

Only one configuration is possible, where the instrument is mounted on the nadir face of the platform. For the telescope, the Cassegrain design is the natural choice. Adapting the sizing model of section 3.3.4, the physical characteristics of the telescopes are found to be as shown in Table 3-10.

Primary mirror diameter	3000 mm	3500 mm
F-number, *f*#	1	1
M1-M2 distance	2590 mm	2960 mm
M2 minimum diameter	75 mm	540 mm
Total length	3870 mm	4390 mm
Total width	3100 mm	3600 m

Table 3-10. Summary of the very large nadir-mounted lidar telescopes.

3.4.2 Aerodynamic properties

Based on the analysis method of section 3.2.2, by approximating the baffle as a succession of flat surfaces at an angle to the incoming flow, a (C_D.A) product can be established, as given in Table 3-11.

The same approach as section 3.3.6 is applied here to determine a range of ballistic coefficients for the orbit analysis. The size of the 3.5-m telescope has some similarities with ESA's Herschel telescope, although Herschel is designed to operate at a Sun-Earth Lagrange point and has therefore very different requirements from a LEO mission. Due to this lack of strong similarities, it is far more difficult to predict its mass, thus a larger range is considered: 2000 to 3000 kg for the 3-m telescope, and 2500 to 3500 kg for the 3.5 m telescope[2]. The corresponding ballistic coefficients are shown in Table 3-12.

Also, the platform is assumed to be 2.5 m (X) by 2.5 m (Y) by 1.5 m (Z). Inaccuracies or approximations are found to have limited impact on the BC, as this is primarily dominated by the telescope volume.

Telescope diameter	$C_D.A$	Reference Area	Equivalent C_D
3000 mm	26.29 m^2	12.0 m^2	2.19
3500 mm	34.64 m^2	15.8 m^2	2.19

Table 3-11. Aerodynamic characteristics of the very large telescopes

Telescope diameter	3000 mm	35000 mm
(C_DA) of instrument	26.29 m^2	34.64 m^2
(C_DA) of platform	9.28 m^2	9.28 m^2
(C_DA) of solar arrays	1.10 m^2	1.10 m^2
Total (C_DA)	36.68 m^2	45.02 m^2
Reference area	15.75 m^2	19.55 m^2
Equivalent C_D	2.33	2.30
Mass range	2000 – 3000 kg	2500 – 3500 kg
Ballistic coefficient range	55 – 82 kg/m^2	56 – 78 kg/m^2

Table 3-12. Spacecraft aerodynamic characteristics for the very large telescope options.

[2] It will be shown in section 6.5 that the actual spacecraft mass are indeed with these ranges.

3.5 Conclusions

Following a trade-off of different accommodation options, two configurations have been retained. For each of these, two sizes of telescopes have been considered, giving four concepts which will be evaluated through the rest of this thesis. Their characteristics are summarised in Table X.

	Concept 1	Concept 2	Concept 3	Concept 4
Primary mirror diameter	1150 mm	1800 mm	3000 mm	3500 mm
Lidar accommodation on spacecraft	Front	Front	Nadir	Nadir
Overall length	1832 mm	2588 mm	3870 mm	4390 mm
Overall width	1350 mm	2000 mm	3100 mm	3600 mm
Satellite (C_DA)	8.12 m^2	15.21 m^2	36.68 m^2	45.02 m^2
Satellite mass range	1000 – 1500 kg	1400 – 2000 kg	2000 – 3000 kg	2500 – 3500 kg
Ballistic coefficient	123 – 185 kg/m^2	92 – 131 kg/m^2	55 – 82 kg/m^2	56 – 78 kg/m^2

Table 3-13. Summary of the four lidar mission concepts to be investigated

In concepts 1 and 2, the lidar instrument is mounted on the front (+X) wall of the platform. A telescope design has been chosen to maximise the diameter of the primary mirror, which would depend on the launcher: Vega for concept 1 and Soyuz (dual launch) for concept 2.

For concepts 3 and 4, the lidar instrument is mounted on the nadir face of the satellite, similar to Aeolus. This allows a much larger primary mirror to be accommodated, but with an equally much larger cross-section area exposed to the air flow. Both concepts would fly on Soyuz, and have been sized according to the requirements of the Aeolus of WALES missions as specified in section 2.6.4.

Having identified the likely aerodynamic characteristics of the satellite, these can be fed into an orbit simulator to derive the propulsion requirements for a lidar satellite in a low altitude orbit (Chapter 4), from which a propulsion system can be selected (Chapter 5).

Chapter 4

Low-Thrust Trajectory Modelling

4.1 Introduction

The motion of a satellite propelled by a low-thrust system and subject to small external forces is governed by a set of time-varying equations of motion. These forces can be in-plane, out-of-plane, or a combination of both. It is of interest to model the motion of the satellite to derive requirements as inputs to the trade-off of propulsion systems. In order to model the trajectory, a suitable set of equations of motion must be found. It will be shown that the equinoctial orbital elements are best suited for the problem at hand.

There are many forces that disturb the motion of a satellite in a low-Earth orbit. Atmospheric drag has been mentioned already, but it is also essential to model the gravity of a non-spherical Earth as a pre-requisite for a sun-synchronous orbit. Other forces that are included are third-body perturbation and solar radiation pressure. A simplifying assumption is made for thrust, which is considered here to compensate for the atmospheric drag with some errors to account for hardware inaccuracies.

4.2 Low altitude dawn-dusk orbit

As presented in Chapter 2, most lidar missions fly in sun-synchronous orbits, and most often, these orbits are dawn-dusk orbits.

In this section, the Classical Orbit Elements used to describe orbits are introduced, followed by an algebraic explanation of the requirements for a sun-synchronous orbit. We also determine the eccentricity and argument of perigee that make a frozen orbit.

4.2.1 The Classical Orbit Elements

Given a stable, unperturbed orbit, the motion of a satellite around the Earth can be completely described using five constants – representing the size, shape and orientation in space of the orbit– and a time variable specifying the position of the satellite on the orbit relative to a defined epoch [Welch, 1992]. These are known as the Classical Orbit Elements (COE), which are defined for an Earth-centred orbit as follow:

- The semi-major axis, a, describes the size of the orbit;
- The eccentricity, e, represents its shape;
- The inclination, i, describes the tilt of the orbit plane with respect to the equatorial plane;
- The longitude of ascending node, Ω, is the angle from the principal direction to the ascending node, the point where the orbit plane and the equatorial plane intersect with the spacecraft travelling from the southern hemisphere into the northern hemisphere;
- The argument of perigee, ω, is the angle giving the position of the perigee in the orbit with respect to the ascending node;
- The true anomaly, ν, is the angle in the orbit plane from the perigee to the position of the spacecraft.

Figure 4-1 is a graphical representation of some of the COEs, in particular angular displacements.

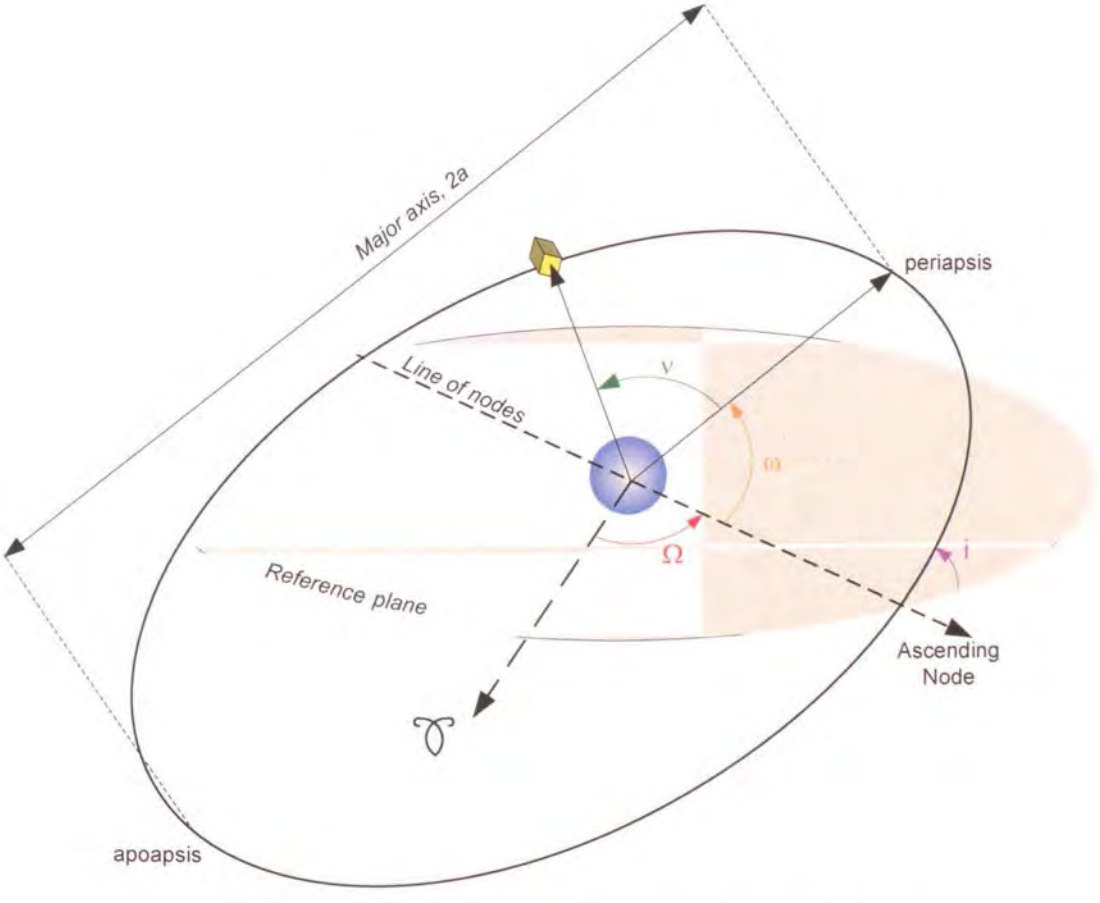

Figure 4-1. Representation of Classical Orbital Elements

4.2.2 Sun-synchronous orbit

The rotation of the line of nodes is made possible by the aspheric shape of the Earth and the associated inhomogeneous gravity field. The nodal regression over time is expressed mathematically by the equation:

$$\frac{d\Omega}{dt} = -\frac{3}{2} R_E^2 J_2 \frac{\mu_E^{1/2}}{a^{7/2}\left(1-e^2\right)^2} \cos(i) \tag{4-1}$$

where R_E is the mean radius of the Earth, J_2 is the second zonal harmonic of the Earth gravitational potential, μ_E is the gravitational parameter of the Earth, and the other symbols corresponds to COEs as defined earlier.

For a sun-synchronous orbit, the nodal regression must match the mean motion of the Earth around the Sun and is thus [Vallado, 2007]:

$$\dot{\Omega}_{SunSync} = \frac{360°}{365.2421897 days} \equiv 1.991\,063\,853 \times 10^{-7} \frac{rad}{\sec} \tag{4-2}$$

Re-arranging Equation (4-1), the inclination is found to be:

$$\cos(i) = -\frac{2}{3} \frac{\dot{\Omega}_{SunSync} a^{7/2}\left(1-e^2\right)^2}{R_E^2 J_2 \mu_E^{1/2}} \tag{4-3}$$

4.2.3 Frozen orbit

A frozen orbit is desirable to minimise variation in altitude over a given point. This can be achieved if the eccentricity and the argument of perigee do not change. For near-polar, low earth orbits, this is possible by selecting a slightly elliptic orbit with a perigee near the north or south poles. Indeed, the rate of change of eccentricity over a long period of time is given by [Vallado, 2007]:

$$\frac{de}{dt} = -\frac{3}{2} \frac{n}{\left(1-e^2\right)^2} J_3 \left(\frac{R_E}{a}\right)^3 \sin(i)\left(1-\frac{5}{4}\sin^2(i)\right)\cos\omega \tag{4-4}$$

where J_3 is the third zonal harmonic of the geopotential. Clearly, a way of nulling this equation is to set either i = 0, which is not possible in our case, or ω = 90° or 270°.

The long-periodic rate of change of the argument of perigee is [Vallado, 2007]:

$$\frac{d\omega}{dt} = \frac{3n}{\left(1-e^2\right)^2} J_2 \left(\frac{R_E}{a}\right)^2 \left(1 - \frac{5}{4}\sin^2(i)\right)\theta \tag{4-5}$$

Where θ is a simplifying term written as:

$$\theta = 1 + \frac{J_3}{2J_2}\left(\frac{R_E}{a}\right)\frac{1}{\left(1-e^2\right)}\left(\frac{\sin^2(i) - e^2\cos^2(i)}{\sin(i)}\right)\frac{\sin(\omega)}{e} \tag{4-6}$$

A simple solution to avoiding a change in the argument of perigee is to set θ to zero. Ignoring terms in e^2, and re-arranging Equation (4-6) for $\theta = 0$, we obtain [Vallado, 2007]:

$$e_0 \approx -\frac{1}{2}\frac{J_3}{J_2}\frac{R_E}{a}\sin(i)\sin(\omega) \tag{4-7}$$

Figure 4-2 shows the relevant orbital elements for sun-synchronous, frozen orbits with an argument of perigee ω of 90°, and a range of perigee altitude between 250 and 400 km.

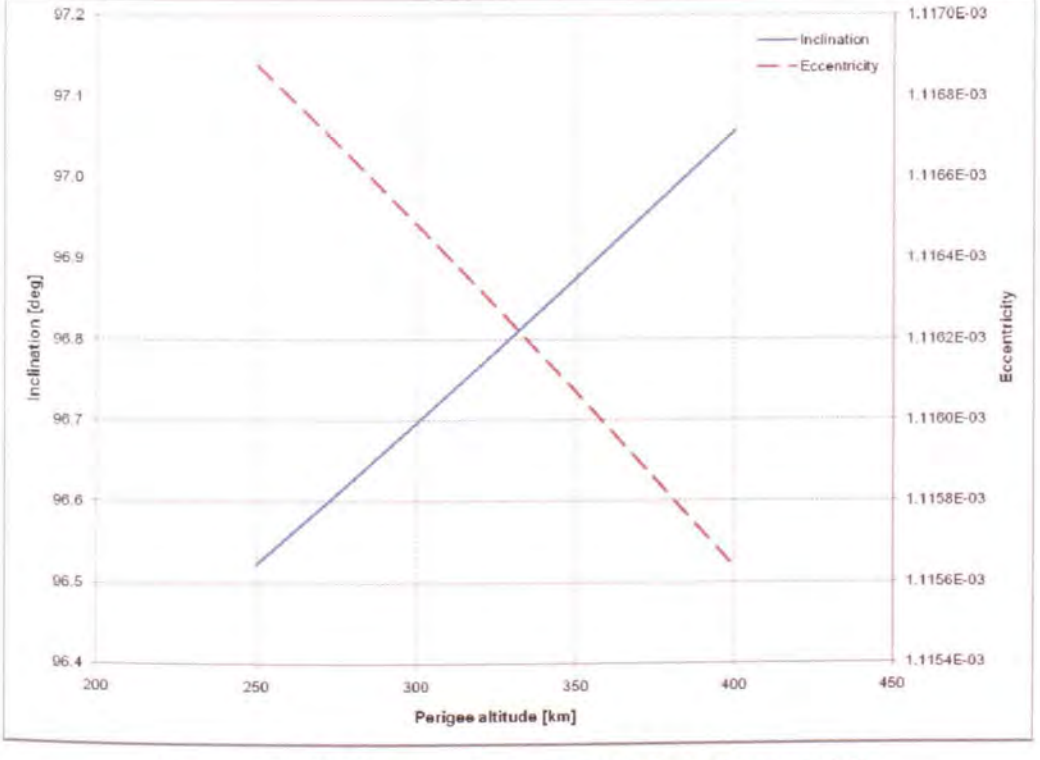

Figure 4-2 Orbit parameters required for a frozen orbit.

4.3 Equations of motion for a low-thrust spacecraft

In the restricted two-body problem only the true anomaly is a time variable. However, under the influence of external forces, such as drag, third-body perturbation, solar radiation pressure but also propulsive thrust, the five other parameters become time variables too. Therefore, variational equations of the COEs need to be derived.

4.3.1 Gauss Equation

One of the most commonly used methods to predict the motion of a spacecraft is to compute the COEs by mean of the Gauss' equations. These are a set of time-derivative variational equations based on Lagrange's planetary equations and are particularly useful in computing the trajectory of a spacecraft under the influence of perturbation forces. These can also be applied to low-thrust trajectories since the acceleration is very small and quasi-continuous, a perturbation for the ideal two-body problem. The Gauss' variational equations are written as [Battin, 1999]:

$$\frac{da}{dt} = \frac{2a^2}{h}\left(e\sin\nu \cdot a_R + \frac{p}{r} a_T \right) \tag{4-8}$$

$$\frac{de}{dt} = \frac{1}{h}\left\{ p\sin\nu \cdot a_R + \left[(p+r)\cos\nu + re \right] a_T \right\} \tag{4-9}$$

$$\frac{di}{dt} = \frac{r\cos u}{h} a_N \tag{4-10}$$

$$\frac{d\Omega}{dt} = \frac{r\sin u}{h\sin i} a_N \tag{4-11}$$

$$\frac{d\omega}{dt} = \frac{1}{he}\left[-p\cos\nu \cdot a_R + (p+r)\sin\nu \cdot a_T \right] - \frac{r\sin u\cos i}{h\sin i} a_N \tag{4-12}$$

$$\frac{dM}{dt} = n + \frac{b}{ahe}\left[(p\cos\nu - 2re) a_R - (p+r)\sin\nu \cdot a_T \right] \tag{4-13}$$

In these equations, r is the distance from the centre of the reference frame to the spacecraft, h is the specific angular momentum, u is the argument of latitude, n is the mean motion and b is the semi-minor axis. These are given by:

$$h = n \cdot a \cdot b \tag{4-14}$$

$$u = \omega + \nu \tag{4-15}$$

$$n = \sqrt{\mu / a^3} \tag{4-16}$$

$$b = a\sqrt{1 - e^2} \tag{4-17}$$

In Gauss's equations, the terms (a_R , a_T , a_N) are the disturbing accelerations components along the main axes (radial, tangential and normal directions, respectively) of the local osculating polar coordinate system – i.e. this frame follows the spacecraft, with the satellite position vector $\vec{r}$ always pointing towards it.

Equation (4-13) is the time-derivative of the mean anomaly M, used to compute through an iterative method the eccentric anomaly, E, which in turn allows to find the true anomaly, ν:

$$M = E - e\sin E \tag{4-18}$$

$$\tan\frac{1}{2}\nu = \sqrt{\frac{1+e}{1-e}}\tan\frac{1}{2}E \tag{4-19}$$

It is interesting to note that in the absence of disturbing accelerations, Equations (4-8) to (4-12) will see their right-hand side terms equal to zero, meaning that the corresponding orbit elements will be constant, while the rate of change of the mean anomaly, dM/dt, will be equal to the mean motion, n. This is consistent with the two-body problem which exists only in the absence of disturbing forces.

However, the Gauss' form of the variational equations can become useless due to singularities. For orbits with zero inclination, the ascending node does not exist. Singularities would appear in Equations (4-11) and (4-12), the variational equations for the right ascension of ascending node and argument of periapsis, repesctively [Battin, 1999]. Indeed,

sin(i) becomes zero and the right-hand side of these equations tend toward infinity. Similarly, for obits of zero eccentricity – i.e. circular orbits – the periapsis cannot be defined; Equations (4-11) and (4-12) would display singularities with terms tending towards infinity.

Hence, while Gauss' variational equations are useful in many cases, their inadequacy for some specific cases is a major limitation. Within the frame of the present work, their inability to solve the motion of a satellite in a near-circular orbit is the main issue. This is aggravated by the fact that atmospheric drag tends to circularise elliptical orbits [Vallado, 2007]. An alternative method is therefore required.

4.3.2 Equinoctial Orbital Elements

The equinoctial orbit elements were used as early as the 18th century by Lagrange in the study of secular effects due to mutual planetary perturbations [Broucke and Cefola, 1972]. This set of elements is particularly well adapted to orbits of small eccentricity and small inclination [Broucke and Cefola, 1972; Betts, 1994; Betts and Erb, 2003; Kluever and Oleson, 1998; Massari et al, 2003; Battin, 1999].

The six equinoctial orbit elements are expressed as functions of the classical orbit elements [Welch, 1992; Betts, 1994]:

$$p = a\left(1 - e^2\right) \tag{4-20}$$

$$f = e \cdot \cos\left(\Omega + \omega\right) \tag{4-21}$$

$$g = e \cdot \sin\left(\Omega + \omega\right) \tag{4-22}$$

$$h = \tan\frac{i}{2}\cos\Omega \tag{4-23}$$

$$k = \tan\frac{i}{2}\sin\Omega \tag{4-24}$$

$$L = \Omega + \omega + \nu \tag{4-25}$$

The equinoctial variables can be computed after numerically solving their differential equations. The time derivative expressions of the equinoctial variables are given as [Welch, 1992, Betts, 1994, Battin, 1999]:

$$\dot{p} = a_T \sqrt{\frac{p^3}{\mu}} \frac{2}{W} \tag{4-26}$$

$$\dot{f} = \sqrt{\frac{p}{\mu}} \frac{1}{W} \left[a_R W \sin L + a_T A(L) - a_N g\left(h \sin L - k \cos L\right) \right] \tag{4-27}$$

$$\dot{g} = \sqrt{\frac{p}{\mu}} \frac{1}{W} \left[- a_R W \cos L + a_T B(L) + a_N f\left(h \sin L - k \cos L\right) \right] \tag{4-28}$$

$$\dot{h} = a_N \sqrt{\frac{p}{\mu}} \frac{X}{2W} \cos L \tag{4-29}$$

$$\dot{k} = a_N \sqrt{\frac{p}{\mu}} \frac{X}{2W} \sin L \tag{4-30}$$

$$\dot{L} = \sqrt{\frac{\mu}{p^3}} W^2 + a_N \sqrt{\frac{p}{\mu}} \frac{1}{W} \left(h \sin L - k \cos L\right) \tag{4-31}$$

The parameters *X, W, A(L) and B(L)* are given by:

$$X = 1 + h^2 + k^2 \tag{4-32}$$

$$W = 1 + f \cos L + g \sin L \tag{4-33}$$

$$A(L) = f + \cos L (1 + W) \tag{4-34}$$

$$B(L) = g + \sin L (1 + W) \tag{4-35}$$

The terms (a_R, a_T, a_N) are the radial, tangential and normal components of the spacecraft acceleration, respectively. This acceleration is indifferently due to thrust or any other form of perturbations.

Equations (4-26) to (4-31) are the translational dynamics equations. Similar to Gauss' variational equations, in the absence of disturbing forces the right-hand terms of the first five

equations are equal to zero, and only the true longitude L will vary. Once again, this is consistent with the two-body problem when no acceleration disturbs the motion of the satellite.

It should be noted that the equinoctial orbital elements are not entirely free of singularities, with such cases occurring for e = 1 or i = 180°. However, equinoctial elements are applicable to near-circular, polar orbits.

The equations to compute the COE from the equinoctial variables are [Welch, 1992]:

$$e = \sqrt{f^2 + g^2} \tag{4-36}$$

$$\Omega = \tan^{-1}\left(\frac{k}{h}\right) \tag{4-37}$$

$$\nu = \tan^{-1}\left(\frac{f \cdot \sin L - g \cdot \cos L}{f \cdot \cos L + g \cdot \sin L}\right) \tag{4-38}$$

$$u = \tan^{-1}\left(\frac{h \cdot \sin L - k \cdot \cos L}{h \cdot \cos L + k \cdot \sin L}\right) \tag{4-39}$$

$$\omega = u - \nu \tag{4-40}$$

$$i = \tan^{-1}\left(\frac{2\sqrt{h^2 + k^2}}{1 - h^2 - k^2}\right) \tag{4-41}$$

However, if the eccentricity is zero, f and g will be zero. [Betts, 1994] suggests the following equations as alternatives:

$$\tan(\omega + \Omega) = \frac{g}{f} \tag{4-42}$$

$$\omega = \tan^{-1}\left(\frac{g}{f}\right) - \tan^{-1}\left(\frac{k}{h}\right) = \tan^{-1}\left(\frac{g}{f}\right) - \Omega \tag{4-43}$$

$$\nu = L - \tan^{-1}\left(\frac{g}{f}\right) \tag{4-44}$$

The latter equations are deemed to be interesting here from a computer memory view-point as they limit the number of mathematical operations, especially trigonometric ones which require more computational power.

4.3.3 Equinoctial-to-Cartesian transformation

The equinoctial reference frame, depicted in Figure 4-3, is obtained from the Cartesian inertial reference frame by a series of three rotations:

1. Rotation by $+\Omega$ around Z_{ECI};
2. Rotation by $+i$ around the new X axis;
3. Rotation by $-\Omega$ around Z_{EQF}.

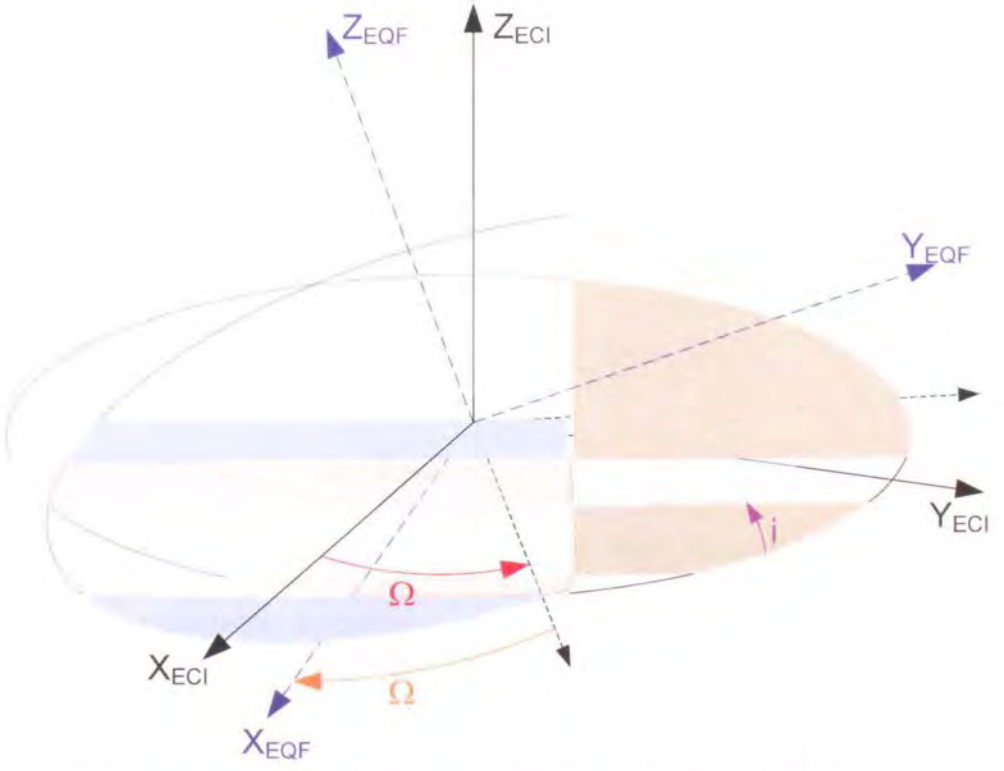

Figure 4-3. Representation of the Equinoctial Reference Frame.

Adapted from [Welch, 1992]

This rotation sequence allows us to derive the direction cosine matrix (DCM) that transforms the Cartesian Earth-Centred Inertial (ECI) reference frame into the Equinoctial reference frame:

$$R_{ERF\leftarrow ECI} = \begin{bmatrix} \cos^2\Omega + \sin^2\Omega\cos i & \cos\Omega\sin\Omega - \cos\Omega\sin\Omega\cos i & -\sin\Omega\sin i \\ \cos\Omega\sin\Omega - \cos\Omega\sin\Omega\cos i & \sin^2\Omega + \cos^2\Omega\cos i & \cos\Omega\sin i \\ \sin\Omega\sin i & -\cos\Omega\sin i & \cos i \end{bmatrix} \quad (4\text{-}45)$$

We note the following identities derived from the definition of the Equinoctial frame [Betts, 1994]:

$$\begin{aligned} \cos\Omega &= \frac{h}{T} & \sin\Omega &= \frac{k}{T} \\ \cos i &= \frac{1-T^2}{1+T^2} & \sin i &= \frac{2T}{1+T^2} \\ \text{where } T &= \sqrt{h^2+k^2} \end{aligned} \quad (4\text{-}46)$$

Substituting these in Equation (4-45) and inversing to obtain the DCM that transforms the Equinoctial frame into the ECI frame:

$$R_{ECI\leftarrow EQF} = \frac{1}{1+h^2+k^2}\begin{bmatrix} 1+h^2-k^2 & 2hk & 2k \\ 2hk & 1-h^2+k^2 & -2h \\ -2k & 2h & 1-h^2-k^2 \end{bmatrix} \quad (4\text{-}47)$$

4.3.4 The rotating radial frame

The rotating radial frame (Figure 4-4) is a reference frame attached to the satellite and its principal axes are defined by the position and orbit plane:

- The Radial axis is along the radius vector from the centre of the Earth to the satellite;
- The Normal axis is along the angular momentum vector;
- The Tangential axis completes the triad and is roughly in the direction of flight.

The Radial, Tangential, Normal (RTN) rotating radial frame is obtained by rotating the Equinoctial frame (EQF) about the Z axis by the true longitude, L. From the corresponding DCMs, it is possible to express the position vector in inertial frame by:

$$\vec{r}_{ECI} = \frac{r}{1+h^2+k^2}\begin{bmatrix}\left(1+h^2-k^2\right)\cos L + 2hk\sin L \\ 2hk\cos L + \left(1-h^2+k^2\right)\sin L \\ -2k\cos L + 2h\sin L\end{bmatrix} \tag{4-48}$$

This equation matches that derived by [Betts & Erb, 2003], who also give the equation for the velocity in the ECI frame:

$$\vec{v}_{ECI} = \frac{1}{1+h^2+k^2}\sqrt{\frac{\mu}{p}}\begin{bmatrix}2hk\cos L - \left(1+h^2-k^2\right)\sin L - \left(1+h^2-k^2\right)g + 2fhk \\ \left(1-h^2+k^2\right)\cos L - 2hk\sin L + \left(1-h^2+k^2\right)f - 2ghk \\ \left(f+\cos L\right)h + \left(g+\sin L\right)k\end{bmatrix} \tag{4-49}$$

The (RTN) coordinate system can be defined by [Betts & Erb, 2003]:

$$Q = \begin{bmatrix}\hat{i}_R & \hat{i}_T & \hat{i}_N\end{bmatrix} = \begin{bmatrix}\dfrac{\vec{r}}{\|\vec{r}\|} & \hat{i}_N \times \hat{i}_R & \dfrac{\vec{r}\times\vec{v}}{\|\vec{r}\times\vec{v}\|}\end{bmatrix} \tag{4-50}$$

Equation (4-50) can be used as a transformation from the rotating radial frame (RTN) into the inertial axes, and its transpose for the reverse transformation, from the position and velocity vectors in the ECI frame, calculated from Equations (4-48) and (4-49).

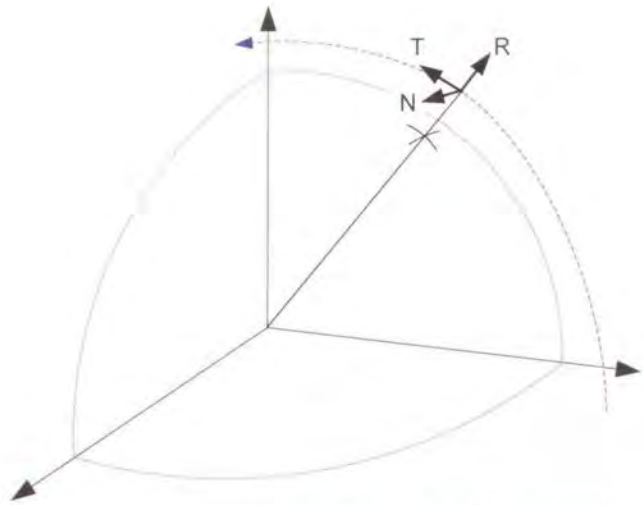

Figure 4-4. Representation of the RTN frame

4.4 Perturbation forces and modelling

4.4.1 Forces relevant to dawn-dusk orbits

Various perturbation forces are exerted on a satellite in low-Earth orbit (LEO). Many factors are known to affect the prediction of a satellite's orbit:

- Atmospheric drag;
- Non-spherical Earth gravitation;
- Third-body perturbations (primarily from the Moon and Sun, but also other planets and, in the absolute, from every body in the Universe);
- Solar radiation pressure;
- Earth radiation pressure;
- Solid Earth and ocean tides;
- Relativistic effects.

The relative importance of the main forces is shown in Figure 4-5.

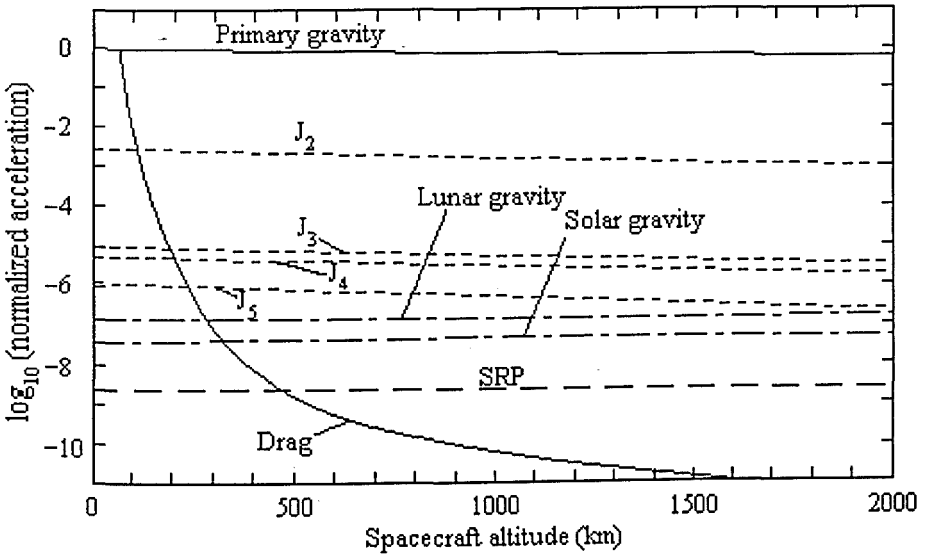

Figure 4-5 Magnitude of various accelerations exerted on a spacecraft in LEO [Fortescue et al, 2003]

Some of the forces are clearly minute, while it is essential to take into account the dominant ones in the satellite trajectory model. We will thus only consider the atmospheric drag, the non-spherical Earth gravitation, the third-body perturbation from the Sun and the Moon, and solar radiation pressure.

The atmospheric drag is mostly an in-plane disturbance force, affecting the semi-major axis and eccentricity of the orbit. This is the main force that the propulsion system must compensate for.

The other perturbations will mostly result in out-of-plane accelerations. It is essential to model the non-spherical Earth gravitation, as it is the reason why Sun-synchronous orbits are possible. Because the satellite is in a dawn-dusk orbit, solar radiation pressure and gravitational force from the Sun will mostly average out over an orbit. Because of the local time of the descending node (LTDN) of 06:00, the gravitational force from the Sun will be marginally stronger over the North Pole than over the South Pole. This would tend to increase the inclination of the orbit and combine with the Earth geopotential to rotate the line of apsides. Inversely, eclipses would occur near the South Pole during the northern hemisphere summer, and the asymmetry in radiation pressure would tend to rotate the orbit around the line of apsides towards the poles.

The gravity from the Moon is cyclical on a monthly basis as the Moon orbits the Earth. Wertz [2001] shows that there are secular effects on the line of apsides and argument of perigee.

Each of these perturbation forces are described in the following sections along with their mathematical models that will be incorporated into the trajectory model.

4.4.2 Atmospheric drag

4.4.2.1 Acceleration due to atmospheric drag

The density of the atmosphere varies exponentially with the inverse of the altitude; hence, while atmospheric drag has no effect on satellites in high altitude orbits, LEO satellites experience a large atmospheric drag force.

The atmospheric drag is usually given by the equation:

$$\vec{a}_d = -\frac{1}{2}\rho\frac{SC_D}{m_{SC}}V_{rel}^2\frac{\vec{V}_{rel}}{\left|\vec{V}_{rel}\right|} \tag{4-51}$$

The term SC_D/m_{SC} is the inverse of the ballistic coefficient BC, where m_{SC} is the mass of the spacecraft, S is the cross-sectional area of the spacecraft normal to the velocity vector and C_D is the drag coefficient.

The velocity in this equation is that of the spacecraft relative to the atmosphere. The drag force acts in the exact opposite direction to the velocity vector thus it is important to take into consideration the motion of the atmosphere with respect to the inertial frame. By definition, the velocity of the spacecraft can be written as:

$$\vec{V}_{SC} = \vec{V}_{rel} + \vec{V}_{atm} \tag{4-52}$$

Note that the velocity vector of the spacecraft relative to the atmosphere and the velocity vector of the atmosphere must both be expressed in the inertial frame ECI.

The motion of the atmosphere is mostly due to the rotation of the Earth and can therefore be described as a rotation around the polar axis. Due to friction with the Earth, the atmosphere nearer to the surface rotates faster than at higher altitudes [Vallado, 2007]. Hence, the velocity of the spacecraft relative to the atmosphere is:

$$\vec{V}_{rel} = \vec{V}_{SC} - \vec{\omega}_{atm} \times \vec{r} \tag{4-53}$$

As a first approximation, the rotation of the atmosphere is taken as that of the Earth. Applications requiring high accuracy should also take into account the winds field. This is done by superimposing the winds on the mean motion of the atmosphere $\vec{V}_{atm}$ used above [Vallado, 2007]. However, this is ignored in the relatively simple model developed here.

Calculating the atmospheric drag is a very difficult task and depends on how accurate we want the model to be. Looking back at Equation (4-50), apart from the velocity there are another three parameters that need to be determined: the density ρ, the cross-sectional area

S and the drag coefficient C_D. The mass of the spacecraft is normally well known throughout the mission operational lifetime.

Provided that the satellite is three-axes stabilised and its attitude accurately known during its operational lifetime, the cross-section area is sufficiently well known and nearly constant, albeit minor variations due to attitude and relative vector direction. At the end of life however, the satellite is passivated and its attitude is uncontrolled. Its cross-sectional area would vary with time and only a mean surface area can be employed. This needs to be considered to ensure an atmospheric re-entry within the recommended 25 years after end of operation. However, this is an issue for satellites above about 600 km but not in a very low orbit below 400 km.

The drag coefficient of the satellite and especially the atmospheric density are more difficult to determine. These are addressed in the next two sections.

Finally, drag is only one of three components of the aerodynamic forces acting on the vehicle, but the lift and side forces are negligible. For most spacecraft, and where moderate accuracy is sufficient, this is a satisfactory assumption since the drag dominates.

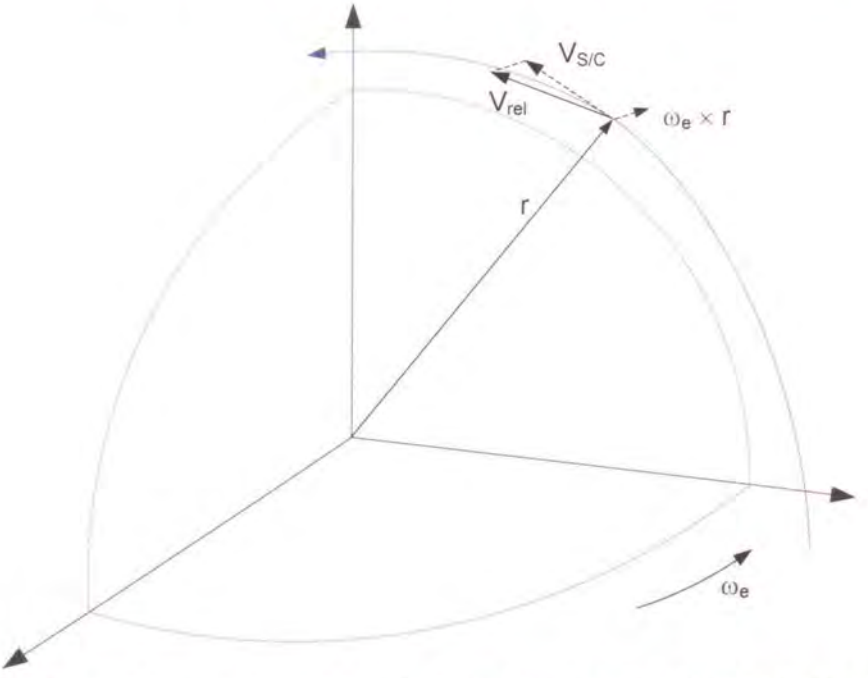

Figure 4-6. Effect of the rotation of the Earth on the velocity of the satellite relative to the atmosphere

4.4.2.2 Ballistic coefficient

The difficulty in estimating the ballistic coefficient of a satellite has been discussed in section 3.2.2. Here, the objective is to try to predict a range of ballistic coefficients that are representative of the different spacecraft configurations selected in Chapter 3.

Figure 4-7 shows the predicted drag coefficient (as calculated by the method described in section 3.2.2) as a function of the ratio of lateral areas (side walls and solar arrays) to the frontal area of the satellite, and incidence angle of the flow. Note than there is a coupling between the ratio and the incidence angle: for a zero incidence angle, all lateral walls (and both sides of the solar arrays) would be included in the drag calculation. However, as the incidence angle increase, only half of the lateral area is contributing due to the other half being shadowed from the flow. This is represented by the grey area.

Furthermore, the incidence angle will vary over an orbit within ±5°, and thus C_D will also change. Thus an average value of C_D should be taken, which would not exceed 4, represented by the red line in Figure 4-7.

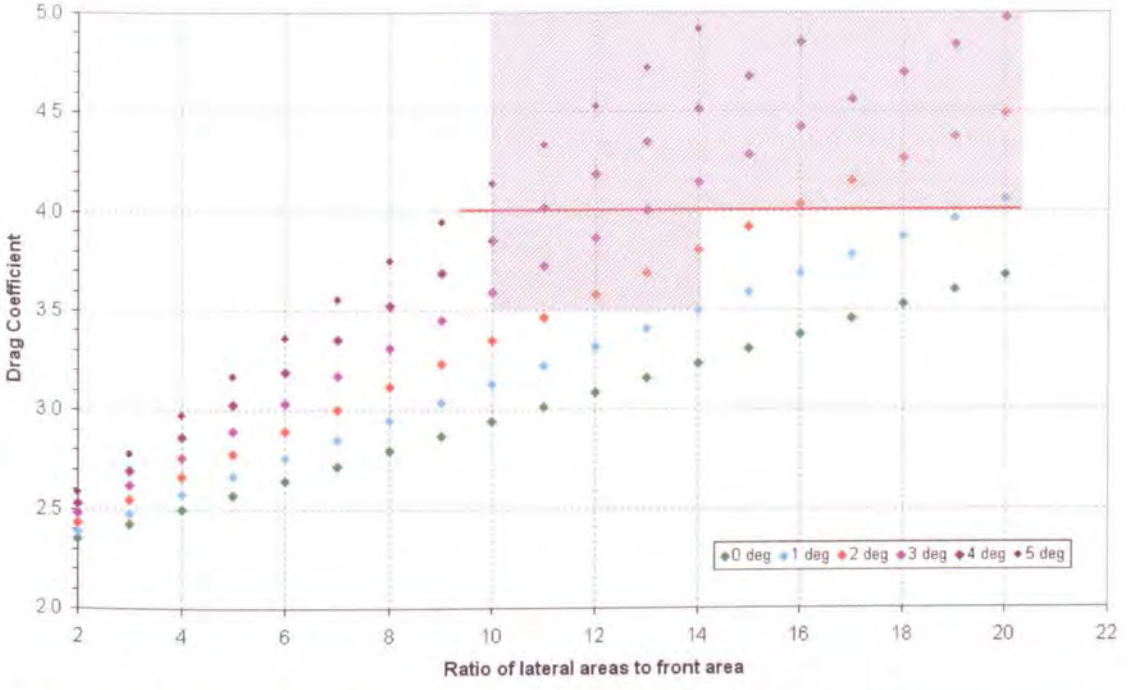

Figure 4-7. Drag coefficient as a function of the satellite's lateral-to-front area ratio (including solar arrays) and incidence angles

Based on the preliminary size estimates of sections 3.3.6 and 3.4.2, ballistic coefficients have been calculated for a range of cross-section areas, drag coefficients and masses. Some combinations are unlikely, for instance, a large cross-section area means that lateral surfaces will play a lesser role and the drag coefficient will be smaller (Figure 4-7). Also, large cross-section areas are associated with very large telescopes and heavy satellites. Thus possible combinations have been determined based on three sub-groups, as shown in Table 4-1. The resulting ballistic coefficients are plotted in Figure 4-8. Four representative values of ballistic coefficients are used in the simulations: 60, 90, 130 and 180 kg/m^2.

	Small satellites	Medium satellites	Large satellites
Cross-section area	2.5 – 5	7.5 – 10	12.5 – 15
Mass	1000 – 2000	1500 – 3000	2500 – 3500
C_D	3 – 4	2.5 – 3.5	2.2 – 3

Table 4-1. Likely combinations of cross-section areas, masses and drag coefficients.

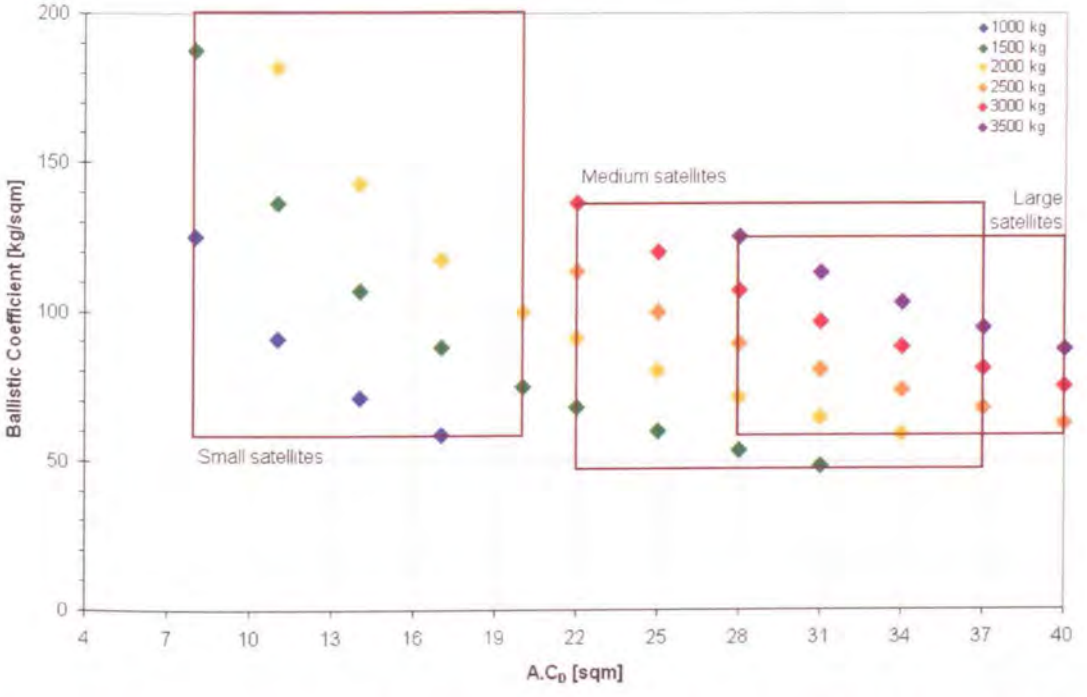

Figure 4-8. Ballistic Coefficient distribution for various combinations of cross-section areas, drag coefficients and masses.

4.4.2.3 Atmospheric density model

Many factors contribute to variations in atmospheric density and predicting it is a very difficult process. This is shown by the number of models that have been developed over the last half-century alone (most notably from the 1960's through to the 1980's), each with their relative strengths, weaknesses, and limitations. Atmospheric density is mostly influenced by three factors: the molecular structure of the atmosphere, the incident solar flux, and geomagnetic interactions [Vallado, 2007].

Density greatly varies with the altitude, in an exponential manner; the most famous, highly simplified way of estimating the mean density is given by the basic formula:

$$\rho = \rho_0 e^{-\frac{h}{H_0}} \tag{4-54}$$

The scale height H_0 can be derived from the hydrostatic equation and the gas law as [Montenbruck and Gill, 2000]:

$$H_0 = \frac{R_g T}{M g_0} \tag{4-55}$$

where R_g is the universal gas constant, T the absolute temperature, M the mean molecular weight (not mass) of the atmospheric constituents, and g_0 is the Earth gravitational acceleration.

While Equation (4-54) is acceptable at very low altitudes (below 25 km, see Table 4-2), it becomes highly erroneous above, calling for a slightly improved alternative:

$$\rho(h_{ellp}) = \rho(h_0) e^{-\frac{h_{ellp}-h_0}{H(h_0)}} \tag{4-56}$$

where h_0 is a reference altitude, with $\rho(h_0)$ and $H(h_0)$ the density and the density scale height at this reference altitude, respectively, and $\rho(h_{ellp})$ is the density at the height above the ellipsoid h_{ellp}.

Altitude h_{ellp} [km]	Reference altitude h_0 [km]	Nominal density ρ_0 [kg.m^{-3}]	Scale height $H(h_0)$ [km]
0-25	0	1.225	7.249
25-30	25	3.899×10^{-2}	6.349
30-40	30	1.774×10^{-2}	6.682
40-50	40	3.972×10^{-3}	7.554
[...]	[...]	[...]	[...]
200-250	200	2.789×10^{-10}	37.105
250-300	250	7.248×10^{-11}	45.546
300-350	300	2.418×10^{-11}	53.628
350-400	350	9.518×10^{-12}	53.298
400-450	400	3.725×10^{-12}	58.515
450-500	450	1.585×10^{-12}	60.828
[...]	[...]	[...]	[...]

Table 4-2. Exponential atmospheric model for selected altitudes, adapted from [Wertz, 1978].

Table 4-2 gives the necessary values to compute the density from Equation (4-56). This method ensures that the variation with altitude of the partial densities of the different atmospheric constituents is taken into account.

While this model is acceptable for applications where moderate accuracy is sufficient, it ignores however some significant time-varying phenomena. The most important source of the density variation in time is related to the solar radiation interactions with the upper atmosphere, which are mainly of three forms.

First, ultraviolet (UV) radiations heat the atmosphere by conduction and therefore increases the density at higher altitudes [Long et al, 1989]. The maximum density occurs approximately at the latitude of the sub-solar point, and roughly two hours after local noon, i.e. ~30° East of the sub-solar point. Similarly, the minimum density is found three hours past midnight near the same latitude but in the opposite hemisphere, hence the density variation is dependent

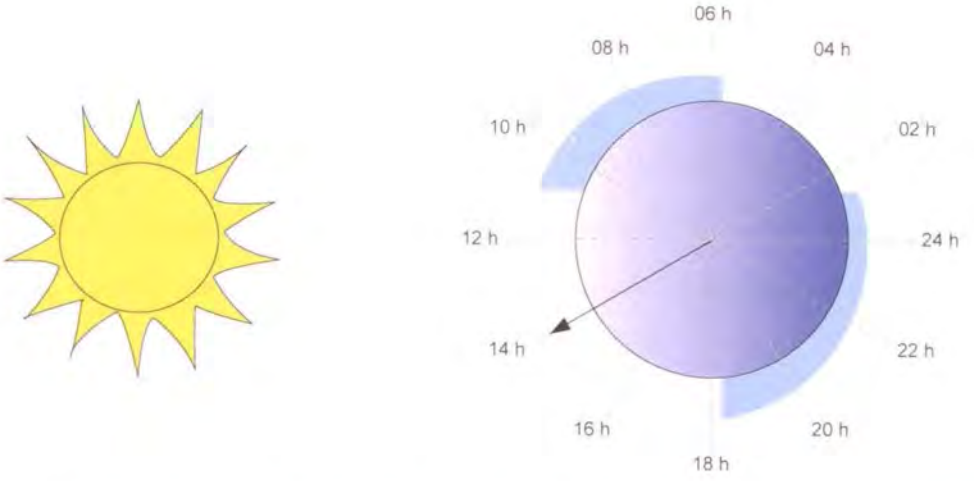

Figure 4-9. Illustration of the atmospheric bulge occuring 2 hours after noon

on the geographical latitude [Montenbruck and Gill, 2000]. This day-night effect causes a redistribution of density, resulting in a diurnal atmospheric bulge (Figure 4-9).

Secondly, extreme ultraviolet (EUV) radiations produce the same heating and density effect but on a short time scale linked to the Sun rotation period of 27 days. It has been found that the fluctuation in the EUV emission can be correlated with the flux of radiation at 10.7-cm wavelength, also known as decimetric flux, $F_{10.7}$ [Long et al, 1989; Montenbruck and Gill, 2000], which is not blocked by the atmosphere and can thus be measured.

Thirdly, the charged particles that constitute the solar winds are the largest single factor affecting short-term fluctuations in the atmospheric density [Long et al, 1989]. The solar winds are related to the Sun spots and hence their magnitude varies with the 11-year cycle. A polynomial equation matching the last few solar cycles only can be used to relate the sunspot number, R, averaged over a month or longer, and $F_{10.7}$, assuming that the next solar cycle will not differ dramatically from the previous [Vallado, 2007]:

$$F_{10.7} = 63.7 + 0.728R + 0.00089R^2 \tag{4-57}$$

Finally, atmospheric temperature and density vary greatly during geomagnetic storms but are very brief, in the order of one or two days. Thus, geomagnetic activity has an impact on atmospheric density too.

4.4.2.4 Overview of upper atmosphere density models

There exist many different models of the upper atmosphere; many of these are presented in the AIAA's Guide to Reference and Standard Atmosphere Models [AIAA/ANSI, 2004]. Some of the most popular models include the Jacchia models J70, J71 or J77 and their variants (e.g. Jacchia-Roberts), and the Mass Spectrometer – Incoherent Scatter (MSIS) models MSIS-86, MSIS-90 and NLRMSISE-00.

Models tend to be all empirical rather than purely theoretical but can be classified by the type of data they are developed from. The Jacchia model series was primarily based on total density derived from satellite tracking assuming a drag coefficient of 2.2 [Jacchia, 1977]. The MSIS series of models come from data measured in situ by mass spectrometers on board many scientific satellites and from ground-based incoherent scatter stations [Hedin, 1988].

There have been many studies attempting to compare the relative merits of the various atmospheric density models. For instance, Healy and Akins [2004] compared the Jacchia and MSIS models using more than 5000 catalogued satellites, and found MSIS performing better with a 1999 data set (around the sunspot cycle maximum) but obtained the opposite result with a data set from 2004. This shows that certain models perform better for certain conditions, and that there is unfortunately no perfect model.

One should eventually distinguish between a density model for use in rough prediction of orbits and orbit maintenance, and more advanced atmospheric models to represent as accurately as possible the various interactions and processes that influence the upper atmosphere, which would appeal to the atmospheric science community or mission planners requiring high-accuracy orbit prediction.

Since the present work only requires a moderately accurate representation of atmospheric drag, we shall concentrate on a fast and simple atmospheric density model. Indeed, Montenbruck and Gill [2000] argue that models are inherently inaccurate by 15%, and they thus point out that a model with moderate complexity, computational effort and number of coefficients to be stored, is sufficient for the purpose of satellite orbit determination and prediction.

Vallado [2007] recommends the Russian GOST atmosphere model as mathematically simple yet comprehensive in its physical content. An alternative is the model developed by Harris and Priester [1962a] and upgraded by Long et al [1989]. While it was initially developed as early as the 1960s, Vallado [2007] recommends it for comparing propagation algorithms due to its fairly accurate results and computational efficiency while Montenbruck & Gill [2000] note that this model is still widely used as a standard upper atmosphere and may be adequate for many applications. This is exemplified by NASA GSFC's Goddard Trajectory Determination System (GTDS) which offers the Harris-Priester model in parallel with the Jacchia-Roberts model, giving the user a choice of a rapid computation of the density [Long et al, 1989].

4.4.2.5 The Harris-Priester upper atmosphere density model

Harris and Priester [1692b] solved the heat conduction equation under quasi-hydrostatic conditions, producing models of the upper atmosphere (above 120 km) for different levels of solar activity. The original model includes approximations for fluxes from the EUV radiations and corpuscular (i.e. the solar wind) heat sources, but semi-annual, seasonal latitudinal and EUV 27-day variations have been averaged out [Montenbruck & Gill, 2000].

[Long et al, 1989] modified the original model to account for the diurnal bulge by means of a cosine variation between a maximum density profile $\rho_M(h)$ at the apex of the diurnal bulge and a mimimum density profile $\rho_m(h)$ at the antapex of this bulge. While they present a table of these maximum and minimum profiles (also available from Montenbruck & Gill [2000]) for a mean solar activity, the original report by Harris and Priester [1962b] gives 250 pages of tables of hourly variation in density for five different level of monthly-averaged solar activity index.

Long et al. [1989] present the following method. The atmospheric density at the location of the satellite is:

$$\rho_0(h) = \rho_m(h) + [\rho_M(h) - \rho_m(h)]\cos^n\left(\frac{\psi}{2}\right) \tag{4-58}$$

where ρ_m and ρ_M are the minimum and maximum densities, respectively, at the altitude of the satellite, at a given time in the solar activity cycle, and ψ is the angle between the satellite position vector and the apex of the diurnal bulge. The angle ψ and the exponent n can help taking into account the latitudinal density variations, with n equal to 2 for low-inclination orbits and up to 6 for polar orbits.

The cosine function in Equation (4-58) can be computed directly by:

$$\cos^n\left(\frac{\psi}{2}\right) = \left[\frac{1}{2} + \frac{\vec{r}\cdot\hat{U}_B}{2|\vec{r}|}\right]^{n/2} \tag{4-59}$$

where $\vec{r}$ and $\hat{U}_B$ are the satellite position vector and unit vector directed toward the apex of the diurnal bulge, respectively, expressed in the inertial geocentric frame. The unit vector $\hat{U}_B$ is related to the position of the Sun in the ECI frame and the longitudinal angle between the Sun vector and the apex of the diurnal bulge, and its components are:

$$\hat{U}_B = \begin{bmatrix} \cos\delta_s \cos(\alpha_s + \lambda_{lag}) \\ \cos\delta_s \sin(\alpha_s + \lambda_{lag}) \\ \sin\delta_s \end{bmatrix} \tag{4-60}$$

where δ_S and α_S are the declination and right ascension of the Sun, and λ_{lag} represents the 2-hour delay between the apex of the bulge and the sub-solar point, corresponding to an angle of about 30° due to the rotation of the Earth.

The minimum and maximum densities can be computed by exponential interpolation between two reference altitudes h_i and h_{i+1}:

$$\begin{cases} \rho_m(h) = \rho_m(h_i)\exp\left(\dfrac{h_i - h}{H_m}\right) & (h_i \le h \le h_{i+1}) \\ \rho_M(h) = \rho_M(h_i)\exp\left(\dfrac{h_i - h}{H_M}\right) & (h_i \le h \le h_{i+1}) \end{cases} \tag{4-61}$$

where H_m and H_M are the respective scale heights given by:

$$\begin{cases} H_m = \dfrac{h_i - h_{i+1}}{\ln\left[\dfrac{\rho_m(h_{i+1})}{\rho_m(h_i)}\right]} \\ H_M = \dfrac{h_i - h_{i+1}}{\ln\left[\dfrac{\rho_M(h_{i+1})}{\rho_M(h_i)}\right]} \end{cases} \tag{4-62}$$

Long et al [1989] recommend using the following equation to compute the altitude in order to account for the non-sphericity of the Earth:

$$h = r - \frac{R_e(1-f)}{\sqrt{1-(2f-f^2)\cos^2\delta}} \tag{4-63}$$

where r is the magnitude of the satellite position vector, R_e is the mean equatorial radius of the Earth, and f is a coefficient representing the physical bulge of the Earth with a value of 1/298.257 [Vallado, 2007]. The declination of the satellite, δ, can be approximated as the geocentric latitude of the sub-satellite point.

The next step is to generate the minimum and maximum densities at the reference altitudes. The tables from Harris and Priester [1962b] cover the altitude range 120-2050 km, at the local time (in steps of one hour), and for solar activity indexes of 250, 200, 150, 100, and 70. However, we are only interested in a fairly reduced altitude range, between 250 and 350 km roughly, and we only need the minimum and maximum values of density. While Harris and Priester [1962b] give densities in altitude steps of 20 km, the exponential interpolations of Equations (4-61) and (4-62) return satisfactory accuracy with altitude steps of 60 km. The necessary data is shown in Table 4-3. Figure 4-10 shows the error between the computed density and the original data for the minimum density case.

Five reference solar activity indexes are used. For intermediate values, second-order polynomial equations are used to compute the density as a function of the F10.7 index, for each reference altitude and for both the minimum and maximum cases.

Solar activity index, F10.7		240 km	300 km	360 km
250	Min	175.4	51.07	17.75
	Max	206	76.41	33.89
200	Min	128.8	31.71	9.667
	Max	166.5	55.49	22.37
150	Min	83.02	16.46	4.241
	Max	122.5	34.81	12.33
100	Min	43.87	6.553	1.321
	Max	75.57	16.88	4.882
70	Min	25.53	3.01	0.4828
	Max	47.56	8.532	2.083

Table 4-3 Reference data for the Harris-Priester upper atmospheric density model, as extracted from [Harris & Priester, 1962b]

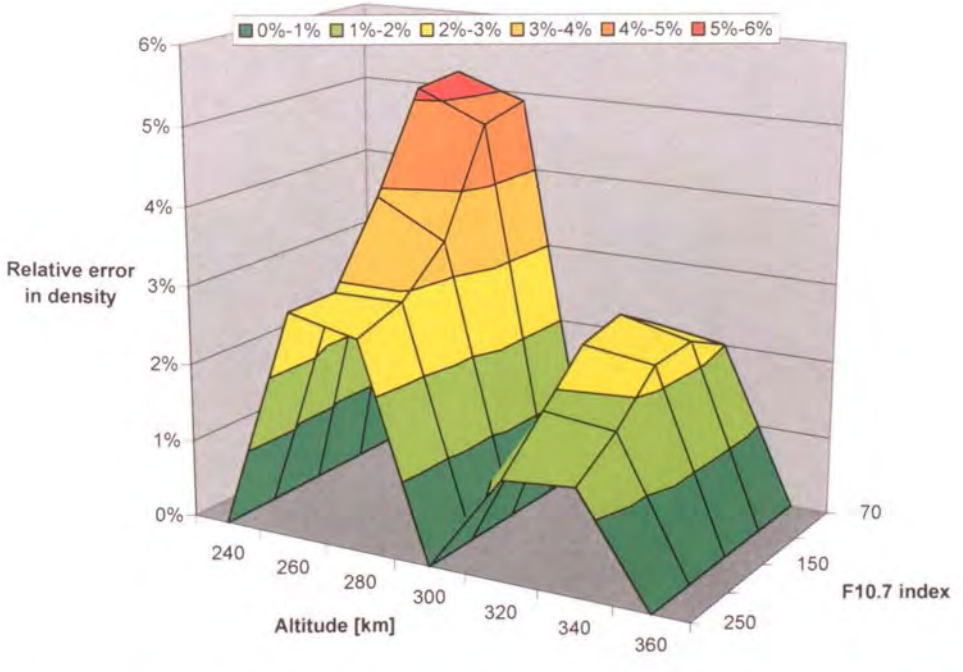

Figure 4-10 Relative error in density for intermediate altitudes between the reference altitudes of 240, 300 and 360 km.

4.4.3 Non-spherical Earth gravity

4.4.3.1 Theory

The two-body problem assumes that the bodies in question act as point masses where their masses are concentrated at their centre. This is true for a perfect, homogeneous sphere, and is particularly important for the larger body around which the smaller one orbits. In the case of interest to us, the Earth is certainly not a perfect sphere. This is noticeable along the latitudes, due to the Earth oblateness at the poles, which we conveniently use to maintain Sun-synchronous orbits. This is also true along the longitudes as the planet mass distribution is not homogeneous, and this is particularly observable in the East-West station keeping of geostationary orbits. The latter effect, known as triaxiality perturbation, translates in geostationary positions being stable at longitudes of 75°E and 105°W, while unstable locations are situated at 90° from these two points [Fortescue et al, 2003].

This results in an inhomogeneous gravity field around the Earth, illustrated by Figure 4-11.

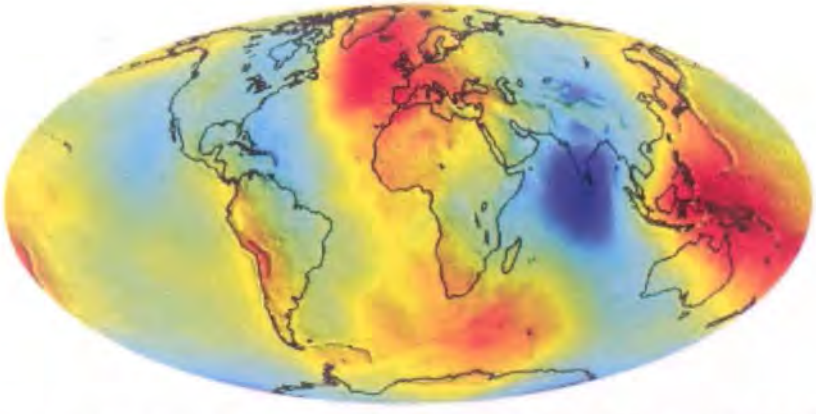

Figure 4-11 Geoid of equal gravitational potential (EGM96 model) [ESA, 2006]

The gravitational potential, or geopotential, can be mathematically expressed as a central force expanded by a series of spherical harmonics [Wertz, 2001], which are represented in Figure 4-12. The geopotential can be written as [Henderson, 2006; Danielson et al, 1995]:

$$U(r,\phi,\lambda)=\frac{\mu}{r}\left\{1+\sum_{n=2}^{\infty}\sum_{m=0}^{n}\left(\frac{R}{r}\right)^{n}P_{nm}(\sin\phi)\left(C_{nm}\cos(m\lambda)+S_{nm}\sin(m\lambda)\right)\right\} \tag{4-64}$$

In this equation, μ is the gravitational parameter of the Earth, r is the distance of the spacecraft from the centre of the Earth, and R is the semi-major axis of the reference ellipsoid, which we take as the mean equatorial radius of the Earth. C_{nm} and S_{nm} are the Earth's tesseral ($n \neq m$) and sectorial ($n = m$) harmonic coefficients. For $m = 0$, $C_{n,0}$ are the zonal harmonics, more commonly known by the notation J_n (but of opposite sign), while $S_{n,0}$ do not exist. $P_{nm}(\sin\phi)$ are the associated Legendre polynomials of the first kind, of degree n and order m. The geopotential is also a function of the geocentric latitude ϕ and the longitude λ.

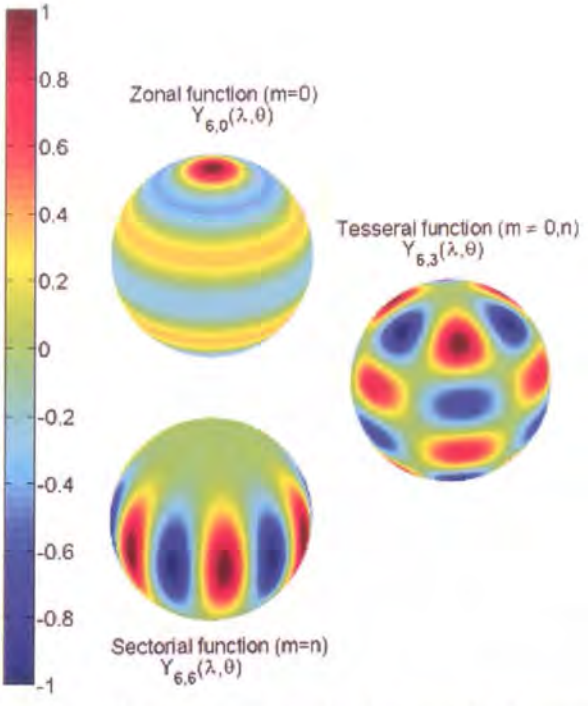

Figure 4-12. Examples of the different kinds of spherical harmonics [Universität Stuttgart, 2009]

4.4.3.2 Simplifying assumptions

The first six degrees of the un-normalised zonal, tesseral and sectorial harmonics are shown in Table 4-4 and Table 4-5. It is apparent that the term $C_{2,0}$, largely dominates, and any term of order m = 3 and above is negligible compared to its associated term $C_{n,0}$. More generally, tesseral and sectorial harmonics tend to be considered only in the case where very precise orbit determination is required, such as for geodetic missions [Fortescue et al, 2003].

		m						
		0	1	2	3	4	5	6
n	2	-1082626.9	-0.241	1574.4				
	3	2532.3	2190.9	308.9	100.6			
	4	1620.4	-508.8	78.3	59.2	-3.983		
	5	227.1	-50.6	105.7	-14.9	-2.298	0.431	
	6	-540.8	-59.9	6.052	1.202	-0.327	-0.216	0.002

Table 4-4. Values of un-normalised coefficients C_{nm} (units of 10^{-9}) from JGM-2 model to degree (n) and order (m) 6.

		m						
		0	1	2	3	4	5	6
n	2		1.543	-903.8				
	3		268.7	-211.5	197.2			
	4		-449.1	148.2	-12.0	6.526		
	5		-81.8	-52.4	-7.106	0.387	-1.649	
	6		20.9	-46.5	0.187	-1.785	-0.433	-0.055

Table 4-5. Values of un-normalised coefficients S_{nm} (units of 10^{-9}) from JGM-2 model to degree (n) and order (m) 6.

In our case, this high precision is not required, and therefore we will only take into consideration the zonal harmonics. This is similar to assuming that the Earth is a body with an axial symmetry, which is a valid assumption for most planets in the solar system [Battin, 1999]. As a consequence, m = 0 and Equation (4-64) can be simplified to:

$$U(r,\phi)=\frac{\mu}{r}\left\{1+\sum_{n=2}^{\infty}\left(\frac{R}{r}\right)^{n}P_n(\sin\phi)C_n\right\} \tag{4-65}$$

It appears that the longitude λ disappears from the equation, meaning that the gravitational geopotential becomes independent of longitudinal distribution. This is in line with our assumption of an axially symmetric body.

Since C_2 dominates largely and the trajectory accuracy is fairly relaxed, it is not necessary to consider coefficients above a certain degree n. Various publications tend to consider zonal harmonics up to the 4th degree [Battin, 1999; Betts & Erb, 2003] or 6th degree [Walker et al, 1985]. Hence, up to the sixth degree provide sufficient accuracy.

4.4.3.3 Disturbing acceleration due to a non-spherical Earth

The acceleration due to a non-spherical Earth can be expressed as a vector in an Earth-fixed spherical coordinate system as [Henderson, 2006]:

$$\vec{a}_{r,\phi,\lambda}=\nabla U=\frac{\partial U}{\partial r}\vec{u}_r+\frac{1}{r}\frac{\partial U}{\partial \phi}\vec{u}_\phi+\frac{1}{r\cos\phi}\frac{\partial U}{\partial \lambda}\vec{u}_\lambda \tag{4-66}$$

Betts & Erb [2003] express the gravitational disturbing acceleration in a North-East-Down frame, but this can equally be expressed in a Zenith-East-North (ZEN) frame as:

$$\vec{a}_g\big)_{ZEN}=\left[\frac{\mu}{r^2}\sum_{n=2}^{4}(n+1)\left(\frac{R}{r}\right)^{n}P_nJ_n\right]\hat{i}_{Zen}-\left[\frac{\mu\cos\phi}{r^2}\sum_{n=2}^{4}\left(\frac{R}{r}\right)^{n}P_n'J_n\right]\hat{i}_{Nor} \tag{4-67}$$

where i_{Zen} and i_{Nor} are the Zenith and North direction of the ZEN local vertical, local horizontal frame. Note that there is no East component because of our assumption of an axially symmetric Earth. In Equation (4-67), J_n is the well known notation of the zonal harmonics, but the sign differs from the other notation C_n, i.e. $J_n = -C_n$. The Legendre polynomial P_n of

the function sin(ϕ) and its partial derivative P'_n (with respect to sin ϕ) can be found from the recursions:

$$P_n = \frac{(2n-1)\sin\phi}{n} P_{n-1} - \frac{(n-1)}{n} P_{n-2} \tag{4-68}$$

$$P'_n = \sin\phi P'_{n-1} + nP_{n-1} \tag{4-69}$$

It follows that knowing P_0 and P_1 are sufficient to find all the other terms, with:

$$\begin{cases} P_0 = 1 \\ P_1 = \sin\phi \end{cases} \tag{4-70}$$

Table 4-6 summarises the calculation of the Legendre polynomials.

Based on the method described by [Betts and Erb, 2003], the ZEN frame is defined with respect to the ECI frame from the position vector expressed in ECI terms, so that the disturbing acceleration in the ECI frame can be found from:

$$a_g)_{ECI} = R_{ECI \leftarrow ZEN} a_g)_{ZEN} \tag{4-71}$$

where

$$R_{ECI \leftarrow ZEN} = \left[\hat{i}_{Zen} \quad \hat{i}_{East} \quad \hat{i}_{Nor}\right] = \left[\frac{\vec{r}}{\|\vec{r}\|} \quad \frac{\hat{Z} \times \left[\vec{r} - \left(\hat{Z} \cdot \vec{r}\right)\right]}{\left\|\hat{Z} \times \left[\vec{r} - \left(\hat{Z} \cdot \vec{r}\right)\right]\right\|} \quad \frac{\hat{Z} - \left(\hat{Z}^{\mathrm{T}} \hat{i}_{Zen}\right)\hat{i}_{Zen}}{\|\vec{r}\|}\right] \tag{4-72}$$

Subsequently, the disturbing gravitational acceleration is transformed into the RTN frame by:

$$a_g)_{RTN} = R_{RTN \leftarrow ECI} a_g)_{ECI} \tag{4-73}$$

where

$$R_{ECI \leftarrow RTN} = \left[\hat{i}_R \quad \hat{i}_T \quad \hat{i}_N\right] = \left[\frac{\vec{r}}{\|\vec{r}\|} \quad \hat{i}_N \times \hat{i}_R \quad \frac{\vec{r} \times \vec{v}}{\|\vec{r} \times \vec{v}\|}\right] \tag{4-74}$$

		P_n	P'_n	J_n ($\times 10^{-9}$)
n	0	1	–	–
	1	$\sin\phi$	1	–
	2	Equation (4-68)	Equation (4-69)	1 082 626.9
	3			-2 532.3
	4			-1 620.4

Table 4-6. Zonal harmonic coefficients, Legendre polynomial and its derivative for the first four degrees.

4.4.4 Luni-solar gravity perturbation

4.4.4.1 Acceleration due to third-body gravity

The disturbing acceleration due to third-bodies is written as [Betts, 1994]:

$$\vec{a}_d = -\sum_{j=1}^{n} \mu_j \left[\frac{\vec{d}_j}{d_j^3} + \frac{\vec{s}_j}{s_j^3} \right] \tag{4-75}$$

where d_j is the vector from the perturbing body j to the spacecraft (the secondary body), and s_j the vector from the primary body (Earth) and the disturbing body, as illustrated by Figure 4-13. When the vector r from the Earth to the spacecraft becomes small compared to the distance to the perturbing body (such as the Sun), the equation above can cancel out. Battin [1999] suggests the introduction of the function:

$$F(q) = q \left[\frac{3 + 3q + q^2}{1 + (1+q)^{3/2}} \right] \tag{4-76}$$

where

$$q_j = \frac{\vec{r} \cdot (\vec{r} - 2\vec{s}_j)}{\vec{s}_j \cdot \vec{s}_j} \tag{4-77}$$

and the disturbing acceleration due to third bodies becomes:

$$\vec{a}_d = -\sum_{j=1}^{n} \frac{\mu_j}{d_j^3}\left[\vec{r} + F(q_j)\vec{s}_j\right] \tag{4-78}$$

This form avoids rounding errors and cancellations that may otherwise occur for the gravitational perturbation of the Sun on a LEO satellite.

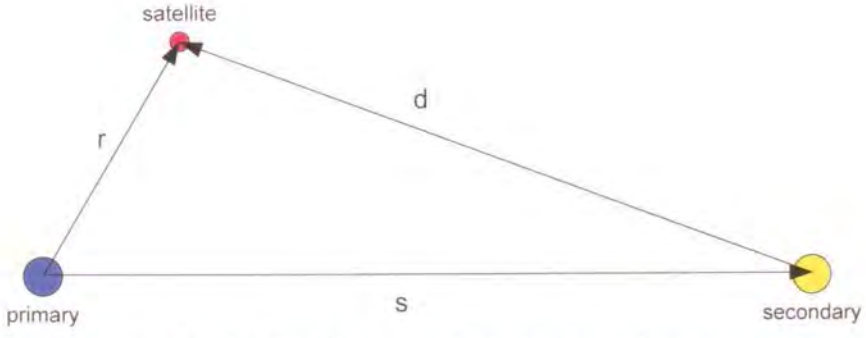

Figure 4-13. The third-body perturbation problem geometry.

Adapted from Betts [1994].

4.4.4.2 Sun and Moon ephemeris

The equations above require that the positions of the Moon and the Sun are known at any given time. Only moderate accuracy is required, so a simple, low-precision ephemeris is sufficient.

For the Sun, this can be rather straightforward: the Earth is in a fairly stable orbit, only slightly perturbed, and of very low eccentricity and negligible inclination. Montenbruck and Gill [2000] give simple series expansions for the Sun's ecliptic longitude λ_{Sun} and distance r_{Sun}, of the form:

$$\lambda_{Sun} = \Omega + \omega + M + 6892'' \sin(M) + 72'' \sin(2M) \tag{4-79}$$

$$r_{Sun} = \left[149.619 - 2.499\cos(M) - 0.021\cos(2M)\right] \cdot 10^6\, km \tag{4-80}$$

with the additional equations:

$$\begin{aligned} &\Omega + \omega = 282.9400° \\ &M = 357.5256° + 35999.049° \times T \\ &T = (JD - 2{,}451{,}545.0)/36525.0 \end{aligned} \tag{4-81}$$

JD is the Julian date at the time of interest, and T is the number of Julian centuries since 1.5 January 2000 (J2000) [Montenbruck & Gill, 2000].

The position vector of the Sun in the earth-centred equatorial frame is expressed as:

$$\vec{r}_{Sun})_{ECI} = \begin{bmatrix} r_{Sun} \cos \lambda_{Sun} \\ r_{Sun} \sin \lambda_{Sun} \cos \in \\ r_{Sun} \sin \lambda_{Sun} \sin \in \end{bmatrix} \tag{4-82}$$

The angle $\in$ is the obliquity of the ecliptic and is about 23.4393°. Over a long period of time (decades and centuries), the result of these equations should be corrected for the motion of the equinox due to precession. However, for a simulated period of 3 years, these equations provide sufficient accuracy.

Similarly, the ephemeris of the Moon can be obtained from an expansion series, as given by Montenbruck and Gill [2000]; however, these series are far more complicated than that of the Sun as the lunar orbit is greatly perturbed by the Earth and the Sun.

Alternatively, the coordinates of the Moon for a period of 4 years have been obtained from Horizons, the NASA JPL's online ephemeris tool [JPL, 2005]. Expansion series have been found to fit the data, thus providing a quick way of computing the Moon's coordinates. While the expansion series provided by Montenbruck & Gill [2000] is presumably applicable over long periods of time (assumed in the order of many decades) with distance errors of about 500 km, the following method described by Equations (4-83) to (4-85), can only be applied for the period 1 January 2000 to 1 January 2004, and with an error of up to 16,000 km (4%) compared to the Horizons data, as shown in Figure 4-14.

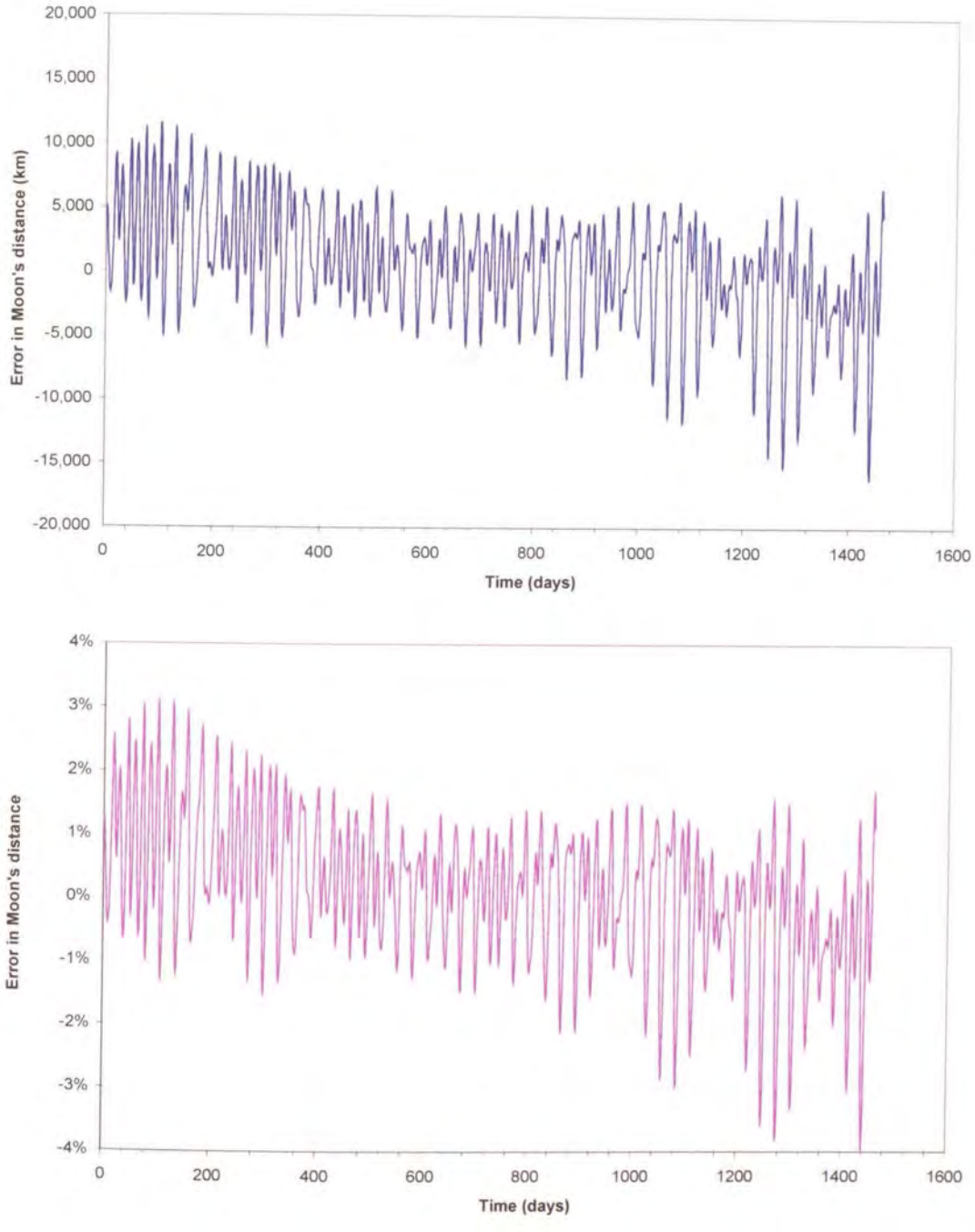

Figure 4-14. Error in Moon's distance from the Earth as calculated by the expansion series with respect to the JPL's Horizons data: absolute (top) and relative (bottom).

The coordinates of the Moon in the ECI frame are found to be approximately:

$$X_{Moon})_{ECI} = 16{,}600 + 382{,}000 \times \sin\left[\frac{2\pi}{27.3215}(t-4.43)\right] + \\ +16{,}000 \times \sin\left[\frac{2\pi}{2065}(t-363)\right] + 5{,}600 \times \sin\left[\frac{2\pi}{194}(t+16)\right] + \\ +10{,}450 \times \sin\left[\frac{2\pi}{13.7}(t-12)\right] \tag{4-83}$$

$$Y_{Moon})_{ECI} = -1{,}370 + 351{,}100 \times \sin\left[\frac{2\pi}{27.3215}(t-11.1)\right] + \\ +28{,}750 \times \sin\left[\frac{2\pi}{3134}(t-806)\right] + 5{,}566 \times \sin\left[\frac{2\pi}{195.6}(t-29.5)\right] + \\ +9{,}600 \times \sin\left[\frac{2\pi}{13.7}(t-1.62)\right] \tag{4-84}$$

$$Z_{Moon})_{ECI} = -1{,}300 + 158{,}800 \times \sin\left[\frac{2\pi}{27.322}(t-12.5)\right] + \\ +10{,}500 \times \sin\left[\frac{2\pi}{2710}(t-855)\right] + 2{,}480 \times \sin\left[\frac{2\pi}{195.1}(t-31)\right] + \\ +\left[10{,}200 + 9{,}500 \times \cos\left(\frac{2\pi}{1{,}518}t\right)\right] \times \sin\left[\frac{2\pi}{27.58}(t+2.9)\right] \tag{4-85}$$

In these equations, t is the time since 1 January 2000 midnight (JD 2,451,544.5) and is expressed in days.

4.4.5 Solar radiation pressure

4.4.5.1 Acceleration equation

Strictly speaking, there are two components of the solar radiation pressure. One part is due to absorption, and the other results from reflection (Figure 4-15). The absorption component is exerted in the direction opposite from the Sun, while the reflection one is normal to the reflective surface, and their respective mathematical expression are [Montenbruck & Gill, 2000]:

$$\vec{F}_{abs} = -p_{SR}\cos(\theta)A(1-\rho)\hat{e}_{Sun} \tag{4-86}$$

$$\vec{F}_{refl} = -2p_{SR}\cos(\theta)A\rho\cos(\theta)\hat{n} \tag{4-87}$$

The illuminated surface area is A and the incidence angle is θ. The solar radiation pressure p_{SR} varies with the distance of the satellite from the Sun. The reflectivity of the surface is represented by ρ, and varies between 0 (no reflection, i.e. blackbody) and 1 (no absorption, i.e. mirror-like). In fact, reflectivity and absorptivity of a material varies with the wavelength. It is common practice to consider an average wavelength of about 556 nm [Vallado, 2007].

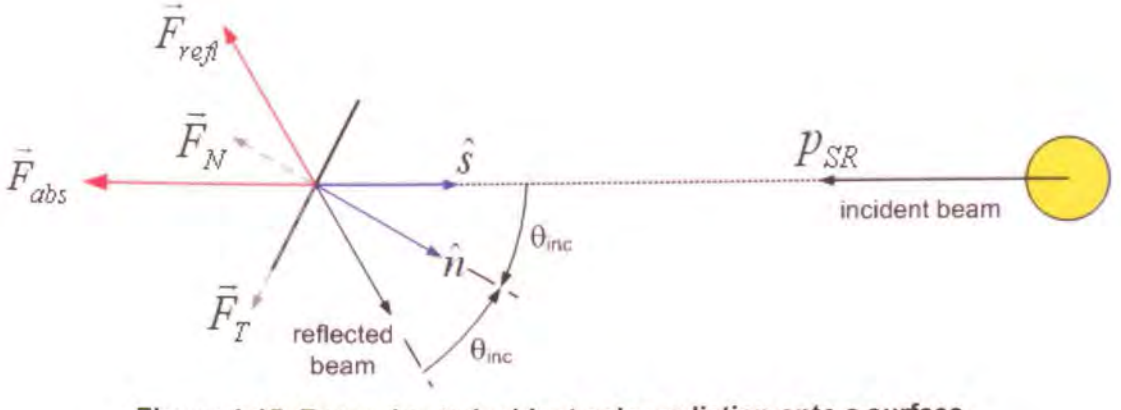

Figure 4-15. Force due to incident solar radiation onto a surface.

Adapted from Vallado [2007].

Both Vallado [2007] and Montenbruck & Gill [2000] point out that in most cases, it is an adequate approximation to consider the reflecting surface normal to the Sun's direction (θ = 0) at all time in order to simplify the problem. This is particularly adequate in our case because the satellite is in a dawn-dusk orbit and the solar arrays can be offset to be constantly pointing roughly in the direction of the Sun, apart from seasonal variations.

Thus Equations can be simplified to [Vallado, 2007]:

$$\vec{a}_{SR} = -\frac{p_{SR} C_R A_n}{m} \frac{\vec{r}_{sat-Sun}}{\left\| \vec{r}_{sat-Sun} \right\|} \tag{4-88}$$

The radiation pressure coefficient C_R is equal to 1 + ρ (see Table 4-7), and the solar radiation pressure is obtained by [Vallado, 2007]:

$$p_{SR} = \frac{SF}{c} \tag{4-89}$$

where

$$SF = \frac{1358}{1.004 + 0.0334 \cos\left(2\pi \frac{JD - 2{,}451{,}730}{365.25} \right)} \tag{4-90}$$

SF is the solar flux which varies due to the eccentricity of the Earth orbit. The reference Julian date of 2,451,730 corresponds to the 4th July 2000, the day in the year when the Earth is usually at the aphelion, although this may vary.

Part	Absorptivity, α	Reflectivity, ρ	Radiation pressure coefficient, C_R
Platform (VDA coated MLI)	0.14	0.86	1.86
Solar cells	0.90	0.10	1.10

Table 4-7. Properties of common MLI and solar cells.

4.4.5.2 Eclipse conditions

Knowing whether the satellite is in the shadow of the Earth or not can be easily established from a 2-D geometrical analysis, described by Montenbruck and Gill [2000]. Their method is described hereafter, based on the conical shadow model shown in Figure 4-16.

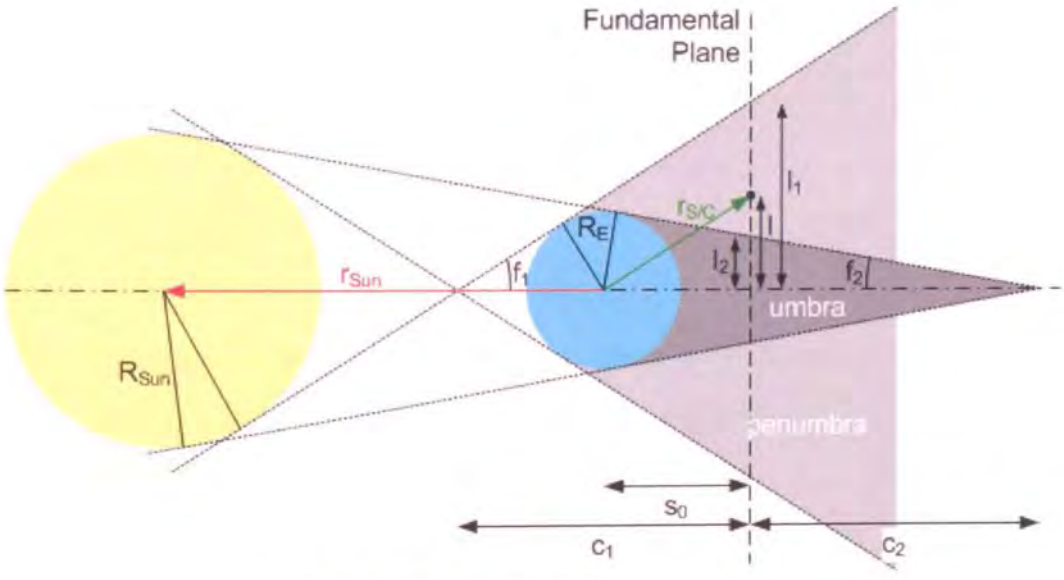

Figure 4-16. Conical shadow model.

Adapted from [Montenbruck & Gill, 2000].

Given the position vectors $r_{S/C}$ and r_{Sun} of the satellite and the Sun in an Earth-centred frame – such as the ECI coordinate system – a fundamental plane passing through the satellite and perpendicular to the Sun-Earth axis is located at a distance s_0 from the centre of the Earth:

$$s_0 = \frac{\left(-\vec{r}_{S/C}\right) \cdot \vec{r}_{Sun}}{\left\|\vec{r}_{Sun}\right\|} \tag{4-91}$$

and by trigonometry the distance of the satellite from the Sun-Earth axis is:

$$l = \sqrt{r_{S/C}^2 - s_0^2} \tag{4-92}$$

It follows that the parameters relative to the umbra are:

$$\begin{aligned} \sin f_2 &= \frac{R_{Sun} - R_E}{r_{Sun}} \\ c_2 &= s_0 - \frac{R_E}{\sin f_2} \\ l_2 &= c_2 \tan f_2 \end{aligned} \tag{4-93}$$

and those relative to the penumbra are:

$$\begin{aligned} \sin f_1 &= \frac{R_{Sun} + R_E}{r_{Sun}} \\ c_1 &= s_0 + \frac{R_E}{\sin f_1} \\ l_1 &= c_1 \tan f_1 \end{aligned} \tag{4-94}$$

When the satellite is on the day-side of the Earth where it cannot be in eclipse, $s_0 < 0$. It is only when $s_0 > 0$ that the satellite can potentially be in the shadow of the Earth. Under the latter condition, a test should be conducted to assess the actual situation of the spacecraft:

- If $l > l_1$, the satellite is in clear view of the Sun;
- If $l < l_2$, the satellite is in complete shadow (umbra);
- If $l_1 < l < l_2$, the satellite is in penumbra.

In the range of altitudes considered for a dawn-dusk orbit, the penumbra only lasts less than 20 seconds, and the solar flux received by the satellite varies during this time from 0 to 100% of the nominal value. Hence, we will simplify the problem by considering the worst case that the penumbra is part of the umbra and the satellite does not see the Sun during that time, hence that the satellite is in complete shadow when $l < l_1$. This is justified by the fact that the simulation time step may be greater than the penumbra duration, missing it altogether in some orbits.

4.4.6 Propulsive force

The propulsion module is not anticipated to be a very precise drag compensation system, but rather an orbit maintenance device.

The control of the thrust should be performed using on-board accelerometers. Indeed, McInnes [2003] has shown that a fixed, low-thrust drag compensation system based on expected atmospheric drag would be exponentially unstable.

The error between the thrust produced by the propulsion system and the actual drag force measured by the accelerometer would primarily depend on the accuracy of the accelerometer and the control error in the thrust level and direction, as shown by Bernelli Zazzera et al [1997] in their study of a drag-free control system for LEO satellites.

In the present model, these error contributors are merged together and are represented by a random error of 1% along the tangential direction (along the velocity vector), and 3% along the normal and radial directions of the RTN frame. These values are justified by assuming an absolute pointing error of 1° between the drag force vector and the thrust vector. The tangential direction would then be affected by $\cos(1°) = 0.9998$, and the other directions by $\sin(1°) = 0.017$. Hence, the 1% and 3% allocations appear to be sufficiently conservative, without providing excessive errors.

4.5 Trajectory model

4.5.1 Overview

The trajectory model has been implemented in MATLAB / Simulink. The equations of motion and disturbing forces are written as MATLAB functions which are called by the Simulink model. The latter uses the ode45 solver by default, which employs a pair of fourth- and fifth-order equations of the Runge-Kutta method, known as the Dormand-Prince pair [Shampine, 1994]. This solver tends to be the best to use as a first try in most cases [The MathWorks, 2005]. Riley et al [1997] point out however that the accuracy (and thus the complexity of the calculation) increases with the order, but that rounding errors cannot be avoided anyway.

Practically, ode45 is a variable-step solver which varies the step size during the simulation. The step size is reduced when the model's states are changing rapidly in order to increase accuracy. Respectively, it increases the step size when these states are changing slowly and thus avoids computing unnecessary steps [The MathWorks, 2005]. In the present work, the time step is constrained to a maximum of 225 seconds, providing at least 24 computational steps per orbit (based on a 90-minute orbit, 274-km altitude).

The Simulink model is shown in Figure 4-17. The MATLAB functions are represented in green, with the function name shown underneath. All the MATLAB function scripts are given in Appendix A. Orange boxes represent the results sent to the workspace. Many important parameters, such as classical orbital elements and spacecraft position and velocity, are not sent to the workspace in order to free up memory for the computations. Instead, these parameters can be recalculated after a simulation from the equinoctial orbital elements.

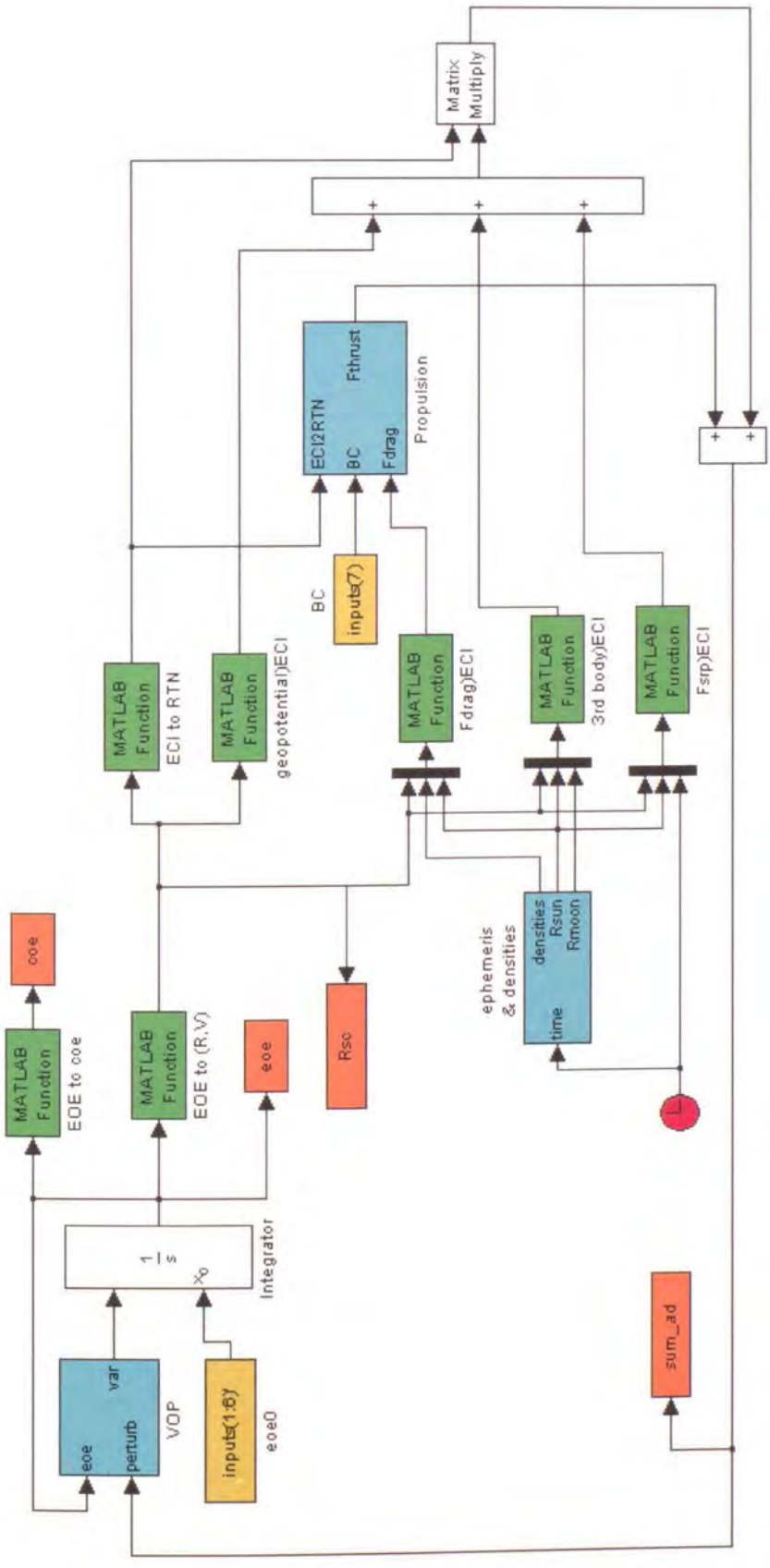

Figure 4-17. Illustration of the Simulink model for the trajectory simulations.

An important aspect of the model is its ability to avoid calculating atmospheric density as a function of solar activity and the positions of the Sun and Moon at every time step. These parameters not only vary much more slowly than the position of the spacecraft, but the way the reference densities are calculated (through interpolation of tabulated data) is extremely computer intensive.

4.5.2 Model validation

4.5.2.1 Predictions from theory

Whereas a semi-analytical model uses averaging techniques to eliminate short-periodic effects and only includes secular and often (but not always) long-periodic changes, models based on the Variation Of Parameters (VOP) method retain all effects irrespective of their timescale. Short-periodic effects would repeat over a period of time smaller that the satellite's orbit period, and therefore drives the minimum time step of the simulation. The advantage of a semi-analytical model is its ability to remain accurate with larger time steps (resulting in faster simulations); however, orbit propagation errors become too large when the atmospheric drag force is significant [Chao, 2005]. In view of the importance of drag to the present study, the VOP technique is preferred.

Klinkrad [2006] and Vallado [2007] summarise the perturbations of the LEO environment on satellite orbits, shown in Table 4-8. The model has been run with individual perturbations to show they are in line with what the theory predicts. For instance, Figure 4-18 shows that the semi-major axis, eccentricity and inclination as calculated by the model under J_2 effects only are in line with the behaviour predicted by the theory.

	Geopotential	Drag	Luni-solar	Solar radiation
Semi-major axis, a	Short-periodic variations due to J_2 at periods of T/2 and amplitudes of up to ±9 km	Secular decrease. Periodic change due to density and Earth rotation	Long-periodic variations	Long-periodic variations
Eccentricity, e	Short-periodic variations due to J_2 at periods of T and T/3. Long-periodic variations due to odd zonal harmonics J_{2n+1}.	Secular decrease. Periodic change due to density and Earth rotation	Long-periodic variations	Long-periodic variations
Inclination, i	Short-periodic variations due to J_2 at periods of T/2. Long-periodic variations due to odd zonal harmonics J_{2n+1}.	Small secular variation. Periodic change due to density and Earth rotation	Small secular variations.	Long-periodic variations
Right ascension of ascending node, Ω	Short-periodic variations due to J_2 at periods of T/2. Long-periodic variations due to odd zonal harmonics J_{2n+1}. Secular change due to even zonal harmonics J_{2n}.	Periodic change due to density and Earth rotation	Secular and periodic.	Secular and periodic.
Argument of perigee, ω	Short-periodic variations due to J_2 at periods of T and T/3. Long-periodic variations due to odd zonal harmonics J_{2n+1}. Secular change due to even zonal harmonics J_{2n}.	Periodic change due to density and Earth rotation	Secular and periodic.	Secular and periodic.
Mean anomaly, M	Short-periodic variations due to J_2 at periods of T and T/3. Long-periodic variations due to odd zonal harmonics J_{2n+1}. Secular change due to even zonal harmonics J_{2n} and central attraction term.	Periodic change due to density and Earth rotation	Secular and periodic.	Secular and periodic.

Table 4-8. Summary of perturbation effects from Klinkrad [2006] and Vallado [2007].

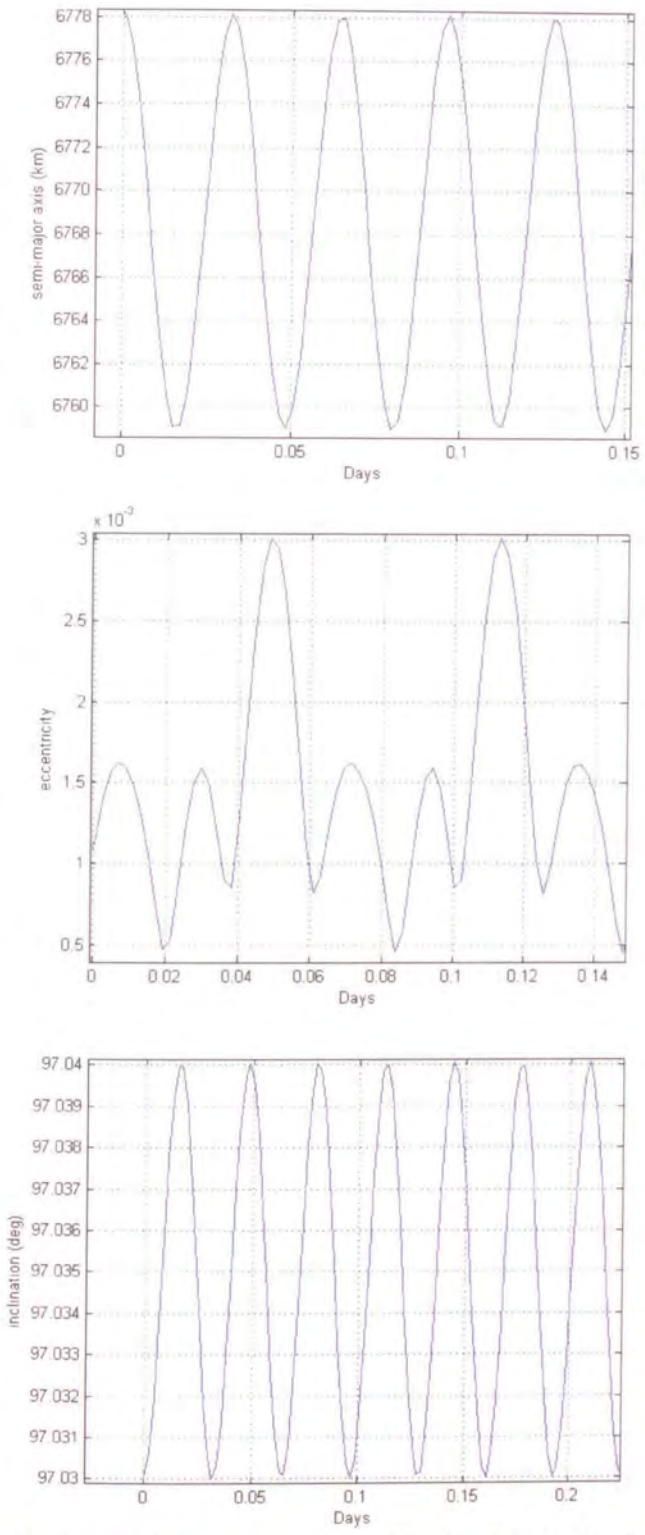

Figure 4-18. Semi-major axis, eccentricity and inclination behaviour under J_2 effect only, for the first couple of orbits.

These show that the results of the simulation model are in line with the theory (Table 4-8).

4.5.2.2 Validation against STK

The modelled perturbations have been individually compared to those simulated by the industry-standard STK with its High Precision Orbit Propagator (HPOP) as a way to validate the MATLAB/Simulink model.

The J_2 model is shown to accurately replicate the results obtained by STK (Figure 4-19). The atmospheric drag force is somewhat different (Figure 4-20) due to inevitable differences in the atmospheric model itself: under drag force alone, the difference in semi-major axis is only 8 km over a period of 120 days, with the initial conditions shown in Table 4-9.

Semi-major axis, a	6728.136 km
Eccentricity, e	0.0011
Inclination, i	96.849 deg
Right ascension of the ascending node, Ω	90 deg
Argument of perigee, ω	90 deg
True anomaly, ν	-90 deg
$F_{10.7}$ index	150
Ballistic coefficient, BC (A/m, Cd)	100 (0.01, 1)

Table 4-9. Initial conditions for the validation of the drag model against STK.

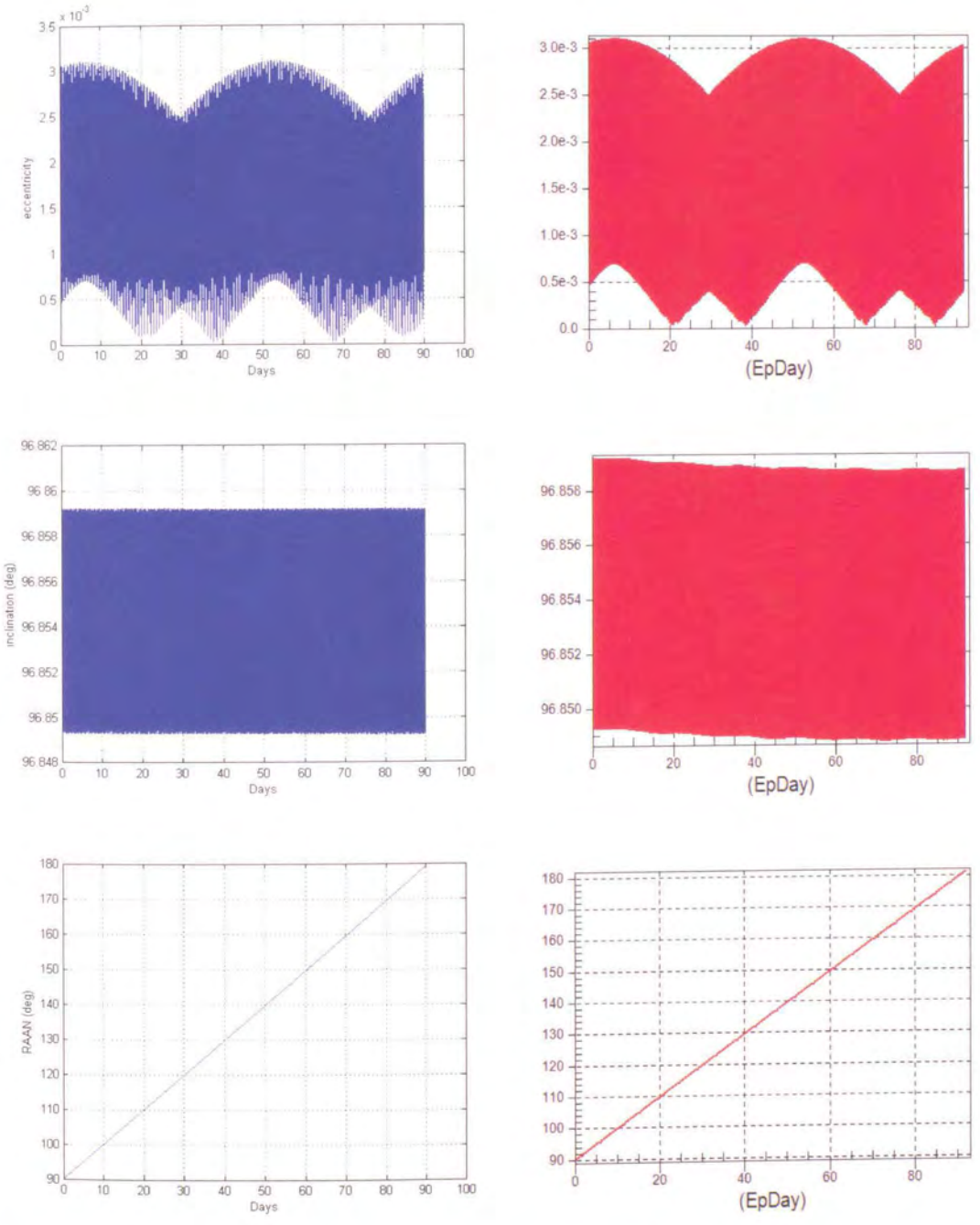

Figure 4-19. Examples of COEs under J2 only, for the developed model (left) and STK simulation (right).

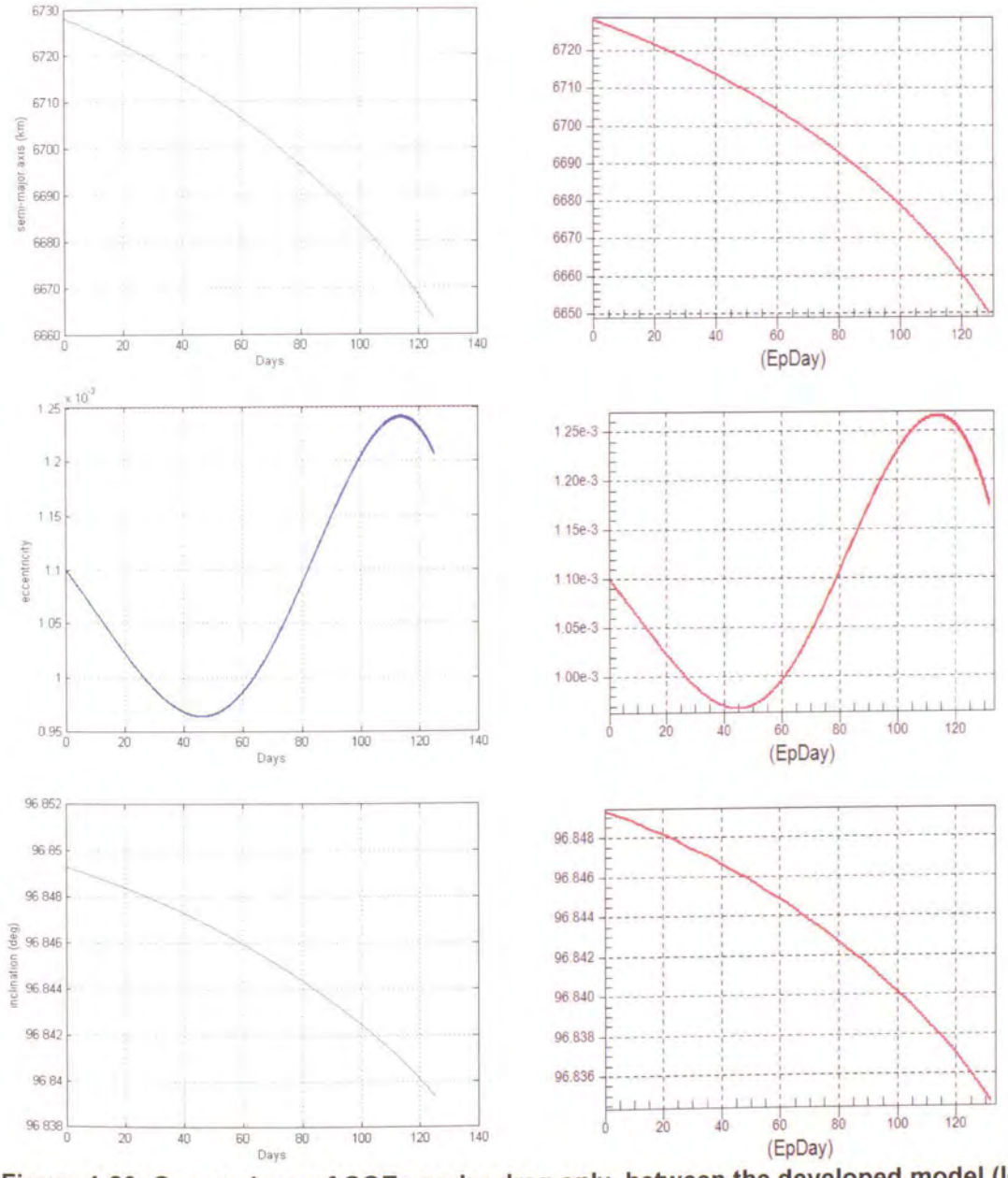

Figure 4-20. Comparison of COEs under drag only, between the developed model (left) and STK (right).

4.5.3 Solar activity and atmospheric density

The atmospheric density varies with the solar activity. Two simulation time intervals are chosen to represent the extremes of the solar activity cycle, as represented in Figure 4-21. Note that the reference epoch for the computation of the F10.7 index is the 1st of January 1981. The simulation starts at the spring equinox, since this is the reference date to compute the sun's position. The two simulation time intervals are given in Table 4-10 and shown graphically in Figure 4-21.

	Start date	Duration
Solar minimum	Spring equinox 2004	3.25 years
Solar maximum	Spring equinox 2009	3.25 years

Table 4-10. Simulations start date.

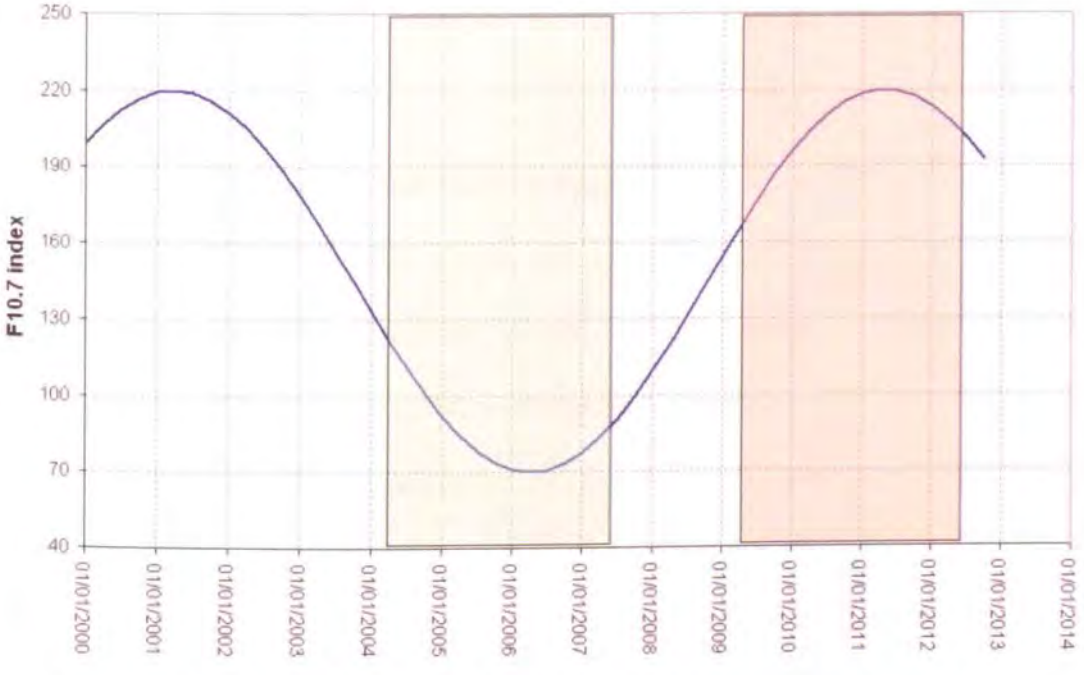

Figure 4-21. F10.7-cm flux theoretical curve, and simulation periods.

4.5.4 Simulation cases and initial conditions

In addition to the two epochs and corresponding solar activities just discussed, the simulation cases cover four values of ballistic coefficient and four altitudes as initial conditions. These are summarised in Table 4-11. Thus, a total of 32 simulations have been run.

Solar activity	Altitudes	Ballistic coefficients
Peak / minimum	260, 290, 320, 350 km	60, 90, 130, 180 kg/m^2

Table 4-11. Trajectory simulation cases.

4.6 Results

By keeping the ballistic coefficient to a fixed value, the mass variation due to the propellant utilisation is not taken into account. Smaller ballistic coefficients with small cross-section areas are more affected by mass change. This must be kept in mind when using the results presented here.

4.6.1 Propulsive acceleration required

The thrust profiles are presented for the two extreme cases of maximum density and minimum ballistic coefficient (Figure 4-22) and minimum density with maximum ballistic coefficient (Figure 4-23). A factor of 100 separates the two cases.

Figure 4-24 compares the maximum thrust value for a range of altitude and ballistic coefficients during a period of maximum solar activity. The maximum thrust is inversely proportional to the ballistic coefficient, which can be expected from Equation (4-51).

Figure 4-25 presents the same plots during minimum solar activity.

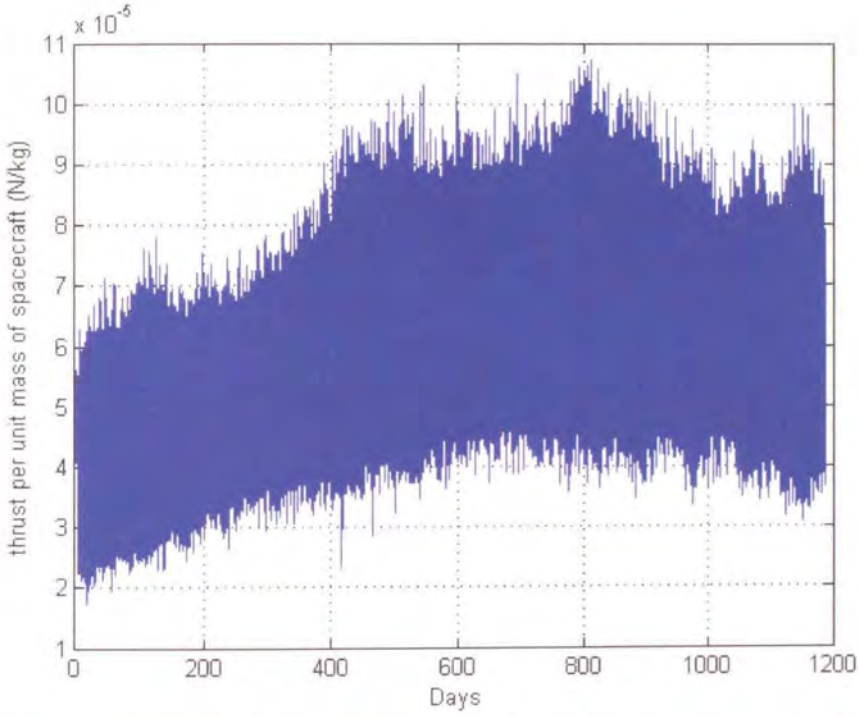

Figure 4-22. Thrust profile for BC = 60 kg/m^2, h = 260 km and peak solar activity

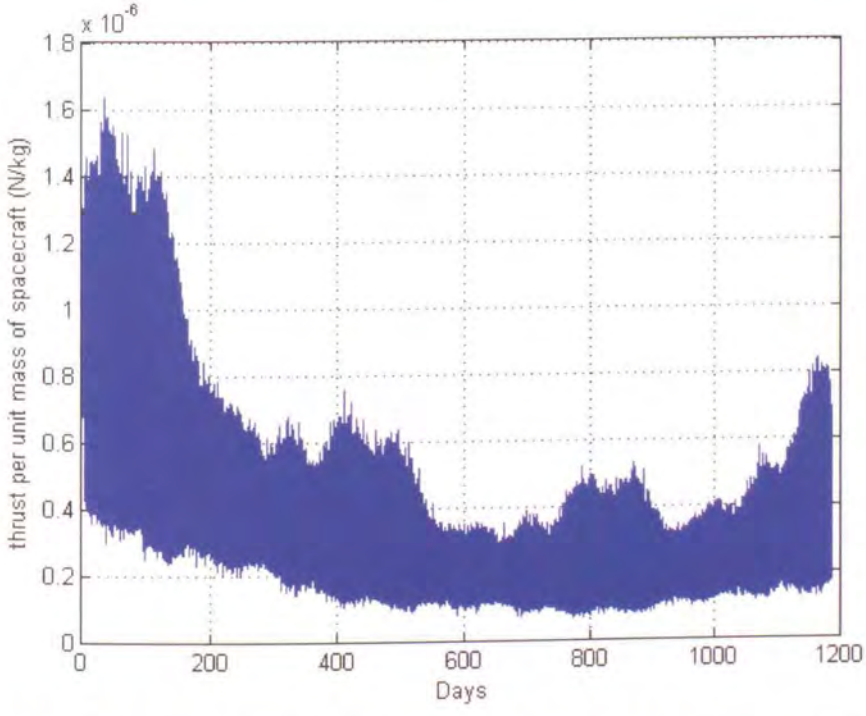

Figure 4-23. Thrust profile for BC = 180 kg/m^2, h = 350 km and minimum solar activity

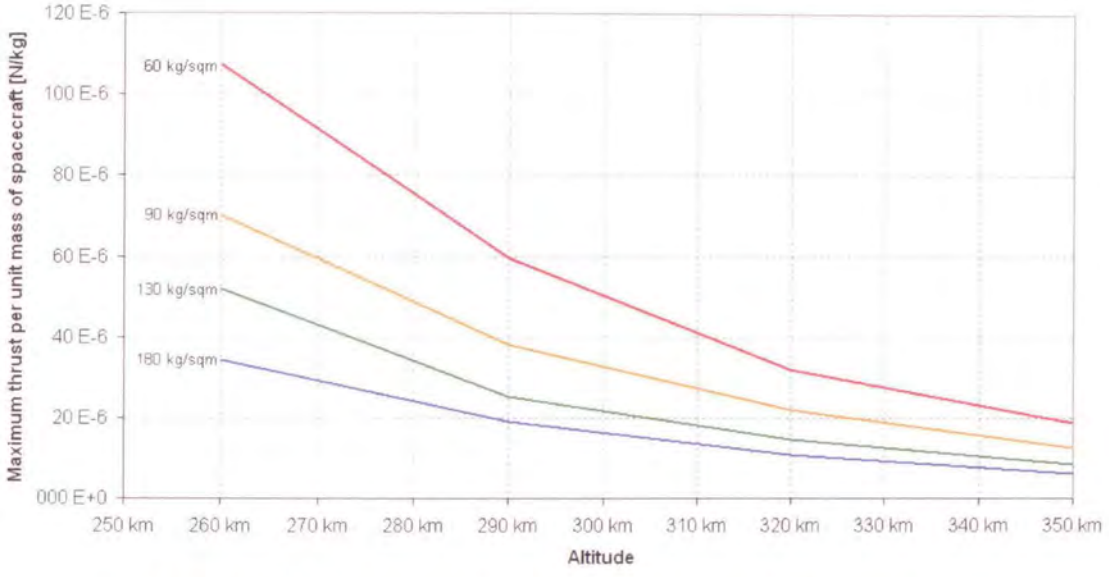

Figure 4-24. Maximum thrust level during peak solar activity.

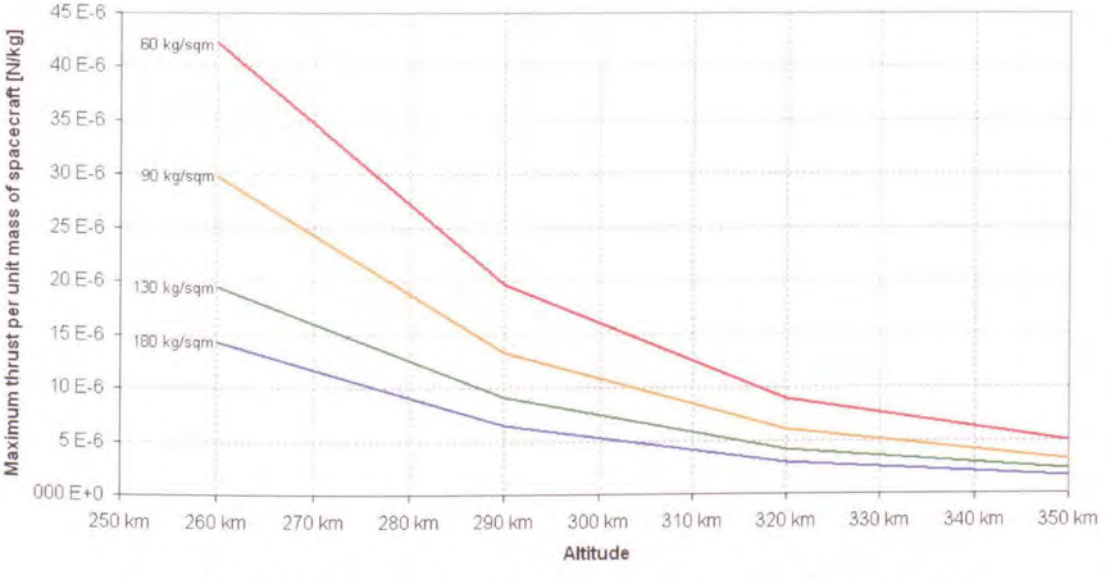

Figure 4-25. Maximum thrust level during minimum solar activity.

4.6.2 Total impulse

Figure 4-26 and Figure 4-27 represent the impulse per unit spacecraft mass as a function of altitude and ballistic coefficient, during peak and minimum solar activity, respectively. The total impulse increases exponentially with lower altitudes, due to the exponential increase in density. As with the thrust, the impulse is linear with the inverse of the ballistic coefficient at a given altitude.

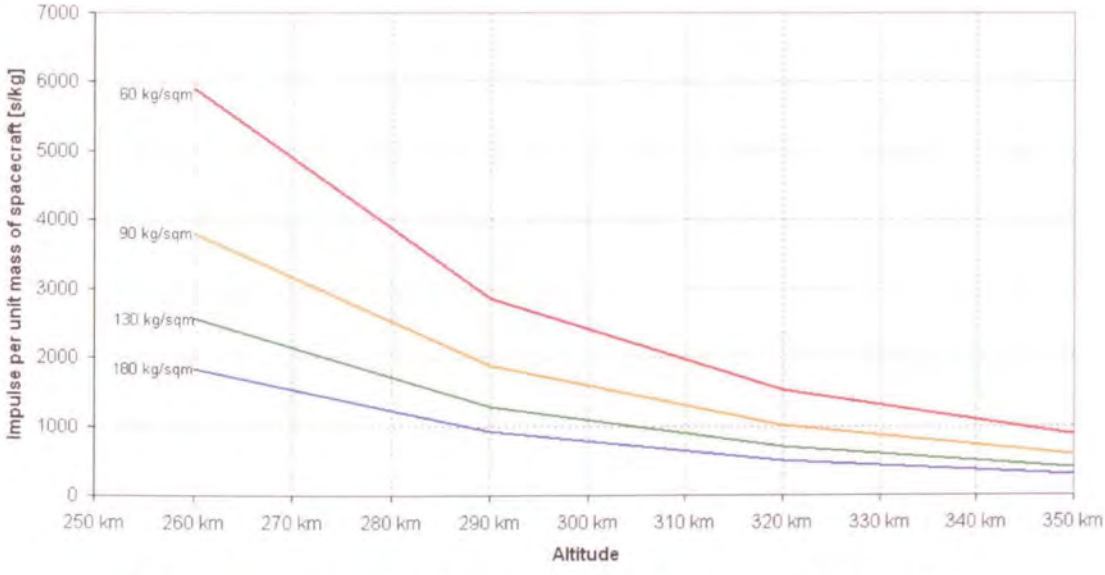

Figure 4-26. Total impulse for a mission during peak solar activity.

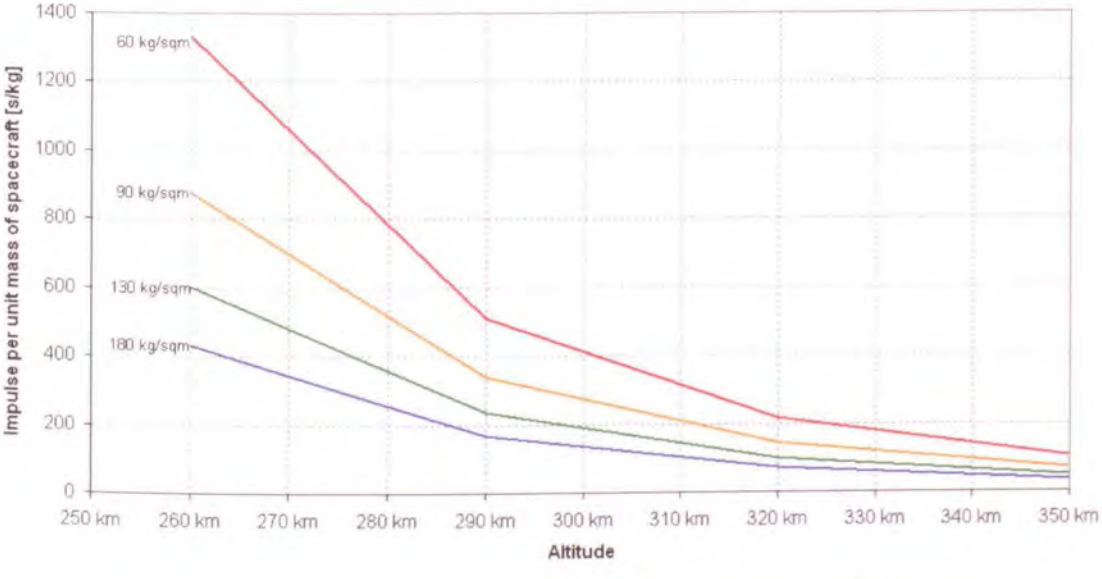

Figure 4-27. Total impulse for a mission during minimum solar activity.

4.7 Conclusion

In order to derive the propulsion requirements to maintain the spacecraft in a low altitude orbit, a trajectory model has been developed. The models include the main perturbation forces: atmospheric drag, geopotential, third-body perturbation and solar radiation pressure.

The model uses the VOP technique, working with osculating orbital elements, and thus displays the associated short-periodic variations. This has been validated against the STK-HPOP propagator.

The propulsive force is modelled as a continuous, low-thrust variable, compensating the atmospheric drag. In practice, the propulsion system would consist of a set of accelerometers as sensors, and thrusters on a gimbal mechanism as actuators. Each subsystem would include some errors, and an overall random error has been included in the thrust model to account for these.

The model can now be used to derive the requirements of the propulsion system for each of the four spacecraft concepts, from which a suitable propulsion system can be identified. This is the subject of Chapter 5.

Chapter 5

Electric Propulsion for Low-Earth Orbits

5.1 Introduction

Electric Propulsion (EP) seems to be a fairly recent technology, but the concept was studied by Robert Goddard, back in 1906 [Choueri, 2004]; and experimental ion thrusters were used in orbit in the early 1960s by both the USA and USSR [Goebel & Katz, 2008].

Electric propulsion has been proposed and/or implemented for a wide range of applications, such as interstellar missions, interplanetary and asteroid/comet rendezvous, station keeping of geostationary satellites [Monheiser, 1994] and orbit raising and transfer missions, again mostly to geostationary altitudes [Martin et al, 2000].

Another class of missions that can greatly benefit from electric propulsion is to be found in low-earth orbits to compensate for the atmospheric drag. This has been suggested for orbit maintenance of space stations [Martin & Cresdee, 1987] but most interestingly for the investigation of the Earth gravity field, where the electric propulsion system provides a "drag-free" environment where external disturbances are continuously cancelled [Marchetti et al, 2006]. Such recent missions include NASA's GRACE mission [Marchetti et al, 2006] or ESA's GOCE mission [Bassner et al, 2000]; although the concept of drag-free satellite dates

back to the 1960's [Fleck & Starin, 2003]. Fearn & Rijm [2002] also suggest this method for high-resolution imagery. A study by QinetiQ for ESA has investigated the application of electric propulsion to remote sensing missions [Price et al, 2005].

This chapter describes the key characteristics against which the performance of a propulsion system is measured (section 5.2). The results of the orbit simulation results are then presented together with the propulsion requirements that can be derived (section 5.3). This is followed by a review of EP technologies (section 5.4) leading to a trade-off and selection of a propulsion baseline 5.5). After a review of the electric propulsion system on GOCE (section 5.6) and aspects of thruster durability (section 5.7), the propulsion system for drag compensation of a lidar mission is presented (section 5.8).

5.2 Key Characteristics of a Propulsion System

There are a few parameters that help compare the performance of propulsion systems and enable us to select one.

The total impulse, I, is defined as a change in momentum caused by a force F_T over time [Brown, 2002]:

$$I = \int F_T \cdot dt \tag{5-1}$$

It is also the product of the total mass of propellant m_p used by the thruster and the exhaust velocity V_e which the propellant is accelerated to by the thruster.

$$I = m_p \cdot V_e \tag{5-2}$$

The specific impulse I_{SP} is another characteristic of thrusters and is a measure of the velocity of the expelled propellant:

$$I_{sp} = \frac{V_e}{g_0} \tag{5-3}$$

with g_0 the mean gravitational acceleration of the Earth at sea level.

Thus, Equation (5-2) can be rewritten as:

$$I = m_p \cdot I_{sp} \cdot g_0 \tag{5-4}$$

Hence, if the total impulse over a mission lifetime and the mean specific impulse of a thruster are known, then the propellant mass can be found by re-arranging Equation (5-4). It follows that the amount of propellant needed is inversely proportional to the specific impulse.

Thrusters are mechanical parts that eventually fail and they can only handle a certain amount of propellant over their lifetime. From Equation (5-4), it can be seen that the total impulse is effectively a measurement of this lifetime and thrusters are characterised by a maximum guaranteed total impulse.

The selection of a particular propulsion technology over another will thus be determined by whether a thruster (or a cluster of thrusters) can deliver the thrust level required to compensate for the atmospheric drag, the amount of propellant it requires to complete the mission, and the thruster lifetime in the form of its total impulse.

In addition, the aim is to reduce the power of the lidar instrument but not necessarily that of the overall satellite. At this stage, there is no firm requirement on the maximum electrical power of the propulsion system; this will be introduced in section 5.5.2.

5.3 Propulsion Requirements

Four lidar mission concepts are being assessed, with a telescope aperture diameter ranging from 1.15 to 3.5 m. The smaller two can be mounted at the front of the platform, thus reducing the cross-section area, while the larger ones are nadir-mounted.

The propulsion requirements of each concept are presented in the following sections.

5.3.1 Concept 1

The first concept is the front-mounted instrument with a primary mirror of 1150 mm in diameter. Its physical characteristics, presented in Chapter 3, are summarised in Table 5-1. The case is driven by the lower ballistic coefficient of ~123 kg/m^2.

Specific propulsion requirements can be derived from the simulation results of Chapter 4. These are shown in Table 5-2 for the case of peak solar activity.

Parameter	Value
Total (C_DA)	8.12 m^2
Mass range	1000 – 1500 kg
Ballistic coefficient range	123 – 185 kg/m^2

Table 5-1. Aerodynamic characteristics of the 1150 mm front-mounted lidar

Altitude	260 km	290 km	320 km	350 km
Maximum thrust [mN]	50.5	28.0	16.0	9.1
Total impulse [s]	2.72×10^6	1.36×10^6	0.73×10^6	0.42×10^6

Table 5-2. Propulsion requirements of Concept 1 for peak solar activity

5.3.2 Concept 2

Concept 2 is the 1800 mm telescope mounted on the front wall of the satellite, and a ballistic coefficient of 90 kg/m^2 is representative of the worst case (Table 5-3). Table 5-4 summarises the requirements for the propulsion system.

Parameter	Value
Total (C_DA)	15.21 m^2
Mass range	1400 – 2000 kg
Ballistic coefficient range	92 – 131 kg/m^2

Table 5-3. Aerodynamic characteristics of the 1800 mm front-mounted lidar

Altitude	260 km	290 km	320 km	350 km
Maximum thrust [mN]	95.9	52.3	30.3	17.2
Total impulse [s]	5.21×10^6	2.57×10^6	1.38×10^6	0.79×10^6

Table 5-4. Propulsion requirements of Concept 2 for peak solar activity

5.3.3 Concept 3

Concept 3 is the nadir-mounted, 3 m diameter instrument. A ballistic coefficient of about 60 kg/m^2 is considered to be the worst-case (Table 5-5). The corresponding propulsion requirements are shown in Table 5-6.

Parameter	Value
Total (C_DA)	36.68 m^2
Mass range	2000 – 3000 kg
Ballistic coefficient range	55 – 82 kg/m^2

Table 5-5. Aerodynamic characteristics of the 3000 mm nadir-mounted lidar

Altitude	260 km	290 km	320 km	350 km
Maximum thrust [mN]	236.2	131.3	70.1	41.2
Total impulse [s]	13.0×10^6	6.28×10^6	3.35×10^6	1.92×10^6

Table 5-6. Propulsion requirements of Concept 3 for peak solar activity

5.3.4 Concept 4

Concept 4 is the largest telescope (3.5 m in diameter) mounted on the nadir face. Table 5-7 summarises its aerodynamic properties, and Table 5-8 gives its propulsion requirements.

Telescope diameter	35000 mm
Total (C_DA)	45.02 m^2
Mass range	2500 – 3500 kg
Ballistic coefficient range	56 – 78 kg/m^2

Table 5-7. Aerodynamic characteristics of the 3500 mm nadir-mounted lidar

Altitude	260 km	290 km	320 km	350 km
Maximum thrust [mN]	289.9	161.1	86.0	50.5
Total impulse [s]	16.0×10^6	7.71×10^6	4.11×10^6	2.36×10^6

Table 5-8. Propulsion requirements of Concept 4 for peak solar activity

5.4 Types of Electric Propulsion

There are different types of electric propulsion, varying in their physical principles and performances. A brief overview of these propulsion techniques (namely, electrothermal, electrostatic and electromagnetic) is given in the sections below; followed by a summary of typical performances. This provides the basis for a trade-off and baseline selection for each of the four lidar mission lidar concepts.

5.4.1 Electrothermal

Of all electric propulsion systems, electrothermal is the one that is closest to conventional rocket propulsion.

The resistojet uses a resistor to heat up the propellant before it passes through a nozzle. Like chemical propulsion, an increase in temperature is synonymous with an increase in pressure, resulting in a higher exhaust velocity [Goebel & Katz, 2008]. Since the specific impulse is directly related to the exhaust velocity by the gravitational acceleration constant at sea level, g_0, it is not surprising that resistojets typically achieve specific impulses similar to bipropellant rockets, i.e. in the order of 300 seconds. Typical thrust level of past and present resistojets is in the order of 0.1 to 1 N.

Arcjets are another form of electrothermal thrusters; in this case, the propellant is heated up by a high current arc. This technique heats the propellant to even higher temperatures, and an I_{SP} in the order of 400 to 600 seconds can typically be achieved [Turner, 2000]. The thrust produced by arcjets is usually in the order of 0.1 to 0.3 N.

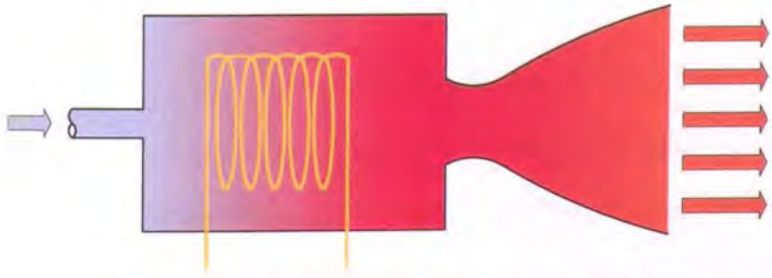

Figure 5-1. Schematic view of a resistojet

5.4.2 Electrostatic

Electrostatic propulsion is probably the most popular technique of all electric propulsion systems. They rely on the acceleration of ions by an electrostatic field. Electrostatic thrusters can be divided into three sub-categories.

Ion thrusters, or Gridded Ion Engine (GIE) – and also previously known as Kaufman-type thrusters, after Dr Harold Kaufman who pioneered this field – work on the extraction and acceleration of ions from a cold plasma through a set of electrostatic grids.

There are mainly two different techniques to ionise the propellant: electron bombardment and radiofrequency. Ion thrusters can typically operate at a range of thrust from the mN to hundreds of mN, with high specific impulses (usually 2000 to more than 3000 seconds) and higher efficiency (approximately 60 to 80%) than other thrusters [Goebel & Katz, 2008].

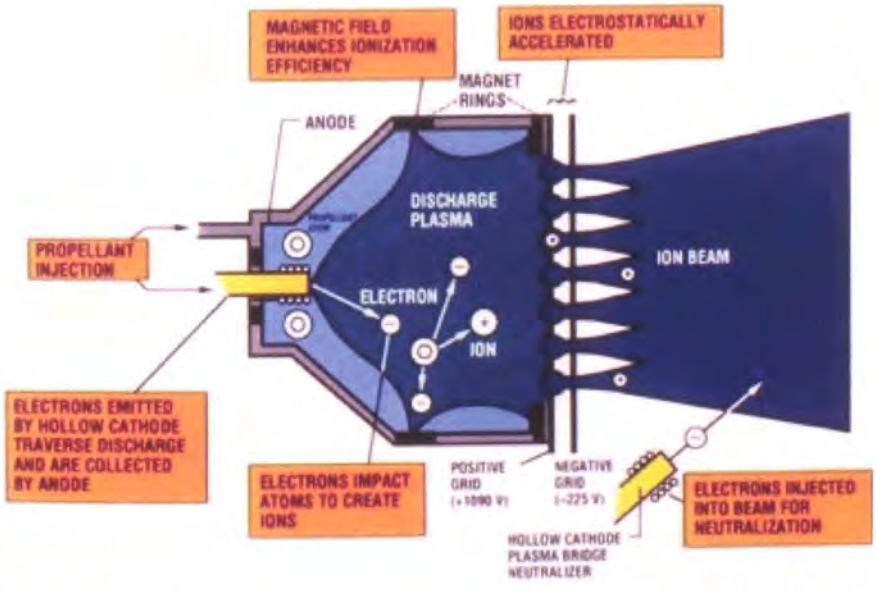

Figure 5-2. Operation principle of a Gridded Ion Engine [NASA, 2008]

Hall-Effect Thrusters (HET) – also known as Stationary Plasma Thrusters (SPT) – accelerate ions by means of an axial electric field. However, their operation relies on a magnetic field which constrains the path of electrons, preventing them from reaching the anode where the gas is fed in. The electrons are thus forced to rotate around the thruster axis, forming the

Hall current ($\vec{E} \times \vec{B}$) [Goebel & Katz, 2008]. The electrons ionise the gas by bombardment creating ions which are accelerated by the electric field that exists between the anode and the plasma (which has the potential of the cathode). The operation lifetime is shorter than ion thrusters, but the thrust level and propellant mass flow rate are greater, while the total impulse capabilities of each type are of the same order [Goebel & Katz, 2008]. The thrust level is usually in the hundreds of milliNewtons, although scaled-down versions can deliver 10 mN; for a smaller power than GIEs.

Field Emission Electric Propulsion (FEEP) are small devices that produce very low thrust levels (a fraction of a milliNewton) and are thus suitable only for attitude control of high accuracy.

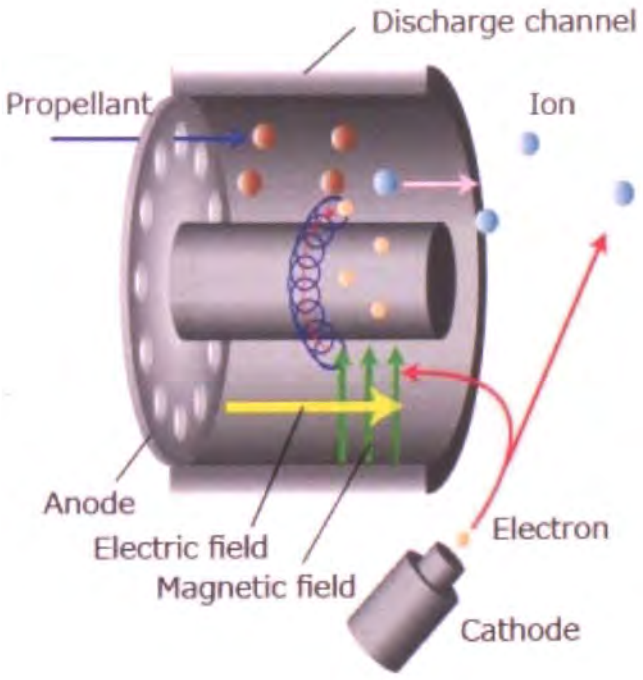

Figure 5-3. Operation principle of a HET [Arakawa & Komurasaki Lab., 2007]

5.4.3 Electromagnetic

Two types of thrusters in particular fall under this category: Pulsed Plasma Thrusters (PPTs) and Magnetoplasmadynamic (MPD) thrusters.

In a PPT, some solid propellant is ablated and ionised by a pulsed discharge and the ions are accelerated electromagnetically [NASA, 2004a]. The thrust level is determined by the pulse repetition rate; existing PPTs operating at 1 Hz generate in the order of 0.1 to 1mN of thrust for less than 100 W.

MPD thrusters operate on very high power (100 kW to 1MW) but can deliver both high thrust (hundreds of Newtons) and very high specific impulses (into the 10,000 s). The plasma is accelerated by the Lorentz force, which results from the interaction of the electric current between the anode and the cathode and the magnetic field which itself is induced by the electric current [NASA, 2004b]. Clearly, MPD thrusters will be advantageous on very large, power-rich space vehicles.

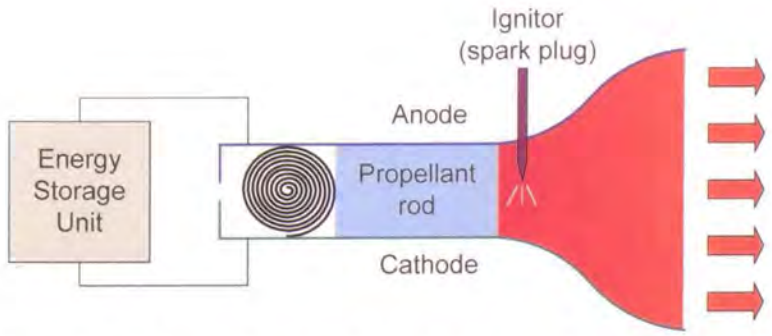

Figure 5-4. Schematic view of a Pulsed Plasma Thruster (PPT)

5.4.4 Summary of EP characteristics

Table 5-9 is a summary of the typical characteristics of the electric propulsion systems discussed above. Figure 5-5 represents various thrusters that have been developed, tested and/or flown.

EP Type	Thrust	Specific Impulse [s]	Specific Power [W/mN]
Resistojet	0.1 - 1 N	70 - 800	0.1 - 5
Arcjet	0.1 - 0.3 N	250 - 600	5 - 10
GIT	1 - 250 mN	2000 - 6000	25 - 40
HET	10 - 300 mN	1000 - 2000	15 - 20
FEEP	0.001 - 1 mN	4000 - 8000	150 - 200
PPT (1 Hz)	0.1 - 1 mN	800 - 1500	50 - 100
MPD	5 - 200 N	1000 - 8000	40 - 100

Table 5-9. Typical performance characteristics of some electric propulsion systems.

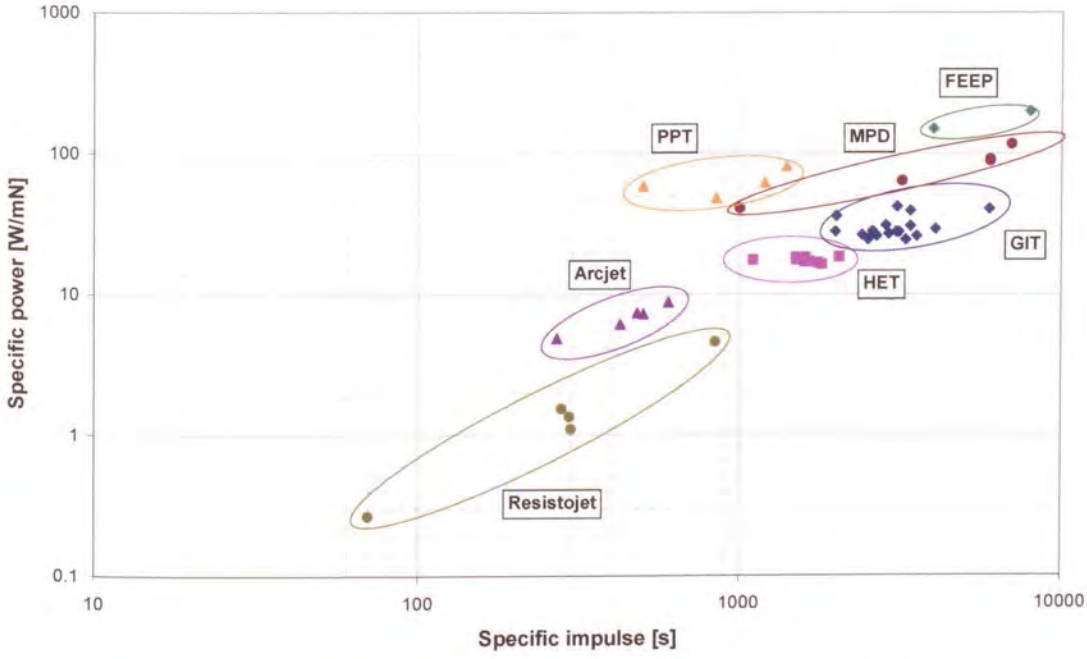

Figure 5-5. Specific power vs. specific impulse for various electric propulsion systems.

A high specific impulse with low specific power (bottom-right area of the graph) is preferable.

5.5 Trade-off for Atmospheric Drag Compensation

5.5.1 Unsuitable options

It is possible to eliminate some electric propulsion systems based on their thrust level and specific power.

From Table 5-9, it can be seen that FEEPs have too low a thrust level requiring many dozens of them as a minimum. Besides their power consumption would be prohibitive. The other extreme on the thrust scale is the MPD which has far too high a thrust. Coupled with a high specific power, their power consumption would also be excessive.

5.5.2 Trade-off criteria

The fraction of propellant mass to the spacecraft mass shall be less than 10%, based on recent operational missions, with an absolute threshold of 15% deemed acceptable here. Also a larger fraction would result in large variations in inertia, which would make it particularly difficult for the AOCS design and pointing performance.

The power consumption of the electric propulsion system must also remain reasonable, although this can be somewhat subjective. Based on recent missions, a mass fraction of 5-8% of the satellite mass is typical for operational missions, with a specific power of 38 W per kilogram of solar array. Here, we will assume 5% of the mass fraction is dedicated to the portion of solar arrays used for providing power to the propulsion system, with the rest providing power to the platform and instrument. This is not a stringent limit and can be broken if marginal.

5.5.3 Trade-off for Concept 1

For concept 1, the propulsion power would be limited to about 1400 W.

Looking at the propellant mass fraction in Figure 5-6, The HET and GIT meet the requirement for an altitude above 280 km. The arcjet and resistojet are unsuitable, while a

PPT could be considered above 310 km. From a power perspective, all options are satisfactory, with PPT only suitable above 290 km.

Thus Concept 1 is feasible from an altitude of about 290 km, with GIT or HET preferred over the PPT because of both propellant mass and power.

Figure 5-7 shows the thrust profile experienced by Concept 1 at an altitude of 290 km. The thrust ranges from about 4 to 29 mN during peak solar activity, and 0.5 to 10 mN during solar minimum.

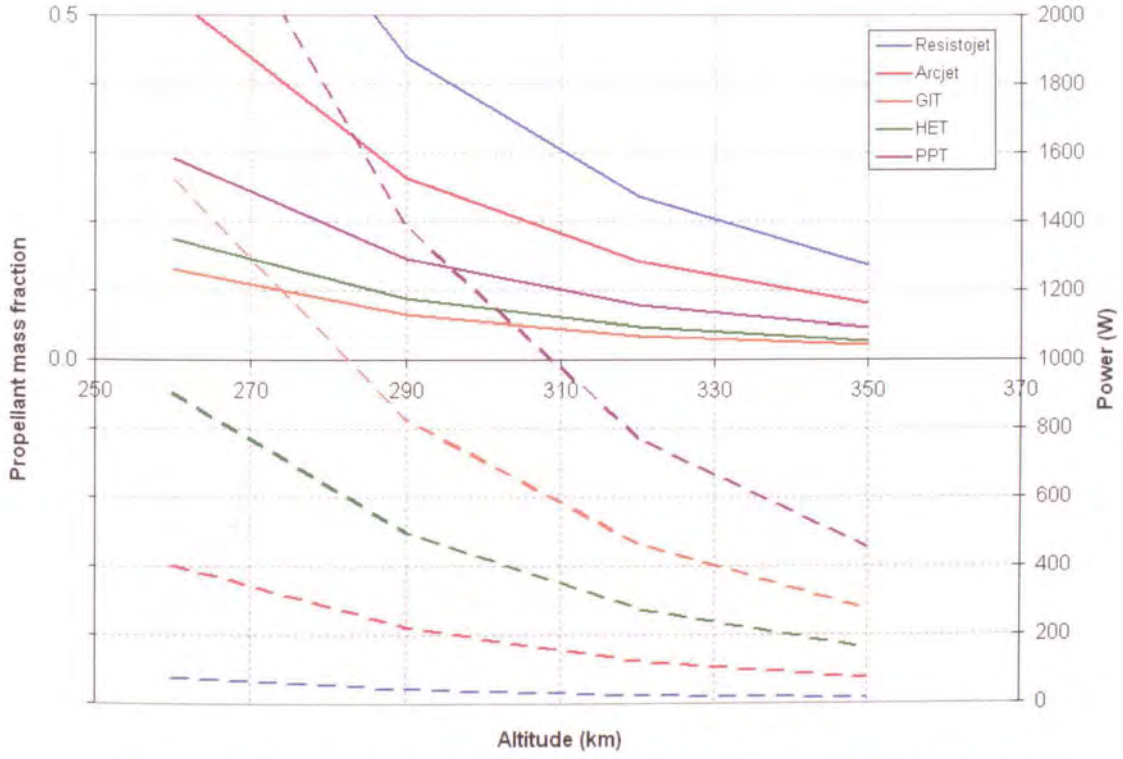

Figure 5-6. Propellant mass fraction (continuous) and power (dashed) of propulsion systems for Concept 1

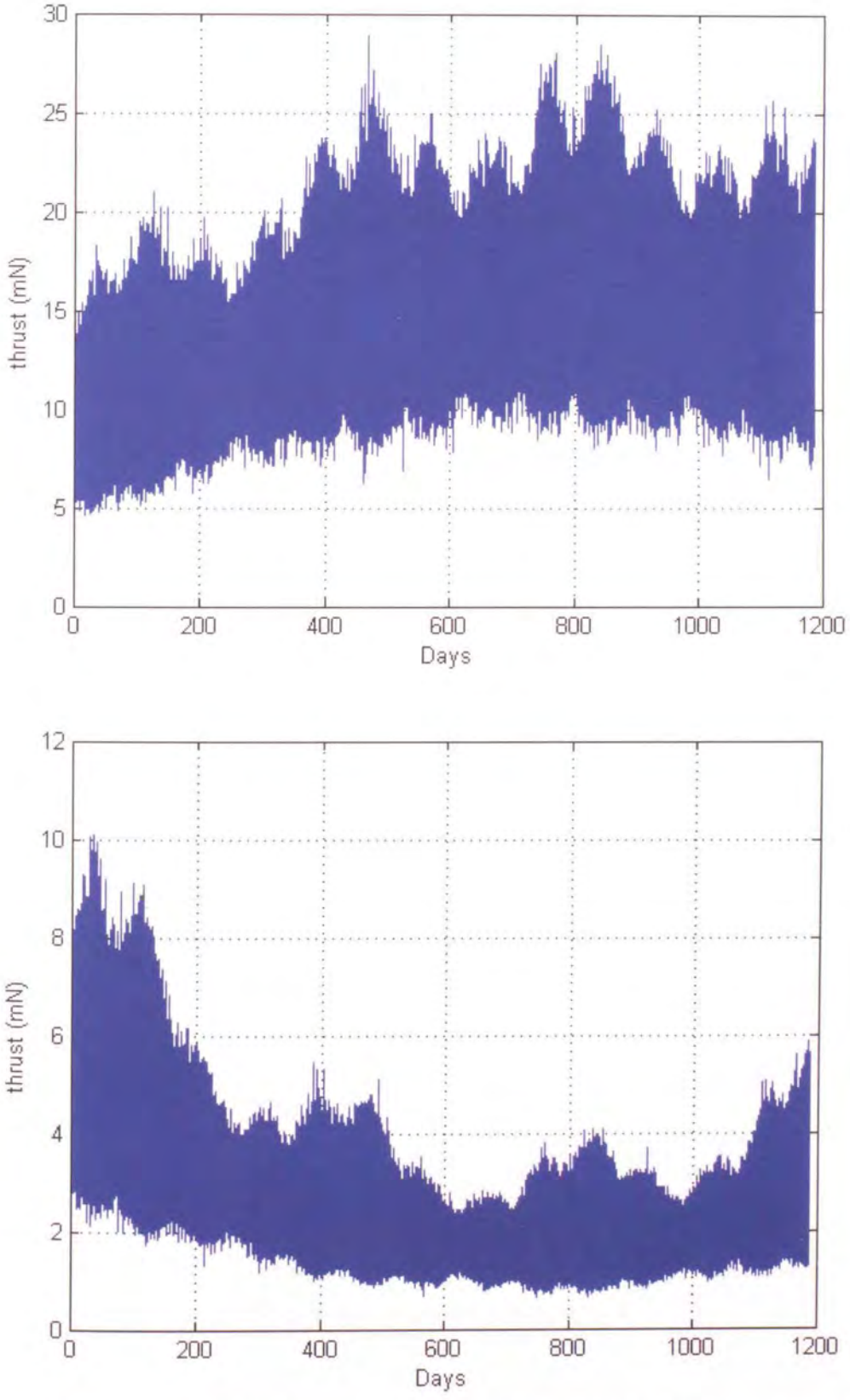

Figure 5-7. Thrust profile for Concept 1, during peak (top) and minimum solar activity.

5.5.4 Trade-off for Concept 2

For concept 2, the power limit is about 1700 W, with all options except PPT compatible above 290 km (Figure 5-8). However, only the GIT and the HET could meet the propellant mass restriction.

The conclusion for concept 2 is therefore similar to concept 1, i.e. using a GIT or HET above 290 km.

Figure 5-9 shows the thrust profile experienced by Concept 2 at an altitude of 290 km. The thrust ranges from about 8 to 54 mN during peak solar activity, and 1 to 20 mN during solar minimum.

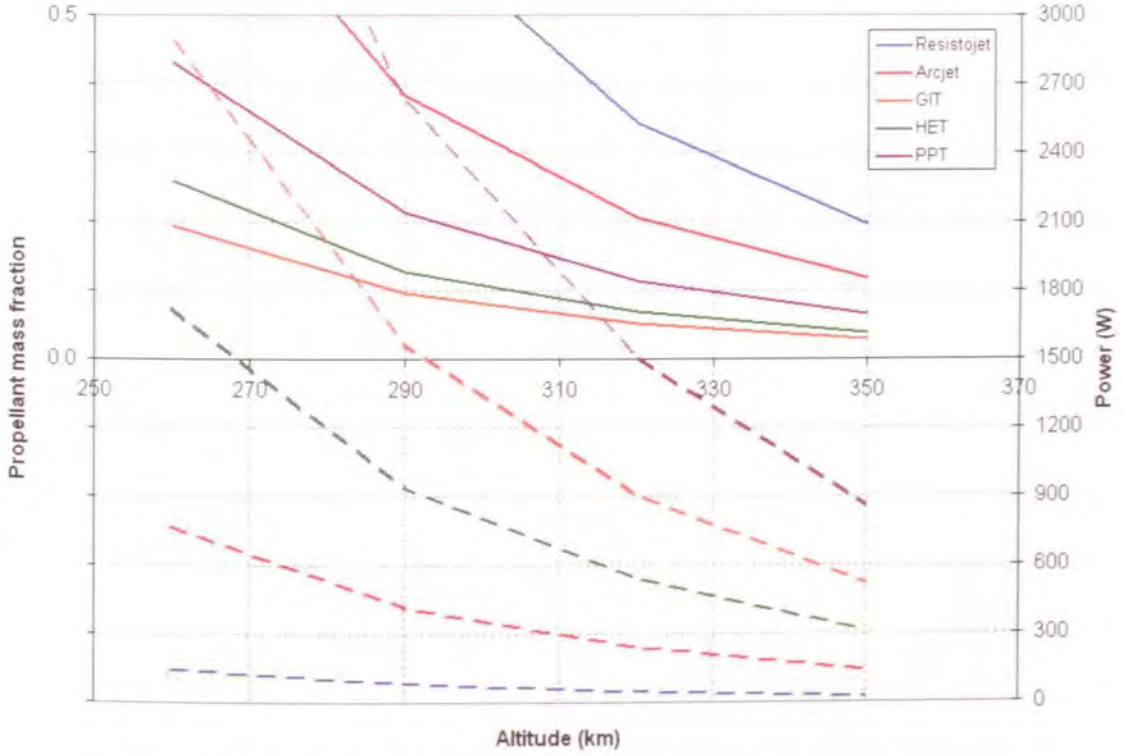

Figure 5-8. Propellant mass fraction (continuous) and power (dashed) of propulsion systems for Concept 2

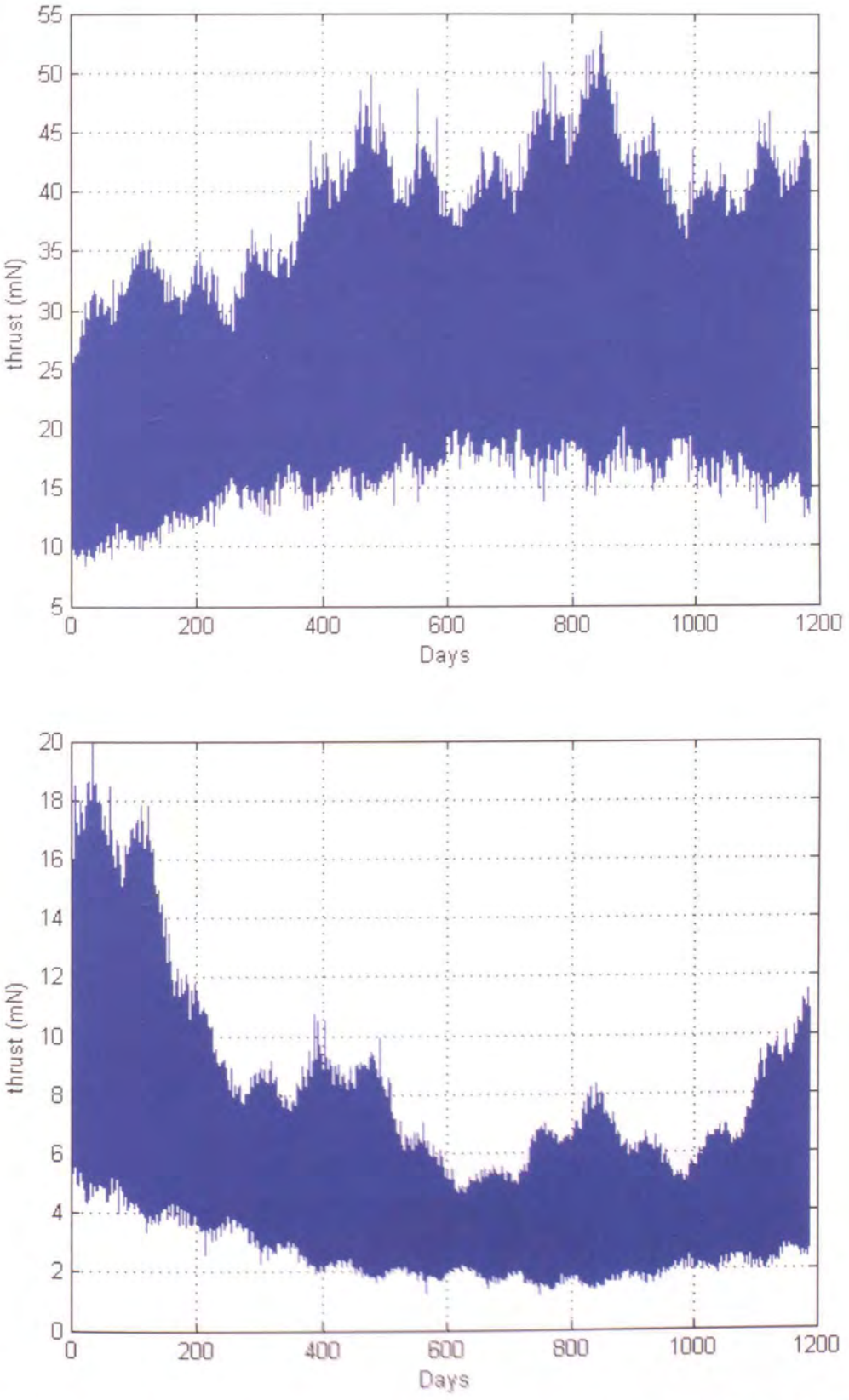

Figure 5-9. Thrust profile for Concept 2, during peak (top) and minimum solar activity.

5.5.5 Trade-off for Concept 3

The power limit of Concept 3 would be around 2.7 kW. Concept 3 is only feasible at an altitude of at least 310 km, with GIT or HET (Figure 5-10). PPT could be considered at an altitude of 350 km but due to higher power and propellant mass, GIT and HET are better options.

Figure 5-11 shows the thrust profile experienced by Concept 3 at an altitude of 320 km. The thrust ranges from about 9 to 65 mN during peak solar activity, and 1 to 18 mN during solar minimum.

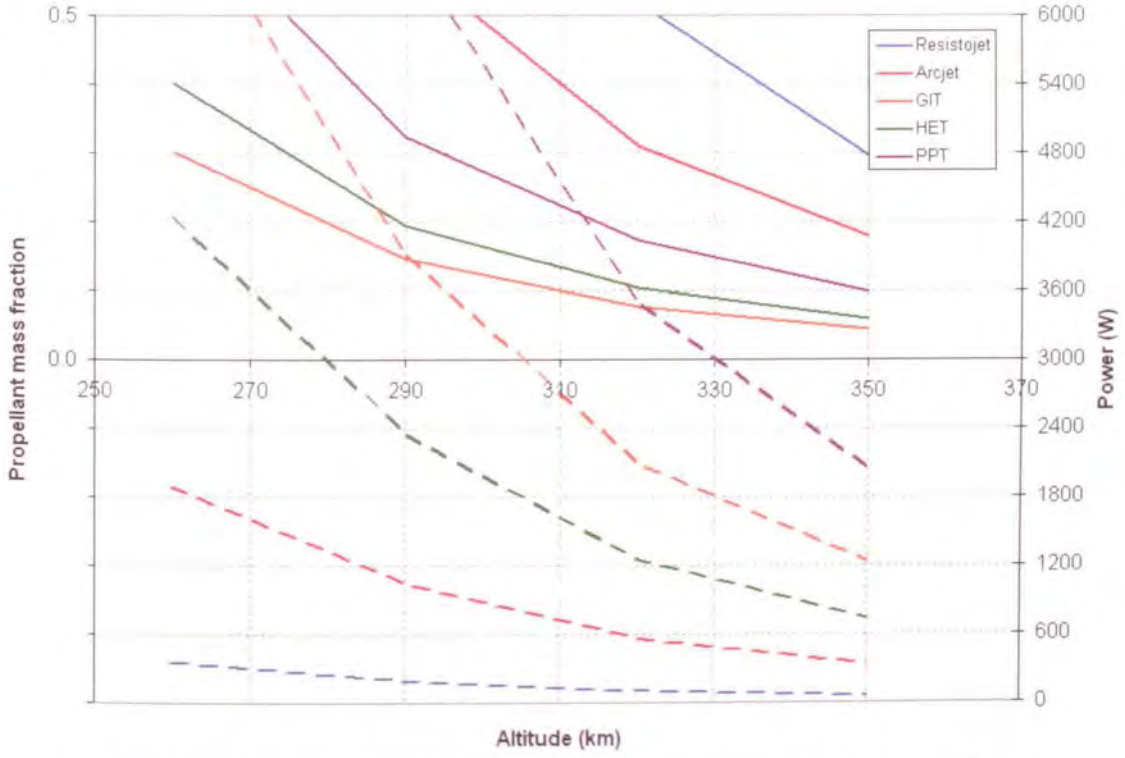

Figure 5-10. Propellant mass fraction (continuous) and power (dashed) of propulsion systems for Concept 3

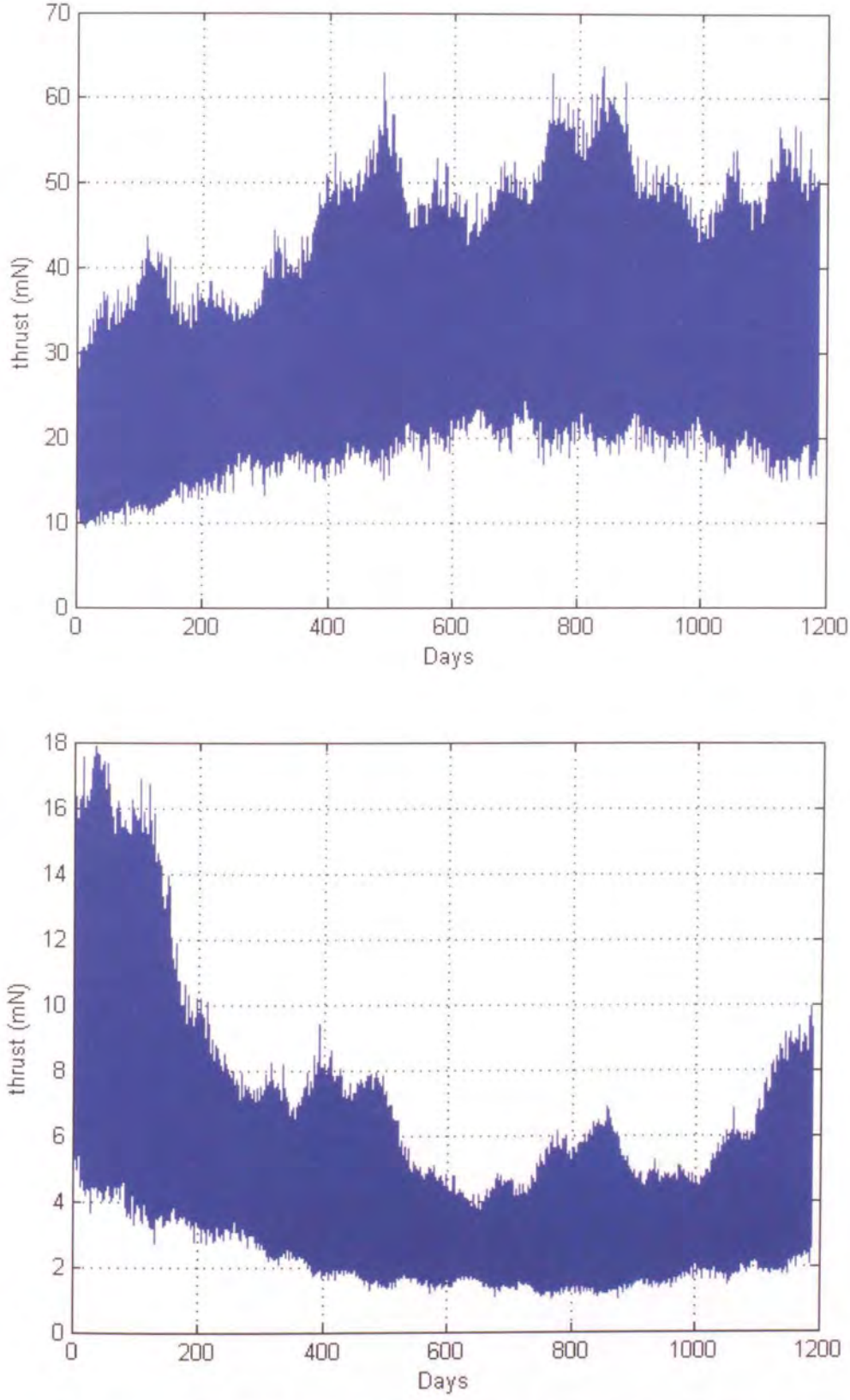

Figure 5-11. Thrust profile for Concept 3 during peak (top) and minimum solar activity.

5.5.6 Trade-off for Concept 4

For Concept 4, the power limit is set to about 3.5 kW. The conclusion is the same as for the Concept 3, i.e. that only GIT and HET are suitable candidates from an altitude of 320 km.

Figure 5-13 shows the thrust profile experienced by Concept 4 at an altitude of 320 km. The thrust ranges from about 11 to 80 mN during peak solar activity, and 2 to 22 mN during solar minimum.

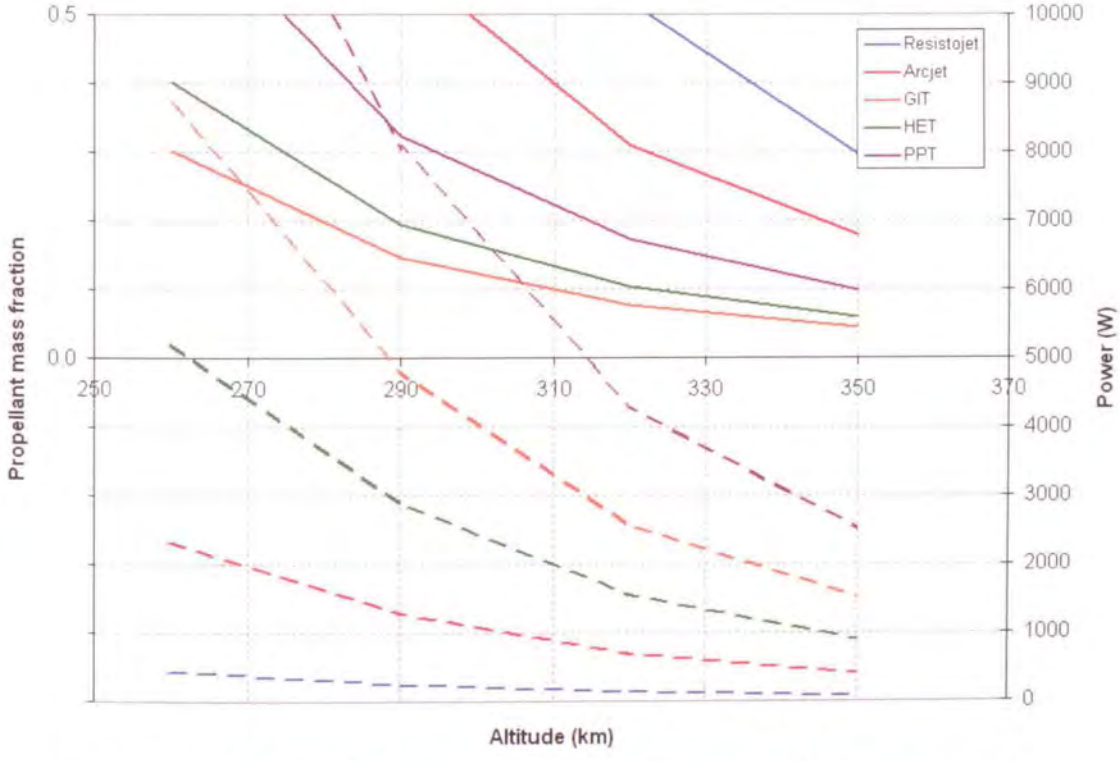

Figure 5-12. Propellant mass fraction (continuous) and power (dashed) of propulsion systems for Concept 4

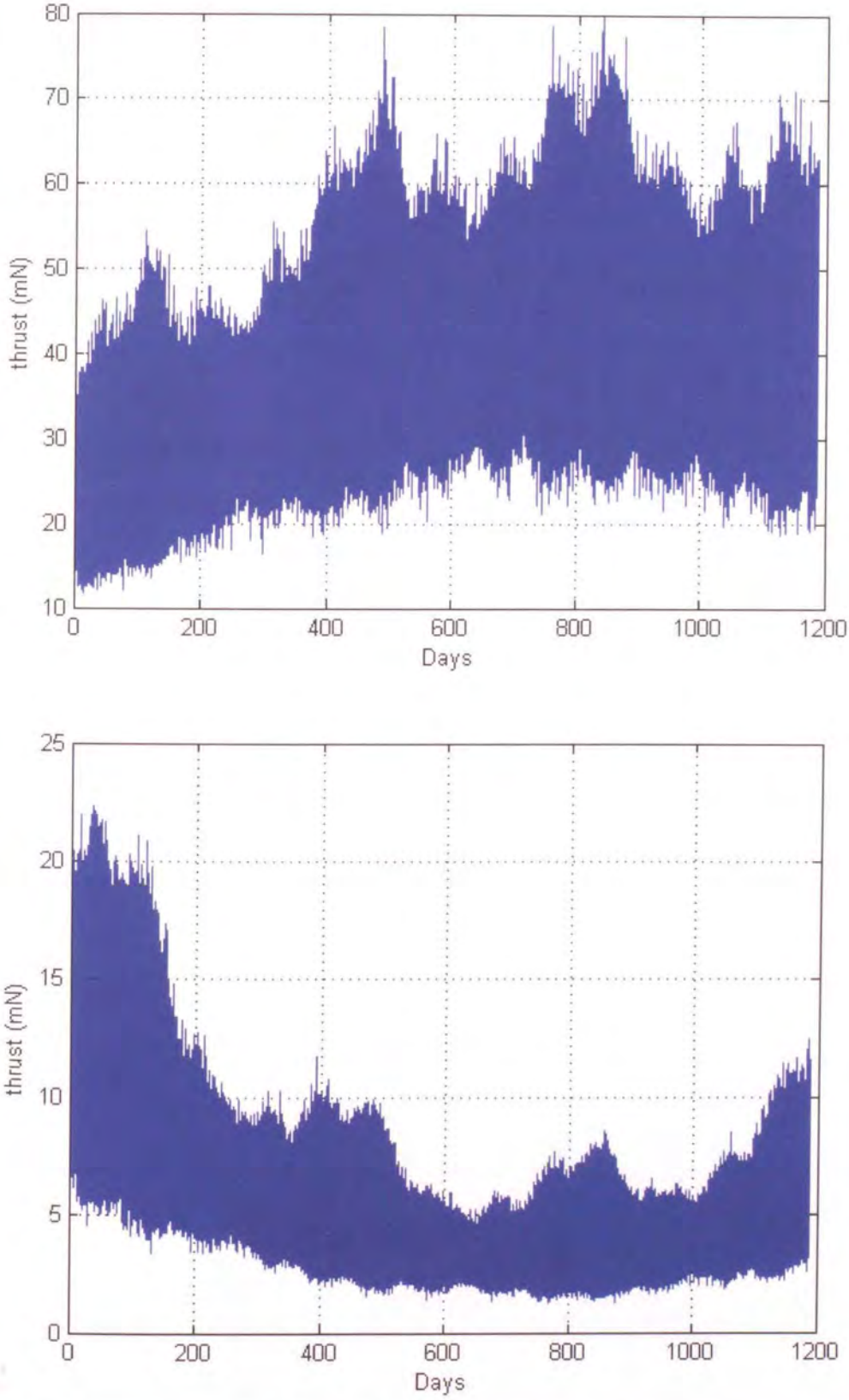

Figure 5-13. Thrust profile for Concept 3 during peak (top) and minimum solar activity.

5.5.7 Summary

From the trade-off performed for each concept, the most versatile propulsion systems for drag compensation are the gridded ion thrusters and the Hall effect thrusters, as summarised in Table 5-10.

	Concept 1	Concept 2	Concept 3	Concept 4
Altitude	> 290 km	> 290 km	> 320 km	> 320 km
Peak thrust	29 mN	54 mN	65 mN	80 mN
Propulsion option(s)	GIT, HET	GIT, HET	GIT, HET	GIT, HET

Table 5-10. Summary of requirements and suitable propulsion options.

The GIT is more propellant-efficient, whereas the HET consumes less power. Many studies (Price et al, 2005; Rossetti & Valentian, 2007) tend to agree that the two technologies are similar, with the propellant efficiency counter-balanced by the power reduction. In the example of concept 1 at 290 km altitude, the power difference is 382 W, which is about 10 kg based on the earlier assumption of 38 W/kg of solar array. The GIT enables a saving of 23 kg of Xenon. Thus, any difference is marginal.

As the two systems are so similar, it would be possible to consider either. However, a gridded ion engine has been designed for drag compensation on the GOCE mission, and is thus selected on the basis of maturity. It is discussed in further details in the next section.

Table 5-11 presents a summary of various European electrostatic thrusters for comparison. Only the T5 and the RIT-10 have the thrust range to operate over the wide range of drag force, either as a single unit or in a cluster of thrusters.

	Mission	Thrust (mN)	Power (W)	Total Impulse (N.s)	Specific Impulse (s)
T5	GOCE	1 – 20	55 – 585	$> 1.5 \times 10^6$	500 – 3000
T6	Geostationary, Bepi Colombo	30 – 230	2430 – 4500	$> 10 \times 10^6$	3710 - 4120
RIT-10	Geostationary	0.3 – 41	< 1500	$> 1 \times 10^6$	2500 – 3700
RIT-XT	Development	50 – 150	1700 – 4800	$> 8 \times 10^6$	4200 – 4500
PPS1350	Geostationary	90	1500	3.4×10^6	1660
HT400	Development	20 – 50	200 – 1000	?	< 1780

Table 5-11. Characteristics of some European ion thrusters.

5.6 The GOCE mission and the T5 Thruster

This section provides an overview of the electric propulsion system of the GOCE mission, from which the propulsion system for the lidar mission concepts can be derived.

5.6.1 Overall Description

The Gravity Field and Ocean Circulation Explorer (GOCE), launched in March 2009, is one of ESA's Core Mission of its Earth Explorer program. It measures with high accuracy and high resolution the Earth gravity to improve gravity field and geoid models [Bassner et al, 2000]. This will support many practical applications such as geodynamics, ocean circulation, geodesy, as well as the study of ice sheets and sea-level changes [Kramer, 2002]. The payload consists of a gradiometer that can measure gravitational acceleration in three dimensions with extremely high precision by observing the displacement of six proof masses. While this allows to measure high-resolution features of the gravity field, satellite-tracking via GPS is used to obtain low-resolution data [ESA, 2006]. However, the gradiometer requires a near free fall motion, in particular free of the atmospheric drag. This is achieved by the Drag-Free and Attitude Control System (DFACS), of which the main

feature is the Ion Propulsion Assembly (IPA). The functional architecture of the latter is represented in Figure 5-14.

The IPA comprises of two Ion Thruster Assemblies (ITAs) in cold redundancy; these are essentially T5 thrusters. Xenon flow is regulated and fed to the cathode, discharge chamber and neutraliser of the ITAs by the Proportional Xenon Feed Assembly (PXFA), which is connected to the Xenon tank. The design of the PXFA is greatly driven by the stringent microdisturbance requirements set by the mission [van Put et al, 2004]. The Ion Propulsion Control Unit (IPCU) serves as the electrical interface (power conditioning and telemetry and control) between the IPA and the spacecraft bus [Tato et al, 2007].

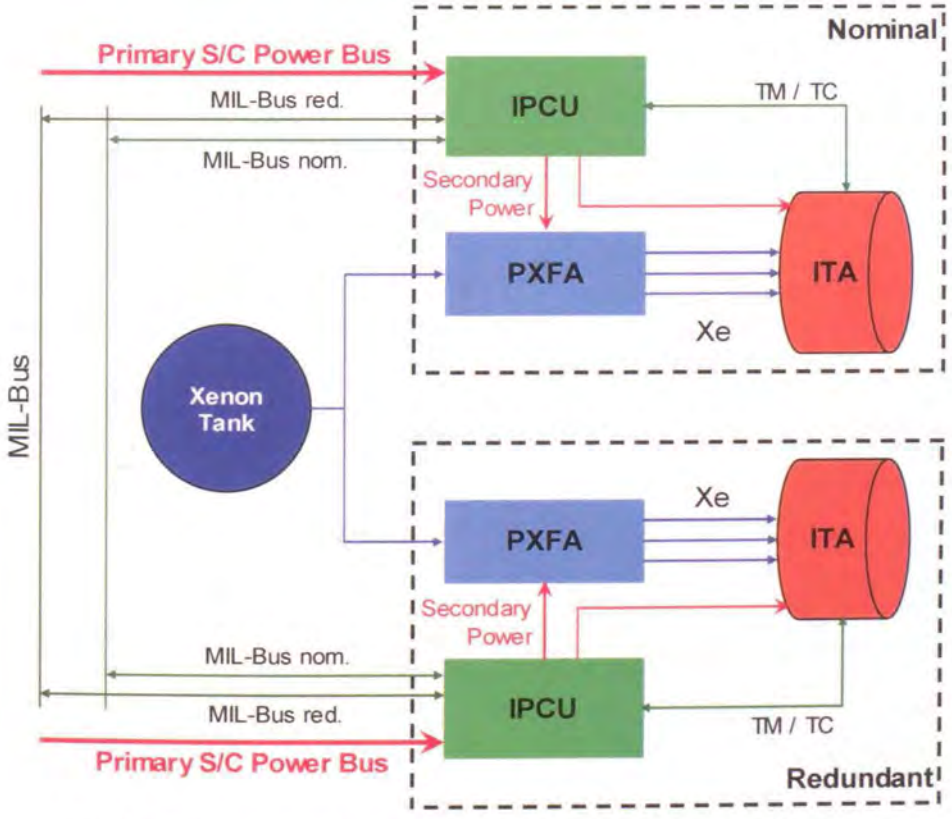

Figure 5-14. Schematic diagram of the GOCE IPA architecture

Adapted from Edwards, Wallace et al [2004].

5.6.2 The T5 Thruster

The T5 is a 10-cm diameter ion thruster that was developed by the RAE (later DERA and now QinetiQ) and Culham Laboratory [Wallace et al, 1998]; Figure 5-15 shows a schematic view of the T5. It is a Kaufman-type thruster, where a gas is ionised in a discharge chamber by bombardment of electrons produced by a hollow cathode. The path of the free electrons within the discharge chamber is optimised by a magnetic field, thus maximising the efficiency of the ionisation process. The positively-charged ions are extracted and accelerated through a set of perforated grids by an electrostatic field applied between these grids. A second cathode emits electrons downstream of the grid system to neutralise this external plasma and avoid a possible charge build-up on nearby surfaces of the satellite.

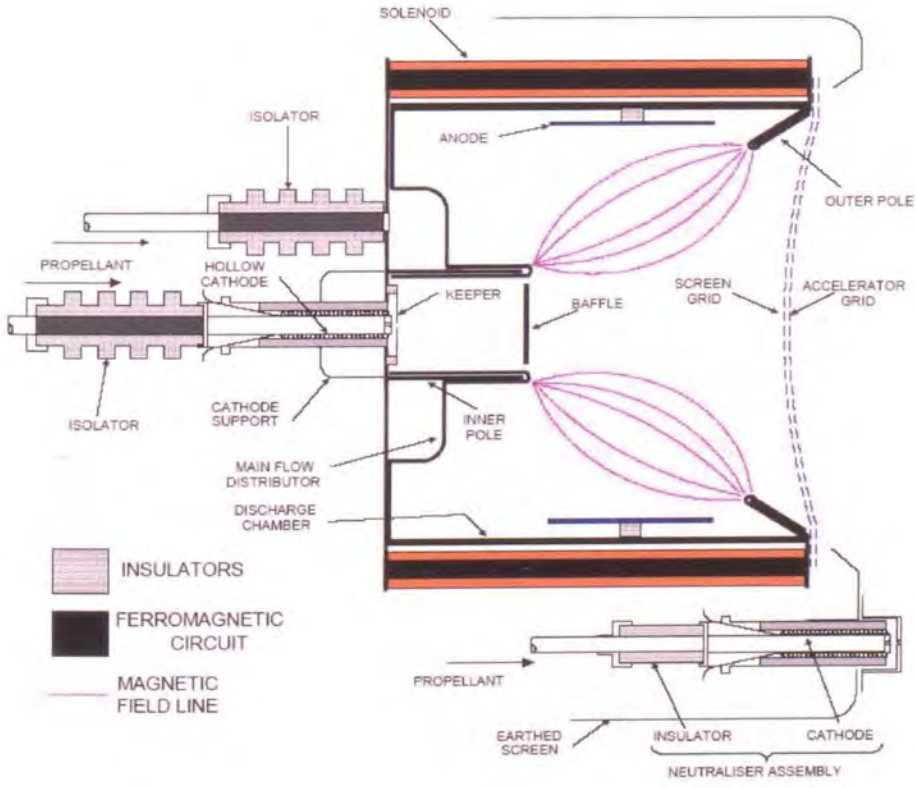

Figure 5-15. Schematic view of the T5 mkV Thruster.

Reproduced from Corbett & Edwards [2007].

In its simplest form, the grid system is made of an acceleration grid (commonly referred to as accel grid) with a negative potential, which attracts and thus accelerates the positively-charged ions. To avoid ions in the discharge chamber to impinge directly onto the accel grid, a screen grid is placed in between. The latter operates at the same potential as the discharge chamber, thus protecting the accel grid by focussing the ion beams. It is possible to introduce a third grid, called deceleration (decal) grid, whose function it is to protect the accel grid from excessive erosion by charge-exchange ions (see section 5.7 on ion thruster durability). Figure 5-16 shows both grid systems.

The configuration of the grid system (number of grids, hole patterns in the grids) is often optimised for a specific mission. For GOCE a lifetime of 21,000 hours is required with a thrust range 1-20 mN at a resolution of 12 μN; a two-grid configuration has been selected and QinetiQ have demonstrated a lifetime of the GOCE grid system well over 45,000 hours [Edwards et al, 2004].

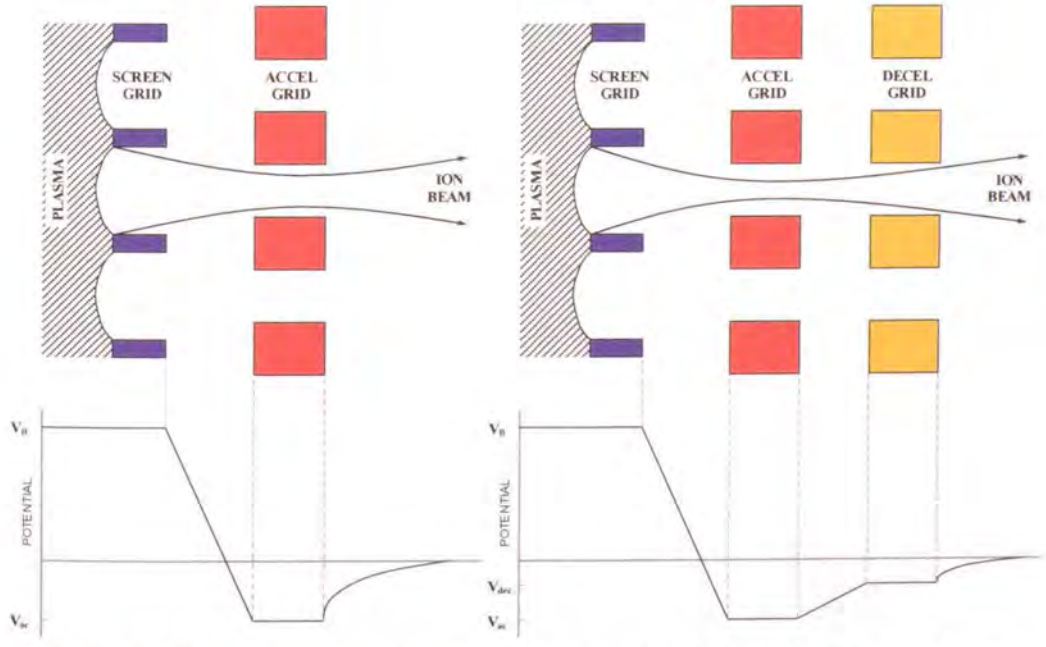

Figure 5-16. Geometric configuration and electric potential for two- and three-grid systems.

Reproduced from [Wallace et al, 1998].

The T5 has a unique combination of features that differentiate it from most other GITs [Wallace et al, 1998]:

- Inward dishing of the grids (rather than outward, or even flat) provides better thermo-elastic distortions of the grid system, preventing arcs between the grids;
- The magnetic field is generated by controllable solenoids, rather than permanent magnets, allowing for a wide throttling range and maintaining a high propellant utilisation efficiency under almost all conditions;
- Separately controllable flows to the cathode, discharge chamber and neutraliser ensure longer lives of the cathode and neutraliser in particular.

These gives the T5 a range of high specific impulse from 2500 to 4000 seconds [Fearn and Rijm, 2002], with high efficiencies over a thrust range of 0.2-70 mN, although operation above 30 mN is not recommended for long periods [Wallace et al, 1998].

5.7 Ion Thruster Durability

Extensive work worldwide currently focuses on extending the life of ion thrusters. Indeed, during the development of the NSTAR thruster that flew on NASA's Deep Space 1, ten damage-accumulation failure modes have been identified and are listed below [Duchemin, 2001].

- Electron-backstreaming due to enlargement of the accelerator grid apertures by ion sputtering;
- Structural failure of the accelerator grid due to charge-exchange ion erosion;
- Unclearable short between the screen and accelerator grids due to a flake of material formed from the deposition and subsequent flaking of sputtered material;
- Structural failure of the screen grid due to erosion by ion sputtering;

- Structural failure of the accelerator grid due to direct ion impingement from defocused beamlets caused by flakes of material on the screen grid;
- Depletion of the cathode low-work-function material;
- Cathode heater failure due to thermal cycling;
- Unclearable short between the keeper electrode and the cathode due to a flake of material formed from the deposition of material sputtered off the cathode orifice plate;
- Erosion of the keeper orifice plate resulting in its structural failure;
- Erosion of the neutralizer orifice plate due to operation in plume mode for extended duration.

One of the main foci of gridded ion engine research is to solve the problem of erosion by ion sputtering and charge-exchange erosion. Charge exchange occurs in the beam flow region between neutral atoms travelling at thermal velocity and high velocity ions, resulting in high velocity neutrals and slow ions, as illustrated in Figure 5-17. If this happens in the vicinity of the accel grid, then it largely attracts these charge-exchange ions, resulting in sputtering erosion of the accel grid and a reduction of its life expectancy [Peng, 1991].

This is an important issue as some operation modes can enhance the production of charge-exchange ions. For a given input power, it is possible to increase the thrust (through a greater mass flow rate) at the cost of reducing the specific impulse (i.e. exhaust velocity); this is achieved by reducing the voltage of the discharge chamber and screen grid. This must be counter-balanced by an even more negative potential of the accel grid in order to maintain a high electric field between the screen and accel grids. However, the latter would then more strongly attract ions, increasing its erosion [Wallace et al, 1998]. Such a mode of operation can only be considered for short periods of time, for instance during altitude boosts. Three-grid systems, where a decel grid is placed behind the accel grid, help reduce the erosion of the accel grid by charge-exchange ions formed downstream of the grid

assembly and prevent backstreaming of electrons from the external plasma [Wallace et al, 1998]. Figure 5-18 illustrates the erosion pattern on the accel grid due to charge-exchange ions.

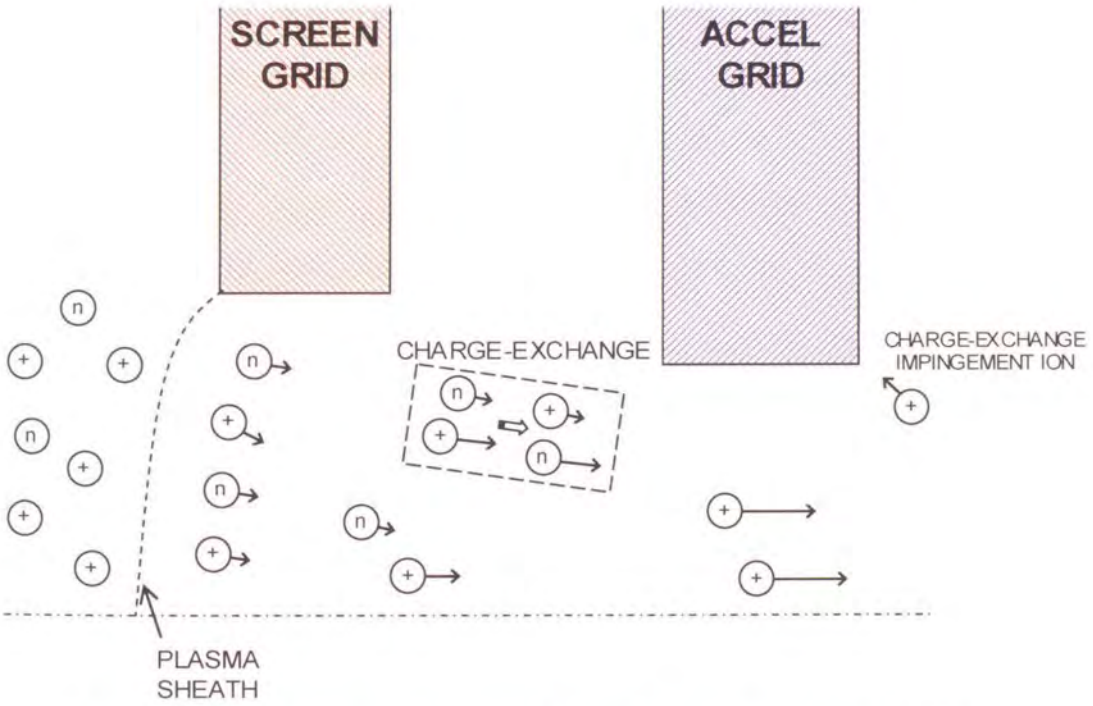

Figure 5-17. Schematic representation of the charge-exchange process.

Adapted from Monheiser [1994].

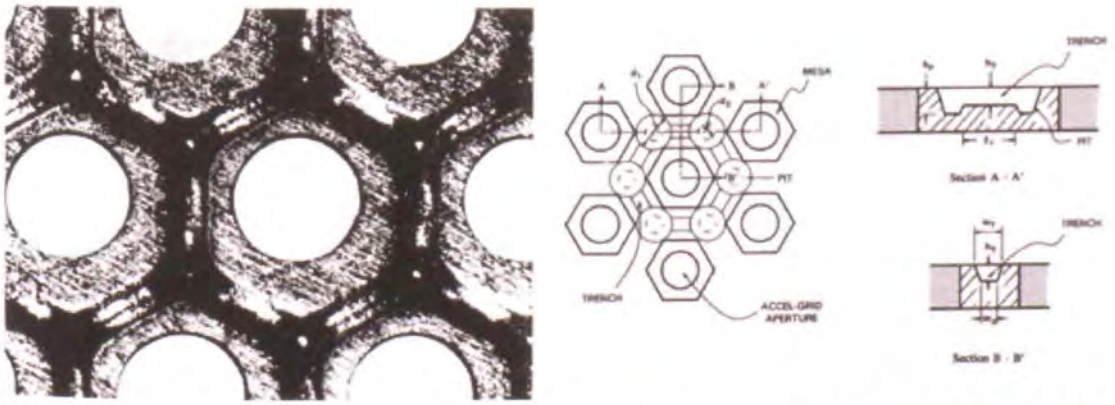

Figure 5-18. Actual erosion pattern on the downstream side of an accel grid due to charge-exchange erosion (left) and corresponding idealised patterns (right).

Reproduced from Barker [1996]

However, charge exchange erosion remains the main limitation of a grid lifetime only when the ion engine operates at moderate thrusts. In the case of extreme thrust levels (very high or very low), grid systems with conventional hole patterns on the screen grid are more affected by the direct impingement of badly focussed, highly energetic beam ions [Edwards et al, 2004]. In such a case, a three-grid system does not solve the problem and a configuration with two grids made of graphite (rather than molybdenum) improves the lifetime [Edwards et al, 2004]. Direct impingement is also the reason for high erosion rates in the first few hundred hours of operation because of small misalignments between the screen grid and the accel grid, as well as small variations in the distance between the grids [Edwards et al, 2004].

5.8 Electric Propulsion System for the Lidar Concepts

Depending on the size of the satellite, the electric propulsion system for a low-altitude Lidar mission could be the propulsion system of GOCE or a scaled-up version. However, GOCE's requirement for a drag-free environment to a high-degree of precision means that the electric propulsion system is designed for much more stringent conditions.

As mentioned earlier in this chapter, the T5 thruster from QinetiQ is selected as the baseline. It should be noted, however, that the RIT-10 is an equally capable gridded ion thruster for a Lidar mission. The lifetime and the level of thrust required means that a single or a cluster of multiple thrusters are needed depending on the lidar concept and altitude. In any case, a minimum of two thrusters should be implemented to provide redundancy.

The PXFA developed for GOCE had to meet some particularly demanding constraints to limit the micro-disturbances, while providing precise controllability of the Xenon flow rates [van Put et al, 2004]. Thus, the PXFA is over-engineered for a Lidar mission, with more relaxed requirements. Price et al [2005] suggest an alternative, simpler design made up of a single, internally redundant pressure regulation system and two flow control units (one nominal and one redundant). For GOCE, the control of the mass flow rate by the PXFA is too slow for the precision required. Hence, the high control precision of the thrust is mainly achieved by

varying the electrical parameters [Corbett and Edwards, 2007] thus affecting the specific impulse. Indeed in GOCE operation regime, the T5 specific impulse is reduced to 2000 seconds, whereas a typical value of 3000 seconds is often considered for GIEs. This is a consequence of the reduced exhaust velocity associated with a decreased beam voltage that is necessary to achieve a greater thrust for a given input power. The main consequence is that the accel grid voltage must be made more negative (in order to maintain a high electric field between the grids) and is therefore more prone to erosion by charge-exchange ions impingement [Wallace et al, 1998]. Indeed, while the T5 has a total impulse up to 3×10^6 N.s, but in GOCE operation conditions (i.e. continuously throttling), this drops to 1.5×10^6 N.s [QinetiQ, 2004].

This means that there may be an opportunity for an improved specific impulse for a lidar mission if the thrust control can be relatively coarse and achieved primarily through the control of the Xenon flow rate.

The design of the Power Control Unit is mostly driven by the thruster. For the control of the modified Xenon distribution system, some changes would be required both to the electrical interface (TM/TC) and to the software, but in terms of the mass and power consumption, any deviation would be minimal compared to GOCE's IPCU design.

The capacity of the Xenon tank depends on the requirements of the mission. Figure 5-19 shows the required mass of Xenon as a function of the total impulse of the mission, for three values (average over mission lifetime) of specific impulse. The Xenon mass required for each concept is given in Table 5-12.

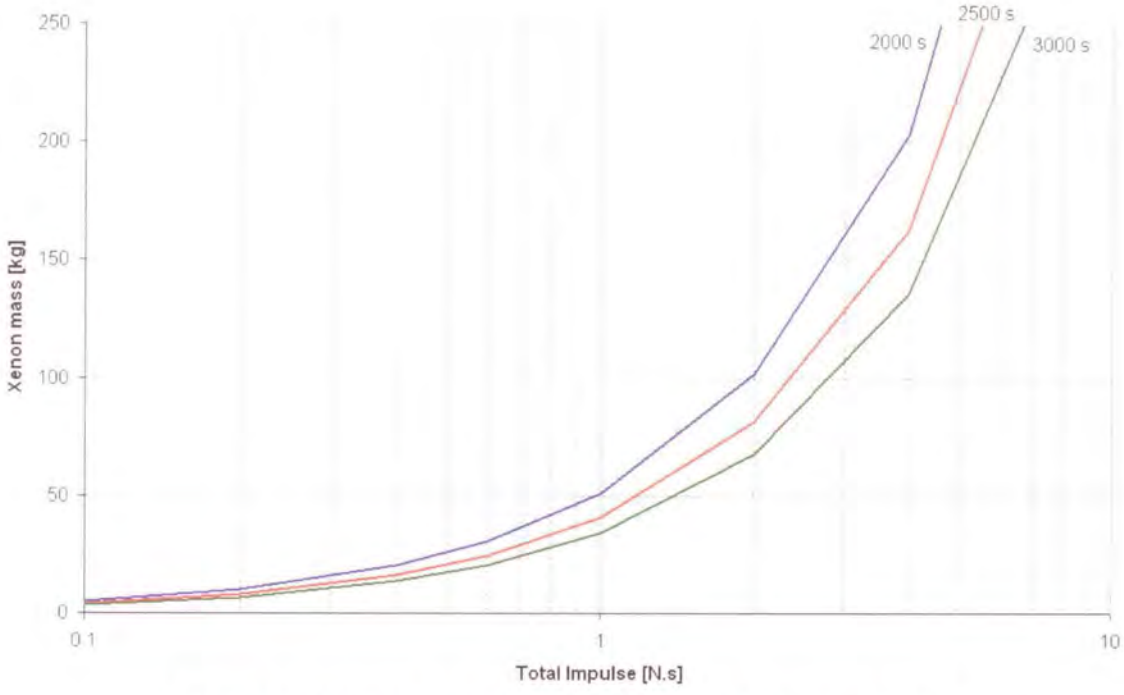

Figure 5-19. Mass of Xenon for a range of total impulse and three values of specific impulse.

Solar activity	Concept 1	Concept 2	Concept 3	Concept 4
Peak	55.5 kg	104 kg	136.6 kg	167.6 kg
Minimum	10.1 kg	18.9 kg	19.5 kg	23.9 kg

Table 5-12. Xenon mass required for each concept.

A specific impulse of 2500 s is assumed, and no margin has been added.

Pressure Systems have designed a Xenon tank with a capacity of 50 L (89 kg); the mass of the tank alone is 7 kg [Tam et al, 2000]. Smaller tanks have slightly lighter masses in the range of 5-6 kg [Price et al, 2005; Coletti et al, 2007].

Two pointing mechanisms have been identified: the Thruster Pointing Mechanism (TPM) developed by Austrian Aerospace [Falkner et al, 2005], and the Thruster Orientation Mechanisms (TOM) made by Thales-Alenia Space [TAS, 2000]. Both are designed to carry two thrusters, canted at about 45° with respect to the surface of the satellite interface. This cant angle is due to the fact that they are designed primarily for North-South station-keeping

of GEO platforms. Thus a major re-design would be required in order to make them suitable for a main propulsion system. Their pointing performance is similar, and their masses are 10.35 kg (TPM) and 9.5 kg (TOM). Thus, a redesigned gimbal system would have characteristics similar to these.

5.8.1 Mass budget

From the above, a mass budget for each concept has been established, adapted from [Price et al, 2005].

For Concept 1, the system consists of one nominal and one redundant thruster.

For Concept 2, two nominal thrusters are needed, with an additional redundant unit.

Concepts 3 and 4 both need 3 nominal thrusters and one redundant. These could be implemented as two systems identical to concept 1.

Their respective mass budgets are presented from Table 5-14 to Table 5-17.

5.8.2 Power budget

The power consumption of the T5 thruster varies with the thrust level. It is assumed that the power consumption of the flow control units and pressure regulation system is negligible.

The relationship between the total power of the thruster P_T and the thrust T is:

$$T = \frac{2\eta_T P_T}{I_{sp} g_0} \tag{5-5}$$

where I_{sp} is the specific impulse and η_T is the total efficiency, which is the product of the propellant utilisation efficiency, η_m, and the electrical efficiency, η_e. The latter is defined as the ratio of the power utilised in accelerating the beam to the input power [Wallace et al, 1998]. The propellant and electrical efficiencies vary with the operation regime, and can only be obtained from experimental data.

Equation (5-5) requires good knowledge (obtained through testing) of the performance and efficiencies of the thruster. As these parameters are not known here, a mathematical model

has been derived from the data presented in the study by QinetiQ for ESA [Price et al, 2005] for missions requiring atmospheric drag compensation. The data collected is presented in Table 5-13. This model estimates the power consumption of the electric propulsion system based on the thrust level required, by means of a second-order polynomial:

$$P_T = 0.34T^2 + 21T + 59 \tag{5-6}$$

where the thrust is in millinewtons and the power in watts. However, this relationship only works for a mean specific impulse of 2000 seconds, but is conservative for a higher specific impulse.

Mean SI [s]	Thrust level [mN]	Power per unit thrust [W/mN]	Power [W]
2000	5.127	35	179.5
	6.147	32	196.7
	7.501	31	232.5
	8.624	31	267.4
	9.171	31	284.3
	13.349	30	400.5

Table 5-13. Characteristics of the T5 gridded ion thruster when used for atmospheric drag compensation [Price et al, 2005].

For GOCE, the power consumption and dissipation of the IPCU are assumed to be identical, which is a typical assumption for all electronic devices on board a satellite. In reality, the power dissipation would vary with the power to be processed (and hence with the thrust level). The maximal power dissipation of the IPCU will be taken for all thrust levels i.e. 140 W + 5% margin [Price et al, 2005], however this must be multiplied by the number of nominal thrusters. Further details on the GOCE IPCU can be found in Tato, Palencia and de la Cruz [2004].

The gimbal mechanism has a power consumption of 2.9 W average and 15.7 W peak, under worst-case (hot) conditions [Falkner et al, 2005].

5.8.3 Summary

The mass and power budgets for each concept are presented in the next tables, for maximum solar activity period and altitudes specified in Table 5-10.

The average thrust over an orbit has been calculated for the whole mission lifetime, and the highest average thrust level has been used to calculate the power budget. This approach is explained by the fact that the energy budget of the satellite must balance over one orbit. Taking the peak thrust would result in the over-sizing of the solar arrays.

	Qty	Unit mass (kg)	Margin	Total mass (kg)
Ion thruster	2	1.6	5%	3.4
Flow control units	2	0.5	5%	0.9
Power processing units	2	18.0	10%	39.6
Pressure regulation system	1	4.5	10%	5.0
Pipework and harness	1	4.0	20%	4.8
Gimbal mechanism	1	10.4	15%	11.9
Tank	1	4.9	15%	5.6
Total				71.2

	Qty	Unit power (W)	Margin	Total power (W)
Ion thruster	1	553.8	10%	609.2
Power processing units	1	140.0	10%	154.0
Gimbal mechanism	1	3.0	15%	3.5
Total				766.6

Table 5-14. Mass and mean power budgets for the electric propulsion system for concept 1.

	Qty	Unit mass (kg)	Margin	Total mass (kg)
Ion thruster	3	1.6	5%	5.0
Flow control units	3	0.5	5%	1.4
Power processing units	3	18.0	10%	59.4
Pressure regulation system	1	4.5	10%	5.0
Pipework and harness	1	4.0	20%	4.8
Gimbal mechanism	1	10.4	15%	11.9
Tank	1	8.7	10%	9.6
Total				97.1

	Qty	Unit power (W)	Margin	Total power (W)
Ion thruster	2	491.4	10%	1081.1
Power processing units	2	140.0	10%	308.0
Gimbal mechanism	1	3.0	15%	3.5
Total				1392.5

Table 5-15. Mass and mean power budgets for the electric propulsion system for concept 2.

	Qty	Unit mass (kg)	Margin	Total mass (kg)
Ion thruster	4	1.6	5%	6.7
Flow control units	4	0.5	5%	1.9
Power processing units	4	18.0	10%	79.2
Pressure regulation system	2	4.5	10%	9.9
Pipework and harness	2	4.0	20%	9.6
Gimbal mechanism	2	10.4	15%	23.8
Tank	1	11.0	10%	12.1
Total				143.2

	Qty	Unit power (W)	Margin	Total power (W)
Ion thruster	3	413.2	10%	1363.7
Power processing units	3	140.0	10%	462.0
Gimbal mechanism	2	3.0	15%	6.9
Total				1832.6

Table 5-16. Mass and mean power budgets for the electric propulsion system for concept 3.

	Qty	Unit mass (kg)	Margin	Total mass (kg)
Ion thruster	4	1.6	5%	6.7
Flow control units	4	0.5	5%	1.9
Power processing units	4	18.0	10%	79.2
Pressure regulation system	2	4.5	10%	9.9
Pipework and harness	2	4.0	20%	9.6
Gimbal mechanism	2	10.4	15%	23.8
Tank	1	12.8	10%	14.0
Total				145.2

	Qty	Unit power (W)	Margin	Total power (W)
Ion thruster	3	481.7	10%	1589.5
Power processing units	3	140.0	10%	462.0
Gimbal mechanism	2	3.0	15%	6.9
Total				2058.4

Table 5-17. Mass and mean power budgets for the electric propulsion system for concept 4.

5.9 Conclusion

Electric propulsion is an enabling technology for a spaceborne Lidar mission flying at a very low altitude, where atmospheric drag has a strong impact on the amount of propellant necessary for orbit maintenance.

After an analysis of the mission requirements, it has been demonstrated through a trade-off of various electric propulsion systems that gridded ion thrusters are particularly suited for this type of mission because of their thrust level, specific power consumption and specific impulse. Grid erosion, which is the main lifetime-limiting factor of GIT, has been shown to be compatible with the duration of the mission.

An electric propulsion system design that can inherit from the GOCE mission has been suggested as the baseline for the proposed Lidar concepts. Mass and power budgets have been generated and will be used in the sizing of the overall spacecraft in Chapter 6.

Chapter 6

Instrument and Platform Sizing

6.1 Introduction

The primary function of the satellite bus is to fulfil the needs of the payload, such as power, heat, pointing, data transmission, etc. The main restrictions on the design of the spacecraft come from the limited volume of the launch vehicle fairing and the mass that it can deliver into a given orbit.

This chapter starts with satellite-specific requirements (section 6.2) as a necessary complement to the mission requirements stated in Chapter 2. Based on the work presented in Chapter 3, a more detailed instrument design is provided in section 6.3. In section 6.4, we address the overall configuration of the satellite and the sizing of its subsystems. Many of these will not vary much between the four concepts, and could be assumed constant. Others, such as the electrical power subsystem, will vary more strongly with the altitude and instrument size. Table 6-1 describes briefly for each spacecraft subsystem the relative dependence to altitude and lidar aperture diameter, so as to separate the strongly variable ones (highlighted in green) from the others.

Subsystem	Variability	Comments
Structure	Yes	Because of the very different telescope sizes, the satellite structure design and mass will be dramatically different.
Propulsion	Yes	The power requirement of the electric propulsion depends on the thrust level, and in turn on the atmospheric drag, atmospheric density and thus altitude.
AOCS	Yes	The sensors will be unchanged. The size of the actuators will depend on the mass moments of inertia and the environmental disturbance torques. The most noticeable difference will be in the choice between reaction wheels and control moment gyro.
PDHT	No	The amount of payload data will vary only marginally. Because the amount of data is rather small in the first place, variations in contact time with the ground station in every pass have no effect.
OBDH	No	The on-board data handling will not vary much. There is likely to be some discrepancies, but these should be sufficiently small to be neglected.
Thermal	Yes	The thermal control system depends on the power dissipation of the transmitter electronics in particular.
Electrical Power System	Yes	Its size must be adjusted for the variable power demands of the Electric Propulsion and the lidar in particular.

Table 6-1. Degree of variability of the platform systems with altitude.

Section 6.5 presents the resulting mass and power budgets of the satellite for each of the four concept.

The sizing of the lidar instrument and the platform would very much be affected by the type of mission considered. While the study has been kept generic, it is inevitable that some assumptions will need to be made. Where such specific requirements are needed, these will be taken from amongst the known missions (Aeolus, A-SCOPE, EarthCARE, etc.), depending on what is deemed the most generic.

6.2 Overall Requirements

6.2.1 General configuration

The general configuration of the satellite is driven by the requirements of the orientation and fields of view (FoV) of many spacecraft elements, as discussed below.

6.2.1.1 Lidar Tx and Rx FoV

The requirement on the pointing direction of lidars has already been discussed in Chapter 2. The line of sight should be pointing towards nadir with an offset angle of about 2 degrees around the roll axis (depending on the mission) to avoid specular reflection from the ground. Note that Aeolus needs a larger offset of 35°as required by the measurement of the Doppler shift for the retrieval of winds in the troposphere and lower stratosphere.

In safe mode, when the nadir pointing may be compromised, it is nevertheless required to exclude the sun from the field of view of the receiver. For practical reasons, it is often desirable for the lidar to be able to withstand the sun drifting through the FoV over a small period of time (a few tens of seconds). However, this has a major impact on the detailed instrument design. Similarly, it is necessary to avoid pointing the lidar in the flight direction to limit the contamination of the optical surfaces by atomic oxygen.

The FoV of both Rx and Tx telescopes should be clear of any obstructions, even partial. This has an effect on deployable appendages in particular.

6.2.1.2 Lidar radiator

The radiator of the lidar must dissipate excess heat, in particular from the laser heads, as these are very sensitive to temperature variation. The radiator must predominantly be in view of deep space in a rather uniform manner with no direct sun illumination possible. Its field of view of deep space (2π steradians, except for the Earth) should not be obstructed by any appendage, especially if they could reflect sunlight onto the radiator.

6.2.1.3 Star trackers

The star trackers too must have an unobstructed view of deep space, with a clear exclusion of the sun and the earth. The typical FoV of a star tracker is in the order of 15-20° half-cone, with a sun exclusion angle of 30-40° from the boresight. The orientation of the star tracker depends on the pointing performance around each axis, as star tracker performance in the cross direction is approximately a factor of 5 times better than around the boresight.

6.2.1.4 Electric thrusters

The plume of the electric thruster(s) should be clear of any spacecraft surfaces to avoid a charge build-up from un-neutralised ions. More generally, a thruster plume should be clear from any element of the spacecraft in order to be efficient. The divergence of the T5 varies between 12° at 20 mN up to 25° at 1 mN [Edwards et al, 2004].

6.2.1.5 Solar arrays

To minimise the size of the solar arrays, they should be nearly normal to the direction of the Sun. If deployed, they should be positioned at a sufficient distance from the spacecraft main body to avoid shadowing of cells. They should be parallel to the inertial velocity vector in order to minimise additional atmospheric drag. For a satellite in a dawn-dusk orbit, these requirements can easily be met with the solar arrays roughly in the orbit plane. The actual angle between the solar panels and the orbit plane depends on the seasonal sun declination and power flux.

6.2.1.6 TM/TC and PDHT antennas

The antennas to communicate with the ground would ideally need a clear view of the ground station. Because the payload data volume of lidars tends to be small and does not require the whole pass duration to be downlinked to the ground, some degree of flexibility exists.
Two antennas mounted on opposite sides of the satellite are often used for TM/TC so as to provide 4π steradian coverage at any time. Having clear FoV is even more important as the

exchange of data can be crucial to the life of the satellite in critical cases (e.g. non-autonomous FDIR requiring commands from the ground).

6.2.1.7 Resulting configuration

Figure 6-1 illustrates the general configuration that has been established for concepts 1 and 2 in order to meet all the requirements above. The FoVs in yellow represent sun exclusion requirements. Also shown are the FoV of the Rx telescope (red), the star trackers (white) and the GIT beam divergence (blue). The details of the configuration will be refined in the rest of this chapter.

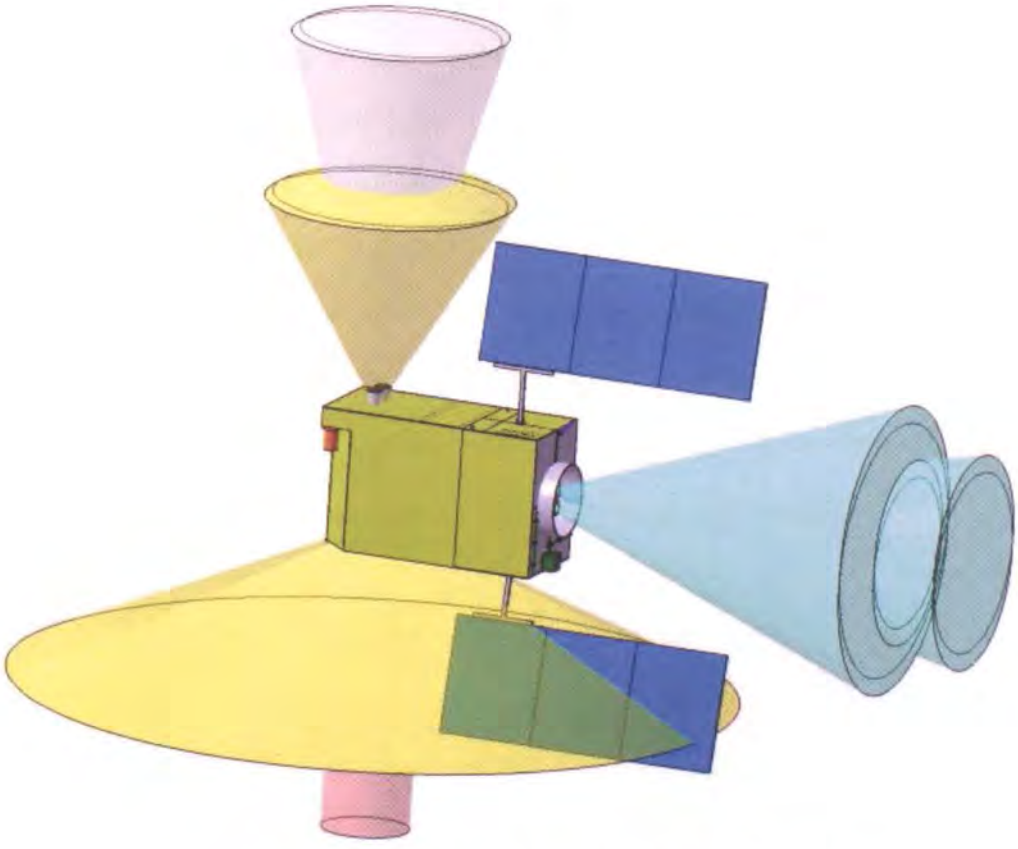

Figure 6-1. CAD model illustrating the FoV constraints

6.2.2 Pointing requirements

Pointing requirements are very specific to a lidar mission, and will vary substantially from one to another. Pointing requirements of the latter are discussed briefly in the A-SCOPE Assessment Report [ESA, 2008].

The pointing accuracy (APE) can be driven by Doppler shift in the pitch and roll, while errors around the boresight of the telescope have little impact, if any. Pointing knowledge (AME) is usually derived from geolocation requirements.

The Relative Pointing Error (RPE) relates to pointing accuracy over a period of time. It is particularly important in DIAL and IPDA lidars, between the online and offline shots. This type of RPE is usually outside the control bandwidth of the AOCS and cannot be actively controlled. Instead it falls in the microvibration domain, with structural damping and limited speed of actuators (reaction wheels or CMGs) being the typical solutions.

The performance of the satellite against these requirements is affected by the AOCS actuators and/or sensors and contributors (such as misalignment) internal to the instrument. It is good practice to mount the fine attitude sensors (star trackers and/or gyros) as close to the lidar telescopes as possible, in order to reduce the misalignments (bias, thermo-elastic distortions) between the attitude reference and the instrument. This results in the configuration shown in Figure 6-2, where the STR is mounted on the opposite side of the telescope baseplate, with their boresights parallel but in opposite direction.

Figure 6-2. In Concept 1 and 2, the star trackers (white) are mounted on the opposite side of the baseplate from the Rx telescope (brown) and the Tx telescope (orange).

6.2.3 Thermal requirements

Electric components have different temperature requirements; Table 6-2 gives an example of typical operating temperature ranges for selected components. These would dictate where temperature-sensitive equipment should be mounted.

The elements in a Lidar most sensitive to the temperature are the laser units. To operate correctly and avoid risks of damage, a temperature between roughly 20 and 25°C is required. However, during operation, the laser needs a temperature stability of ±1°C; thus the minimum and maximum temperatures of 21-22°C have been considered.

Subsystem	Op. temp. [°C]	Subsystem	Op. temp. [°C]
On-Board Computer	-10 to +50	TT&C antennas	-65 to +95
TT&C units	-10 to +50	Tanks and lines	15 to 40
Electrical Power PCDU Li-ion batteries	-20 to +55	AOCS Reaction wheels Star trackers	 -10 to 40 0 to 30

Table 6-2. Typical operating temperature ranges for spacecraft subsystems. Adapted from Gilmore et al. (2003) and Panetti (1999).

6.3 Instrument Detailed Design

6.3.1 Instrument Architecture

The functional architecture of a lidar instrument will be specific to its mission objectives. The A-SCOPE instrument architecture is shown in Figure 6-3, identifying the elements generic to most lidars, although each subsystem may vary internally between missions. As mentioned in Chapter 2, the transmitter optical subsystem is optional; its presence depends on the mission requirements.

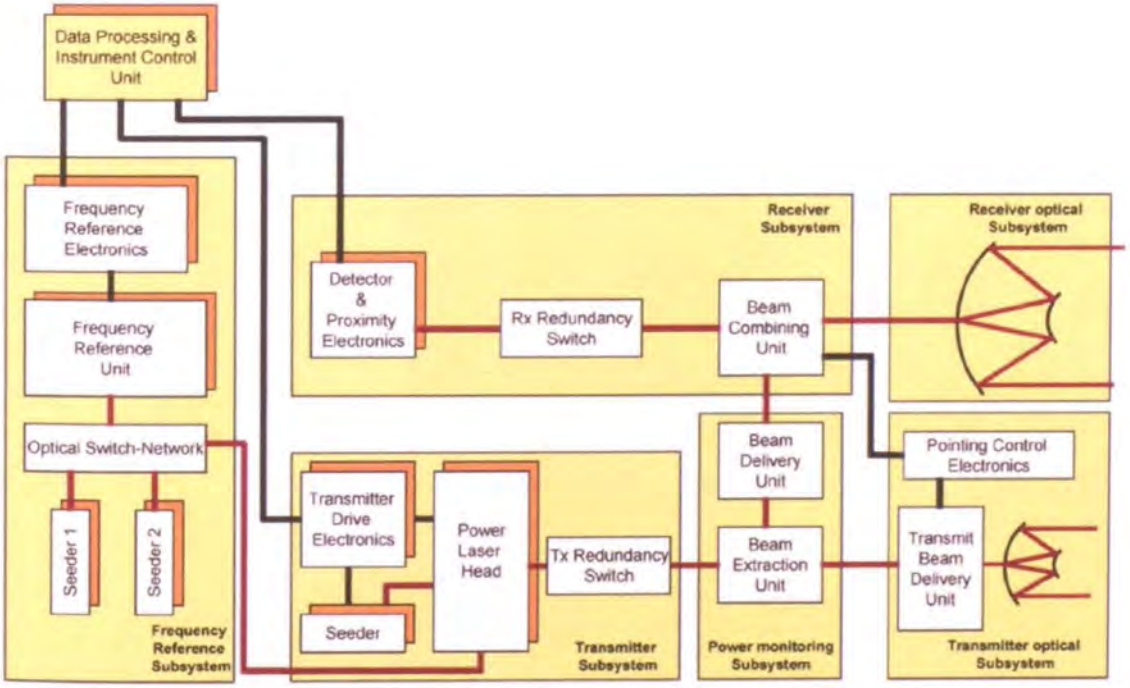

Figure 6-3. A-SCOPE instrument architecture [ESA, 2008].

A CAD representation of the 1.57-μm A-SCOPE lidar concept is shown in Figure 6-4. The lasers, detectors and electronics are mounted on two baseplates with the telescope and its baffle on top. It is proposed to maintain this two-baseplate configuration, with the following logic:

- Upper face of top baseplate: Rx telescope, Tx telescope and attitude sensors and supporting structure (where required).
- Lower face of top baseplate: receiver stage.
- Upper face of bottom baseplate: opto-electronic units of the transmitter stage.
- Lower face of bottom baseplate: interface to the platform primary structure.

The two transmitter drive electronics (nominal and redundant) can be located on the lower face of the bottom baseplate, or on a side wall of the platform, as these are voluminous and dissipate a large amount of heat.

Figure 6-4. Overall opto-mechanical configuration of the 1.57-μm A-SCOPE instrument concept proposed at Phase 0 [ESA, 2008].

6.3.2 Opto-mechanical configuration of the four concepts

The opto-mechanical configuration for the front-mounted instrument is shown in Figure 6-5, and for the nadir-mounted lidar in Figure 6-6.

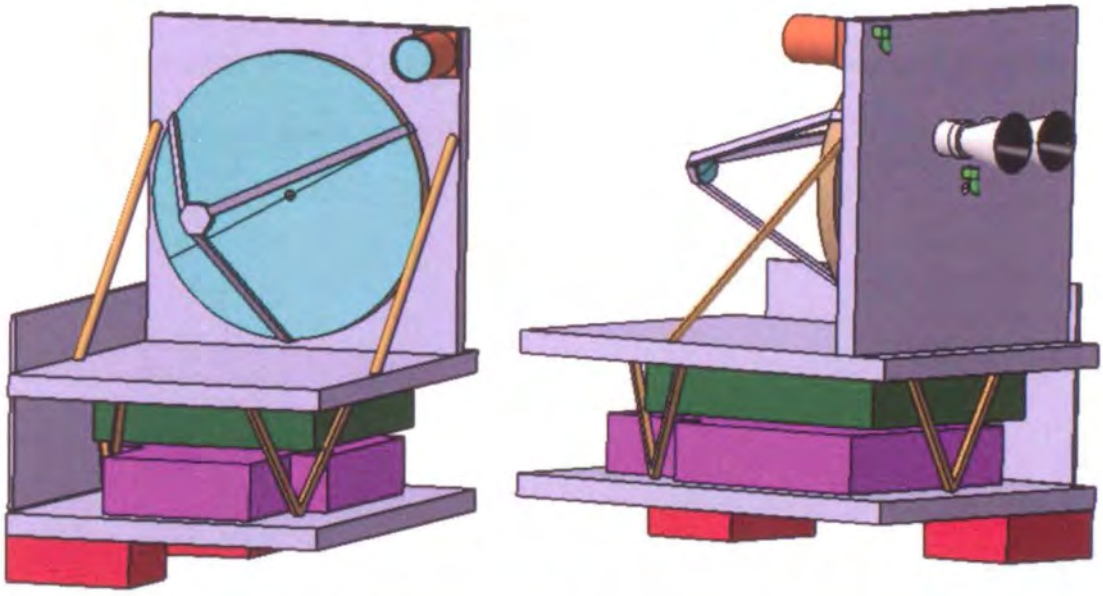

Figure 6-5. CAD views of the front-mounted instrument

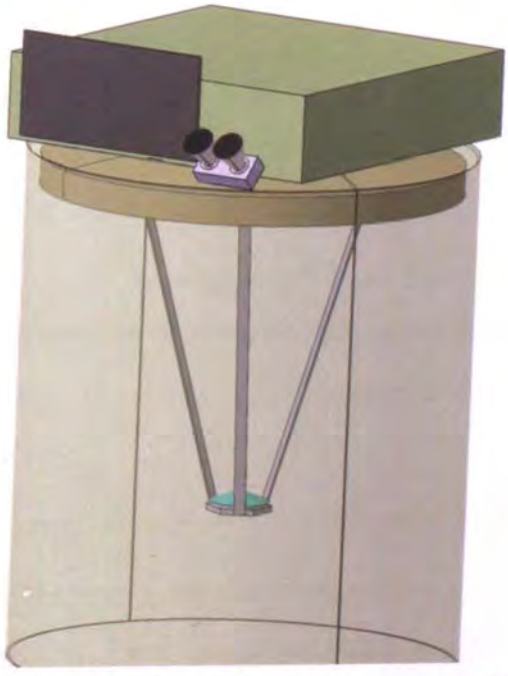

Figure 6-6. CAD view of the nadir-mounted concept

6.3.3 Mass budget

The mass budgets for the four concepts assume that the telescope is made of Cesic ®, a Silicon Carbide (SiC) ceramic with excellent thermal properties (high thermal conductivity, κ, and low Coefficient of Thermal Expansion, α) and excellent mechanical properties (high Young Modulus, E, and low density, ρ). Figure 6-7 shows that SiC ceramics have better properties than other frequent telescope mirror material such as Beryllium or Zerodur®. Cesic® mirrors have a typical mass per surface area in the range 18-22 kg/m^2 [Devilliers & Kroedel, 2008; Yui et al, 2008].

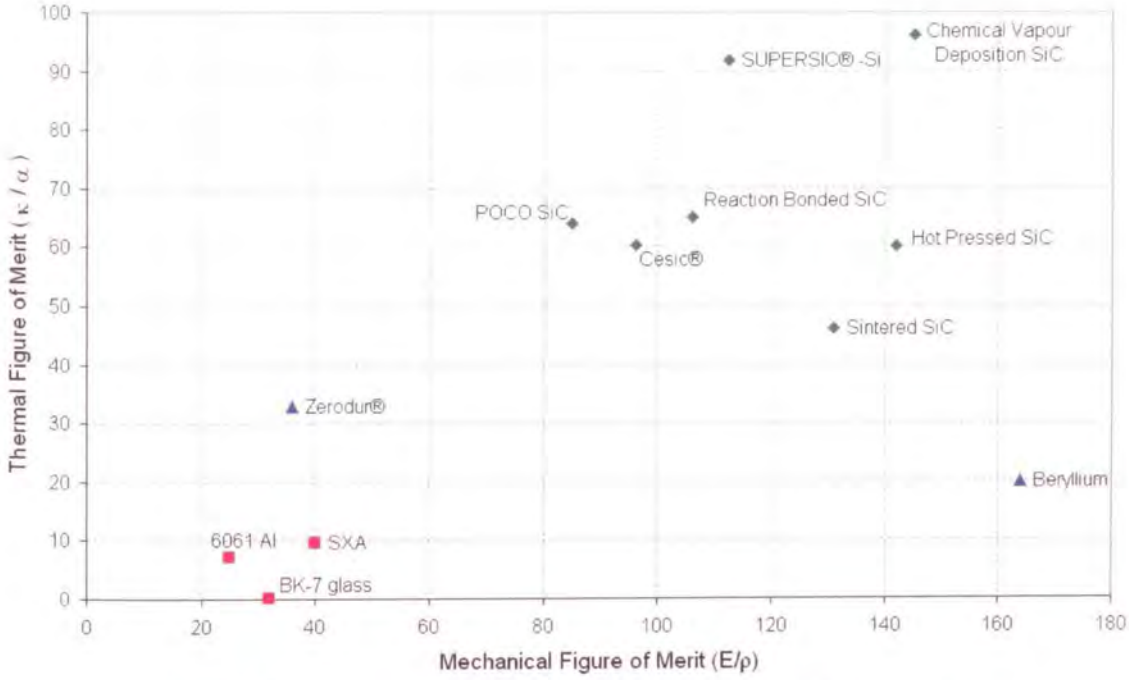

Figure 6-7. Properties of some common telescope materials.

Reproduced from Duston [2006] based on data from Bray et al [2004].

The mass budgets for each of the concepts are shown in Table 6-3 to Table 6-6. It is assumed that the mass of the transmitter stage would not vary with the transmitter power. While this may not be quite true, it is a conservative assumption that would not have a significant impact on the overall spacecraft design. Similarly, the mass of the Rx stage is

assumed constant, and the values of A-SCOPE are used. This would in fact differ from one mission to another, but again, differences are negligible with respect to the total mass of the instrument.

The calculation of the primary and secondary structures differs greatly, with similarities between concept 1 and 2 on one side, and concepts 3 and 4 on the other, reflecting the configuration specificities (front-mounted vs. nadir-mounted, respectively). The telescope mass is calculated with a mass per unit surface area of 28 kg/m^2, which is the case of ALADIN [Breysse et al, 2004], and this parametric model gives errors of less than 10% when compared to ALADIN or the Herschel telescope, before margin is added.

A margin of 20% is added to all the elements of the instrument and is standard practice where there are large uncertainties (e.g. for new equipment with some heritage).

Element	Unit mass	Margin	Mass
Primary structure	76.3	20%	91.5
Secondary structure	61.3	20%	73.6
Telescopes	50.5	20%	60.6
Rx stage	41.5	20%	49.8
Tx stage and electronics	129.5	20%	155.4
Total			430.9

Table 6-3. Mass budget for Concept 1 lidar (1150 mm)

Element	Unit mass	Margin	Mass
Primary structure	194.1	20%	233.0
Secondary structure	154.3	20%	185.1
Telescopes	102.0	20%	122.4
Rx stage	41.5	20%	49.8
Tx stage and electronics	129.5	20%	155.4
Total			745.6

Table 6-4. Mass budget for Concept 2 lidar (1800 mm)

Element	Unit mass	Margin	Mass
Primary structure	207.0	20%	248.4
Secondary structure	268.8	20%	322.6
Telescopes	247.3	20%	296.8
Rx stage	41.5	20%	49.8
Tx stage and electronics	129.5	20%	155.4
Total			1072.9

Table 6-5. Mass budget for Concept 3 lidar (3000 mm)

Element	Unit mass	Margin	Mass
Primary structure	281.8	20%	338.1
Secondary structure	354.3	20%	425.1
Telescopes	327.7	20%	393.2
Rx stage	41.5	20%	49.8
Tx stage and electronics	129.5	20%	155.4
Total			1361.7

Table 6-6. Mass budget for Concept 4 lidar (3500 mm)

6.3.4 Power Budget and Thermal Load

The power requirement of the lidar instrument is split between the power used by the transmitter stage (P_{TX}) and the power of the other elements (receivers, frequency reference electronics and ICU) which would not depend much on the lidar performance.

It is possible to relate the mean laser power, $\overline{P_0}$, to the power consumption of the transmitter stage through the wall-plug efficiency, derived from Wirth et al [2009]:

$$\eta_{wp} = \frac{\overline{P_0}}{P_{TX}} \tag{6-1}$$

And the mean laser power simply depends on the beam energy, E_0, and the pulse repetition frequency, f_{rep} [Wandinger, 2005]:

$$\overline{P_0} = E_0 f_{rep} \tag{6-2}$$

The PRF may depend on the sampling distance between two shots and the altitude (and thus speed) of the satellite. A variation in altitude for a constant PRF does not have a big impact on the gap between ground pixels, as shown in Table 6-7. Furthermore, one observation usually consists of an accumulation of shot measurements over some distance (50 km for both Aeolus and A-SCOPE). Therefore we will assume that the PRF remains constant at all altitudes.

Altitude [km]	400	350	300
Sub-Satellite Point (SSP) velocity [km/s]	7.216	7.297	7.379
PRF [Hz]	50	50	50
Distance between measurements [m]	144.3	145.9	147.6

Table 6-7. Effect of altitude on distance between measurements.

Combining Equations (6-1) and (6-2), the wall-plug efficiency is:

$$\eta_{wp} = \frac{E_0 f_{rep}}{P_{TX}} \tag{6-3}$$

The wall-plug efficiency is a measure of how well the transmitter stage transforms electric power into laser beam power. Note that the PRF must be adjusted for the number of beam wavelengths. Spaceborne lidars in general tend to have a wall-plug efficiency in the range 0.5-2% (Table 6-8).

	Beam energy (mJ)	PRF (Hz)	Tx power	Wall-plug efficiency
Aeolus	120	100	510	2.35%
A-SCOPE	50	50 (×2)	400	1.25%
WALES	72	25 (×4)	1125	0.6%

Table 6-8. Wall-plug efficiency for three European lidar missions.

The electric power not converted into laser beam power is transformed into heat which must be taken away, especially from the laser where the heat would raise the temperature of the laser medium. This would result in a larger population of the lower energy levels, thus reducing the population inversion and the gain [Weichel, 1993]. About 15-20% of the heat is dissipated by the transmitter drive electronics (due to power conditioning efficiency) and the rest by the Nd:YAG laser itself.

As stated in Chapter 2, the aim is to investigate the possibility to reduce the laser beam energy in the range 5-15 mJ. The transmitter power for a range of wall-plug efficiencies is given in Table 6-9 with a PRF of 100 Hz. Wall-plug efficiency depends on the wavelength desired and the frequency conversion technique employed. A conservative value of 150 W is considered. To put it in perspective, a difference of 150 to 200 W is approximately equivalent to 1 m^2 of solar array.

	0.5%	1.0%	1.5%	2.0%
5 mJ	100 W	50 W	33.3 W	25 W
10 mJ	200 W	100 W	66.6 W	50 W
15 mJ	300 W	150 W	100 W	75 W

Table 6-9. Transmitter power for a range of beam energy and wall-plug efficiency at 100 Hz PRF.

For the other units (receivers, etc.), it can be assumed that they dissipate the same amount of heat as the amount of electric power they consume. As shown in section 2.6.4, this can

vary substantially from one mission to another, from 150 W for A-SCOPE, to 320 for Aeolus or 520 W for WALES. In the scope of this study, 400 W will be assumed: this is an intermediate value between Aeolus and WALES, which are the most challenging, where a value closer to that of A-SCOPE would be too optimistic for many cases.

Element	Operational
Transmitter	150 W
Other elements (receiver stage, ICU)	400 W

Table 6-10. Power budget of the lidar instrument for spacecraft sizing.

Table 6-11 summarises the thermal load budget. It also indicates the temperature range for operational and non-operational conditions, as these are important for the sizing of the payload radiator and heaters.

Element	Heat load [W]	Temp. [°C]
Transmitter Drive Electronics	30	25 ± 10
Laser	119	20 ± 1
Other elements	400	20 ± 2

Table 6-11. Heat load budget and temperature requirement of the lidar instrument under operational conditions for the spacecraft sizing.

6.3.5 Data Rate and Volume

In the case of A-SCOPE, the payload data rate ranges between 0.38–1.7 Mbps [ESA, 2008], although these values correspond to the respective designs of the two industrial teams. The worst-case situation of 1.7 Mbps remains quite low compared to other earth observation missions (such as hyperspectral instruments). This confirms the earlier statement in section 6.2.1 that payload data transmission is not a mission driver.

6.4 Sizing of platform subsystems

6.4.1 Thermal control system

The aim of the thermal control system is to maintain the various electronics on board the spacecraft, and in particular the laser elements of the payload, within a suitable temperature range.

A thermal control system can be made up of a combination of passive and active systems. In the present study, most of the passive components are likely to remain sensibly similar between two concepts. For instance, multi-layer insulation (MLI) covering the external surfaces has a mass in the order of 0.73 kg/m^2 [Gilmore et al, 2003]; with a total surface area of the spacecraft in the order of 10-20 m^2, any variation would not have a dramatic impact and would be absorbed within the system margin.

What is more important here is the size and mass of the radiators needed to dissipate extra heat, and the power consumption of electric heaters to maintain the temperature of the electronic components during eclipses.

For the most sensitive electronic elements of the spacecraft (platform and payload), the radiators are sized by evaluating their energy balance, assuming that the radiator is the only thermal interface with the environment. While this is not strictly true, it is an adequate assumption for elements with strictly controlled environment such as the transmitter stage of the lidar.

6.4.1.1 Analytical model

The starting point is the observation that an energy balance equation based on the principle of conservation of energy will yield the body to adopt an equilibrium temperature [Panetti, 1999]:

$$q_{absorbed} + q_{dissipated} - q_{emitted} = 0 \qquad (6\text{-}4)$$

where $q_{absorbed}$ corresponds to the energy coming from the spacecraft environment that is absorbed by the external surfaces of the satellite, $q_{dissipated}$ represents the energy dissipated by the electronic unit connected to the radiator, and $q_{emitted}$ stands for the energy that is emitted by the radiator.[3]

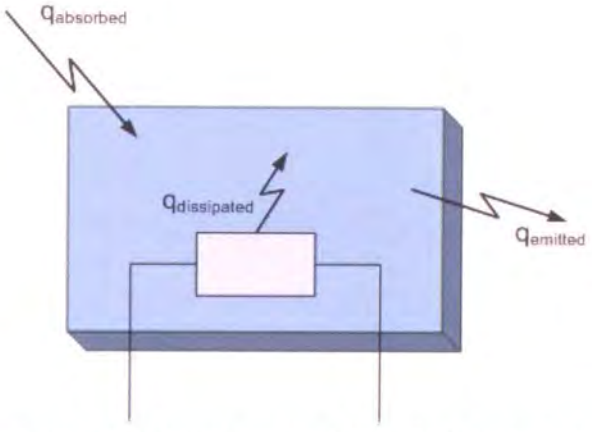

Figure 6-8. Heat exchanges of an electrical system.

The energy exchanges between the radiator and its environment are:

- Power from direct sunlight;
- Power from sunlight reflected off the Earth (albedo);
- IR radiation to and from the Earth;
- IR radiation to space.

The equations for each of these power sources, adapted from Griffin & French [2004], are summarised in Table 6-12. In this table, G_S is the direct solar flux which varies seasonally with the distance of the Earth from the sun, from 1318 W/m^2 in the summer (near the aphelion) to 1422 W/m^2 in the winter (near the perihelion) [NASA, 1991]. In the case of the payload radiator, which is located on the anti-Sun side of the satellite, there is no direct sunlight component, which can thus be ignored.

[3] While the word "energy" is used, q really is a power density in W/m^2.

Parameter	Equation	Comments
Direct solar radiation power	$q_s = G_S \alpha_{rad} \cos\theta_{s/rad}$	G_s: solar radiation flux α_{rad}: absorptance of radiator material $\theta_{s/rad}$: sun incidence angle on radiator
Earth-reflected Solar radiation power	$q_a = F_{rad,El} G_S a \alpha_{rad} K_a$	$F_{rad,El}$: view factor of the radiator to the illuminated part of Earth a: Earth albedo K_a: geometric factor (see text)
Power emitted by the radiator to the Earth, minus Earth infrared emission to the radiator	$q_{rad,E} = \sigma \varepsilon_{rad} F_{rad,E} \left(T_{rad}^4 - T_{Earth}^4\right)$	σ: Stefan-Boltzmann constant ε_{rad}: IR emissivity of the radiator $F_{rad,E}$: view factor of the radiator to the whole Earth T_{rad}: equilibrium temperature of the radiator T_{Earth}: temperature of the Earth
Power emitted by the radiator to space	$q_{rad,s} = \sigma \varepsilon_{rad} F_{rad,s} \left(T_{rad}^4 - T_{space}^4\right)$	$F_{rad,s}$: view factor of the radiator to space T_{space}: temperature of space, approximately 0 K.

Table 6-12. Power exchanges between a radiator and its environment for the purpose of thermal control system sizing

The albedo factor, a, is expressed as a percentage, and is taken here as an average over the year at given latitude regions, obtained from Leffler [1987]. The view factor of the radiator to the illuminated portion of the Earth, denoted $F_{rad,El}$, is expressed as a fraction of the view factor of the radiator to the Earth. This fraction is approximated through geometry analysis, by estimating how much of the Earth viewed by the radiator is illuminated by the sun, so that:

$$F_{rad,El} = F_{rad,E} \times \frac{A_{Earth_viewed_light}}{A_{Earth_viewed_total}} \tag{6-5}$$

The method to compute $F_{rad,E}$ is presented in section 6.4.1.2.

The geometric factor K_a accounts for "the reflection of collimated incoming solar energy off a spherical Earth" [Wertz & Larson, 1999]:

$$K_a = 0.664 + 0.521\rho - 0.203\rho^2 \tag{6-6}$$

$$\rho = \sin^{-1}\left(\frac{R_E}{R_E + h}\right) \tag{6-7}$$

The angular radius of the Earth, ρ, as seen by the spacecraft should be in radians.

The radiator is assumed to have a temperature T_{rad} somewhere in the region of 0-50°C (depending on what electronic component it is connected to) and thus emits in the infrared spectrum. It emits primarily towards deep space, which has a temperature of nearly 0 K, and thus the radiator does not receive radiation from deep space.

However, the radiator can have the Earth in its field of view, in which case there is an infrared radiation exchange between the radiator and the Earth. The temperature and thus IR power emitted by the Earth depends on the solar flux and the albedo of the Earth [NASA, 1991]:

$$q_{IR_Earth} = \frac{(1-a)\times G_s}{4} \tag{6-8}$$

from which the temperature of the Earth (for the purpose of thermal analysis) is derived, assuming a blackbody:

$$q_{IR_Earth} = \sigma T_{Earth}^4 \tag{6-9}$$

Finally, assuming that the radiator has only deep space or the Earth in its 2π steradian FoV, the view factor of radiator to deep space can be found by [Savage, 2003]:

$$F_{rad,s} + F_{rad,E} = 1 \tag{6-10}$$

6.4.1.2 View factors

The European Space Agency [1989] published the PSS-03-108 standards on thermal control data within which a wide range of view factors is compiled. Of particular interest for the albedo and Earth IR radiation cases is a table of the view factor for one face of an elemental plate to a sphere, for a range of altitudes and angles between the normal to the surface and the nadir direction, λ (Figure 6-9). It also gives the analytical expression (after reformulation):

$$F_{12} = \sin^2 \rho \cdot \cos \lambda \tag{6-11}$$

whose applicability is quite restricted ($\lambda + \rho < 90°$). Due to the satellite configuration, there are two values of λ that are of interest: 0° and 90°. For $\lambda = 0°$, this equation yields satisfying results, particularly in the altitude range of interest to this study (300 to 400 km). However, it becomes useless for $\lambda = 90°$, which is the case of the lidar radiator.

Thus, it is proposed to evaluate the view factor by means of a trend line that satisfactorily fits the data given by the PSS-03-108 standards for an altitude range relevant to the concepts studied. The following linear relationship has been derived:

$$F_{12}[\lambda = 90°] \cong 0.5938\rho - 0.4369 \tag{6-12}$$

A word of caution is essential: while this approximation works quite well for altitudes up to $0.1 \times R_E$ (i.e. ~638 km) and thus for the altitude range considered in this study, it becomes inaccurate above $0.2 \times R_E$. In between these altitudes, its reliability is unknown, because of a gap in the data presented in the standards.

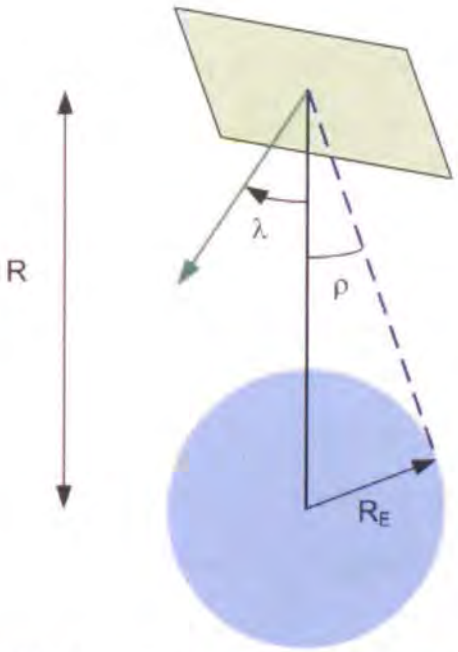

Figure 6-9. Illustration of the parameters involved in the computation of the view factors.

6.4.1.3 Radiator sizing

The radiator sizing assumes the worst case in the lifetime of the satellite. The hot case occurs during the winter solstice when the solar flux is highest (and thus Earth-reflected solar power and Earth temperature too), towards the end of the mission, when the radiator absorptance of visible light degrades to its highest value.

The method follows that presented by Gilmore et al [2003]. The equations of Table 6-12 are evaluated at various positions in the orbit (30° apart in argument of latitude), and the average is taken for each type of power emitted or absorbed. These averages then lead to the computation of the radiator surface area:

$$A_{rad} = \frac{Q_{diss}}{q_{rad,E} + q_{rad,s} - q_a - q_s} \tag{6-13}$$

This equation requires the knowledge of the power dissipated, Q_{diss}, by the device connected to the radiator, and the temperature of the radiator. Gilmore et al (2003) assumes that the radiator temperature is 10 K lower than the maximum allowable temperature of the device in nominal mode (or in whichever mode the device dissipates the most power). This difference is an analysis uncertainty margin, but part of which would represent a real temperature gradient between the device and its radiator, depending on the distance between the two, i.e. where heat pipes provide the thermal interface.

6.4.1.4 Heaters sizing

The heaters are particularly required in the worst cold condition. In the present case, this occurs during the summer when the solar flux is minimal, and which is also the season where the satellite experiences eclipses when flying over the south pole region. Because the radiator is sized for end-of-life (EOL), the heaters are sized for beginning-of-life (BOL) when the radiator is more efficient at dissipating heat.

There are in fact two cases that should be considered for the worst cold condition: operating and non-operating. When operating normally, electronic units dissipate electrical power as

heat which warms them up, but in safe mode only the essential equipments are powered, while others are reverted to a minimum power consumption (or no power at all). In this case, heaters with a lower power consumption may be required to maintain a survival temperature. The latter is generally much lower than the minimum operational temperature, and the heater power level for the worst cold operational case most often tends to be more than enough to keep the temperature well above the survival temperature during the worst cold non-operational case.

The same method as used in the radiator sizing is applied to the heater power sizing. With the average power densities over an orbit determined for the summer solstice, and having determined the size of the radiator, it follows that:

$$Q_{heaters} = A_{rad}\left(q_{rad,E} + q_{rad,s} - q_a - q_s\right) - Q_{diss} \tag{6-14}$$

where the terms are defined as per Table 6-12. In this equation, however, the radiator temperature should now be 10 K lower than the minimum (not maximum as previously) operational temperature of the unit considered.

6.4.1.5 Thermal control system budgets

The mass and power budgets of the thermal control system (TCS) are presented in Table 6-13, and discussed briefly below.

Multi-Layer Insulation (MLI)

While most surfaces of the satellite can be covered in "conventional" MLI with a top layer of Kapton, the front face receives a considerable flux of Atomix Oxygen (ATOX) and thus requires a stronger but heavier Beta cloth material as the top layer [Donabedian & Gilmore, 2002]. Beta Cloth would replace the outer layer of the MLI, and causes the MLI to be heavier by 270 g/m^2, i.e., negligible at this stage.

Radiators

For the radiators, the properties have been assumed to be that of optical solar reflectors (OSR), which not only have an excellent α/ε ratio, but the surface finish is also particularly

resistant to ATOX erosion too. The optical characteristics of the OSR are given in Table 6-14.

Miscellaneous

Determining the mass of heaters (thermostats and thermistors) as well as the MLI adhesives and internal paint cannot be done precisely until a more advanced stage in the satellite design process. As an approximation, this will be assumed to be twice the mass of MLI alone.

Element	Mass	Power
Radiator & heat pipes	15 kg/m^2	0
MLI	0.73 kg/m^2	0
Betacloth	1.00 kg/m^2	0
Heaters (thermostats, thermistors), adhesives, paints, etc.	$= 2 \times \Sigma m_{MLI}$	$Q_{heaters}$

Table 6-13. Mass and power budgets of the Thermal Control System.

Material	Absorptivity, α	Emissivity, ε
ITO + UV reflective coated glass (OSR)	BOL: 0.05	0.78
	EOL: 0.11	

Table 6-14. Radiator optical properties

6.4.2 Electrical power system

The electrical power system (EPS) is composed of a battery to power the spacecraft and instrument during the eclipse period, a solar array to power the spacecraft and recharge the battery during the sun phase of the orbit, and a power conditioning and distribution unit (PCDU) to regulate and distribute the power to the subsystems.

The EPS sizing depends greatly on the power regulation system considered; the direct energy transfer (DET) or maximum peak power tracker (MPPT). The latter is recommended primarily for high-power (above ~1kW) platforms in orbits with regular eclipse period, as it requires a slightly smaller solar array despite more power being dissipated. Furthermore it is more complex, and therefore more expensive, although with an ever growing number of satellites using the MPPT regulation system, more off-the-shelf PCDUs are likely to become available at a lower cost than currently so.

A lidar mission would most often require powers in the order of 2 to 4 kilowatts, and in a dawn-dusk orbits would experience eclipses only during either one of the solstices. Thus, the difference between the two systems could be rather small in terms of overall mass and solar array size. Hence, the DET system is currently assumed on the basis of its suitability for dawn-dusk orbits, and it can be seen as the worst case for solar array size.

Another assumption is made on the design of the solar array. Most commonly, solar arrays would rotate to minimise the sun illumination angle and hence maximise the power generated by an array of a given surface area. In the case of a lidar mission, a non-rotating solar array is preferred due to the micro-vibrations that could be generated and degrade the quality of the lidar measurements. As mentioned in previous chapters, it is important that the solar panel is oriented in such a way that it does not contribute to the generation of drag force. Hence any offset must be in roll, as a yaw angle would generate drag and a pitch angle would not improve the sun incidence angle.

The following sections describe the method to size the solar panels and the batteries.

6.4.2.1 Power requirements

The first step in the sizing of the EPS is to determine the power requirements of the whole spacecraft. Worst-case power conditions must be considered, which corresponds to the period of longest eclipse, i.e. the summer solstice for a 06:00 LTDN dawn-dusk orbit. The power needs of the spacecraft during both the sun-illuminated part of the orbit as well as the

power released by the battery during the eclipse must be taken into account. The mean power consumption can be written as:

$$P_{mean} = \frac{1}{T_{orbit}}\left(\frac{P_1 T_1}{\eta_1} + \frac{P_2 T_2}{\eta_2} + \cdots + \frac{P_n T_n}{\eta_n}\right) \tag{6-15}$$

where $P_{1,2,...n}$ are the power consumptions during operational modes 1,2,...n and $T_{1,2,...n}$ is the duration of each of these modes during one orbit, while T_{orbit} is the orbit period. The power transfer efficiencies $\eta_{1,2,...n}$ are an indication of the power losses in the harnesses, for which Brown [2002] considers two cases:

- daylight: losses from the solar array to the load, $\eta \sim 0.98$;
- eclipse: losses from the array to the battery and from the battery to the load, $\eta \sim 0.95$.

Hence, a power consumption profile must be established. Nominal operational modes have been identified (Table 6-15), and their time of occurrence represented in Figure 6-10.

Mode number	Description	Comments
1	"Normal" mode Lidar and EP on.	Most of the orbit in daylight.
2	Mode 1 + heaters on	During eclipse
3	Mode 1 + X-band on	Payload data transmission during part of a ground station pass

Table 6-15. Operational modes to be considered for the EPS sizing.

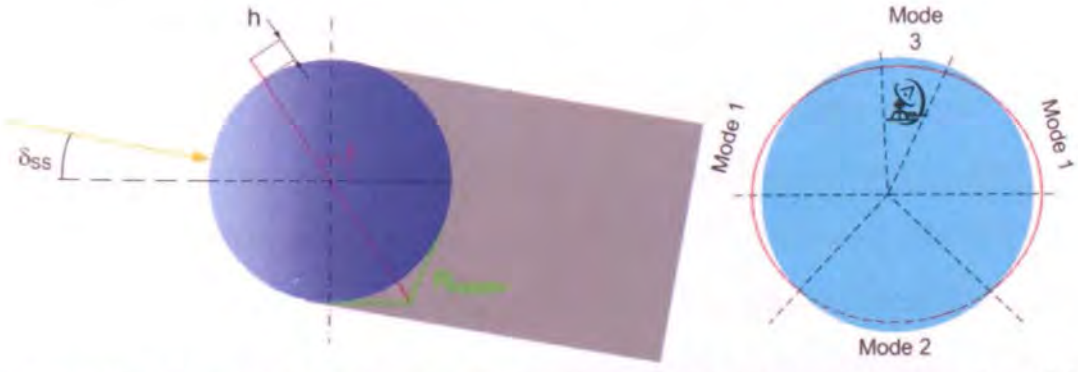

Figure 6-10. Left: eclispse geometry as seen from 18:00 LST, and right: location of the operational modes in the orbit (seen from 12:00 LST)

6.4.2.1.1 Computation of eclipse duration

Mode 2 runs throughout the eclipse period. The eclipse duration can be computed by the following equation, adapted from [Brown, 2002]:

$$T_2 = \frac{T_{orbit}}{180°}\cos^{-1}\left[\frac{R_{horizon}/(R_E + h)}{\cos(180 - i - \delta_{SS})}\right] \quad (6\text{-}16)$$

where T_{orbit} is the orbital period, $R_{horizon}$ is the range of the horizon from the spacecraft, R_E is the mean radius of the Earth, h is the mean orbit altitude, i is the inclination of the orbit and δ_{SS} is the angle of the sun during the summer solstice with respect to the equatorial plane (i.e. 23.46 degrees). $R_{horizon}$ can be obtained by geometry, and by substitution, Equation (6-16) becomes:

$$T_2 = \frac{T_{orbit}}{180°}\cos^{-1}\left[\frac{\sqrt{h^2 + 2R_E h}/(R_E + h)}{\cos(180 - i - \delta_{SS})}\right] \quad (6\text{-}17)$$

The accuracy of this equation has been cross-checked with data obtained from a Satellite Tool Kit (STK) simulation. Equation (6-17) underestimates the eclipse duration by two seconds on average in the altitude range between 300 and 400 km. Compared to eclipse durations of the order of 25-30 minutes, the error is clearly negligible.

6.4.2.1.2 Mode 3 duration

The duration of Mode 3 depends on the time required for the payload data to be transmitted to the ground in every orbit. Typically, a station like Svalbard can be seen for more than 5 minutes in every orbit. The use of a station in lower latitudes would result in blind orbits. However, lidars typically generate a low volume of data: even for the worst case data volume of 10 Gb per orbit, as generated by A-SCOPE (section 6.3.5), a downlink time of about half a minute is required with a standard 300 Mbps X-Band data transmission system.

6.4.2.1.3 Mode 1 duration

From the duration of Mode 2 and 3, it follows that the duration of Mode 1 is simply:

$$T_1 = T_{orbit} - (T_2 + T_3) \tag{6-18}$$

6.4.2.2 Solar array sizing

The basic rule for the sizing of the solar arrays is that they must produce at least the same amount of energy as the energy consumed by the satellite.

Having determined the mean power consumption of the spacecraft, the power that must be generated by the solar arrays, P_{SA}, is:

$$P_{SA} T_{SA} = P_{mean} T_{orbit} \tag{6-19}$$

where T_{SA} is the period during which the solar arrays generate power, i.e. during Modes 1 and 3:

$$T_{SA} = T_1 + T_3 = T_{orbit} - T_2 \tag{6-20}$$

There are many parameters affecting the power generated by a solar array:

- The solar cell characteristics (efficiency, performance degradation over mission lifetime, performance as a function of temperature);
- The temperature of the solar cells;
- The seasonal variations in solar radiation flux;
- The solar radiation incidence angle.

The required surface area of the solar array will also depend on:

- The surface area occupied by a cell;
- The number of cells in a string to meet the bus voltage;
- The number of strings required to provide the necessary power;
- The number of additional strings for redundancy;

- The number of panels and the number of strings per panel.

All these parameters are discussed in the following subsections.

6.4.2.2.1 Solar cell characteristics

The solar array is based on a GaInP/GaAs/Ge triple junction cell on a Ge substrate developed by AZUR SPACE [2009]. Its characteristics are given in Table 6-16.

For satellites in polar orbits below about 700-km altitude, the radiation dose tends to be quite small; Tribble et al [1999] indicate a radiation dose rate in the order of 10^3 Rads per year. For a 3.5-year mission, this is clearly below the lowest value of 5×10^{14} Rads given in the cell brochure; thus taking the latter total radiation dose value provides a robust safety margin.

6.4.2.2.2 Seasonal solar radiation intensity

As the Earth orbit around the sun is elliptical, the solar radiation flux per unit area at the Earth varies through the year. At the summer solstice (~21 June), the Earth is almost at its aphelion, i.e. 1.016 A.U. from the sun, thus the solar radiation intensity is 1324 W/m^2. The performance of the cell is given for laboratory conditions (1367 W/m^2) and must be adjusted accordingly.

6.4.2.2.3 Losses and degradations

There are various factors affecting the ability of a solar cell to generate power. For instance, not all the incident solar energy will interact with the cell; some will be reflected by the glass cover. As shown in Table 6-16, the amount of energy absorbed is 91% for the chosen cell.

The performance of the cell also degrades over the mission lifetime due to the space environment. This includes losses due to radiation, UV discoloration, thermal cycling, surface contamination, etc. In the case of radiation losses, the effect is only taken into account in the voltage and current of the cell. The cell temperature and the sun incidence angle are taken into account separately, and should not be incorporated here.

Table 6-17 lists the losses and degradations that must be added to the solar array sizing, and also gives an estimate of the other losses taken into account in later stages of the sizing process.

Parameter	Value	
Dimensions	40 × 80 mm	
Effective surface area	30.18 cm^2	
Absorptivity	91%	
Radiation dose	BOL	5×10^{14}
Performance under lab conditions (1367 W/m2, 28°C)		
Voltage at max. power, Vpmax [mV]	2379	93%
Current at max. power, Ipmax [mA]	505	98%
Temperature gradients		
Voltage at max. power, dVpmax/dT [mV/°C]	-6.1	-6.3
Current at max. power, dIpmax/dT [mA/°C]	0.28	0.20

Table 6-16. Azur Space triple-junction solar cell characteristics [Azur Space, 2009]

Degradations and losses	Value	Comments
Cell absorptivity	0.91	The rest is mainly reflected
Surface contamination	0.99	[Brown, 2002], e.g. ATOX
UV discolouration	0.98	[Brown, 2002]
Resistance in cell interconnects	0.98	[Brown, 2002]
Thermal cycling	0.995	Limited number of thermal cycles
Total	0.86	
Losses already taken into account		
Radiation damage	0.91	Losses on voltage and current
Cell temperature	0.86	Mean temperature of 65°C

Table 6-17. List of degradations and losses for the sizing of the solar array.

6.4.2.2.4 Sun incidence angle

Assuming that the solar arrays are non-rotating, the Sun incidence angle may vary throughout the orbit if the arrays are not in the plane of the orbit. As such, the angle of the solar array can be optimised.

Figure 6-11 illustrates the sun incidence angle at an altitude of 300 km at the Summer Solstice for 3 solar array angles. When the array is in the orbital plane (0-degree angle), the sun incidence is constant at 30.1 degrees. By setting the solar array angle to 30 degrees, the sun incidence angle at the North Pole becomes zero, but increases rapidly away from this point. The optimal solar array angle in this particular case has been calculated to be about 13 degrees.

It should be stressed that the power generated follows a cosine rule but for large incidence angles, the actual power generated is less than what the cosine law predicts [Brown, 2002]. There is not a clear-cut incidence angle where this occurs, but is between 45° [Brown, 2002] and 60° [Griffin & French, 2004].

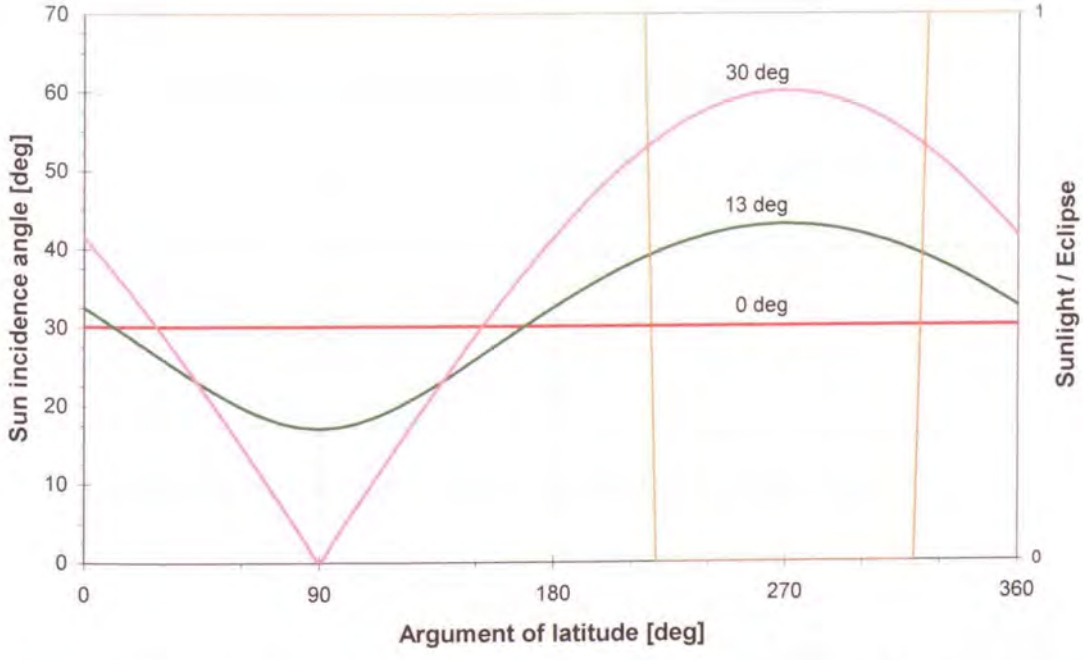

Figure 6-11. Sun incidence angle for 3 angles of the solar array wrt the orbit plane.

6.4.2.2.5 Solar cell temperature

The temperature of the solar array will vary with its orientation with respect to the orbit plane, as well as with the orbit altitude. The solar array angle will have an impact on its view factor of and energy received from the Sun and the Earth (IR emission and albedo). The steady-state temperature of the solar array at various points in the orbit can be computed from the method presented by Panetti [1999].

Based on the previous case (300 km, Summer solstice) the steady-state temperature along the orbit of the solar array at an angle of 13 degrees would vary in a way depicted by Figure 6-12.

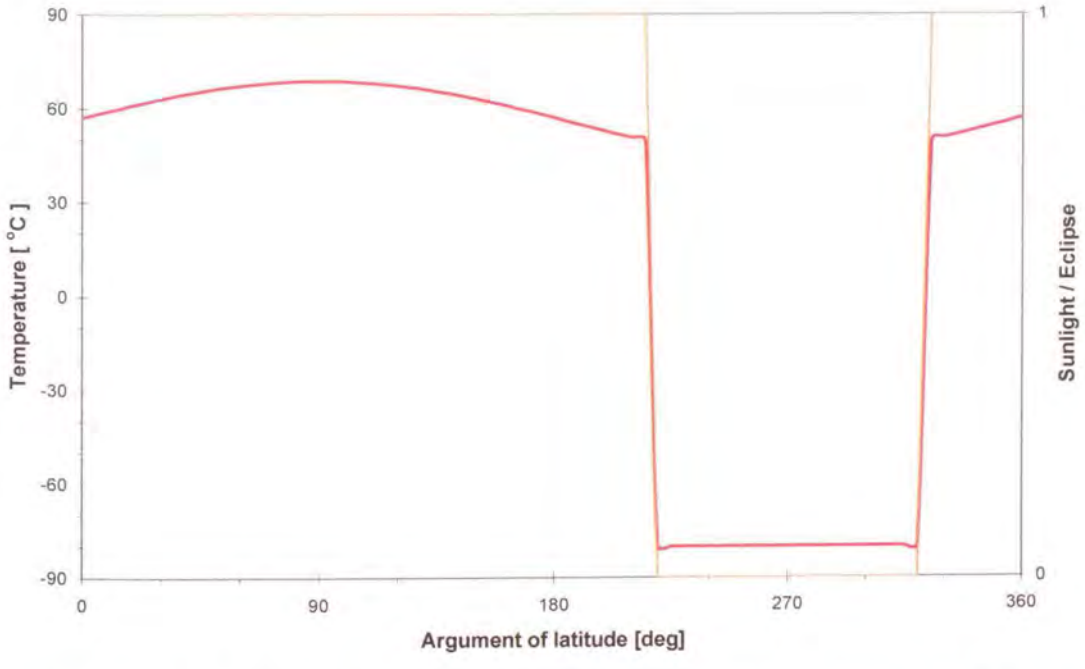

Figure 6-12. Solar array steady-state temperature for a solar panel angle of 13° wrt to the orbit plane (red), during summer solstice at an altitude of 300 km.

The thin orange line represents the sunlight/eclipse condition.

6.4.2.2.6 Surface area occupied by a solar cell

When mounted on the substrate, a cell occupies a space larger than its surface area, as illustrated by Figure 6-13. A small gap between cells is necessary but should not be too large in order to keep the size of the solar array to a minimum. A packing factor of 85% is a good representative value.

6.4.2.2.7 Number of cells per string

The cells are arranged in series of strings to meet the bus voltage, and a number of strings in parallel to meet the current and power.

The most common bus voltage is 28 V, although higher voltages are possible for high-power applications to limit power losses in cables. It is also possible to have multiple power buses on a satellite. For a 28 V bus, Griffin & French [2004] recommend the solar array voltage to be about 20% above the battery voltage for the battery to charge. The nominal battery voltage, as will be shown in Chapter 5.3.3.3 is 28.8 V. The number of solar cells in a string is:

$$n_{cells/string} = \frac{1.2 \times V_{bus}}{V_{cell@EOL}} \tag{6-21}$$

Under the radiation and temperature gradient conditions of Table 6-16, and a cell mean temperature in sunlight of 65°C, it follows that a string must be made of 17 or 18 cells connected in series. 17 cells are deemed sufficient with a voltage at EOL of 33.6 V.

6.4.2.2.8 Number of strings

The power generated by a string under the conditions described above is thus:

$$P_{string} = n_{cells/string} \frac{Q_S}{Q_{lab}} \left(V_{op_cell} I_{op_cell}\right) \eta_{losses} \cos\alpha_{mean} \tag{6-22}$$

The number of strings is the ratio of P_{SA} computed earlier to P_{string}. However, an additional string should be added for contingency.

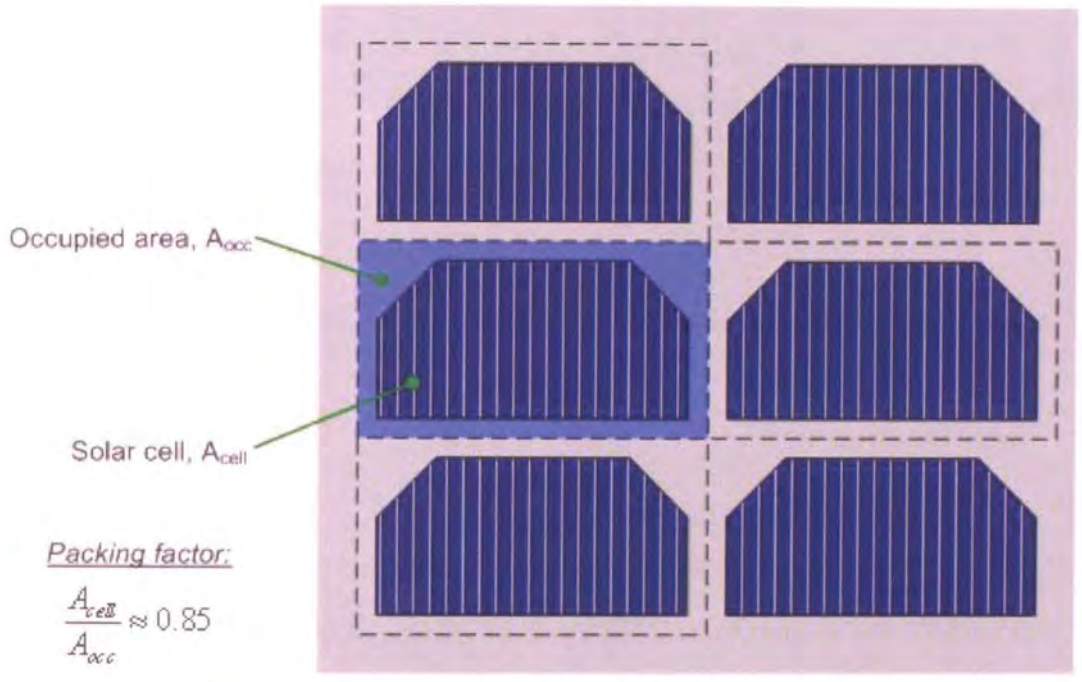

Figure 6-13. Illustration of solar cell packing factor.

In reality though, it is likely that the total number of strings is a multiple of the number of identical panels to avoid non-recurring costs in the procurement of the solar panels. Hence, the number of panels for each wing (we assume 2 symmetric wings) and the number of strings per panel will be set iteratively, so that:

$$2 \times n_{panels/wing} \times n_{strings/panel} = \left(\frac{P_{SA}}{P_{string}} \right)_{rounded_up} + 1 \tag{6-23}$$

6.4.2.2.9 Solar array physical dimensions

The surface area of a single panel is thus the surface area occupied by all the cells on the panel including the packing factor:

$$A_{panel} = \frac{n_{strings/panel} \times n_{cells/string} \times A_{cell_footprint}}{\eta_{packing}} \tag{6-24}$$

And the total surface area is simply the surface area of one panel multiplied by the total number of panels.

6.4.2.2.10 Solar array mass

The mass of one wing, m_{wing}, is computed from a specific mass, M_{panel}, of 4 kg/m^2, which is typical of solar panels with rigid substrate [Brown, 2002]:

$$m_{wing} = n_{panels/wing} \times A_{panel} \times M_{panel} \tag{6-25}$$

The mass of the yoke and the deployment should also be added; these amount to 5 kg per wing, approximately.

6.4.2.3 Battery sizing

The battery size depends on the amount of energy required in eclipse and the battery Depth of Discharge (DOD), i.e. the portion of the battery that is allowed to discharge during the eclipse period. For a dawn-dusk orbit, there must be a compromise between the size of a battery that is used only for part of the year and the DOD that must be small enough so that the spacecraft can operate in safe mode for a couple of orbits in case of a fault with total solar array power loss. The DOD also depends on how fast it can be recharged during normal operation. For their LEO applications batteries, Saft [2007] recommends a 20% DOD at a charge rate of C/5. This means that the battery receives a charge equivalent to a fifth of its total capacity in an hour, which matches the average LEO conditions (approximately 60 minutes of sunlight per orbit to recharge the battery by 20% of its capacity). The DOD with respect to the maximum state of charge (SOC) at end of life is taken here as the fraction of the eclipse duration to the orbit period:

$$DOD = \frac{T_2}{T_{orbit}} \tag{6-26}$$

It is recommended not to charge Li-ion batteries to their full capability, so maximum SOC of 90% is assumed. With T_2 expressed in hours, the maximum energy stored in the battery at the EOL is simply:

$$E_{EOL@90\%SOC} = \frac{P_2 T_2}{DOD} \tag{6-27}$$

It is assumed here that the battery design is based on that of ABSL, illustrated in Figure 6-14, with strings of 8 SONY 18650 HC cells, which have a nominal voltage of 3.6 V and a 1.5-A.h capacity [Pearson et al, 2005]. Batteries with 8 cells in series (8s), can deliver a voltage in the range 20-33.6 V, with a nominal voltage of 28.8 V. Strings of cells are assembled in parallel to provide the required current. With X number of strings in parallel, the battery would be denominated as 8sXp.

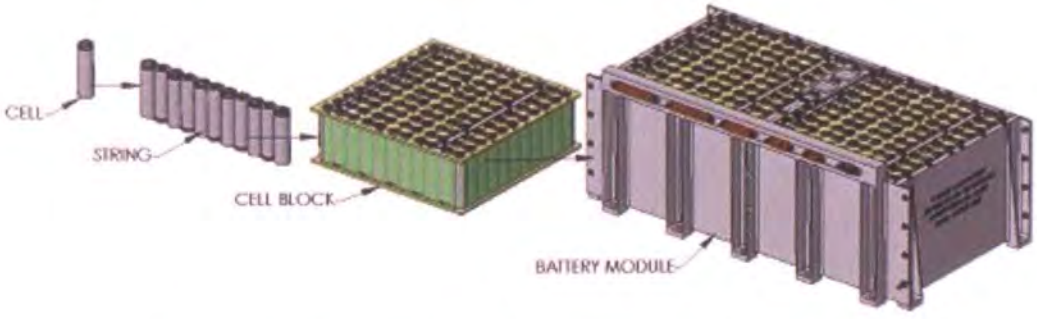

Figure 6-14. Typical ABSL Battery design [ABSL, 2009]

Parameter	Value
Dimensions	18 mm (∅) × 65 mm
Mass	42 grams
Nameplate Cell Capacity	1.5 Ah
Nameplate Cell Energy	5.4 Wh
Cell Voltage: Nominal Range	3.6 V 2.5 to 4.2 V

Table 6-18. Characteristics of the SONY 18650HC, from Spurrett et al [2002].

The battery capacity at the End of Life (EOL) and 90% SOC is then:

$$C_{EOL@90\%SOC} = \frac{E_{EOL@90\%SOC}}{8V_{cell}} \tag{6-28}$$

The battery capacity required at the BOL is obtained by taking into account the cell ageing, η_{ageing}, which for the mission profile considered (small number of cycles per year, short mission) can be assumed to be as much as 28% for worst-case conditions (high temperature and high discharge voltage) over 3,900 charge-discharge cycles, based on test data presented by Neubauer et al (2007). The required battery capacity at BOL and 90% SOC is then:

$$C_{BOL@90\%SOC} = \frac{C_{EOL@90\%SOC}}{1-\eta_{ageing}} \tag{6-29}$$

Hence, the full capacity of the battery at BOL is:

$$C_{BOL} = \frac{C_{BOL@90\%SOC}}{0.9} \tag{6-30}$$

The cells (and strings of cells) have a nominal capacity of 1.5 Ah, thus the number of strings required is:

$$N_{strings_req} = \frac{C_{BOL}}{C_{cell}} \tag{6-31}$$

The number is rounded up and an additional string is added for safety.

Due to the power demands of the satellite, dividing the battery into two battery modules is better than a single one as the accommodation on the platform is more flexible. Furthermore, based on Figure 6-14, each module is made of two stacked blocks. From a cost point of view, it is probably cheaper that the two modules are identical and the blocks in each module are identical too. Thus the number of required strings is divided by two, rounded up, then divided by two and rounded up again to obtain the number of strings per block. The number of strings per block is required to establish the footprint dimensions of the battery module.

Based on ABSL data of their batteries, a value of specific energy per unit mass, $\varepsilon_{battery}$, can be found to be about 100 W.h/kg, as shown in Figure 6-15, inclusive of packaging structure. An estimate of one battery module mass:

$$m_{module} = \frac{E_{module}}{\varepsilon_{battery}} = \frac{N_{strings/module} \times E_{cell}}{\varepsilon_{battery}} \tag{6-32}$$

However, it can be seen from Figure 6-15 that this approximation is very accurate for small batteries, but fairly inaccurate for a battery module with an energy above 1500 Wh. Through analysis of ABSL battery specifications, it can be estimated that the packaging structure of a battery module is equivalent to about 20% of its cells mass. Thus, a better estimation of the module mass is:

$$m_{module} = \left(N_{cells/module} \times m_{cell}\right) \times 1.2 \tag{6-33}$$

6.4.2.3.1 Battery thermal requirements

The temperature requirements for Li-ion batteries are in the range +10 to +35°C during charge, and 0° to 40°C during discharge. The power dissipated by the battery in the form of heat is assumed to be 5% of the power drawn from the battery during eclipse.

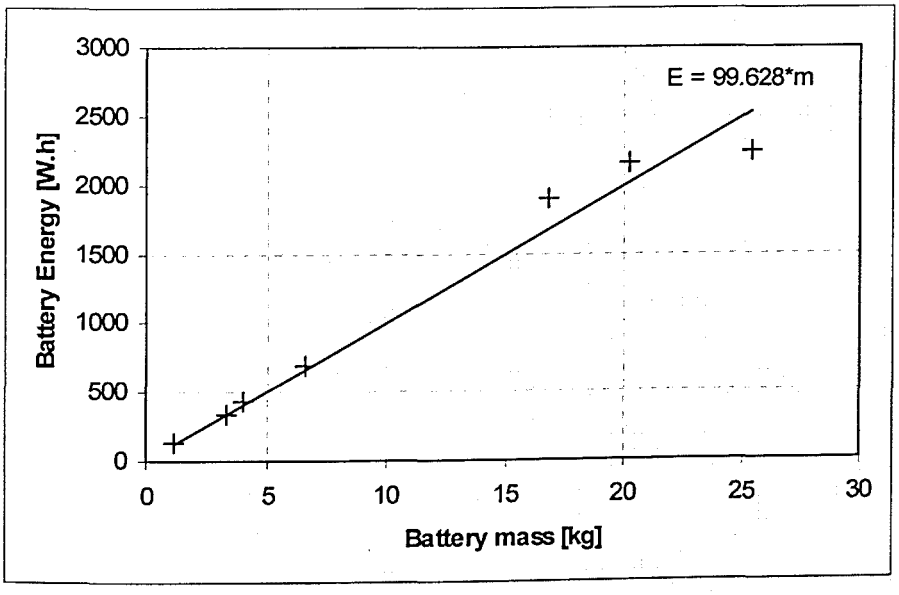

Figure 6-15. Energy vs. mass for a range of AEA Technology batteries.

Based on data from Pearson et al [2005]

6.4.2.4 Power Conditioning and Distribution Unit

The PCDU regulates the power bus characteristics and is the interface between the solar arrays, the batteries, and the loads.

The characteristics of the PCDU depend on the type of bus considered (DET, MPPT) and the number and types of interfaces (solar arrays, batteries, pyros, heaters, etc.).

We will use as a reference the TAS PCDU Medium Power [TAS, 2006]. It is designed to be modular, with the functions implemented in modules of a standardised size, which are plugged into a common baseplate. Each module is 25.5-mm or 33.5-mm wide with a mass between 1.25 and 2.05 kg.

The characteristics of the PCDU, for the desired or anticipated functions, are given in Table 6-19. The consumption (and dissipation) of the PCDU is estimated at 5% of the spacecraft total power during eclipse, and increased by 50% in sunlight when charging the batteries.

6.4.2.5 Electrical Power System budgets

The dimensions and mass and power budgets of the overall Electrical Power System are summarised in Table 6-19.

Element	Dimensions	Mass	Power
Solar panel	variable	m_{SA}	0
PCDU	350 (L) × 340 (W) × 190 (H)	18	5% of total power
Batteries	variable	m_{batt}	P_{batt}

Table 6-19. Electrical Power System mass and power budgets

6.4.3 Structure

The structure design drivers relate to the spacecraft configuration and the accommodation of internal equipment and tanks in particular. Figure 6-16, left, illustrates the central cylinder structure proposed for A-SCOPE Phase 0, while the image on the right is an exploded view of Mars Express (MEX) showing the primary structure made up of five shear panels. In the latter case, large brackets are needed to fix the shear walls to the launch vehicle attachment ring [Houghton, 2003]. The MEX structure is particularly suited when two large tanks are required, as in the case for MEX and Aeolus. For the four lidar mission concepts, the selection of the structure type would depend on the number of tanks preferred.

For the configuration shown on the left in Figure 6-16, the main structural elements are the central cylinder, to which the four shear walls are attached with brackets. The bottom and top floors of the platform are attached to the central cylinder and the shear walls. The side walls constitute the secondary structure and carry many heat-dissipating electronics. The launch loads are carried from the equipment on the side walls to the central thrust by the shear walls.

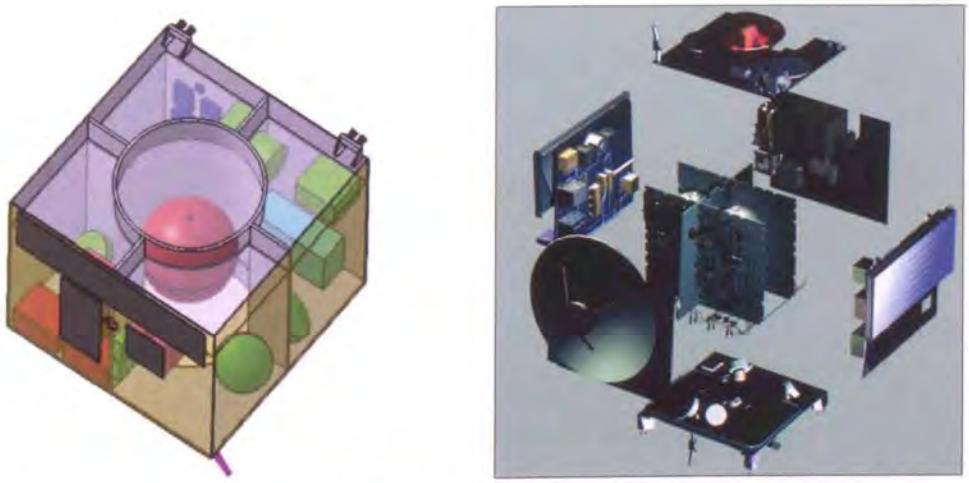

Figure 6-16. Left: A-SCOPE platform structure in Phase 0 [ESA, 2008]; right: Exploded view of Mars Express showing the internal shear walls [ESA, 2001]

The elements of the structure are made of Aluminium honeycomb. The honeycomb core is made of cells which can be of various dimensions; one common size is 1/8". The thickness

can also vary with specifications, and as a first iteration, it will be assumed as 20 mm for primary structure and 10 mm for secondary structure elements. As represented in Figure 6-17, an adhesive is inserted between the aluminium honeycomb and the skin. The latter can either be a sheet of carbon fibre reinforced plastic (CFRP) or aluminium, depending on the thermo-mechanical requirements and cost constraints. Aluminium has a higher density than CFRP (2800 vs. 1675 kg/m^3) and thus represents a worst case mass-wise. Again, the thickness of the skin will depend on the requirements of each structural element. The skin thickness can be assumed to be 1 mm for shear walls, and 0.5 or 0.25 mm for external panels.

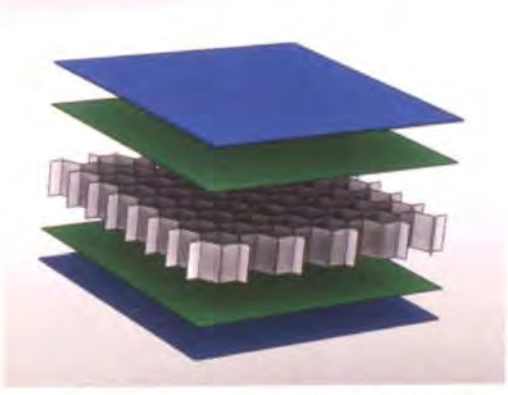

Figure 6-17. Honeycomb sandwich panel with skin (blue) and adhesive (green).

[Bellcomb Technologies Inc., 2007]

	Aluminium honeycomb 1/8 – 5056 – .0007	Aluminium (skin) 2024-T6	Adhesive
Density	3.1 lb/ft^3 49.657 kg/m^3	2800 kg/m^3	367 g/m^2
Reference	[Hexcel, 1999]	[Griffin & French, 2004]	[Hexcel, 2008]

Table 6-20. Mass properties of Aluminium honeycomb sandwich panel materials.

6.4.4 Onboard Data Handling

The onboard data handling (OBDH) system, represented in Figure 6-18, consists of an onboard computer (OBC) and a remote interface unit (RIU).

The OBC handles the telecommands received from the ground, storing, executing or redistributing them. It also runs the commands stored according to the mission scenario (based on time or position), and collects telemetry data from the subsystems for downlink to the control centre on ground.

The remote interface unit (RIU) serves to connect simple equipments with internal control capacity to the main data bus and OBC [Maral &Bousquet, 2002]. This is the case, for instance, with the reaction wheels, reaction control system (propulsion), various AOCS equipment, etc.

The mass and power budgets for the OBC and RIU are given in Table 6-21.

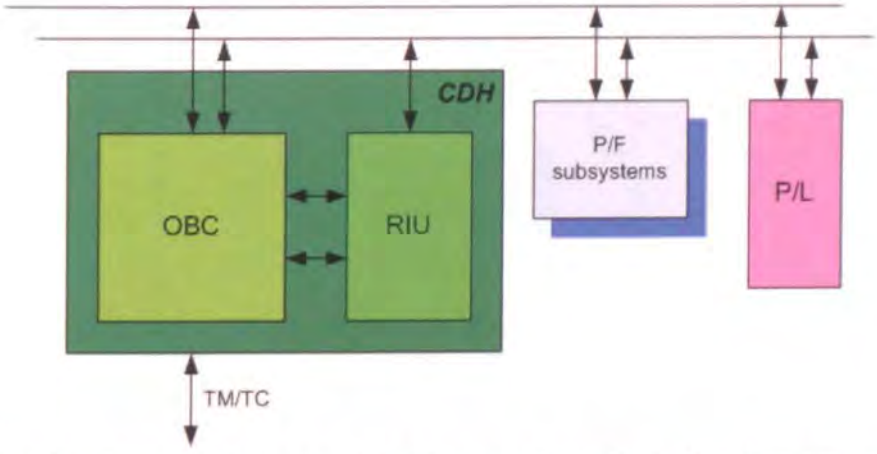

Figure 6-18. Schematic diagram of the Command and Data Handling architecture.

Component	Mass (kg)	Power (W)	Dimensions (mm)
OBC	16	40 W (average) 60 W (peak)	420 (L) × 270 (H) × 276 (W)
RIU			

Table 6-21. Mass and power budgets of a combined OBC/RIU unit [RUAG, 2009].

6.4.5 Payload Data Handling and Transmission

The payload data handling and transmission (PDHT) system records, formats, and downlinks to the ground the scientific data of the payload.

The Solid State Mass Memory (SSMM) unit records the data acquired by the payload. During ground station pass, it encodes and passes the recorded data onto the Payload Data Transmission (PDT) which transmits it to the ground station.

Over the last few years, SSMM units based on non-volatile Flash technology have been developed as a replacement for volatile SDRAM. The storage capacity of these SSMM is very flexible as a number of memory cards can be added to suit the requirements.

The PDT subsystem is made of cold-redundant modulator and amplifier, with a switch connecting the operating chain to an X-band antenna.

The characteristics of the PDHT elements illustrated in Figure 6-19 are given in Table 6-22.

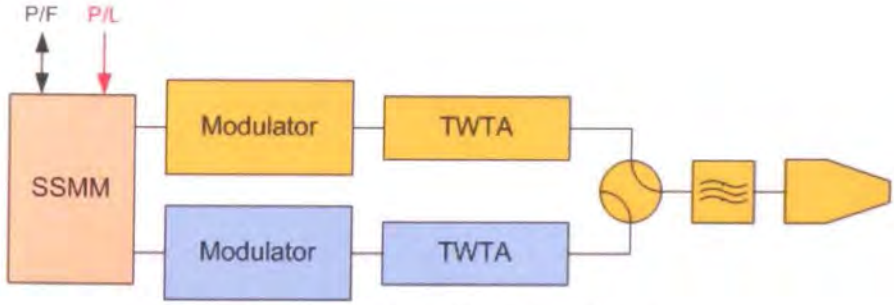

Figure 6-19. PDHT architecture.

Element	Dimensions	Mass	Power
Solid-State Mass Memory	250×250×300	20	70-100
PDT			
Modulator	160×130×65	1.1	5.1
TWTA	165×75×55	0.97	23
X-Band antenna	90 (∅) × 240	0.4	0
RF switch & cabling	-	0.55	0

Table 6-22. PDHT mass and power budgets

6.4.6 Telemetry, Tracking and Command

The TT&C system transmits the telemetry (TM) and receives the telecommands (TC). On earth observation satellites, the TM/TC communication is done in the S-Band.

A typical architecture is shown in Figure 6-20. There are two transponders, each with one receiver and one transmitter modules and a diplexer. The receivers operate in hot redundancy while the transmitters are in cold redundancy. Two S-Band antennas on the nadir and zenith faces of the satellite ensure that communication with a ground station in view can be achieved irrespective of the satellite attitude.

Element	Dimensions	Mass	Power
Transponder (each)	275 × 110 × 197	3	6 (Rx) 26 (Tx)
S-Band antenna	90(∅) × 240	0.4	-
RF switch & cabling	-	0.55	-

Table 6-23. Mass and power budgets of the TT&C subsystem

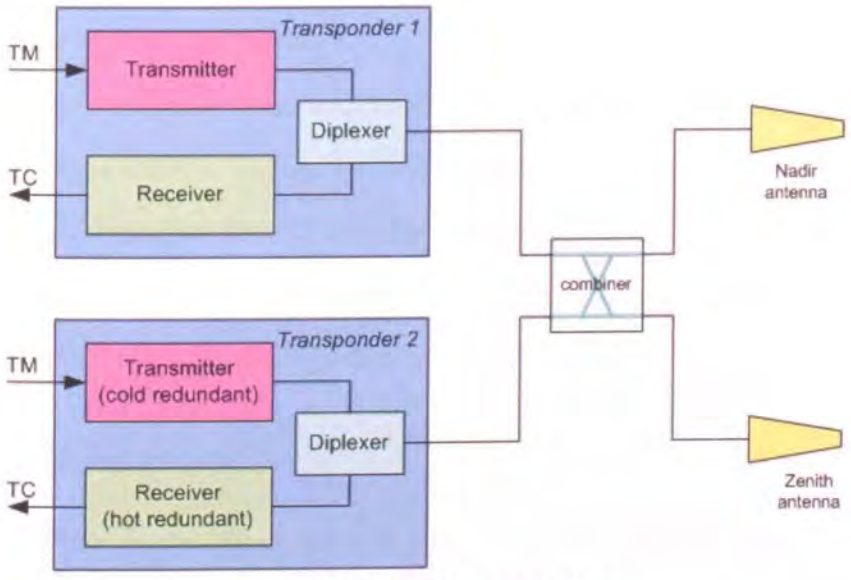

Figure 6-20. TT&C architecture

6.4.7 Attitude and Orbit Control System

The hardware for the AOCS depends on what attitude determination and control strategies are envisaged for the nominal mode and safe mode.

6.4.7.1 AOCS nominal and safe modes

For the nominal mode, the platform is three-axis stabilised, with one axis constrained to a near-nadir direction (2° roll offset in many lidar missions). The attitude determination can be either all-stellar or gyro-stellar. In the latter case, gyros are used to propagate attitude determination when no updated data from the star trackers (STR) is available (such as during moon-blinding) and to remove STR noise, while STR data compensate for long-term gyro drift [Ghezal et al, 2005]. However, a gyroless, all-stellar attitude determination for the nominal mode could also be employed, with the attitude angular rates being determined from the apparent motion of the stars. Grewal & Shiva [1995] demonstrated that this approach is appropriate for three-axis stabilised satellites with slowly varying attitude dynamics, such as earth observation missions. One example of a multi-head star tracker system designed for gyroless attitude determination is the HYDRA Star Tracker developed by EADS SODERN [2009] which will be flown on Sentinel 3.

In safe mode, the priority is to ensure survivability of the satellite, which starts by maintaining power generation capability. Hence, the first objective is to keep the solar array pointing towards the sun. In practice, this will be achievable by constraining the –Y body axis normal to the orbit. The B-dot control law, based on the time-derivation of measurements of the earth magnetic field can help achieving this during acquisition and safe mode (ASM).

6.4.7.2 AOCS hardware

The pointing requirements, discussed in Section 6.2.2, vary with the type of lidar mission. From the A-SCOPE assessment report [ESA, 2008], an AOCS architecture based on commercial off-the-shelf equipment would include:

- High-performance star-trackers and gyroscopes for nominal attitude determination;

- Reaction wheels as nominal actuators;
- Earth- and sun-sensors for acquisition and safe mode;
- Magnetometers / magnetorquers for wheel de-saturation;
- GNSS receiver for position, velocity and time (PVT) data.

The hardware list for nominal and safe modes is presented in Table 6-24, and the mass and power budgets are given in Table 6-25. Included in this list are control moment gyros (CMGs), because of the impact of the electric propulsion on the attitude control, as shown next. These would replace reaction wheels.

	Sensors						Actuators	
	AST	FOG	MAG	CSS	ES	GPS	RW/CMG	MTQ
NM	X	X	X	(FDIR)		X	X	
ASM			X	X	X	X		X

Table 6-24. AOCS hardware involved in Nominal Mode and Safe Mode

Element	Redundancy	Dimensions	Unit Mass	Unit Power
Star Trackers (2 optical heads)	Cold	130×130×225 (w/o baffle)	2.2 (w/ baffle)	1
AST electronics	Cold	145×160×100	1.75	8
Fibre-Optic Gyroscope	Internal	410×260×170	7.5	24
GPS receiver (×2)	Cold	300×240×104	4.0	5.5
Magnetometers (×2)	Cold	85 × 50 × 60	0.3	1
Earth Sensor (×1)	SM only	168×206×206	3.4	6.5
Coarse Sun Sensor (×6)	(FDIR), ASM	23 (∅)×9	0.2	0
Reaction wheels (×4)	Hot	247 (∅) × 84 (H)	4.4 (each)	20 W (mean) 90 W (max.)
CMG (×4)	Hot	270 (∅) × 350 (H)	18.4 (each)	25 W (15 Nms)
Magnetorquers (×3)	Internal	33 (∅) × 768	3.49	7.5

Table 6-25. AOCS mass and power budgets

6.4.7.3 Impact of the electric propulsion system on the AOCS

One particularity of the proposed mission is the fact that its orbit is maintained by constantly firing the ion engines. The orbit control requires that the thrust direction be stirred with respect to the velocity vector to maintain the orbital elements. In doing so, the thrust vector would not be aligned with the Centre of Mass (CoM) and the electric propulsion system would generate perturbation torques. However, the pointing requirements of the lidar are most critical to the mission objectives, and the AOCS would have to compensate the electric propulsion torques. These torques would lead to a momentum build-up, as shown in Figure 6-21 due to variations in atmospheric density over the orbit, and from one orbit to another.

The thrust angle, shown in Figure 6-22, is no more than 4.5°. Depending on the distance between the thruster and the CoM, the torque would be up to 9 mN.m, as shown in Figure 6-23.

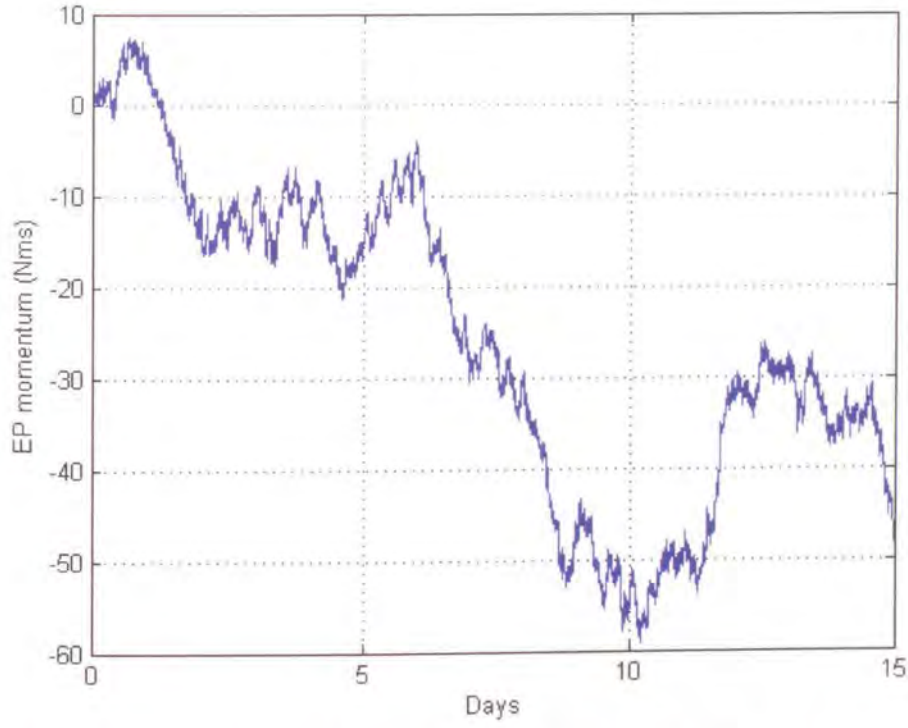

Figure 6-21. Example of electric propulsion momentum build-up (260 km, 180 kg/m^2, 2000 kg)

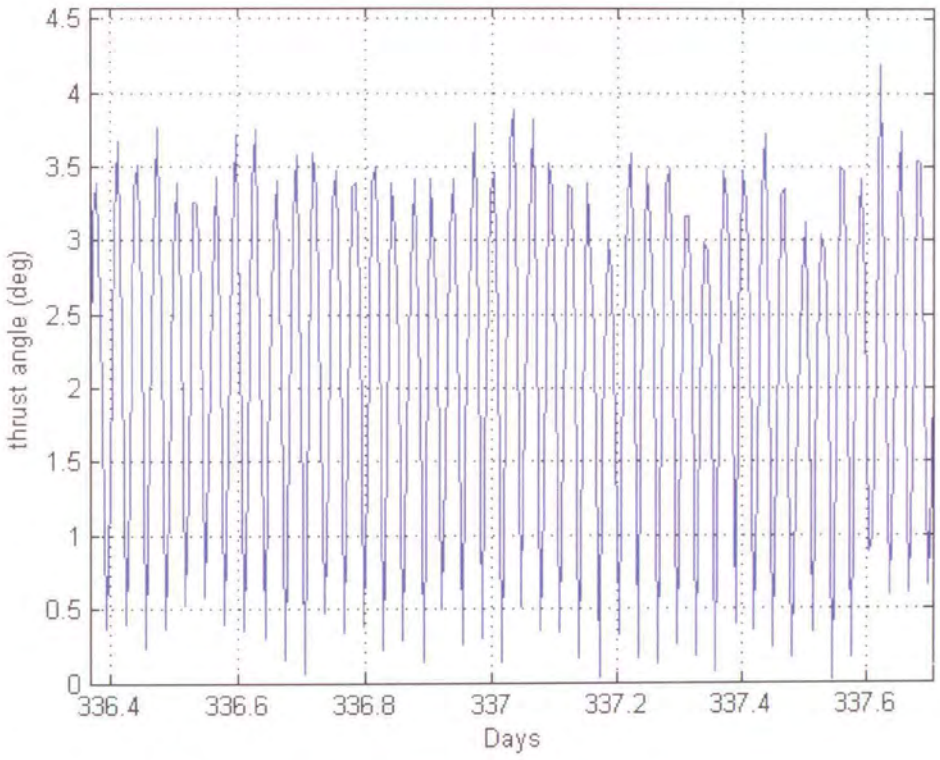

Figure 6-22. Illustration of the thrust vector

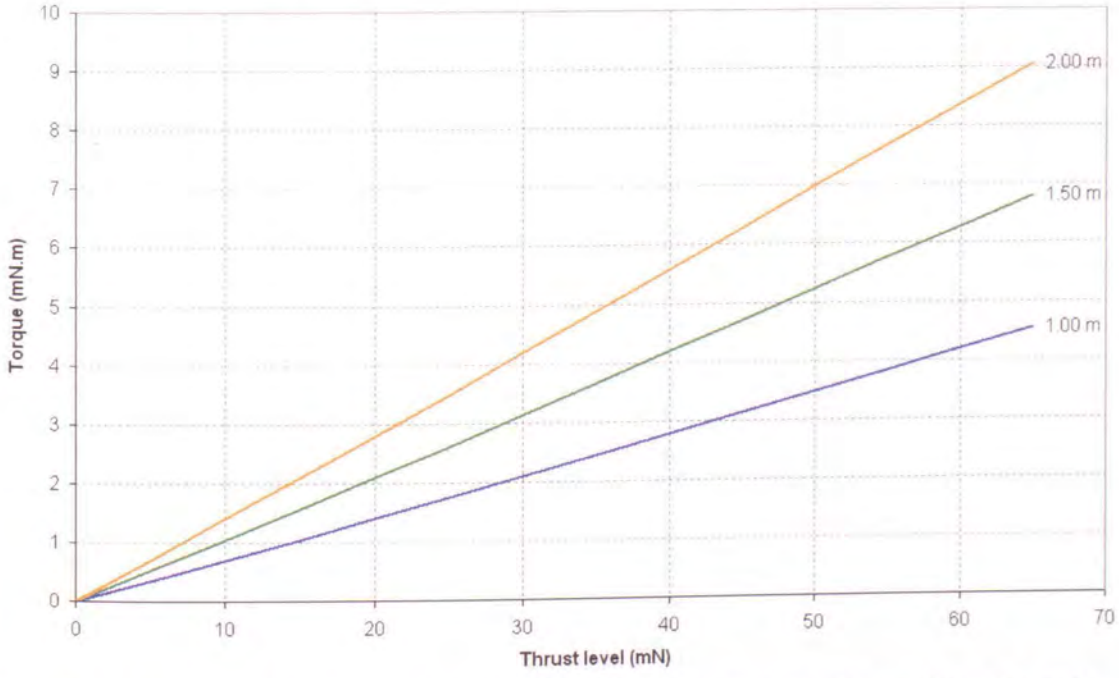

Figure 6-23. Torques generated by electric propulsion thruster for peak thrust angle.

The torque and momentum must be compared to the capabilities of reaction wheels and CMGs. Table 6-26 shows that actuators with the right performance specifications exist to overcome the electric propulsion torque. While both types can manage the angular momentum, only CMGs could handle the torque.

While the implication of the electric propulsion system on the AOCS is only considered at a high level here, it would be of interest to investigate this aspect further in a dedicated study.

Actuator (manufacturer)	Torque	Angular Momentum (nominal speed)
Reaction wheels (Rockwell-Collins)	90, 75 mNm	23, 57, 68 Nms
CMG (Astrium)	45 Nm	15 Nms

Table 6-26. Comparison of the performance of reaction wheels and CMG.

6.4.8 Harness

The mass of the harness is nearly impossible to predict accurately at such an early design stage. Brown [2002] gives the typical mass fraction of the subsystems for various types of satellites. A fraction of 7% of the total spacecraft dry mass is assumed for the harness. However, the harness mass can easily be underestimated, and it is advisable to increase this fraction to 8%.

Similarly to other equipment, the harness dissipates energy in the form of heat. A value of 2% of the total spacecraft power is assumed.

6.5 Mass and Power Budgets

Each concept has been sized for its designed altitudes, assuming the solar activity and atmospheric density to be maximum. The concepts and their applicability will be discussed in detail in Chapter 7.

6.5.1 Margin philosophy

The following margin philosophy, in line with ESA practices as defined in ECSS-E-ST-10C (2009), is assumed for both mass and power:

- 5% for re-used off-the-shelf unit;
- 10% for an off-the-shelf unit with minor modifications;
- 15% for a unit with major modifications;
- 20% for a newly designed/developed unit.

In addition, a 10% system margin is added. The propellant mass includes a 10% margin, as is customary.

6.5.2 Validation of the sizing process

The sizing process has been applied to Aeolus as a way to demonstrate its validity (Table 6-27). The model has been adjusted to take into account Aeolus real specificities (e.g. no electric propulsion). Errors in the solar array size are mostly due to errors in the mean power.

	Dry mass	Platform	Payload	Mean power	Solar array	Payload radiator
Aeolus	1100 kg	650 kg	450 kg	1400 W	13 m^2	~1.56 m^2 TBC
Predictions	1202 kg (incl. 10% system margin)	664.0 kg	435.1 kg	1327 W	12.0 m^2	1.50 m^2

Table 6-27. Errors in the predictions are sufficiently small for a preliminary design.

6.5.3 Concept 1

Table 6-28 gives the mass budget and Table 6-29 the power budgets for concept 1 at an altitude of 290 km.

Subsystem / item	Mass (kg)
Lidar	437.5
Structure	186.7
Electric Propulsion System	71.2
AOCS	117.0
TT&C	7.5
PDHT	28.3
Command and Data Handling	19.2
Electrical Power System	163.9
Thermal	79.6
Harness	99.6
Total Platform	773.0
Total Spacecraft	1210.5
Systems margin (10%)	121.1
Spacecraft dry mass	1331.6
Xe propellant	61.9
Spacecraft launch mass	1393.4

Table 6-28. Mass budget of concept 1, altitude of 290 km.

Subsystem / item	Total power		
	Mode 1	Mode 2	Mode 3
	normal	eclipse	downlink
Lidar Cassegrain	660.0	660.0	660.0
Electric Propulsion System	766.6	766.6	766.6
AOCS	151.3	151.3	151.3
S-Band	6.3	6.3	33.6
PDHT	17.5	17.5	142.6
Command and Data Handling	48.0	48.0	48.0
Electrical Power System	120.0	60.0	132.0
Thermal	36.0	60.0	36.0
Harness	36.1	35.4	39.4
Total	1841.8	1805.1	2009.5
Systems margin (15%)	276.3	270.8	301.4
TOTAL with margin	2118.1	2075.9	2311.0

Table 6-29. Power budget of concept 1, altitude of 290 km.

6.5.4 Concept 2

Table 6-30 gives the mass budget and Table 6-31 the power budgets for concept 2 at an altitude of 290 km.

Subsystem / item	Mass (kg)
Lidar	745.6
Structure	337.0
Electric Propulsion System	75.1
AOCS	117.0
TT&C	7.5
PDHT	28.3
Command and Data Handling	19.2
Electrical Power System	204.1
Thermal	136.5
Harness	99.6
Total Platform	1024.3
Total Spacecraft	1769.9
Systems margin (10%)	177.0
Spacecraft dry mass	1946.9
Xe propellant	110.8
Spacecraft launch mass	2057.7

Table 6-30. Mass budget of concept 2, altitude of 290 km.

Subsystem / item	Total power		
	Mode 1	Mode 2	Mode 3
	normal	eclipse	downlink
Lidar	660.0	660.0	660.0
Electric Propulsion System	1392.5	1392.5	1392.5
AOCS	151.3	151.3	151.3
S-Band	6.3	6.3	33.6
PDHT	17.5	17.5	142.6
Command and Data Handling	48.0	48.0	48.0
Electrical Power System	132.0	66.0	144.0
Thermal	36.0	60.0	36.0
Harness	58.6	57.6	62.6
Total	2502.3	2459.2	2670.6
Systems margin (10%)	250.2	245.9	267.1
TOTAL with margin	2752.5	2705.2	2937.7

Table 6-31. Power budget of concept 2, altitude of 290 km.

6.5.5 Concept 3

Table 6-32 gives the mass budget and Table 6-33 the power budgets for concept 3 at an altitude of 320 km.

Subsystem / item	Mass (kg)
Lidar	1072.9
Structure	331.8
Electric Propulsion System	143.2
AOCS	117.0
TT&C	7.5
PDHT	28.3
Command and Data Handling	19.2
Electrical Power System	237.8
Thermal	165.9
Harness	192.0
Total Platform	1242.7
Total Spacecraft	2315.7
Systems margin (10%)	231.6
Spacecraft dry mass	2547.2
Xe propellant	140.0
Spacecraft launch mass	2687.3

Table 6-32. Mass budget for concept 3, altitude of 320 km.

Subsystem / item	Total power		
	Mode 1	Mode 2	Mode 3
	normal	eclipse	downlink
Lidar	660.0	660.0	660.0
Electric Propulsion System	1832.6	1832.6	1832.6
AOCS	151.3	151.3	151.3
S-Band	6.3	6.3	33.6
PDHT	17.5	17.5	142.6
Command and Data Handling	48.0	48.0	48.0
Electrical Power System	192.0	96.0	216.0
Thermal	36.0	60.0	36.0
Harness	58.9	57.4	62.4
Total	3002.5	2929.1	3182.5
Systems margin (10%)	300.3	292.9	318.2
TOTAL with margin	3302.8	3222.0	3500.7

Table 6-33. Power budget for concept 3, altitude of 320 km.

6.5.6 Concept 4

Table 6-34 gives the mass budget and Table 6-35 the power budgets for concept 4 at an altitude of 320 km.

Subsystem / item	Mass (kg)
Lidar	1361.7
Structure	331.8
Electric Propulsion System	145.2
AOCS	117.0
TT&C	7.5
PDHT	28.3
Command and Data Handling	19.2
Electrical Power System	251.4
Thermal	198.2
Harness	192.0
Total Platform	1290.5
Total Spacecraft	2652.2
Systems margin (10%)	265.2
Spacecraft dry mass	2917.4
Xe propellant	162.4
Spacecraft launch mass	3079.8

Table 6-34. Mass budget for concept 4, altitude of 320 km.

Subsystem / item	Total power		
	Mode 1	Mode 2	Mode 3
	normal	eclipse	downlink
Lidar	660.0	660.0	660.0
Electric Propulsion System	2058.4	2058.4	2058.4
AOCS	151.3	151.3	151.3
S-Band	6.3	6.3	33.6
PDHT	17.5	17.5	142.6
Command and Data Handling	48.0	48.0	48.0
Electrical Power System	216.0	108.0	228.0
Thermal	36.0	60.0	36.0
Harness	63.9	62.2	67.2
Total	3257.3	3171.6	3425.0
Systems margin (10%)	325.7	317.2	342.5
TOTAL with margin	3583.0	3488.8	3767.5

Table 6-35. Power budget for concept 4, altitude of 320 km.

6.6 Conclusion

In this chapter, the detailed instrument and platform design and sizing process has been presented.

The configurations that have been selected result from the analysis of the subsystem requirements.

For the sizing of the platform, subsystems that are very dependent on the configuration, instrument, or altitude (such as the thermal control system and the electrical power system) have been sized according to a detailed methodology. Other subsystems could be assumed to be constant irrespective of the lidar mission.

With the results of this instrument and platform sizing process in place,

Chapter 7

Applicability of the Mission Concepts

7.1 Introduction

This chapter summarises the results of the present work, looking at the four concepts in detail and explores their feasibility and applicability to some of the lidar missions identified in Chapter 2. In particular, missions with challenging power-aperture products (Aeolus, WALES) or recent mission proposals (A-SCOPE) have been considered.

The mission requirements developed in Chapter 2 are summarised in Table 7-1.

Requirement #1	The satellite shall be flown in a dawn-dusk orbit
Requirement #2	The satellite shall be compatible with a small launcher like Vega (Goal) or on Soyuz (Threshold)
Requirement #3	The mission shall minimise the laser beam energy while maintaining performance.
Requirement #4	At UV / Visible wavelengths, the laser beam energy shall be 5 mJ (Goal), 10 mJ (Objective), 15 mJ (Threshold)
Requirement #5	The spacecraft shall be designed for flying in a low orbit (below 350 km).

Table 7-1. Summary of the overall mission requirements

7.2 Concept 1: front-mounted lidar, 1150 mm diameter

7.2.1 Concept summary

This concept has been sized to maximise the telescope aperture diameter in a front-mounted configuration and fit in the Vega launcher, as shown in Table 7-2. The configuration minimises the cross-section area exposed to the air flow and thus the thrust level requirements of the electric propulsion system.

All the results presented here confirm the assumptions taken earlier. The mass is within the range that was anticipated in Table 3-9, and the ballistic coefficient is more favourable than the worst case of 123 kg/m^2 assumed earlier. Note the particularly large drag coefficient, due to the small cross-section area.

Finally, the mission could be extended into a period of lower solar activity at a minimum additional cost of propellant (about 10 kg for 3 years).

Telescope diameter	1150 mm
Altitude	290 km
Power-aperture product (5 – 15 mJ, 100 Hz)	6.2 – 18.5 × 10^{-12} W
Dry mass	1332 kg
Ballistic coefficient	162 kg/m^2
Corresponding C_D	3.27
Maximum thrust (peak solar activity)	28.3 mN
Average satellite power	2.1 kW
Solar array	15.5 m^2
Xenon mass (solar maximum)	61.9 kg (incl. 10% margin)
Total impulse (solar maximum)	1.38 × 10^6 N.s
Total impulse (thruster capability)	1.5 – 3 × 10^6 N.s
Xenon mass (solar minimum)	11.2 kg (incl. 10% margin)
Total impulse (solar minimum)	0.74 × 10^6 N.s

Table 7-2. Key characteristics of the satellite for concept 1.

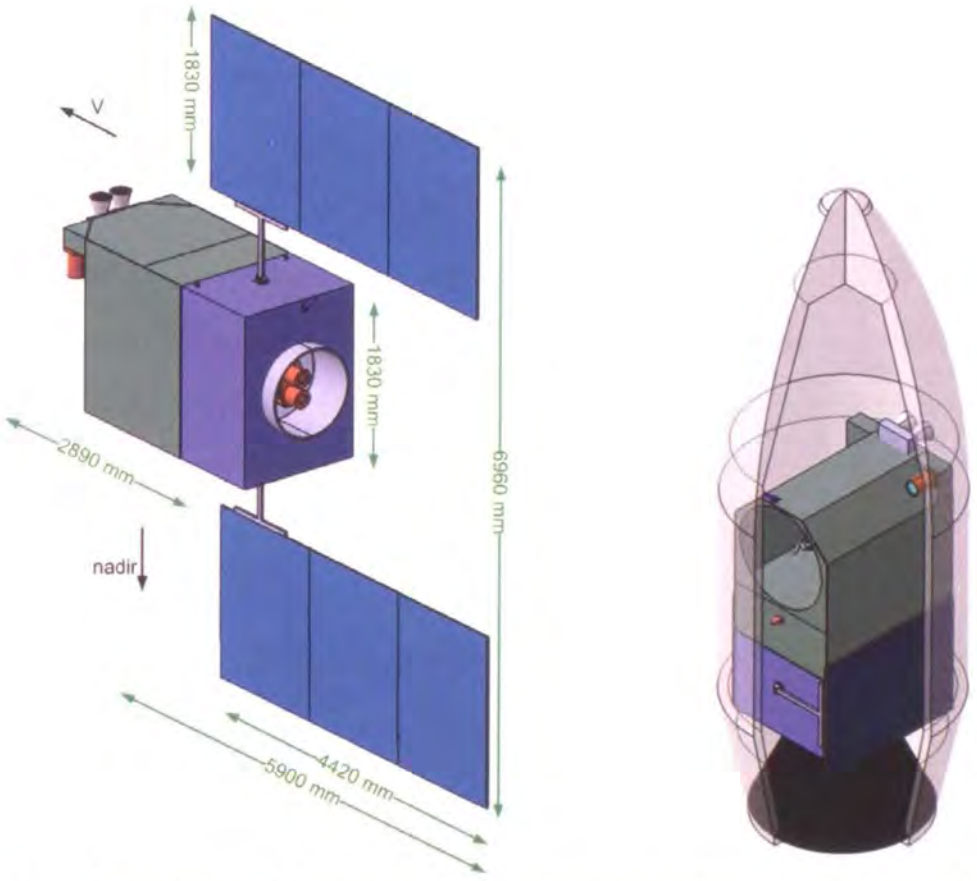

Figure 7-1. Dimensions of concept 1 (left) and accommodation in the Vega fairing.

7.2.2 Applicability of concept

In terms of power-aperture capability, this concept can meet the requirements of ICESat, although the goals of ICESat is to observe the polar regions, and the inclination associated with a sun-synchronous orbit would result in an insufficient coverage of these areas. Furthermore, the variation in sun illumination conditions would make it hard to design a suitable thermal control system.

The power-aperture capability of this concept is very close to that of A-SCOPE. It may be possible to increase the beam energy marginally above the 15 mJ threshold specified in Chapter 2, and still limit contamination of the laser optics.

The idea of reducing the beam energy could be of great importance to a mission like A-SCOPE. For many lidar missions, it is intended to maintain the laser optics in a sealed

container of low-pressure oxygen, so that any free carbon resulting from laser-assisted decomposition of hydrocarbons would form carbon dioxide gas [Soileau, 2010]. While CO_2 is transparent to most lasers operating in the UV, visible and infrared, it is absorbent notably in the 1.56 and 2.05 μm wavelengths, which by definition would be preferred for CO_2 monitoring lidar missions. Although no reference has been found on this matter, this reaction seems a realistic risk to a CO_2 sensing lidar that can only be confirmed or disproved by investigation of the detailed design of the instrument. If it were to be confirmed, the oxygen cleaning would not be a possible option, and a lower beam energy would be the ideal solution.

7.3 Concept 2: front-mounted lidar, 1800 mm diameter

7.3.1 Summary of concept

The characteristics of the satellite with the 1800 mm diameter lidar are listed in Table 7-3.

Telescope diameter	1800 mm
Altitude	290 km
Power-aperture product (5 – 15 mJ, 100 Hz)	$15.1 - 45.4 \times 10^{-12}$ W
Dry mass	1947 kg
Ballistic coefficient	132.5 kg/m^2
Corresponding C_D	2.84
Maximum thrust (peak solar activity)	50.7 mN
Average satellite power	2.75 kW
Solar array	20.6 m^2
Xenon mass (solar maximum)	110.8 kg (incl. 10% margin)
Total impulse (solar maximum)	2.48×10^6 N.s
Total impulse capability (2 thrusters)	$3 - 6 \times 10^6$ N.s
Xenon mass (solar minimum)	20.1 kg (incl. 10% margin)
Total impulse (solar minimum)	1.33×10^6 N.s

Table 7-3. Key characteristics of the satellite for concept 2.

The spacecraft is just within the range anticipated in section 3.3.6, and the ballistic coefficient is marginally outside the expected range due to a larger ($A.C_D$) product. While this concept was envisaged to fly as a secondary payload on Soyuz, it can be seen from Figure 7-2 that it violates the lower volume (represented in fuchsia), as the height of the dual launch adapter is too short for the satellite. Hence, this concept could only fly as a single passenger on Soyuz.

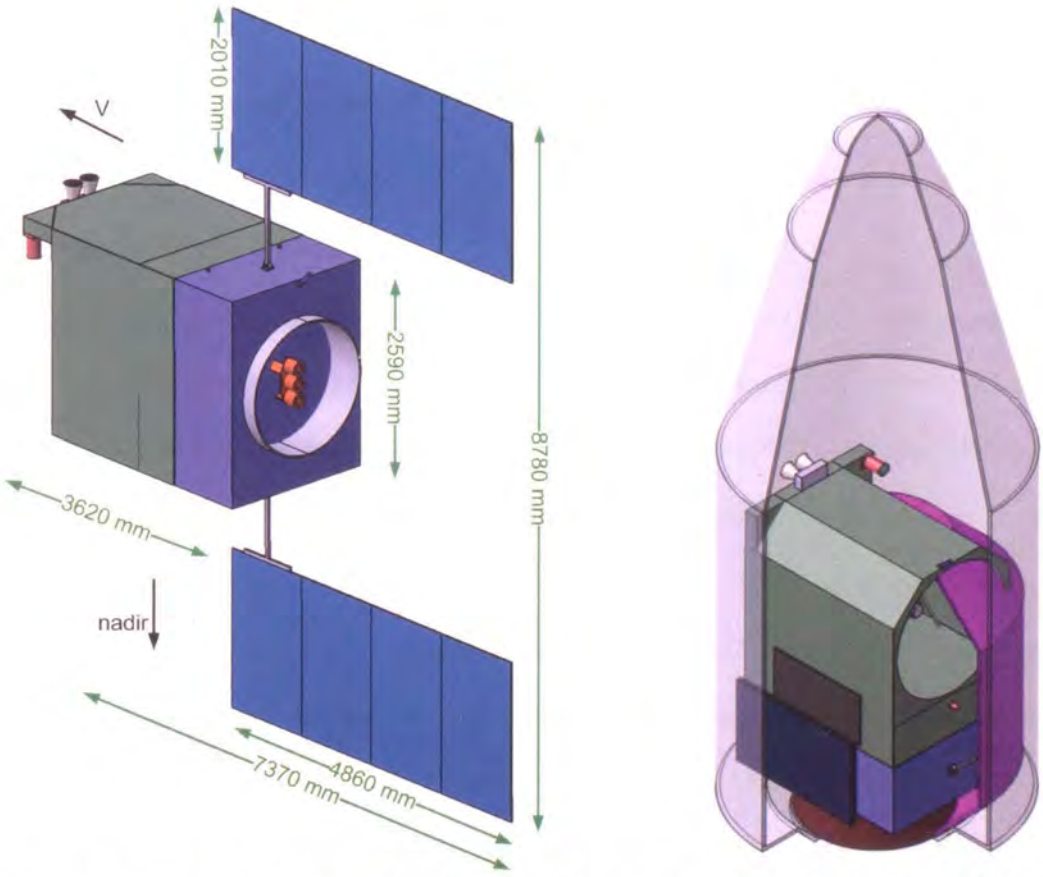

Figure 7-2. Dimensions of concept 2 (left) and accommodation in the Soyuz fairing.

7.3.2 Applicability

In terms of power-aperture product, the capability of this concept fits very well within the requirements of A-SCOPE. However, in its current state, this requires a dedicated flight on Soyuz.

The performance of this concept is some way off the requirements of WALES, and would not be suitable for this mission, unless the beam energy is doubled to 30 mJ. Since concept 2 would fly alone on Soyuz, a nadir-mounted configuration like concepts 3 and 4 may be more suitable to reduce the beam energy to less than 15 mJ.

Nevertheless, concept 2 may be interesting to other missions as it relaxes the propulsion requirements compared to a nadir-mounted telescope.

7.4 Concept 3: nadir-mounted lidar, 3000 m diameter

7.4.1 Summary of concept

The characteristics of the spacecraft with a nadir-mounted 3000 mm diameter lidar instrument are given in Table 7-4.

The electric propulsion system was driven by the maximum thrust level experienced at the peak of the solar activity, and three thrusters were therefore selected. However, it can be seen that the total impulse requirement of the mission is compatible with only two thrusters. As mentioned in 5.6.2, the T5 thruster is capable of reaching 70mN, however it is not recommended to operate it above 30 mN for long periods. There is scope for flying the mission with only two nominal thrusters, similar to concept 2. This would have a limited impact on the design of the rest of the spacecraft, since the power system in particular has been designed based on the total thrust level required, irrespective of the number of thrusters.

It can be noted that the predicted ballistic coefficient is marginally

Telescope diameter	3000 mm
Altitude	320 km
Power-aperture product (5 – 15 mJ, 100 Hz)	34.5 – 103.5 × 10^{-12} W
Dry mass	2547 kg
Ballistic coefficient	73.4 kg/m^2
Corresponding C_D	2.77
Maximum thrust (peak solar activity)	65.6 mN
Average satellite power	3.3 kW
Solar array	24.4 m^2
Xenon mass (solar maximum, 3.25 years)	140.0 kg (incl. 10% margin)
Total impulse (solar maximum, 3.25 years)	3.12 × 10^6 N.s
Total impulse capability (3 thrusters)	4.5 – 9 × 10^6 N.s
Xenon mass (solar minimum, 3.25 years)	20.1 kg (incl. 10% margin)
Total impulse (solar minimum, 3.25 years)	1.80 × 10^6 N.s

Table 7-4. Key characteristics of the satellite for concept 3.

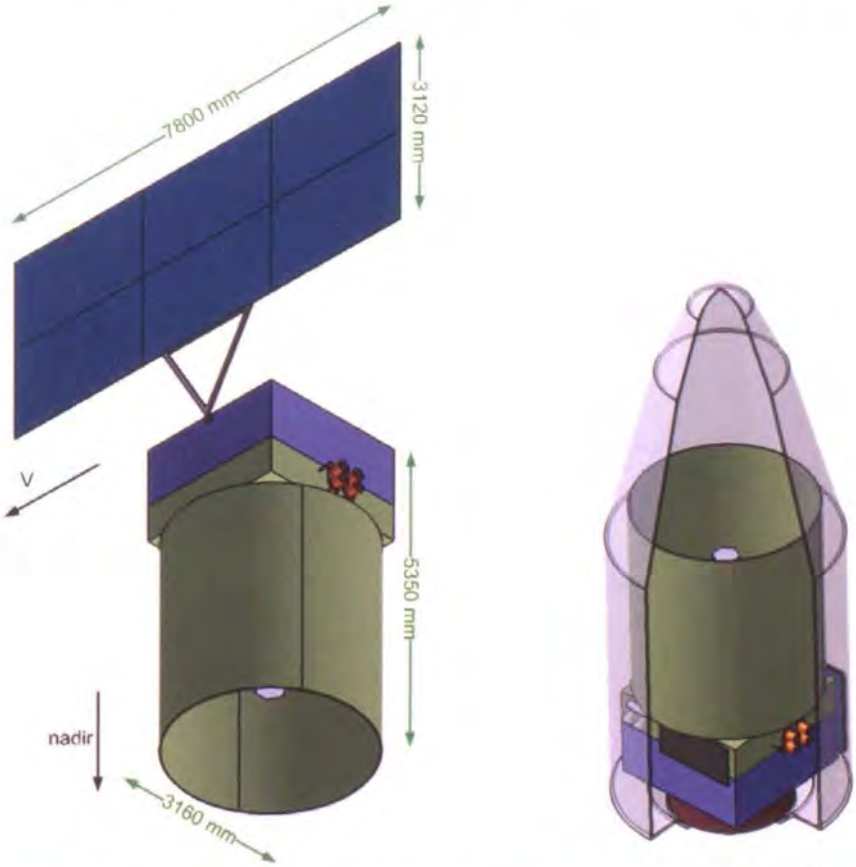

Figure 7-3. Dimensions of concept 3 (left) and accommodation in the Soyuz fairing.

7.4.2 Applicability

Compared to the previous two, this concept is particularly well suited for the WALES mission, reducing the beam energy to nearly 10 mJ, and meeting the mission requirements summarised in section 7.1. At an altitude of 320 km, it is a good starting point for further iteration on the beam energy – aperture diameter. In particular, if it is possible to double the beam energy (20 mJ) at the operation wavelength (936 nm) with little contamination of the optics, it would be possible to launch this mission onboard Vega, as the primary mirror would only need to be 2100 mm in diameter.

7.5 Concept 4: nadir-mounted lidar, 3500 mm diameter

7.5.1 Summary of concept

Table 7-5 shows the characteristics of the satellite with a nadir-mounted lidar instrument, 3500 mm in diameter.

One should notice first from Figure 7-4 that while the telescope diameter just fits within the Soyuz launcher, its length is too large and the telescope baffle protrudes significantly out of the fairing, and the satellite needs to be about 400 mm shorter. A feasible solution to this would be to make the telescope faster: an F-number of 0.9 (like Aeolus, rather than 1.0 as assumed) would reduce the height of the baffle by 300 mm.

Apart from this, the parameters are in line with the earlier assumptions.

Telescope diameter	3500 mm
Altitude	320 km
Power-aperture product (5 – 15 mJ, 100 Hz)	$47.0 - 140.9 \times 10^{-12}$ W
Dry mass	2917 kg
Ballistic coefficient	73.4 kg/m^2
Corresponding C_D	2.75
Maximum thrust (peak solar activity)	76.0 mN
Average satellite power	3.6 kW
Solar array	26.0 m^2
Xenon mass (solar maximum)	162.4 kg (incl. 10% margin)
Total impulse (solar maximum)	3.62×10^6 N.s
Total impulse capability (3 thrusters)	$4.5 - 9 \times 10^6$ N.s
Xenon mass (solar minimum)	23.8 kg (incl. 10% margin)
Total impulse (solar minimum)	2.09×10^6 N.s

Table 7-5. Key characteristics of the satellite with the 3.5 m diameter telescope.

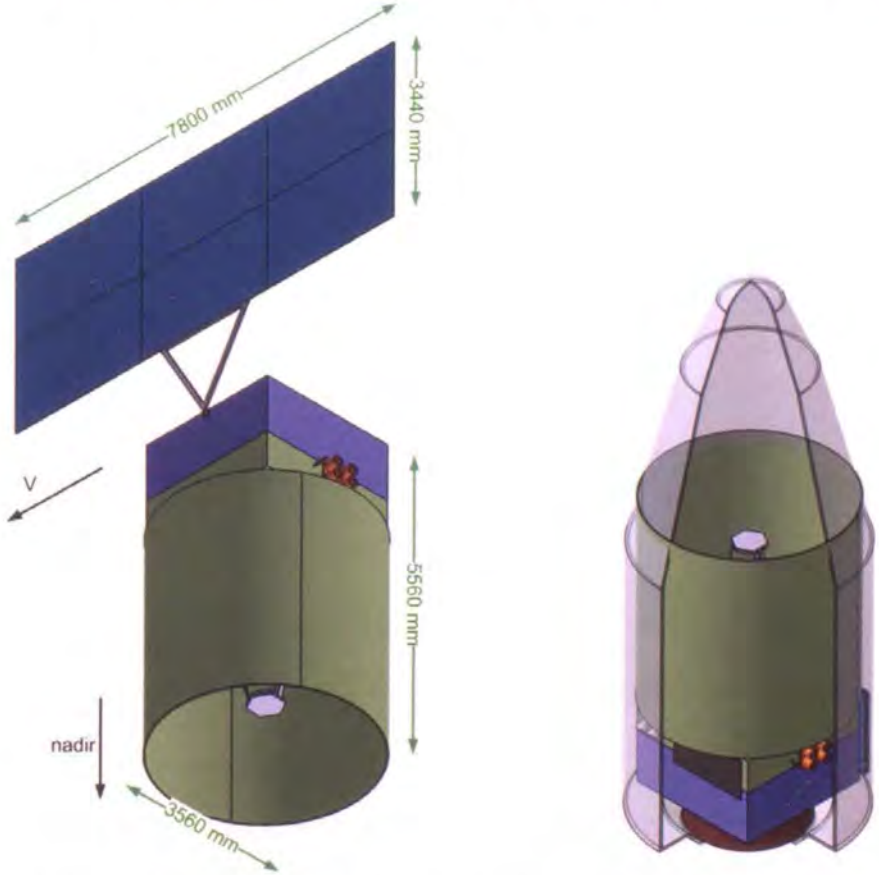

Figure 7-4. Dimensions of concept 4 (left) and accommodation in the Soyuz fairing.

7.5.2 Applicability

The power-aperture that this concept can deliver is very much in line with the requirements of both WALES and Aeolus.

In the latter case, the beam energy can be reduced to less than 15 mJ. At a wavelength of 355 nm, such a drop is of strong interest since the contamination of optics by free carbon is linearly proportional to the total flux. A longer mission lifetime would therefore be possible, not only because of the contamination reduction, but also because of the moderate xenon mass required to extend the mission, about 15%, as shown in Table 7-5.

7.6 Comparison with other studies

Other studies on the use of electric propulsion for lidar missions have been performed before, most notably the study performed by QinetiQ for ESA [Price et al, 2005]. Rossetti & Valentian [2007] performed a similar study, replacing gridded ion engines with Hall-effect thrusters.

It can be seen from Table 7-6 that there is a substantial difference in the maximum drag force between these two studies and the present work. By reverse-engineering, it is possible to determine that these studies have used an atmospheric density of 39×10^{-12} kg/m^3, assuming a drag coefficient of 2.2. There are two possibilities:

- These studies have assumed a $F_{10.7}$ index of up to 200;
- These studies have not taken into account the bulge of the atmosphere and variable densities.

In any case, this density has been calculated with a drag coefficient of 2.2 (typical value), whereas a value of 2.7 is more likely for this type of configuration (section 3.4.2), which would result in an even lower atmospheric density. These under-estimates can also be seen in the total impulse in the propellant mass. We can be confident that these are indeed under-

estimates since the trajectory model developed in the present work has been validated against STK (section 4.5.2.2).

	Price et al. [2005]	Rossetti & Valentian [2007]	Present study
Altitude	300 km	300 km	300 km
Cross-section area	3.4 m^2	3.4 m^2	-
C_D	2.2	2.2	-
Mass	1400 kg	1400 kg	1400 kg
Ballistic coefficient	187 kg/m^2	187 kg/m^2	180 kg/m^2
Maximum thrust	8.7 mN	8.7 mN	13.8 mN
Maximum thrust (geometric correction)	10.0 mN	10.0 mN	13.8 mN
Total impulse (with geometric correction)	0.734×10^6 N.s	0.734×10^6 N.s	1.035×10^6 N.s
Mean specific impulse	2000 s	1500 s	2000 s
Xenon mass			52.7 kg
Specific power	31 W/mN	17 W/mN	31 W/mN
Electric propulsion peak power	312 W	170 W	428 W

Table 7-6. Comparison with previous electric propulsion studies

Hence, these studies have not considered the worst case that the satellite could encounter. This could only be assumed if the launch date can be ascertained many years ahead during the development of the mission, with no slippage of that date. As seen with Aeolus, this is a very optimistic assumption.

Thus, the model developed in this thesis ensures that the worst case scenarios are considered and that the satellite is designed for all possible solar activity conditions.

7.7 Synthesis

The usefulness of the four concepts has been analysed against requirements of various proposed missions.

The 1150 mm diameter concept has the potential to be applied to the A-SCOPE mission. Its small cross-section area reduces the requirements on the electric propulsion system.

The 1800 mm diameter concept was targeted at a dual launch on Soyuz, but eventually the height of the lower volume is not sufficient, so that it could only fly as a single passenger. As a consequence, concept 3 with its 3000 mm diameter telescope would be a preferable option, flying into a higher altitude. The requirements on the electric propulsion system would still be more stringent than the smaller spacecraft in a lower altitude, but the range of lidar applications outweighs these constraints.

The largest 3500 mm concept could cover the requirements of Aeolus. Although currently larger than the available volume in Soyuz, this could be easily resolved by making the telescope faster and hence shorter.

Finally, by comparing our approach with results of other studies of electric propulsion for lidar missions, it is possible to state with confidence that these studies have underestimated the drag force that would be likely to occur.

Chapter 8

Summary and Further Work

8.1 Summary

While lidars have been extensively used on ground, spaceborne lidars are still in their technology development stage. Many challenges and problems have been encountered on past missions (for instance, ICESat) or in the development of yet-to-fly missions (Aeolus). Most of these problems are related to the laser, but the issues are being tackled one by one. Once these problems are solved, lidars would become invaluable operational tools in the observation of the Earth. One area that would greatly benefit from lidar observations is the study of the atmosphere, its composition, structure and dynamics. One particular on-going problem with lidars is the contamination of optics by carbon resulting from the decomposition of hydrocarbons under laser light [Soileau, 2009]. While a short-tem solution is to pressurise the optical system with oxygen to prevent contamination, this is not a long-term solution, at least on its own, for future lidar operational missions.

Since the contamination is linearly proportional to the laser flux, particularly in the UV [Canham, 2004], there is a strong incentive to reduce the laser beam energy. To maintain the measurement performance, it follows from the lidar equation that this can be

counterbalanced by a larger aperture telescope and / or a shorter range to the target. As a satellite flies in ever lower orbits, atmospheric drag represents a major limit to the mission lifetime, which could be compensated by using an electric propulsion system. Furthermore, the drag can also be minimised by reducing the cross-section area of the satellite, implying a specific design of the payload. This overall approach has been the fundamental aim of the present research.

To this end, telescope designs have been investigated, in order to identify configurations which minimise their contribution to drag by reducing the cross-section area and drag coefficient, while maximising their aperture diameter for lidar performance. A telescope and instrument configuration has been found where the lidar is mounted at the front of the platform, thus hiding the latter to the air flow. However, this configuration is strongly limited by the dimensions of the launcher fairing. The more traditional option of a nadir-mounted telescope has also been considered to enable comparison. In total, four concepts were considered, of different telescope sizes for different launch vehicle.

In order to derive the requirements for the propulsion system, a trajectory model based on the variation of parameters (VOP) has been developed in MATLAB/Simulink, and validated against the High Precision Orbit Propagator (HPOP) of Satellite Tool Kit (STK). The model uses a simplified Harris-Priester atmospheric model, and includes geopotential, solar radiation pressure and third-body perturbations. The propulsion requirements were derived for the two cases of solar maximum and minimum, as the solar activity strongly affects the atmospheric density.

Based on these requirements, a trade-off of propulsion systems has been performed. Electrostatic thrusters, such as Hall-effect thrusters and gridded ion engines in particular, were found to be the most suitable for drag compensation, providing the right thrust range, specific impulse for a reasonable electric power. A propulsion system based on that of GOCE has been selected as the baseline.

With the telescope and propulsion system selected, it has been possible to (iteratively) size the overall spacecraft for the different lidar concepts. While some equipment could be

assumed to remain fixed in mass and power, sizing models were developed for some of the subsystems.

The concepts were then compared to the power-aperture requirements of some of the largest missions, such as WALES and Aeolus. It has been shown that even for these missions, it would be possible to reduce the laser beam energy as low as 10 to 15 mJ, thus dramatically reducing the risk of contamination of the laser optics.

8.2 Key Thesis Contributions

The design of a lidar mission cannot be completed without a detailed assessment of its optical performance, which is beyond the scope of the present work. However, a realistic telescope sizing tool has been developed, enabling a more accurate assessment of the physical dimensions of the satellite, and the corresponding aerodynamic characteristics.

This thesis has investigated many aspects of lidar missions flying at a low altitude, and can serve as a starting point for future lidar studies. Based on a desired power-aperture product for a new mission, possible options can be considered and investigated in further details.

Importantly, through a comparison of results obtained from the present model with results from other similar studies, it has been possible to demonstrate that these studies may have underestimated the requirements on the electric propulsion system.

8.3 Further Work

The present work aims to bring answers to the suitability of electric propulsion to enable low-altitude Lidar missions. While practical considerations have been considered in the analysis, some detailed work could bring further valuable answers.

- The telescope design is based on a purely analytical method. This would need to be validated by an in-depth design including ray tracing. It should also assess the possibility of introducing fibre optics path between the receiver telescope and the detector stage so as to relax the stiffness requirements on the structure.

- The trajectory model works with osculating (true of date) orbital elements. Instead, a semi-analytical model would remove short-term variations, handling mean of date elements. This would allow the simple implementation of a control law within the model.

- The electric propulsion system has been considered independently from the AOCS. In reality, there would be strong coupling between the two systems. The trajectory simulation has only modelled the thrust vector on a point mass, the impact on the AOCS of the torques resulting from the thrust vectoring is an area that needs investigating.

- Further options can be investigated to maximise the size of the telescope within the confined volume of the launcher fairing. While the ESA has investigated the option of deployable telescopes [Mazzinghi et al, 2006], this is a complex issue as the mirror segments must be precisely aligned after deployment. Instead, deploying the baffle only is a less risky and critical option, and would enable the telescope to use the maximum space available. This could be based for instance on deployable structures of space telescopes proposed by Slade & Brown [2011].

References

[1] Abo, Makoto, *Resonance Scattering Lidar*, Chapter 11 in *LIDAR: range-resolved optical remote sensing of the atmosphere*, C. Weitkamp, Ed., Springer Science+Business Media, Inc., New York, 2005.

[2] ABSL (2009), *ABSL COTS Battery Design Philosophy*, webpage, last visited 22 February 2010, http://www.abslspaceproducts.com/technical/battery_technology/cots_battery_design_philosophy

[3] Ahmad, A., Amzajerdian, F., Feng, C. and Li,Y. (1996), *Design and fabrication of a compact lidar telescope*, SPIE Vol. 2832, pp. 34-44, 1996.

[4] AIAA / ANSI (2004), *Guide to Reference and Standard Atmosphere Models*, ANSI/AIAA G-003B-2004.

[5] Alves, J., Pettazzi, F., Tighe, A., and Wernham, D. (2010), *Laser-Induced Contamination Control for High-Power Lasers in Space-Based Lidar Missions*, Proceedings of the International Conference on Space Optics 2010, Rhodes Island, Greece, 4-8 October 2010.

[6] Ansmann A., and Müller, D. (2005), *Lidar and Atmospheric Aerosol Particles*, Chapter 4 in *LIDAR: range-resolved optical remote sensing of the atmosphere*, C. Weitkamp, Ed., Springer Science+Business Media, Inc., New York, 2005.

[7] Arakawa & Korumasaki Laboratory (2007), *Hall principle*, image, University of Tokyo, Department of Aeronautics and Astronautics, from webpage http://www.al.t.u-tokyo.ac.jp/hall/en/projects.html, retrieved February 2010.

[8] Arianespace (2006a), *Vega User's Manual*, Issue 3, Revision 0, March 2006.

[9] Arianespace (2006b), *Soyuz from the Guiana Space Centre User's Manual*, Issue 1, Revision 0, June 2006.

[10] Barker, T. (1996*), Impingement-Current-Erosion Characteristics of Accelerator Grids on Two-Grid Ion Thrusters*, NASA Contractor Report 198523, August 1996.

[11] Bassner, H., Killinger, R., Marx, M., Kukies, R., Aguirre, M., Edwards, C., and Harmann, H.-P. (2000), *Ion Propulsion for Drag Compensation of GOCE*, AIAA paper 2000-3417, 36th AIAA/ASME/SAE/ASEE Joint Propulsion Conference and Exhibit, Huntsville, Alabama, 16-19 July, 2000.

[12] Battin, R.H. (1999), *An introduction to the mathematics and methods of astrodynamics*, AIAA Education Series, 1999.

[13] Bely, P. Y. (2003), *The Design and Construction of Large Optical Telescopes*, Springer-Verlag New-York, Inc., 2003.

[14] Bernelli Zazzera, F., de Rocco, L., Fossati, D., and Maltecca, L. (1997), *Application of the drag-free control to low Earth orbiting satellites*, p.47 in Data Systems in Aerospace – DASIA 97, ESA SP-409, European Space Agency, 1997.

[15] Betts, J.T. (1994), *Optimal Interplanetary Orbit Transfers by Direct Transcription*, The Journal of the Astronautical Sciences, Vol. 42, No. 3, July-September 1994, pp. 247-268.

[16] Betts, J.T., and Erb, S.O. (2003), *Optimal Low Thrust Trajectories to the Moon*, SIAM J. Applied Dynamical Systems, Vol. 2, No. 2, pp. 140-170.

[17] Boreman, Glenn D. (1998), *Basic Electro-Optics for Electrical Engineers*, The Society of Photo-Optical Instrumentation Engineers.

[18] Bösenberg, Jens (2005), *Differential-Absorption Lidar for Water Vapor and Temperature Profiling*, Chapter 8 in *LIDAR: range-resolved optical remote sensing of the atmosphere*, C. Weitkamp, Ed., Springer Science+Business Media, Inc., New York, 2005.

[19] Bray, D.J., Wiechmann, L. and Rashed, A.H. (2004), *A Low-Cost Innovative Approach for the Fabrication of Net-Shape SiC Components for Mirror Substrate Applications*, Presentation at the Technology Days in the Government 2004, August 17-19, 2004.

[20] Breysse, J., Castel, D., Laviron, B., Logut, D. and Bougoin, M. (2004), *All-SiC telescope technology: recent progress and achievements*, Proceedings of the 5th

International Conference on Space Optics (ICSO-2004), 30 March – 2 April 2004, Toulouse, France, ESA SP-554, June 2004.

[21] Brown, C.D. (2002), *Elements of Spacecraft Design*, AIAA Education Series.

[22] Canham, J.S. (2004), *Investigation of contamination effects on laser-induced optical damage in space flight lasers*, NASA's Earth Science Technology Conference 2004, Palo Alto, CA, June 22-24, 2004.

[23] Chao, Chia-Chun (2005), *Applied Orbit Perturbation and Maintenance*, AIAA / Aerospace Press.

[24] Choueri, E.Y. (2004), *A Critical History of Electric Propulsion: The First Fifty Years (1906 – 1956)*, AIAA paper 2004-3334, 40th AIAA/ASME/SAE/ASEE Joint Propulsion Conference and Exhibit, Fort Lauderdale, Florida, 11-14 July 2004.

[25] CNES (1976), *Spacelab borne lidar for atmospheric research, phase A study*, Volume 1 and 2, Final Report, ESA contract 2437, May/June 1976.

[26] Coletti, M., Grubisic, A., Wallace, N. and Wells, N. (2007), *European Student Moon Orbiter Solar Electric Propulsion Subsystem Architecture – an All-Electric Spacecraft*, IEPC paper 2007-111, 30th International Electric Propulsion Conference, Florence, Italy, 17-20 September, 2007.

[27] Cook, G.E., *Satellite Drag Coefficients*, Royal Aircraft Establishment Technical Report 65005.

[28] Corbett, M.H., and Edwards, C.H. (2007), *Thrust Control Algorithms for the GOCE Ion Propulsion Assembly*, 30th International Electric Propulsion Conference, 17-20 September 2007, IEPC-2007-210.

[29] Devilliers, C., and Kroedel, M. (2008), *CESIC – Optomechanical technology last development results and new HBCESIC© highly lightweighted space mirror development including corrective function*, 7th International Conference on Space Optics, Toulouse, France, October 14-17, 2008.

[30] Doombos, E, Förster, M., Fritsche, B., van Helleputte, T., van den Ijssel, J., Koppelwallner, G., Lühr, H., Rees, D. and Visser, P. (2009), *Air density models*

derived from multi-satellite drag observations, Final Report, ESTEC contract 21022/07/NL/HE.

[31] Duchemin, O. (2001), *An Investigation of Ion Engine Erosion by Low Energy Sputtering*, PhD thesis, California Institute of Technology, 2001.

[32] Durand, Y., Chinal, E., Endemann, M., Meynart, R., Reitebuch, O., Treichel, R. (2006), *ALADIN Airborne Demonstrator: a Doppler Wind Lidar to prepare ESA's ADM-Aeolus Explorer Mission*, Proceedings SPIE Optics and Photonics, Volume 6296, 13-17 August 2006, San Diego, USA.

[33] Durand, Y., Bézy, J.-L. and Meynart, R. (2008), *Laser Technology Developments in support of ESA's Earth Observation Missions*, Solid State Lasers XVII: Technology and Devices, edited by W.A. Clarkson, N. Hodgson and R.K. Shori, Proc. Of SPIE Vol. 6871, 68710G, 2008.

[34] Durand, Y., Caron, J., Bensi, P., Ingmann, P., Bezy, J.-L., and Meynard, R. (2009), *A-SCOPE: concepts for an ESA mission to measure CO2 from space with a lidar*, Proceedings of the 8th Symposium on Tropospheric Profiling, Delft, The Netherlands, 18-23 October, 2009.

[35] Duston, C. (2006), *Converted SiC for Precision Optics*, Presentation at the Technology Days in the Government 2006, Mirror Development and Related Technologies, September 18-20, 2006.

[36] EADS Astrium (2010), *Satellite Surface Tension Propellant Tanks*, webpage, http://cs.astrium.eads.net/sp/SpacecraftPropulsion/Propellant%20Tanks/Surface_Tension_Tanks.html, last visited July 2010.

[37] EADS SODERN (2008), *HYDRA star tracker selected for the Sentinel-3 programme*, webpage, http://www.sodern.fr/site/FO/scripts/siteFO_contenu.php?noeu_id=30&lang=EN, retrieved February 2010.

[38] EADS SODERN (2009), *HYDRA Star Tracker*, brochure, January 2009.

[39] Edwards, C.H., Potts, M., and Rogers, D. (2004), *Life Verification of the T5 Ion Extraction Grids for the GOCE Apllication*, Proc. 4th International Spacecraft

Propulsion Conference (ESA SP-555, October 2004), Cagliari, Sardinia, Italy, 2-4 June 2004.

[40] Edwards, C.H., Wallace, N.C., Tato, C., van Put, P. (2004), *The T5 Ion Propulsion Assembly for Drag Compensation on GOCE*, Proc. Second Interantional GOCE User Workshop "GOCE, The Geoid and Oceanography", ESA-ESRIN, Frascati, Italy, 9-10 March 2004 (ESA SP-569, June 2004).

[41] Elterman, L. (1966), *Aerosol Measurements in the Troposphere and Stratosphere*, Applied Optics, Vol. 5, No. 11, pp. 1769-1776, November 1966.

[42] ESA (2001), *Exploded View of Mars Express Spacecraft*, 19 October 2001, from webpage: http://sci.esa.int/science-e/www/object/index.cfm?fobjectid=28777, retrieved February 2010.

[43] ESA (2004a), *EarthCARE – Earth Clouds, Aerosols and Radiation Explorer*, Technical and Programmatic Annex, Annex to ESA Publication, Reports for Mission Selection – The Six Candidate Earth Explorer Missions, ESA SP-1279(1), April 2004.

[44] ESA (2004b), *WALES – Water Vapour Lidar Experiment in Space, Technical and Programmatic Annex*, Annex to ESA Publication, Reports for Mission Selection – The Six Candidate Earth Explorer Missions, ESA SP-1279(3), April 2004.

[45] ESA (2005), *ADM-Aeolus, ESA's Wind Mission*, ESA publication BR-236, February 2005.

[46] ESA (2006), *ESA's Gravity Mission – GOCE*, ESA brochure BR-209, Revised, June 2006.

[47] ESA (2008), *A-SCOPE – Advanced Space Carbon and Climate Observation of Planet Earth, Report for Assessment*, ESA SP-1313/1, November 2008.

[48] ESA (2008), *EarthCARE satellite contract signed*, ESA PR 28-2008, 27 May 2008.

[49] ESA (2009a), Aeolus image, website, retrieved 1st August 2009, from www.esa.int/esaLP/SEMQT7ARR1F_LPadmaeolus_0.html

[50] ESA (2009b), EarthCARE image, website, retrieved 1st August 2009, from www.esa.int/esaLP/ASESMYNW9SC_LPearthcare_0.html

[51] ESO (2009), *The European Extremely Large Telescope (E-ELT)*, Brochure, retrieved 2nd August 2009, available from www.eso.org/public/outreach/products/publ/brochures/pdf/elt_highres.pdf

[52] Falkner, M., Nitschko, T., Zemann, J., Mitterbauer, G., Traxler, G., and Demaire, A. (2005), *Electric Propulsion Thruster Pointing Mechanism (TPM) for EUROSTAR 3000: Design & Development Test Results*, IEPC paper 2005-001, 29th International Electric Propulsion Conference, Princeton University, 31 Oct.-4 Nov., 2005.

[53] Fearn, D.G., and Rijm, C. (2002), *Low-Cost Remote Sensing from Low Altitude Using Ion Propulsion for Drag Compensation*, AIAA paper 2002-3674, 38th AIAA/ASME/SAE/ASEE Joint Propulsion Conference and Exhibit, Indianapolis, Indiana, 7-10 July, 2002.

[54] Feng, C., Ahmad, A., and Amzajerdian, F. (1995), *Design and analysis of a spaceborne lidar telescope*, SPIE Vol. 2540, pp. 68-77, 1995

[55] Fleck, M.E., and Starin, S.R. (2003), *Evaluation of a Drag-Free Control Concept for Missions in Low Earth Orbit*, AIAA paper 2003-5747, AIAA Guidance, Navigation, and Control Conference and Exhibit, Austin, Texas, 11-14 August, 2003.

[56] Fortescue, P., Stark, J. and Swinerd, G. (2003), *Spacecraft Systems Engineering*, 3rd Ed., John Wiley & Sons Ltd, 2003.

[57] Ghezal M., Polle, B., Rabejac, C., and Montel, J. (2006), *Gyro stellar attitude determination*, Proceedings of the 6th International ESA Conference on Guidance, Navigation and Control Systems, Loutraki, Greece, 17-20 October 2005, ESA SP-606, January 2006.

[58] Gilmore, D.G., Hardt, B.E., Prager, R.C., Grob, E.W., and Ousley, W. (2003), *Thermal*, in *Space Mission Analysis and Design*, 3rd Edition, fifth printing, edited by J.R. Wertz and W.J. Larson, Microcosm Press and Kluwer Academic Publishers, 2003.

[59] Gimmestad, Gary G. (2005), *Differential-Absorption Lidar for Ozone and Industrial Emissions*, Chapter 7 in *LIDAR: range-resolved optical remote sensing of the atmosphere*, C. Weitkamp, Ed., Springer Science+Business Media, Inc., New York, 2005.

[60] Goebel, D. M., and Katz, I. (2008), *Fundamentals of Electric Propulsion, Ion and Hall Thrusters*, John Wiley & Sons, Inc., 2008.

[61] Goela J.S., and Taylor, R.L. (1991), *Fabrication of Lightweight Si/SiC Lidar Mirrors*, NASA Contractor Report 4389, 1991.

[62] Grewal, M.S. and Shiva, M. (1995), *Application of Kalman filtering to gyroless attitude determination and control system for environmental satellites*, Proceedings of the 34th IEEE Conference on Decision and Control, 13-15 Dec 1995, New Orleans, Vol. 2, 1544-1552.

[63] Harris, I. and Priester, W. (1962a), *Time-dependent structure of the upper atmosphere*, NASA Technical Note D-1443, July 1962.

[64] Harris, I. and Priester, W. (1962b), *Theoretical models for the solar-cycle variation of the upper atmosphere*, NASA Technical Note D-1444, August 1962.

[65] Healy, L.M., and Akins, K.A. (2004), *Effects of solar activity level on orbit prediction using MSIS and Jacchia density models*, AIAA 2004-4977, AIAA/AAS Astrodynamics Specialist Conference and Exhibit, 16-19 August 2004, Providence, Rode Island, USA.

[66] Hecht, E. (1987), *Optics*, 2nd Edition, Addison-Wesley Publishing Company, Inc., 1987.

[67] Hedin, A.E. (1988), *High Altitude Atmospheric Modeling*, NASA Technical Memorandum 100707, October 1988.

[68] Hélière, A., Armandillo, E., Durand, Y., Culoma, A., Meynart, R. (2004), *Lidar Instruments for ESA Earth Observation Missions*, 22nd International Laser Radar Conference (ILRC 2004), Matera, Italy, 12-16 July 2004.

[69] Hexcel Corporation (1999), *HexWeb Honeycomb Attributes and Properties*, Brochure TSB-120, November 1999.

[70] Hexcel Corporation (2008), *Redux ® 319 – High Performance Modified epoxy film adhesive – Product Data*, Publication RTA028c, August 2008.

[71] Hueber, M. F. (1991), *European Space Agency Lidar Technology Programme*, Radars and Lidars in Earth and Planetary Sciences International Symposium, Cannes, France, 2-4 September 1991.

[72] Ismail, S., Peterson, L.D., Hinkle, J.D. and Friedman, E. (2005), *Applications of Deployable Telescopes for Earth-Observing Lidar*, Proceedings of the 5th NASA Earth-Sun System Technology Conference, Hyattsville, Maryland, USA, June, 28th-30th, 2005.

[73] Jacchia, L.G. (1977), *Thermospheric temperature, density, and composition: new models*, Smithsonian Astrophysical Observatory Special Report #375, March 1977.

[74] JPL (2005), *Horizons (version 3.12), user guide*, available at ftp://ssd.jpl.nasa.gov/pub/ssd/Horizons_doc.pdf, last visited January 2010.

[75] Kamerman, G.W. (1993), *Laser Radar*, Chapter 1 in *Active Electro-Optical Systems*, C.S. Fox, Ed., Volume 6 of *The Infrared and Electro-Optical Systems Handbook*, J.S. Accetta, D.L. Shumaker, Executive Editors; SPIE Optical Engineering Press and Environmental Research Institute of Michigan, 1993.

[76] Klinkrad, Heiner (2006), *Space Debris – Models and Risk Analysis*, Springer-Praxis.

[77] Kramer, H.J. (2002), *Observation of the earth and its environment: survey of missions and sensors*, 4th edition, Springer-Verlag, Berlin, 2002.

[78] Korhonen, T., Keinanen, P., Pasanen, M., and Sillanpaa, A. (2008), *Polishing and testing of the 1.5 m SiC M1 mirror of the ALADIN instrument on the ADM-Aeolus satellite of ESA*, in Optical Fabrication, Testing, and Metrology III, edited by A. Duparré and R. Geyl, Proc. Of SPIE Vol. 7102, 2008.

[79] Lambert, S.G. and Casey, W.L. (1995), *Laser communications in space*, Artech House, Inc., Norwood, MA, USA, 1995.

[80] Le Hors, L., Toulemont, Y. and Hélière, A. (2008), *Design and Development of the Backscatter Lidar ATLID for EarthCARE*, International Conference on Space Optics 2008, Toulouse, France, October 14-17, 2008.

[81] Lo, Chor Pang (1986), *Applied Remote Sensing*, Longman Group UK Limited, 1986.

[82] Long, A.C., Cappellari, J.O., Velez, C.E. and Fuchs, A.J. (1989), *Goddard Trajectory Determination System (GTDS) – Mathematical Theory – Revision 1*, NASA GSFC Report FDD/552-89/0001 and Computer Sciences Corporation Report CSC/TR-89/6001, July 1989.

[83] Lutz, H., Armandillo, E., and Battrick, B., Eds. (1989), *Laser Sounding from Space*, Report of the ESA Technology Working Group on Space Laser Sounding and Ranging, ESA SP-1108, January 1989.

[84] Malacara, D. and Malacara, Z. (1994), *Handbook of Lens Design*, Marcel Dekker, Inc., New York, 1994.

[85] Maral, G. and Bousquet, M. (2002), *Satellite Communications Systems*, Fourth Edition, John Wiley & Sons Ltd.

[86] Marchetti, P.J., Blandino, J.J. and Demetriou, M.A. (2006), *Electric Propulsion and Controller Design for Drag-Free Spacecraft Operation in Low Earth Orbit*, AIAA paper 2006-5166, 42nd AIAA/ASME/SAE/ASEE Joint Propulsion Conference and Exhibit, Sacramento, California, 9-12 July, 2006.

[87] Martin, A.R., and Cresdee, M.T. (1987), *The use of Electric Propulsion on Low Earth Orbit Spacecraft*, AIAA paper 87-0989, 19th AIAA/DGLR/JSASS International Electric Propulsion Conference, Colorado Springs, Colorado, 11-13 May, 1987.

[88] Martin, A.R., Pearce, A.J., Kokott, W., and Bassner, H. (1990), *Earth Orbit Missions and Applications Using Electric Propulsion*, AIAA paper 90-2619, 21st International Electric Propulsion Conference, Orlando, Florida, July 18-20, 1990.

[89] The MathWorks, Inc. (2005), *Choosing a Variable-Step Solver*, MATLAB/Simulink help file, 2005.

[90] Mazzinghi, P., Bratina, V., Ferruzzi, D., Gambicorti, L., Simonetti, F., Zuccaro Marchi, A., Salinari, P., Lisi, F., Olivier, M., Bursi, A., Pereira do Carmo, J. (2006), *An ultra-lightweight, large aperture, deployable telescope for advanced lidar applications*, Proceedings of the 6th International Conference on Space Optics, ESTEC, Noordwijk, The Netherlands, 27-30 June 2006 (ESA SP-621, June 2006).

[91] McInnes, Colin R. (2003), *Instability of Fixed, Low-Thrust Drag Compensation*, Journal of Guidance, Control and Dynamics, pp. 655-657, Vol.26, No.4, July-August 2003.

[92] McCormick, M. P. (2004), *Space Lidar for Earth and Planetary Missions*, 22nd International Laser Radar Conference (ILRC 2004), Matera, Italy, 12-16 July 2004.

[93] McCormick, M. P. (2005), *Airborne and Spaceborne Lidar*, Chapter 13 in *LIDAR: range-resolved optical remote sensing of the atmosphere*, C. Weitkamp, Ed., Springer Science+Business Media, Inc., New York, 2005.

[94] Measures, R.M. (1984), *Laser Remote Sensing, Fundamentals and Applications*, John Wiley & Sons, Inc., New York, 1984.

[95] Moe, K. (2006), *Progress in predicting the decay of satellite and debris orbits*, 3rd Annual AIAA Southern California Aerospace Systems and Technology Conference, 3rd May 2006.

[96] Monheiser, J.M. (1994), *Development and Verification of a Model to Predict Impingement Currents for Ion Thrusters*, NASA CR-195322, April 1994.

[97] Montenbruck, O. and Gill, E. (2000), *Satellite Orbits – Models, Methods and Applications*, Springer, 2000.

[98] Morançais, D. (2006), *The ALADIN payload*, presentation at the ADM-Aeolus Workshop, ESA-ESTEC, Noordwijk, the Netherlands, September 2006.

[99] NASA (1979), *Shuttle Atmospheric Lidar Research Program*, Final Report of Atmospheric Lidar Working Group, NASA SP-433, 1979.

[100] NASA (1980), *Atmospheric Lidar Multi-User Instrument System Definition Study*, NASA Contractor Report 3303, August 1980.

[101] NASA (1991), *Earth Orbit Environmental Heating*, Guideline GD-AP-2301 in "NASA Reliability Preferred Practices for Design and Test", NASA TM-4322, September 1991.

[102] NASA (2002), *ICESAT: Ice, Cloud and land Elevation Satellite*, brochure FS-2002-9-047-GSFC.

[103] NASA, *Vegetation Canopy Lidar (VCL): Cas Story & Lessons Learnt*, March 2003.

[104] NASA (2004a), *Pulse Plasma Thruster*, NASA Fact Sheet FS-2004-11-023-GRC, Nov 2004.

[105] NASA (2004b), *Magnetoplasmadynamic Thrusters*, NASA Fact Sheet FS-2004-11-022-GRC, Nov. 2004.

[106] NASA (2008), *Ion Thruster Operation*, image from webpage www.grc.nasa.gov/WWW/ion/overview/overview.htm, retrieved February 2010.

[107] Neubauer, J.S., Bennetti, A., Pearson, C., Simmons, N., Reid, C., and Manzo, M. (2007), *The Effect of Variable End of Charge Battery Management on Small-Cell Batteries*, NASA/TM-2007-215044 and AIAA-2007-4789.

[108] Panetti, A (1999), *Thermal*, in *Space Mission Analysis and Design*, 3rd Edition, second printing, edited by J.R. Wertz and W.J. Larson, Microcosm Press and Kluwer Academic Publishers, 1999.

[109] Peng, X. (1991), *Particle Simulation of Grid Erosion in an Ion Thruster*, PhD thesis, University of Tennessee, Knoxville, 1991.

[110] Price, M.E., Cornara, S., Huddleson, J., Clarke, S., Wallace, N., Wells, N., Saunders, C., and Dewhurst, J. (2005), *Study of Remote Sensing Spacecraft with Electric Propulsion*, Final Report, QinetiQ report for ESA contract 18271/04/NL/CP, November 2005.

[111] Rees, W. G. (2001), *Physical Principles of Remote Sensing*, 2nd Edition, Cambridge University Press, 2001.

[112] Reitebuch, O. Endemann, M., Ingmann, P., and Nett, H. (2008), *The Wind Lidar Mission ADM-Aeolus, Recent Science Activities and Status of Instrument Development*, Lidar Working Group meeting, Monterey, 5 February 2008.

[113] Riley, K.F., Hobson, M.P., Bence, S.J. (1997), *Mathematical Methods for Physics and Engineering*, Cambridge University Press, 1997.

[114] Rossetti, P. and Valentian, D., *Analysis of Hall-Effect Thrusters application to formation flying and drag compensation*, IEPC-2007-307, 30th International Electric Propulsion Conference, Florence, Italy, 17-20 September 2007.

[115] RUAG Space AB (2009), *Command and Data Handling*, brochure, D-I-PRB-00016-SE, November 2009.

[116] Saft (2007), *Rechargeable lithium-ion battery, VL 48-E – high energy space cell*, product data sheet, Doc No 54058-2-0907, September 2007.

[117] Schröder, H., Borgmann, S., Riede, W., and Wernham, D. (2008), *Investigation of laser induced deposit formation under space conditions*, Proceedings of the International Conference on Space Optics 2008, October 14-17, Toulouse, France.

[118] Schroeder, D.J. (2000), *Astronomical Optics*, 2nd Edition, Academic Press, London, 2000.

[119] Schulte, H.-R., (2009), Private Communication, 4 July 2009.

[120] Shampine, L. F. (1994), *Numerical Solution of Ordinary Differential Equations*, Chapman & Hall, 1994.

[121] Silfvast, W.T. (2008), *Lasers*, Module 5 of *Fundamentals of Photonics* edited by A. Guenther, L.S. Pedrotti and C. Roychoudhuri, SPIE Press Book, 2008, available at http://spie.org/x17229.xml

[122] Singh, U.N., Heaps, W., and Komar, G.J. (2005), *Laser/Lidar Technologies for NASA's Science and Exploration Mission's Applications*, AIAA Space 2005 paper 2005-6773, American Institute of Aeronautics and Astronautics, 2005.

[123] Slade, R. and Brown, C. (2011), *A large self-deploying structure concept for space telescope missions*, Proceedings of the 14th European Space Mechanisms &

Tribology Symposium – ESMATS 2011, Constance, Germany, 28-30 September 2011, pp. 465-472.

[124] Soileau, M. (2009), *Laser-Induced Damage to Optical Materials*, in *Handbook of Optics*, Third Edition, Volume IV: Optical Properties of Materials, Nonlinear Optics, Quantum Optics, edited by Michael Bass, McGraw-Hill Professional.

[125] Spurrett, R., Thwaite, C., Slimm, M., and Lizius, D. (2002), *Lithium-Ion Batteries for Space*, Proceedings of the Sixth European Conference, Porto, Portugal, 6-10 May, 2002, and ESA SP-502, 2002.

[126] Szekielda, K.-H. (1988), *Satellite Monitoring of the Earth*, John Wiley & Sons, Inc.

[127] Tam, W.H., Jackson, A.C., Nishida, E., Kasai, Y., Tsujihata, A.,and Kajiwara, K. (2000), *Design and Manufacture of the ETS VIII Xenon Tank*, AIAA paper 2000-3677, 36th AIAA/ASME/SAE/ASEE Joint Propulsion Conference, Huntsville, AL. July 16 – 19, 2000.

[128] Tato, C., de la Cruz, F., and Palencia, J. (2007), *Power Control Unit for Ion Propulsion Assembly in GOCE Program*, IEPC paper 2007-295, 30th International Electric Propulsion Conference, Florence, Italy, 17-20 September, 2007.

[129] Telescope-optics.net (2009), *Two-mirror tilted component telescopes*, Retrieved 2nd August 2009, from http://www.telescope-optics.net/tilted_component_telescopes.htm

[130] Thales Alenia Space (2000), *Thruster Orientation Mechanisms (TOM)*, datasheet, Thales Alenia Space France, updated March 2000.

[131] Thales Alenia Space (2006), *Low-Medium Power PCDU*, datasheet DPC_DOC_050515_20, updated January 2006.

[132] Turner, M.J.L. (2000), *Rocket and Spacecraft Propulsion, Principles, Practice and New Developments*, Springer-Praxis, 2000.

[133] Universität Stuttgart (2009), *Regional recovery of the gravity field from SST observations*, webpage, http://www.uni-stuttgart.de/gi/research/projects/project8/index.en.html, last changed 24 June 2009, last visited 06 February 2010.

[134] Vallado, D.A. (2007), *Fundamentals of Astrodynamics and Applications*, Third Edition, Microcosm Press and Springer, 2007.

[135] Vallado, D.A., Finkleman, D. (2008), *A Critical Assessment of Satellite Drag and Atmospheric Density Modeling*, AIAA-2008-6442, AIAA/AAS Astrodynamics Specialist Conference and Exhibit, Honolulu, Hawaii, 18-21 August 2008.

[136] van Put, P., van der List, M.C.A.M., and Yuce, V., *Development of an Advanced Proportional Xenon Feed Assembly for the GOCE Spacecraft*, Proc. 4th International Spacecraft Propulsion Conference (ESA SP-555), Cagliari, Sardinia, Italy, 2-9 June 2004.

[137] Walker, M.J.H., Ireland, B., and Owens, J. (1985), *A set of modified equinoctial orbit elements*, Celestial Mechanics 36, pp. 409-419.

[138] Wallace, N.C., Fearn, D.G., and Copleston, R.E. (1998), *The Design and Performance of the T6 Ion Thruster*, AIAA paper 98-3342, 34th AIAA/ASME/SAE/ASEE Joint Propulsion Conference and Exhibit, Cleveland, Ohio, 13-15 July, 1998

[139] Wandinger, U. (2005), *Introduction to Lidar*, Chapter 1 in *LIDAR: range-resolved optical remote sensing of the atmosphere*, C. Weitkamp, Ed., Springer Science+Business Media, Inc., New York, 2005.

[140] Weichel, H. (1993), *Lasers*, Chapter 10 in *Electro-Optical Components*, William D. Rogatto, Ed., Volume 3 of *The Infrared and Electro-Optical Systems Handbook*, J.S. Accetta, D.L. Shumaker, Executive Editors; SPIE Optical Engineering Press and Environmental Research Institute of Michigan, 1993.

[141] Weitkamp, C., Foreword to *LIDAR: range-resolved optical remote sensing of the atmosphere*, C. Weitkamp, Ed., Springer Science+Business Media, Inc., New York, 2005.

[142] Welch, C.S. (1992), *Servicing Polar Platforms Using Electric Propulsion*, PhD Thesis, Cranfield University, 1992.

[143] Werner, C. (2005), *Doppler Wind Lidar*, Chapter 12 in *LIDAR: range-resolved optical remote sensing of the atmosphere*, C. Weitkamp, Ed., Springer Science+Business Media, Inc., New York, 2005.

[144] Wertz, J.R. (2001), *Mission Geometry; Orbit and Constellation Design and Management*, Microcosm Press and Kluwer Academic Publishers, 2001.

[145] Wilson, R. and Munzenmayer, R. (2004), *Phase A System Study for the EarthCARE Mission: Final Report*, EADS Astrium report EarthCARE-RP-ASG-0001, Iss. 1, Rev. 0, 20 February 2004.

[146] Winker, D., Hostetler, C., and Hunt, W. (2004), *CALIOP: The CALIPSO Lidar*, 22nd International Laser Radar Conference, Matera, Italy, 12-16 July 2004.

[147] Wirth, M., Fix, A., Mahnke, P., Schwartzer, H., Schrandt, F., and Ehret, G. (2009), *The airborne multi-wavelength water vapor differential absorption lidar WALES: system design and performance*, Applied Physics B: Lasers and Optics, Volume 96, Issue 1, pp. 201-213, Springler-Verlag, July 2009.

[148] Yui, Y.Y., Goto, K., Kaneda, H., Katayama, H., Kotani, M., Miyamoto, M., Naitoh, M., Nakagawa, T., Saruwatari, H., Suganuma, M., Sugita, H., Tange, Y., Utsunomiya, S., Yamamoto, Y., Yamawaki, T. (2008), *Performance of lightweight large C/SiC mirror*, 7th International Conference on Space Optics, Toulouse, France, October 14-17, 2008.

[149] Zwally, H.J. et al (2002), *ICESat's laser measurements of polar ice, atmosphere, ocean, and land*, Journal of Geodynamics, 34 (2002) 405-455.

Appendix A

Trajectory Model

A.1 Introduction

This appendix contains the MATLAB scripts of the trajectory model. The structure of this appendix follows the structure of the Simulink model.

Each Matlab function is preceded by a small introduction of its role.

A.2 Initialisation

The altitude and spacecraft wet mass are set by the user. The altitude is used to compute the initial semi-major axis and inclination. The "initial" function also sets the other classical orbital elements. These are then converted to Equinoctial Orbital Elements by the "C2E" function.

A.2.1 Function "initial"

```
function inputs = initial(alt,BC)

% global constants
global MU;
global Rearth;
BC;
simu = 1;    % 1 for equinoctial, not normalised
             % 2 for cartesian normalised

if simu == 2
    MU = 1;
    Rearth = 1;
    omega_dot_earth = 1.606378006e-4; % rad/TU
    sma = (6378136.1+alt*1000)/6378136.1;
elseif simu == 1
    MU = 398600.4415e9;
    Rearth = 6378136.1;
    omega_dot_earth = 1.991063853e-7;    % rad/sec
    sma = (6378136.1+alt*1000);
else
    error
end
% other constants
J2 = 1.0826267e-3; % e-9
J3 = -2.5327e-6;   % e-9
JDini = 0;  % first point of Aries

% initial classical orbital elements
n = sqrt(MU/sma^3);
OM = 90*pi/180;
om = 90*pi/180;
ta = -90*pi/180;
% e and i by iteration
inc = 96.75*pi/180;
for iter = 1:5
    ecc = -J3/J2/2*Rearth/sma*sin(inc)*sin(om);
    cosi = -2/3*(omega_dot_earth)*(1-ecc^2)^2/n/J2*(sma/Rearth)^2;
    inc = acos(cosi);
end
coe0 = [sma,ecc,inc,OM,om,ta];
eoe0 = C2E(coe0);
inputs = [eoe0,BC];
```

A.2.2 Function "C2E"

```
function [rv] = coe2rv(COE)

format long;
global MU;
% equinoctial elements
a = COE(1);
e = COE(2);
i = COE(3);
OM = COE(4);
om = COE(5);
nu = COE(6);
% intermediate variables
Cnu=cos(nu);
Snu=sin(nu);
p = a*(1-e^2);
Rpqw = [p*Cnu/(1+e*Cnu);...
    p*Snu/(1+e*Cnu);...
    0];
Vpqw = [-sqrt(MU/p)*Snu;...
    sqrt(MU/p)*(e+Cnu);...
    0];

rotA = [cos(-om)    sin(-om)    0;...
    -sin(-om)   cos(-om)    0;...
    0   0   1];
rotB = [1   0   0;...
    0   cos(-i) sin(-i);...
    0   -sin(-i)    cos(-i)];
rotC = [cos(-OM)    sin(-OM)    0;...
    -sin(-OM)   cos(-OM)    0;...
    0   0   1];
% position and velocity vectors
Rijk = rotC*rotB*rotA*Rpqw;
Vijk = rotC*rotB*rotA*Vpqw;
rv = [Rijk;Vijk];
```

A.3 Equations of Motion

The time-derivative of the equations of motion are computed in the "equinoc" function. These are then integrated in Simulink.

```
function var = equinoc(inputs)
%format long e;
p = inputs(1);
f = inputs(2);
g = inputs(3);
h = inputs(4);
k = inputs(5);
L = inputs(6);

radial = inputs(7);
tangential = inputs(8);
normal = inputs(9);

global MU;
cL=cos(L);
sL=sin(L);
X=1+h^2+k^2;
W=1+f*cL+g*sL;
A=f+(1+W)*cL;
B=g+(1+W)*sL;
% ---------------------- Equations of motion ---------------------------
MATr = [0;...
    sL;...
    -cL;...
    0;...
    0;...
    0];
MATt = [2*p/W;...
    (f + cL*(W+1))/W;...
    (g + sL*(W+1))/W;...
    0;...
    0;...
    0];
MATn = [0;...
    -g*(h*sL-k*cL)/W;...
    f*(h*sL-k*cL)/W;...
    X*cL/2/W;...
    X*sL/2/W;...
    (h*sL-k*cL)/W];

var = [MATr MATt MATn]*[radial; tangential; normal]*sqrt(p/MU)...
    +[0;0;0;0;0;sqrt(MU*p)*(W/p)^2];
```

The Equinoctial Orbital Elements are then used to compute the position and velocity vector of the satellite in the Earth Centred Inertial (ECI) frame by the function "E2RV".

```
function [rv]=E2RV(EOE)

format long;
global MU;
% equinoctial elements
p = EOE(1);
f = EOE(2);
g = EOE(3);
h = EOE(4);
k = EOE(5);
L = EOE(6);
% intermediate variables
cL=cos(L);
sL=sin(L);
X=1+h^2+k^2;
W=1+f*cos(L)+g*sin(L);
alpha = h^2-k^2;
%beta = 1-h^2+k^2;
% position and velocity vectors
rx = p/W/X*(cos(L) + alpha*cL + 2*h*k*sL);
ry = p/W/X*(sin(L) - alpha*sL + 2*h*k*cL);
rz = 2*p/X*(h*sin(L)-k*cL)/(1+f*cL+g*sL);
vx = - sqrt(MU/p)/X*(sin(L) + alpha*sL - 2*h*k*cL + g - 2*h*k*f + alpha*g);
vy = - sqrt(MU/p)/X* (-cL + alpha*cL + 2*k*h*sL - f + 2*g*h*k + alpha*f);
vz = 2*sqrt(MU/p)/X* (h*cL + k*sL + f*h + g*k);
rv = [rx;ry;rz;vx;vy;vz];
```

A.4 Densities and Ephemerides

The following functions computes various parameters used by other functions to, in turn, determine disturbing forces.

The "densities" function computes the minimum and maximum densities for three reference altitudes (240, 300 and 360 km) for the $F_{10.7}$ index estimated at a given simulated time.

Two ephemerides functions "sunephemeris" and "moonephemeris" compute the position of the Sun and the Moon, respectively, at a given simulated time.

A.4.1 Densities

```
function [ref_dens] = densities(t)
% ----------------- Reference densities --------------------
% the columns of the tables are:
% ---- F10.7 index ¦ 240 km ¦ 300 km ¦ 360 km --------------
% minimum densities
ref_min = [...
    70 25.53 3.01 0.4828;...
    100 43.87 6.553 1.321;...
    150 83.02 16.46 4.241;...
    200 128.8 31.71 9.667;...
    250 175.4 51.07 17.75];

% maximum densities
ref_max = [...
    70 47.56 8.532 2.083;...
    100 75.57 16.88 4.882;...
    150 122.5 34.81 12.33;...
    200 166.5 55.49 22.37;...
    250 206.0 76.41 33.89];

% ------  Find F10.7 index, min & max densities and scale heights --------
tzero = 2454911;     % 20 Mar 2004 (lo) = 2,453,085
                     % 20 Mar 2009 (hi) = 2,454,911
tref = 2444606;      % 1st Jan 1981
days = t/3600/24 + (tzero - tref);
Findex = 145 + 75*cos(0.001696*days+0.35*sin(0.00001695*days));

% ---------------- Look up table of densities -------------------
min_rhos = interp1(ref_min(:,1),ref_min(:,2:4),Findex,'spline');
max_rhos = interp1(ref_max(:,1),ref_max(:,2:4),Findex,'spline');

% ----------------- Formatting the output ----------------------
ref_dens = [min_rhos,max_rhos];
```

A.4.2 Sun Ephemeris

```
function Rsun = sunephemeris(time)
% Sun ephemeris returning Sun vector in ECI frame (in km)
%
% ------------ Convert time to days ------------------
tdays = time / 3600/24;
tzero = 2451625.0;  % Descending node / spring equinox = start of sim
tref = 2451545.0;   % J2000 reference date
tcent = (tzero - tref + tdays) /36525;

% ------------ Computation of Sun's position -------------
M = 357.5256 + 35999.049 * tcent;   % in degrees
Mrad = M *pi/180;
% Sun's ecliptic longitude
lambdasun = 282.94+ M+6892/3600*sin(Mrad)+72/3600*sin(2*Mrad);  % in deg
rsun = (149.619 - 2.499*cos(Mrad)-0.021*cos(2*Mrad))*1e6;        % in km
lsunrad = lambdasun*pi/180;
% Sun's position vector in ECI
ecliptic = 23.4393*pi/180;
Rsun = rsun*[cos(lsunrad);...
    sin(lsunrad)*cos(ecliptic);...
    sin(lsunrad)*sin(ecliptic)];
%------------- End of sun ephemeris function -------------
```

A.4.3 Moon Ephemeris

M-file

```
function Rmoon = moonephemeris(time)
% Moon ephemeris returning Moon vector in ECI frame, in km.

% ----------------- Convert time to days -----------------
tdays = time / 3600/24;

% ------------ Computation of Sun's position -------------
Xm = 16.6...
    + 382*sin(2*pi/27.3215*(tdays-4.43))...
    + 16*sin(2*pi/2065*(tdays-363))...
    + 5.6*sin(2*pi/194*(tdays+16))...
    + 10.45*sin(2*pi/13.7*(tdays-12));

Ym = -1.37...
    + 351.1*sin(2*pi/27.3215*(tdays-11.1))...
    + 28.75*sin(2*pi/3134*(tdays-806))...
    + 5.566*sin(2*pi/195.6*(tdays-29.5))...
    + 9.6*sin(2*pi/13.7*(tdays-1.62));

Zm = -1.3...
    + 158.8*sin(2*pi/27.322*(tdays-12.5))...
    + 10.5*sin(2*pi/2710*(tdays-855))...
    + 2.48*sin(2*pi/195.1*(tdays-31))...
    + (10.2 + 9.5*cos(2*pi*tdays/1518)) * sin(2*pi/27.58*(tdays+2.9));

Rmoon = [Xm;Ym;Zm]*1e3;  % position in km
% ------------- End of moon ephemeris function -------------
```

A.5 Drag Force

The drag force is computed in the ECI frame by the "drag" function, and has for inputs the position and velocity of the spacecraft, the reference densities and the position of the Sun.

```
function [Fdrag] = drag(in);
global Rearth;
R = [in(1);in(2);in(3)];
V = [in(4);in(5);in(6)];
refdens_min = in(7:9);
refdens_max = in(10:12);
Rsun = in(13:15);


% ------------------ Compute relative velocity -------------------
om = 72.921e-6;       % Earth rotation in rad/s
Vrel = V - (cross([0 0 om],R))';

% ----------------------- Altitude domain -----------------------
h = norm(R)-Rearth;

h_lo = 240000;
h_hi = 300000;
option = 1;
if h > h_hi
    h_lo = 300000;
    h_hi = 360000;
    option = 2;
end

if option==1
        rhom_lo = refdens_min(1);
        rhom_hi = refdens_min(2);
        rhoM_lo = refdens_max(1);
        rhoM_hi = refdens_max(2);
else
        rhom_lo = refdens_min(2);
        rhom_hi = refdens_min(3);
        rhoM_lo = refdens_max(2);
        rhoM_hi = refdens_max(3);
end
```

```
% ---------------- associated scale heights --------------------
    Hm = (h_lo-h_hi)/log(rhom_hi/rhom_lo);
    HM = (h_lo-h_hi)/log(rhoM_hi/rhoM_lo);

% ----------- minimum and maximum densities at altitude h ------
rho_min = rhom_lo * exp((h_lo-h)/Hm);
rho_max = rhoM_lo * exp((h_lo-h)/HM);

% --------------------- Sun's position -------------------------
rias = atan2(Rsun(2),Rsun(1));
decl = atan2(Rsun(3),sqrt(Rsun(1)^2+Rsun(2)^2));

% diurnal bulge vector in ECI frame
lambdalag = pi/6; % 30 deg * pi/180
UB = [cos(decl)*cos(rias+lambdalag);...
    cos(decl)*sin(rias+lambdalag);...
    sin(decl)];

% --------------------- actual density -------------------------
halfn = 3;                                  % n = 6 for polar orbits
cosn_halfpsi = (1/2 + R'*UB/norm(R)/2)^halfn;
rho = (rho_min + (rho_max - rho_min) * cosn_halfpsi)*1e-12;

% ---------------------- drag force ----------------------------
% per unit ballistic coefficient:
Fdrag = -.5 * rho * norm(Vrel) * Vrel;

output = Fdrag;
% ---------------------- END OF FUNCTION ----------------------------
```

A.6 Geopotential disturbance

The "geopotential" function computes the disturbing acceleration in the ECI frame of a non-spherical, non-homogenous Earth. Its sole input is the position and velocity of the satellite in the ECI frame, coming from the "E2RV" function.

```
function [aECI] = geopotential(rv)
%-------------------------------------------------------------------------
% This function computes the acceleration in ECI coordinates due to
% a non-spherical Earth.
% Nicolas Leveque, 12 February 2010
%-------------------------------------------------------------------------
global MU;
global Rearth;
format long e;
% J1    J2          J3       J4      J5      J6
J=[0 1082626.7 -2532.7 -1619.6 -227.3 540.7]*1e-9;
J2 = 1082626.7e-9;
% The position vector r must be in inertial coordinates.
ri=rv(1);
rj=rv(2);
rk=rv(3);
normR = sqrt(ri^2+rj^2+rk^2);

    P0=1;
    P(1) = rk/normR;          %P(1) = sin(phi) = rk / sqrt(ri^2+rj^2+rk^2)
    P(2) = 1.5*P(1)*P(1)-0.5;  % eq. for P(2-6) simplified
    P(3) = 5*P(1)*P(2)/3 - 2*P(1)/3;
    P(4) = 7*P(1)*P(3)/4 - 3*P(2)/4;
    P(5) = 9*P(1)*P(4)/5 - 4*P(3)/5;
    P(6) = 11*P(1)*P(5)/6 -5*P(4)/6;

    % Computation of the partial derivative of the Legendre polynomial
    Pprime(1)=1;
    Pprime(2)=P(1)*3;         % simplified with P(1) = sin(phi)
    Pprime(3)=P(1)*Pprime(2) + 3*P(2);
    Pprime(4)=P(1)*Pprime(3) + 4*P(3);
    Pprime(5)=P(1)*Pprime(4) + 5*P(4);
    Pprime(6)=P(1)*Pprime(5) + 6*P(5);
```

```
% Computation of the ACCELERATION in a LVLH frame
% ------------------------------------------------
% Sum for the Zenith component
 z2 = 3*(Rearth/normR)^2*P(2)*J(2);
z3 = 4*(Rearth/normR)^3*P(3)*J(3);
z4 = 5*(Rearth/normR)^4*P(4)*J(4);
z5 = 6*(Rearth/normR)^5*P(5)*J(5);
z6 = 7*(Rearth/normR)^7*P(6)*J(6);
sum1 = z2 + z3 + z4 + z5 + z6;

% Sum for the North component
 n2 = (Rearth/normR)^2*Pprime(2)*J(2);
n3 = (Rearth/normR)^3*Pprime(3)*J(3);
n4 = (Rearth/normR)^4*Pprime(4)*J(4);
n5 = (Rearth/normR)^5*Pprime(5)*J(5);
n6 = (Rearth/normR)^6*Pprime(6)*J(6);
sum2 = n2+ n3 + n4 + n5 + n6;

% acceleration in the Zenith-East-North (ZEN) LVLH frame
 gz = MU/normR^2 * sum1;
 gn = -MU/normR^2 * (sqrt(ri^2+rj^2)/normR) * sum2;
 aZEN = [gz;0;gn];

% Transform ZEN into ECI
 Z = [ri;rj;rk]/normR;
 E = [-rj;ri;0]/norm([-rj;ri;0]);
 N = [-rk*ri;-rk*rj;rj^2+ri^2]/norm([-rk*ri;-rk*rj;rj^2+ri^2]);
 aECI = [Z E N]*aZEN;

%------------------------ END OF THE FUNCTION ----------------------------
```

A.7 Third-body perturbations

The "thirdbody" function computes in the ECI frame the disturbing gravitational force of the Sun and the Moon on the satellite. Its inputs are the position and velocity of the satellite, and the positions of the Sun and the Moon.

```
function aTB = thirdbody(in)
% Acceleration due to third-body perturbation from the Sun and Moon
% All parameters are in km.
Rsc = in(1:3)/1000; % converted from metres into kilometres
Rsun = in(7:9);
Rmoon = in(10:12);

% ------------ Computation of parameter q -----------------
qm = Rsc'*(Rsc-2*Rmoon)/norm(Rmoon)^2;    %(Rmoon'*Rmoon);
qs = Rsc'*(Rsc-2*Rsun)/norm(Rsun)^2;      %(Rsun'*Rsun);
% ----------------- Computation of F(q) -------------------
Fqm = qm*(3+3*qm+qm^2)/(1+(1+qm)^1.5);
Fqs = qs*(3+3*qs+qs^2)/(1+(1+qs)^1.5);
% ------- Computation of disturbing acceleration ----------
dm = norm(Rsc-Rmoon);
ds = norm(Rsc-Rsun);
mum = 4902.8;    % gravitational parameter of the moon, km3/s2
mus = 132.7e9;   % gravitaitonal parameter of the sun, km3/s2
am = -mum/dm^3 * (Rsc + Fqm*Rmoon);
as = -mus/ds^3 * (Rsc + Fqs*Rsun);
aTB = (am+as)*1000; % Computed in km/s2, converted to m/s2
% ------------ End of the thirdbody function --------------
```

A.8 Solar Radiation Pressure

The solar radiation pressure is computed by the "SRP" function. Its inputs are the position and velocity of the satellite, the position of the Sun and the simulated time. Note that for all simulated cases, the surface area of the solar array is assumed to be that of the 1.1-m instrument at 290-km altitude, which corresponds to the worst-case.

```
function Fsrp = SRP(in)
% Force due to solar radiation pressure on the SC body and solar arrays.

% ------- Inputs -------
Rsc = in(1:3);
Vsc = in(4:6);
Rsun = in(7:9);
time = in(10);

% ------- Solar flux --------
tzero = 2451625.0;
JD = tzero + time/3600/24;
cos_a = cos(2*pi*(JD-2451730)/365.25);
SF = 1358 / (1.004 + 0.0334*cos_a);

% ------- Sun vector wrt SC in ECI frame --------
RssECI = Rsun - Rsc;

% ------- SRP force in ECI frame ------
Abody = 6;  % approximate surface area of the spacecraft body
Asa = 13.1; % Solar array surface area for the worst case (1.1-m @ 290 km)
Fsrp = -(SF/3e8) * (1.86*Abody + 1.1*Asa) * RssECI / norm(RssECI);
% ---------------------- End of the SRP function ------------------------
```

A.9 Remaining Functions

A.9.1 Transformation from ECI to RTN

The disturbing forces and accelerations are all computed in the ECI frame. They are pre-multiplied in Simulink by the output of the "rotframe" function so as to be transformed into the RTN frame.

```
function Q = rotframe(rv)
R=[rv(1);rv(2);rv(3)];
V=[rv(4);rv(5);rv(6)];

%cRVcR=cross(cRV,R);
Ir = R/norm(R);
In = cross(R,V)/norm(cross(R,V));
It = cross(In,Ir)/norm(cross(In,Ir));
Q=[Ir It In]';
```